# Mathematical modelling of the dynamic response of metamaterial structures

*Thesis submitted in accordance with the requirements of the University of Liverpool for the degree of Doctor in Philosophy by*

*Daniel John Colquitt*

*July 2013*

**Mathematical modelling of the dynamic response of metamaterial structures**

*Daniel John Colquitt*

**Abstract**

This thesis constitutes an exposition of the work carried out by the author whilst examining several physical problems under the broad theme of the dynamic response of metamaterial structures. An outline of the thesis is provided in chapter 1. Chapter 2 introduces some notation and preliminary results on general lattice equations. Chapter 3 examines the dispersive behaviour of non-classical discrete elastic lattice systems. In particular, the effect of distributing the inertial properties of the lattice over the elastic rods, in addition to at the junctions, is considered. It is demonstrated that the effective material properties in the long wavelength limit are not what one would expect from the static response of the lattice. The effect of various interactions on the dispersive properties of the triangular cell lattice is considered, including so-called truss, frame, and micro-polar interactions. Compact analytical estimates for the band widths are presented, allowing the design of metamaterial structures possessing pass and/or stop bands at specific frequencies and in specified directions.

The finite frequency response of several lattice structures is considered in chapter 4. In particular, the dynamic anisotropy of both scalar and elastic lattices is examined. The resulting strongly anisotropic material response is linked, explicitly, to the dispersive properties of the lattice. A novel application of dynamic anisotropy to the focusing, shielding, and negative refraction of elastic waves using a flat discrete "*metamaterial lens*" is presented.

Chapter 5 is devoted to the analysis, using the dynamic Green's function, of a finite rectilinear inclusion in an infinite square lattice. Several representations of the Green's function are presented, including expression in terms of hypergeometric functions, which are employed in deriving band edge expansions. It is shown that localised defect modes, characterised by displacements which decay rapidly away from the defect, can be initiated by reducing the mass of one or more lattice nodes, whilst ensuring that the mass of the nodes remains positive. For one- and three-dimensional multi-atomic lattices, there exists a bound on the contrast in mass between the defect and ambient lattice such that localised defect modes exist. However, it is shown that for the two-dimensional lattice, no such bound exists, provided that the masses remain positive. The analysis of a finite-sized defect region is accompanied by the waveguide modes that may exist in a lattice containing an infinite chain of point defects. A numerical simulation illustrates that the solution of the problem for an infinite chain can be used to predict the range of eigenfrequencies of localised modes for a finite but, sufficiently long, array of masses representing a rectilinear defect in a square lattice.

Continuing with the theme of defects, chapter 6 examines response of a triangular thermoelastic lattice, with an edge crack under mode I loading. The response of the triangular lattice is compared with that of the corresponding continuum. The model is related to the phenomenon of thermal striping, which occurs when a structure is exposed to periodic variations in temperature. In the thermal striping regime, crack propagation is a fatiguing processes with the rate of crack growth being proportional to some power of the peak-to-peak amplitude of the stress intensity factor. An *"effective stress intensity factor"* for the lattice is introduced and it is demonstrated that, in the homogenised limit, the *"effective stress intensity factor"* is lower than the stress intensity factor of the continuum for sufficiently long cracks and low frequencies.

Finally, chapter 7 presents a detailed analysis of a non-singular square cloak for acoustic, out-of-plane shear elastic, and electromagnetic waves. The propagation of waves through the cloak is examined analytically and is complemented with a range of numerical illustrations. The efficacy of the regularised cloak is demonstrated and an objective numerical measure of the quality of the cloaking effect is introduced. The results presented show that the cloaking effect persists over a sufficiently wide range of frequencies. To illustrate further the effectiveness of the regularised cloak, a Young's double slit experiment is presented. The stability of the interference pattern is examined when a cloaked and uncloaked obstacle are successively placed in front of one of the apertures. A significant advantage of this particular regularised square cloak is the straightforward connection with a discrete lattice. It is shown that an approximate cloak can be constructed using a discrete lattice structure. The efficiency of such a lattice cloak is analysed and several illustrative simulations are presented. It is demonstrated that effective cloaking can be achieved by using a relatively simple lattice, particularly in the low frequency regime. This discrete lattice structure provides a possible avenue toward the physical realisation of invisibility cloaks.

# Contents

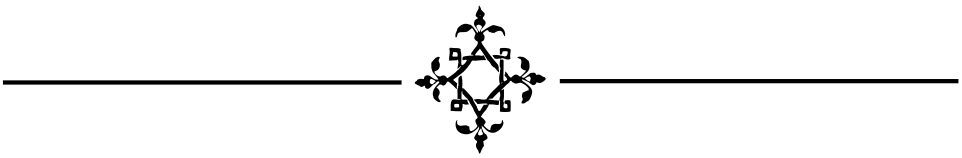

# List of Figures

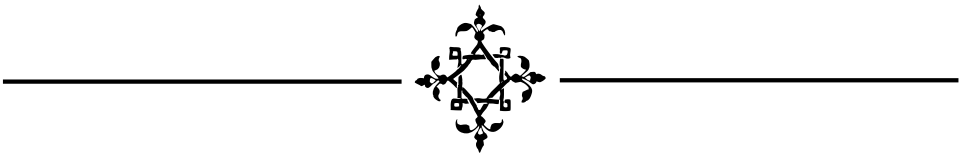

# List of Tables

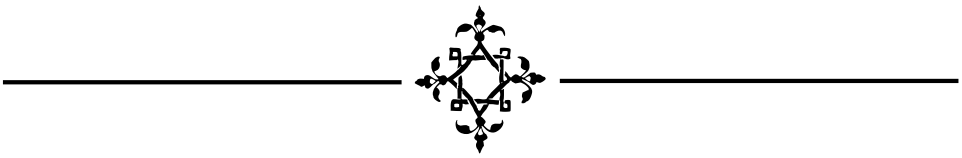

# Acknowledgements

Carrying out the requisite work and then writing this thesis was, undoubtably, the most arduous task I have undertaken. However, one of the joys of having completed the thesis is looking back at everyone who has helped me over the past three, seven, and twenty-five years.

I would like to begin by thanking my three supervisors: Professors Sasha Movchan, Ian Jones, and Natasha Movchan. It is an often used cliché, but in this case it is no overstatement to say that without the consistent guidance, support, encouragement, and unparalleled knowledge of my three supervisors, this thesis would never have existed. In particular, I would like to thank Natasha who went above and beyond to read every line of the manuscript in meticulous detail. I must say a special thank you to Sasha and Ian who, during my third year as an undergraduate, whetted my appetite for research and gave me the opportunity to study mathematics further.

Thank you also to Will Daniels and Serco Assurance for piquing my interest in industrial mathematics and providing me with such an interesting project to study during my third year as an undergraduate. Examining a thesis is a substantial and often thankless task. Therefore, I would like to express my sincere gratitude to Professor Mishuris and Dr Piliposyan for taking the time to examine my thesis in detail and for the stimulating for discussion during my viva voce.

I would also like to thank the co-authors of my papers: Dr Mike Nieves for his encouragement, support and guidance; Dr Michele Brun for his hard-work, willingness to help, and knowledge, but mostly for his sense of humour; and Professor Ross McPhedran for his unsurpassed experience and knowledge of Mathematical Physics. I should also like to thank fellow graduate student Stewart Haslinger, and indeed all the graduate students at the Department of Mathematical Sciences, primarily for giving me someone to moan at when work wasn't progressing according to plan.

To my family, particularly my parents and sister, thank you for your love, support, and unwavering belief in me. Without you, I would not be the person I am today. Above all I would like to thank my wife Nicola for her love and constant support, for all the late nights and early mornings, and for keeping me sane over the past few months. Thank you for being my muse, editor, proofreader, and sounding board. But most of all, thank you for being my best friend. I owe you everything.

Finally, despite my love for mathematics, the work reported in this thesis would not have been possible without the financial support of an EPSRC studentship (EP/H018514/1), for which I am grateful.

D.J. Colquitt
Liverpool, August 2013

# Declaration

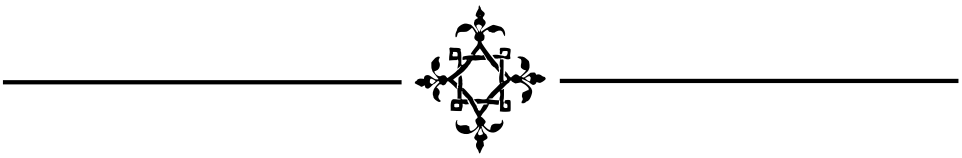

Unless otherwise stated, the work reported herein is the result of my own research activities carried out in the Department of Mathematical Sciences at the University of Liverpool during the period of August 2010 until July 2013. No part of the work presented in this thesis has been submitted in partial or whole fulfilment of the requirements for another degree.

The work which constitutes this theis is based on the following contributions that have previously been published.

- Colquitt DJ, Movchan AB, Movchan NV, & Jones IS. (2011) Elastic Waves and Defect Modes in Micropolar Lattices. *Proc. Int. Conf. on Vibration Problems* (ed. J Náprstek et al.), 707–714. Springer Proceedings in Physics **139**.
(doi: 10.1007/978-94-007-2069-5_95)

- Colquitt DJ, Jones IS, Movchan NV, & Movchan AB. (2011) Dispersion and localisation of elastic waves in materials with microstructure. *Proc. R Soc. A* **417**(2134), 2874–2895.
(doi: 10.1098/rspa.2011.0126)

- Colquitt DJ, Jones IS, Movchan NV, Movchan AB, & McPhedran RC. (2012) Dynamic anisotropy and localization in elastic lattice systems *Waves Random Complex* **22**(2),143–159.
(doi: 17455030.2011.633940)

- Colquitt DJ, Nieves MJ, Jones IS, Movchan NV, & Movchan AB. (2012) Trapping of a crack advancing through an elastic lattice. *Int. J Eng. Sci.* **61**, 129–141.
(doi: j.ijengsci.2012.06.016)

- Colquitt DJ, Nieves MJ, Jones IS, Movchan AB, & Movchan NV. (2013) Localisation for a line defect in an infinite square lattice. *Proc. R Soc. A* **469**:20120579
(doi: 10.1098/rspa.2012.0579)

- Colquitt DJ, Jones IS, Movchan NV, Movchan AB, Brun M, & McPhedran RC. (2013) Making Waves Round a Structured Cloak: *Lattices, Negative Refraction and Fringes*. *Proc. R. Soc. A* **469**:20130218
(doi: 10.1098/rspa.2013.0218)

# *Chapter One*

# Introduction

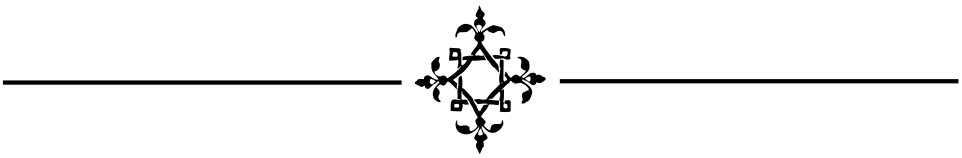

This thesis is devoted to the analysis of a wide range of physical problems which are encompassed by the unified theme of the dynamic response of metamaterial structures. In particular, the present text deals with wave propagation, shielding, focusing, fracture and defects, and cloaking in structured materials. The present chapter provides an overview of the thesis together with a brief review of the most relevant scholarly literature.

The study of wave propagation in structured media can be traced as far back as the $17^{\text{th}}$ century with the publication of Newton's Principia [112]. For instance, Newton [112] studied a one-dimensional mass-spring lattice system and derived an expression of the speed of sound propagation. Despite being studied for several centuries, wave propagation in structured media and the contemporary fields of photonics, phononics and platonics remains an active area of research. An extensive bibliography of research in photonics, phononics, and metamerials can be found in [42]. As noted in [42], the number of publications in these areas is growing year on year. The classic monograph by Brillouin [14] remains an excellent introductory text for wave propagation in structured media. In his monograph, Brillouin treats a wide range of physical problems beginning from a simple one-dimensional mass spring chain, to crystal dynamics, and linear particle accelerators. The unifying theme of the book [14] is the periodic arrangement of elementary units to create a large, often infinite, structure. The book by Born and Huang [9] is considered the classical treatise on lattice dynamics from the viewpoint of quantum mechanics. The overarching aim of the book [9] is the linkage of macroscopic properties of crystals to their microstructure in the long wavelength limit; it deals with the optical, thermal, piezoelectric, and elastic properties of lattices. For example, Born and Huang use potential theory motivated by the underlying quantum mechanical principles to deduce the macroscopic elastic response of the crystal; these types of interaction are referred to as *central interactions* in the present thesis. In order to deduce the thermal properties of the crystal, Born and Huang resort to the framework of finite deformations. In terms of defects in lattices, the excellent monograph by Maradudin et al. [98] focuses on defects in crystallography in three dimensional lattices. Many of the approaches and results presented in [9, 14, 98] are nowadays considered as standard and are often

presented in upper-graduate level texts such as Kittel [85]. The book by Joannopoulos et al. [70] provides a comprehensive overview of the propagation of light through photonic crystals. This very accessible text [70] begins with elementary examples of one-dimensional problems leading to a discussion on the design of photonic crystals for specific applications. Musgrave's *Crystal Acoustics* [110], also provides an excellent introduction to wave propagation in crystals and lattices. The book [110] deals not only with lattice dynamics but also with the mechanics of continuous anisotropic media. In particular, [110] provides a good introduction to the concepts of group and phase velocity, and slowness and wave surfaces in the setting of anisotropic media. Such concepts are usually introduced for isotropic media and their generalisation to anisotropic media are non-trivial.

Some preliminary results for lattices, together with some necessary notation, are introduced in chapter 2. Chapter 3 is devoted to the study of the dispersive properties of elastic lattice structures and, in particular, their homogenised properties in the low frequency range. Usually, these effective properties are determined from the static response of the material [27, 50, 100, 123] and are regarded as being valid for small, but not necessarily zero, frequencies. However, it is shown in chapter 3 that for lattices with inertial links, their dynamic response is not necessarily accurately described by their static response, even at small frequencies. The study of two-dimensional elastic discrete systems, accompanied by the analysis of dispersion properties of waves, was included in the paper by Martinsson and Movchan [101]. It has been demonstrated that it is possible to control the position of stop bands by re-distributing the mass across the junctions of the lattice structure. In [101], the techniques required to analyse the dynamic properties of discrete structures were summarised. The method used to analyse the dispersive properties of discrete structures in the present thesis is similar to those described in [14, 98, 101], and many other texts which treat periodic structures. The spectral properties of two-dimensional triangular, hexagonal, square, and Kagomé lattices have also been examined by Phani et al. [127]. In particular, for so-called *"cellular solids"* formed from a uniform continuous array of slender ligaments without additional mass at the junctions, Phani et al. [127] demonstrated that the effective material properties determined from long-wave asymptotes to the dispersion curves agree with the effective material properties determined from the static response (see, for example, the book by Gibson and Ashby [50], the paper by Christensen [27], and the review by Ostoja-Starzewski [123]). The method of using long-wave asymptotics to approximate the dispersion curves and, hence, determine the effective elastic moduli has also been applied to structured continua (see, for example, the paper by Carta and Brun [22]). Long wavelength homogenisation using finite difference formalism to derive governing equations for the corresponding effective continuum has also been considered by many authors (see [51] and reference therein).

In the early 1980's Kunin [88], Morozov [107], and Nazarov and Paukshto [111] studied static lattices with torsional interactions. Later, Maz'ya along with Morozov and Nazarov [102] also considered two-dimensional static lattices, within the context of homogenisation, and introduced a potential of torsional interaction between elastic ligaments at the junction points. The problem was reduced to a finite difference system of equations and, for triangular and hexagonal lattices with central and torsional interactions, a connection was made with the homogenised isotropic continuum. The homogenised Lamé coefficients were evaluated and a ro-

tational micro-polar interaction was identified. The effects of micro-polar interactions in the continuum have been discussed by Eringen [43, 44], and Kafadar and Eringen [83]. The lattice model involving elastic rods with both longitudinal and flexural stiffness together with the derivation of the long-wave approximation for homogenised equations of motion for the micro-polar medium have been discussed by Askar and Cakmak [4]. More recently, Spadoni et al. [140] examined the phononic properties of chiral hexagonal cellular solids. In this case, Spadoni et al. [140] introduced the chiral lattice as an array of circular elements of finite radius, connected via thin ligaments tangent to the circular elements. Spadoni et al. [140] presented dispersion diagrams and examined the influence of the cell geometry on the dispersive properties of the lattice.

The paper by Jones and Movchan [80] includes a model of dynamic defects within an elastic system induced by thermal pre-stress. In this case, temperature was used as a control parameter and the pre-stressed elastic system responded by changing its filtering properties with respect to elastic waves propagating through the system. The elastic system was composed of a periodic array of multi-scale resonators. Analysis of dispersion properties of waves in periodic solids with pre-stress was also presented in the paper by Gei et al. [49] and the paper by Jones et al. [81]. In the former paper, the authors considered the dispersive properties of an array of piecewise homogeneous beams on an elastic foundation. The authors demonstrated that the effect of pre-stress can significantly affect the position and size of band gaps in the dispersion diagrams. In the latter paper, the authors returned to the elastic system used in [80]. The authors considered the effect of defects, cracks in the ligaments connecting the resonators to the surrounding matrix in this case, on the dispersive properties and the low frequency eigenmodes. Further, the authors presented an interesting application of these multi-scale resonators: using a finite width slab of resonators, the authors were able to simulate a flat elastic lens, which was used to filter or focus waves of certain frequencies. This idea is one which shall be returned to later in the thesis. Chapter 3 is based on the work by the author and his colleagues reported in [29].

The behaviour of scalar and vector lattices in the frequency range where the response of the material is strongly anisotropic is discussed in chapter 4. It is demonstrated that this *dynamic anisotropy* is linked to, and can be predicted from, the dispersive properties of the microstructure. The displacement field resulting from a point load oscillating at a resonant frequency, corresponding to a saddle point on the dispersion surface, is quite striking. In the literature, such displacement fields are often referred to as *primitive waveforms* (see, for example, [5, 121]). These *primitive waveforms* for scalar lattices have been examined in [5, 90, 91, 121]. As shown by the present author and his colleagues in [31], *primitive waveforms* also exist in vector lattices. Moreover it was shown in [31] that, in contrast to the scalar case, for vector problems these *primitive waveforms* are not necessarily linked to resonant frequencies. Chapter 4 also contains several numerical illustrations, which demonstrate some novel applications including filtering and focusing of in-plane elastic waves by a fully discrete *"metamaterial flat lens"*.

For scalar lattice problems at finite frequencies, Craster and his co-workers [34, 37, 38, 96] have developed a two-scale asymptotic procedure to determine the material properties of an effective continuum. The approach used in the aforementioned papers is essentially that of the method of multiple scales (see, for example, [7, 84]). The "*High Frequency Homogenisation*" em-

ployed by Craster et al. involves the introduction of two scales and expresses the solution as a product of the envelope function, that is a function of the slow variable, and some periodic (or quasi-periodic) function, which is a function of the fast variable. The small parameter is the size of the elementary cell (or some other length scale related to the micostructure) scaled by a length related to the macro-structure. Following the introduction of an appropriate ansatz, the problem then decomposes into a series of problems based on powers of the small parameter $0 < \varepsilon \ll 1$. Physically, this approach corresponds to perturbations away from standing wave solutions in periodic systems and the solution is decomposed into the product of a function of the fast variable and a function of the slow variable. The function of the fast variable describes the standing wave solution in the vicinity of the resonant frequency and the function of the slow variable is monotonic, usually decaying, and describes the macroscopic behaviour. The aforementioned series of papers by Craster and his co-workers originates with the paper by Adams et al. [1], which treats the problem of thin acoustic strips using high frequency homogenisation. The paper by Craster et al. [37] introduces the general method for scalar fields in the continuum. Immediately following [37], a further paper by Craster et al. [38] applies the method of high frequency homogenisation to one-dimensional and two-dimensional periodic scalar lattices. This approach has been applied to various configurations including so-called *checkerboard* structures in the continuum leading to interesting phenomena including slow waves and negative refraction [35, 36]. High frequency homogenisation has also been applied to periodic metamaterial composites with resonators [3] as well as platonic crystals formed by arrays of pins in thin elastic (Kirchhoff) plates [2]. Following the work with *checkerboard* materials, Craster et al. published a pair of papers which, in part, examined star shaped waveforms in scalar lattices [34, 96]. In terms of *primitive waveforms*, the result of high frequency homogenisation is a pair of hyperbolic partial differential equations, who's sum describes the *primitive waveforms* at resonant frequencies, and who's coefficients yield the effective material properties. To the best of this author's knowledge, the approach of Craster et al. is restricted to scalar fields at the present time.

Focusing and diffraction in optical systems have been discussed extensively in the literature. The standard approach to refraction, focusing, and diffraction theory can be found in many textbooks including, for example, the classic book by Born and Wolf [10]. More recently, the book by Nye [118] treats diffraction patterns associated with caustics from the point of view of catastrophe theory. Callaway [20] considered the scattering of waves in solids with periodic arrays of defects. In elasticity, Poulton et al. [130] extended the Rayleigh method [133] to examine the scattering of elastic waves for a doubly periodic structure. In terms of lattice dynamics, one can identify so-called *line localised primitive waveforms* (LPW) [5, 121], which consist of a line of oscillating particles with the remaining particles being stationary. As observed in [5, 121], these LPWs are associated with stationary points on the dispersion surfaces. Using the methods of stationary phase, Langley has examined the response of a square scalar lattice subjected to harmonic [90] and transient [91] point loading. Particular attention was given to the nature of the caustics, which requires careful consideration when applying the method of steepest decent. In chapter 4 of the present thesis, the required integrals are computed directly, using numerical techniques. Whilst more computationally intensive, this direct approach is both more convenient and can be applied in the neighbourhood of the source.

In 2002, Bigoni and Movchan [8] introduced the concept of structural interfaces with finite thickness, which join two continuous regions. In the paper [8], the authors noted that the inertial properties of the interface significantly affect the dynamic response and lead to unusual filtering properties for elastic waves. Later Brun et al. [16] employed a structured interface between two continuous domains to demonstrate the focusing of elastic waves via negative refraction. The authors refered to the structural interface as a *"flat lens for elastic waves"*. Similar effects have also been demonstrated in acoustics (see, for instance, Guenneau et al. [62]). In chapter 4 of the present thesis, the effects of focusing and filtering of elastic waves is extended to entirely discrete structures. In particular, a diatomic interface lattice embedded in a monatomic ambient lattice of the same geometry is considered. It is shown that, for certain frequencies, the interface lattice acts as a flat elastic lens.

In chapter 4 of this thesis, an elastic triangular lattice that is isotropic in the long wavelength limit [29] is considered in the setting of plane strain; it is demonstrated that strong anisotropy exists at higher frequencies. In particular, the presence of localised waveforms previously illustrated for scalar lattices [5, 90, 91, 121] is demonstrated. The resulting anisotropy, diffraction patterns, and aberrations are explained classically using the dispersion surfaces and slowness contours. The vector nature of the problem yields several novel and interesting features, including the presence of strongly preferential directions and the ability to *"switch"* these preferential directions by varying the frequency and/or type of applied load. Chapter 4 is based on the work previously reported in [29, 31].

Continuing with the theme of localised waves, the problem of localised defect modes associated with eigenmodes generated by finite and infinite defects in infinite two-dimensional square lattices is considered in chapter 5. The behaviour of a lattice with a single point defect, or point source, can be described by the lattice Green's function, as studied by Martin [99] for a two-dimensional square lattice. The resulting solution was analysed [99] for frequencies within the pass band and the corresponding asymptotics at infinity were also obtained. A year later, Movchan and Slepyan [109] examined several classes of continuous and discrete models with various forcing or defect configurations. Localised modes were identified for the case when the forcing frequency (or natural frequency of the defect) was located in the stop band. For a particular choice of the mass variation, these defect modes were then linked to the stop-band Green's function which were used in the construction of the defect modes.

In the paper [49], Gei et al. considered the effect of uniform pre-stress on the propagation of flexural waves through an elastic beam on a Winkler foundation using methods similar to those of [109]. Particular attention was devoted to band-gap localised modes and control of the position of stop-bands via pre-stress. It was found that a tensile pre-stress can increase the frequency at which a particular band gap occurs. It was also shown that band gaps can be *annihilated* with the application of an appropriate pre-stress.

Lattice Green's functions are often studied in isolation and have proved a rich area of research (see, for example, [11,40,82,150], and references therein). For $d$-dimensional lattices, the Green's function is typically expressed as a $d$-dimensional Fourier integral. It is often possible to evaluate one or more of the integrals, as in the paper by Movchan and Slepyan [109], but for $d > 1$ the Green's function cannot be expressed in terms of elementary functions. In chapter 5, several

different representations of the Green's function for a square lattice are presented, which prove useful for band-edge expansions. In particular, it is useful to express the lattice Green's function in terms of a generalised hypergeometric function. This hypergeometric series is well behaved in the stop band of the ambient lattice, but diverges in the pass band. However, via analytic continuation, compact asymptotic expressions for localised modes near the edge of the pass band can be derived. These band-edge modes are localised, but since they exist at frequencies close to the edge of the pass band, they can be considered as *"almost propagating"*. Such modes are also often referred to as *shallow defect states* in the literature and are of considerable interest in, for example, photonics [41, 95].

Classical applications in the theory of defects in crystals and dislocations follow from the fundamental work of Maradudin [97], where explicit closed form solutions were derived for a heterogeneous lattice system when two distant particles of different masses are interchanged. More recently, the envelope function based perturbation approach was developed by Mahmoodian et al. [95] and Dossou et al. [41] for analysis of waveguides in photonic crystal structures. In the latter case, an array of cylinders (inclusions) represents a waveguide within a two-dimensional structure, and the frequencies of the guided modes are close to the band edge of the unperturbed doubly periodic system.

Localisation of waves due to an infinite line defect embedded in an infinite square lattice, has been considered by Osharovich and Ayzenberg-Stepanenko [122]. For the case of an infinite line defect, dispersion relations can be computed in explicit form allowing spatially localised waveguide modes to be analysed.

The book [139] by Slepyan presents a detailed discussion of applications for dynamic lattice problems involving cracks modelled as semi-infinite faults, for both square and triangular elastic lattices. Localised modes for a structured interface and a crack propagating with constant speed within a square lattice were analysed by Mishuris et al. [106]. In particular, it was shown that the crack propagation can be supported by a sinusoidal wave localised along the crack, which the authors refer to as a *knife wave*. Using the lattice model, Mishuris et al. [106] derived the dispersion relations for the crack within the square lattice. Further, using numerical experiments, Mishuris et al. [106] demonstrated that these relations allow for the prediction of the average crack speed within the lattice when a fracture criterion for the crack path bonds is introduced. More recently, Nieves et al. [115] studied the propagation of a semi-infinite dynamic crack in a non-uniform elastic lattice. Extending the work of Mishuris et al. [106], Nieves et al. [115] analysed the crack stability and it was shown that information regarding unstable crack growth could be obtained from the study of the steady state regime.

In chapter 5 of the present thesis, the problem of the infinite defect considered in [122] is discussed and linked to the problem for a finite but very long inclusion. In particular, a relatively simple homogenised differential equation is derived for the case of long defects, which characterises the low frequency response of the inclusion, as well as the envelope of the highest frequency oscillations. Chapter 5 is based, in part, on the work published in [32].

Remaining with the topic of defects in discrete systems, the problem of a thermally striped discrete elastic lattice is considered in chapter 6. The thermally striped discrete system is analysed and compared with the corresponding problem for the continuum. Thermal striping is a phe-

nomenon that occurs when a thermoelastic solid is exposed to temperature fluctuations on the exterior boundary. These temperature variations may occur as a result of incomplete mixing of fluids at different temperatures. Such phenomena have been observed in the above-core region of fast breeder reactors, which are often cooled by liquid sodium; large temperature gradients may exist between the sodium emerging from the core and sub-breeder assemblies. A thermoelastic structure exposed to such temperature distributions can undergo thermal fatigue damage, as demonstrated by Jones [73]. Much of the analytical and modelling work on thermal striping in the literature has been carried out by Jones and his co-workers [23, 71–79, 108, 114, 149], who considered various physical configurations and methods. In the thermal striping regime, crack growth is a fatiguing process where the rate of crack growth depends on the peak-to-peak amplitude of the stress intensity factor and the material properties. For example, Paris' law [124] (a popular fatigue crack growth model) states that

$$\frac{\mathrm{d}a}{\mathrm{d}N} = c_1(\Delta K)^{c_2}, \tag{1.1}$$

where $a$ is the crack length, $N$ is the number of loading cycles, $c_1$ and $c_2$ are material constants, $K$ is the stress intensity factor, and $\Delta K = \max K - \min K$ is the peak-to-peak amplitude of the stress intensity factor. In 2006 Movchan and Jones [108], studied the model of thermal shock for a semi-infinite body containing a single small edge crack. Asymptotic formulae for the displacement field produced by the temperature load and an analytical expression for the stress intensity factor of an edge crack were obtained using the weight function method (see [18] among many others). An investigation into the behaviour of the peak-to-peak amplitude of the stress intensity factor for a thermally striped plate with multiple edge cracks was carried out by Jones [76]. It was shown that the stress intensity factor is not only a function of crack depth, but also depends on the separation between the edge cracks. Moreover, the stress intensity factor is also strongly influenced by the frequency of the striping load. Using approximate weight functions (see, for example, [47]), Jones and Lewis [78] presented results showing the sensitivity of the stress intensity factor for an edge crack in a finite block to the striping frequency and the aspect ratio of the block. Following the work by Movchan and Jones [76, 108], the effect of small voids and micro-cracks located within a semi-infinite body in the vicinity of a edge crack was analysed by Nieves et al. [113, 114]. For circular voids, Nieves et al. [114] provided numerical simulations showing the perturbation brought to the amplitude of the stress intensity factor for the edge crack. It was demonstrated that, in the presence of voids, the value of the amplitude of the stress intensity factor for the crack could be reduced relative to the stress intensity factor for a medium without voids.

Chapter 6 of the present thesis is devoted to the analysis of the effects of a fully discrete thermoelastic solid on the amplitude of the stress intensity factor. In this case, the discrete structure is a triangular lattice with concentrated mass at the junctions connected by massless conducting rods. It is demonstrated that although all stresses in the lattice are finite, the behaviour of the displacement field close to, but outside a small neighbourhood of the crack tip, follows the same characteristic square-root behaviour as that in the continuum. The above property is used to determine an *"effective stress intensity factor"* for the lattice. The corresponding problem for the case of a thermoelastic continuum is also considered. For this case, the stress intensity factor

is computed using the J-integral, originally introduced in [26, 134] and modified for thermoelastic problems in [147], and compared with the *"effective stress intensity factor"* for the discrete structure. It is demonstrated that the *"effective stress intensity factor"* for the lattice exhibits the same qualitative behaviour as the one for the continuum. However, for the lattice, the peak-to-peak amplitude of the *"effective stress intensity factor"* is lower than that of the continuum for sufficiently long cracks and low frequencies. Chapter 6 is based on the work [33] by the present author and his co-workers.

The final chapter of the main body of the present thesis is devoted to the development of invisibility cloaks for electromagnetic, out-of-plane shear elastic, and acoustic waves. Using the framework of transformation elastodynamics [104, 116, 117], the design of a square invisibility cloak for waves governed by the Helmholtz equation is presented. Since the publication of two seminal papers in the same issue of Science by Leonhardt [92] and Pendry et al. [126], there has been substantial interest in the idea of cloaking via transformation optics (see the review article [61] and references therein). The experimental validation of cloaking for microwaves demonstrated by Schurig et al. [137] in the same year further increased scholarly (and popular) interest. The concept of cloaking via transformation optics is due to an earlier fundamental result by Greenleaf et al. [57, 58] on singular transformations and applications to cloaking for conductivity. The key to achieving cloaking is to ensure that the governing equations (Maxwell's system in electromagnetism, for example) remain invariant under the mapping used to generate the cloak. In this sense, the physical phenomena associated with the untransformed system are the same as those governed by the transformed system. The transformed system will, in general, have different material properties but the overall form of the system should remain unchanged under the mapping. The metric invariance of Maxwell's equations has been understood for many years [129, 144]. However for other systems, such as elasticity, the equations are not in general invariant under transformation [104, 117], at least in the sense that the transformed system does not correspond to a classical elastic material. The invariance of the Helmholtz equation has been demonstrated by Norris [116], who also provided a convenient theoretical framework for cloaking in acoustics.

The classical approach to cloaking via transformation optics involves deforming a region such that a point is mapped to a finite region corresponding to the inner boundary of the cloak. Usually, such transformations involve transforming a point into a finite region with a smooth boundary, such as an ellipse (see [60, 116, 126], among others). The mapping is non-singular everywhere, except at the initial point which is deformed into the inner boundary of the cloak. In the originating paper by Pendry et al. [126], the cloak is created by mapping a disc to an annulus. Maxwell's equations are invariant under the corresponding transformation, as required in order to achieve cloaking. The material properties of the cloak are then determined from the metric of the deformed space [138]. The mapping used in [126] is clearly singular: a point is mapped to the inner radius of the annulus, and this results in discontinuous (singular) material properties. Greenleaf et al. addressed this issue in two papers [55, 56] and derived the condition for finite energy weak solutions of the Helmholtz equation and Maxwell's equations. In [55], it was demonstrated that finite energy solutions to the cloaking problem for the Helmholtz equation exist for an object with a single layer cloak. However, for the case of Maxwell's equations

with internal currents, the cloaking of an infinite cylinder cannot be achieved with a single layer or without imposing a physical surface at the inner boundary of the cloak. In the same paper, Greenleaf et al. derived an identity linking the transformed scalar wave equation to the metric of the deformed space, which may then by linked to the material properties of the cloak [56]. In 2008 Norris [116] studied acoustic cloaking and re-derived an equivalent identity to that in [55] using the framework of finite elasticity, leading to a cloak with a density described by a rank two tensor. Moreover, it was demonstrated that the total mass of the cloak is infinite for the case of perfect cloaking. Norris further demonstrated that the problem of infinite mass could be overcome if both the density and elastic properties of the cloak were anisotropic. An alternative approach to negate the problem of singular material properties is to construct a so-called *near cloak* by regularising the transformation [86]. Rather than mapping a single point to the inner boundary of the cloak Kohn et al. [86] proposed mapping a ball of small, but finite, radius to the inner boundary. A small regularisation parameter which characterises the initial radius of the ball is introduced, which results in a non-singular mapping on the cloak and its boundary. The regularisation procedure was used to create illustrative *near cloaks* in [116].

In 2006, Milton et al. [104] examined how the equations of motion for a general elastic medium transform under an arbitrary curvilinear transformation. It was shown that a priori requiring a symmetric stress tensor enforces a particular choice of the gauge (i.e. the manner in which the displacement vector transforms). It was found that, in general, the equations of motion are not invariant under transformation but are mapped to a more general system with non-scalar density. Milton et al. demonstrated that a special case of the so-called Willis equations [105] remain invariant under general curvilinear transformations. In [104] identities linking the material properties of the cloak to the map, for both classical elasticity and the more general Willis materials are derived. In 2011, Norris and Shuvalov [117] further generalised the work of Milton et al., deriving a more general system of transformed equations without imposing the constraint of symmetric stress. The material properties of the transformed system were derived explicitly and shown to depend on both the transformation and the choice of gauge. Together [104] and [117] provide a comprehensive framework in which to investigate cloaking in elastodynamics.

A design for a cloak to control flexural waves in thin plates was proposed by Farhat et al. [45]. The cloak was constructed of several concentric layers of piecewise constant isotropic elastic material. Farhat et al. also presented a simplified model suitable for practical implementation with ten layers using six different materials. Following [45], an experimental group led by Wegener fabricated a cloak based on the work of Farhat et al. using twenty concentric rings and sixteen different elastic metamaterials [141]. Physical measurements were compared with numerical simulations and found to be in good agreement. Control of in-plane waves governed by the Navier equations was examined by Brun et al. [17]. In [17], the authors modelled a circular cloak using the classical radial transformation by deforming a disc to an annulus. The efficiency of the cloak was illustrated using finite element simulations, and the numerical solution of the cloaking problem was compared with the Green's function for a homogeneous elastic space.

An influential paper by Rahm et al. [132] presents a transformation optics algorithm for a problem of electromagnetism involving a cloak of a square shape. The transformation is performed in Cartesian coordinates and results in a piecewise smooth cloak on the interior

points, with matching regions in the neighbourhood of corners and a singularity at the origin mapped into the inner boundary of the cloak. The model of such a continuum cloak received substantial attention and subsequent use by the modelling community (see, for example, [46,48,69,93,125,136]). In the majority of these papers, the emphasis is on the geometrical aspect of the possible shapes of the cloak, with examples ranging from polygonal and elliptical cloaks to heart-shaped cloaks. Although it is indeed interesting to see a wide range of transformations and geometries, it also remains important to understand the transformed problem in the context of the physical model, address the analysis of the transformed boundary or transmission conditions and furthermore derive the properties of the solutions. The paper [132], which stimulated a good level of discussion on the topic, also admits a deficiency regarding the analysis of the solution near the boundary of the cloak. Apparently, no indication was given about the sensitivity of the result to the type of boundary conditions (Dirichlet or Neumann) on the inner boundary of the cloak. The authors' evaluation of the effectiveness of the cloaking was based on a visual observation linked to a numerical simulation at a single frequency. In [132], the authors admit that the effective material properties of the cloak are inaccurate in the vicinity of the inner boundary of the cloak, owing to the singular nature of the mapping. Indeed, if the authors had attempted to change the frequency range they would have seen significant differences. The cloak advocated in [132] is an approximate cloak, where the boundary effects become important and visible as the frequency of the incident waves increases.

The ideas of metric invariance in Maxwell's equations and cloaking have found extensive use as a technical tool and on many occasions, the researchers omit to look at the physical model corresponding to the transformed equations. For example, on page 99 of [93] the text reads "The square cloak has the same geometry as the cylindrical case, except that we replace the cylindrical shell by a rectangular shell with the same size". This comparison of unlike geometries omits important effects, such as field concentrations near sharp corners, which make cloaking more difficult. Motivated by [132], Farhat et al. [46] attempted to construct an approximate square cloak for out-of-plane shear waves. Using the method of multiple scales, Farhat et al. [46] introduced a microstructure composed of a regular array of perforations and derived a homogenised continuum which would approximate an ideal cloak. However, Farhat et al. admit in [46] that their structured cloak is not as efficient as the authors expected.

Polygonal cloaks have also been the subject of experimental investigation. For example, in [24] Chen et al. report the results for an experimental broadband hexagonal cloak based on a piecewise linear homogeneous transformation. Although the cloak does not render the cloaked object invisible, it does reduce its apparent size. The cloak is demonstrated to work for visible light. However, Chen et al. [24] emphasise that the cloak functions only for light incident from six directions defined by the faces of the hexagon. More recently, Landy et al. [89] produced an experimental uni-directional metamaterial cloak for microwaves. The reported cloak [89] is based on a bilinear transformation which maps a line segment to a two-dimensional region of space. Cloaks based on such transformations are referred to as *carpet cloaks* in the literature (see [94] among others). The advantage of such cloaks is that the requisite material properties are homogeneous and finite. However, Landy et al. admit that such cloaks are only effective over a narrow range of observation angles. The cloak is nonetheless impressive given that the

practical implementation does not rely on the eikonal approximations as is the case with other implementations [25, 128, 148].

It appears that the work reported in [132] has generated a scope for further discussion and indeed further improvement of the model involving "glued transforms" that lead to approximate rectangular cloaks. Such cloaks are by no means exact and are frequency sensitive. A regularisation procedure, as illustrated by Kohn et al. [86] for the spherical cloak, can be applied to make the transformation, and hence the material properties, non-singular on the inner boundary of the cloak. The regularisation procedure not only simplifies the analysis, but also makes it physically meaningful. Furthermore, a lattice approximation is straightforward for a regularised square-shaped cloak. This appears to be efficient and serves a relatively wide frequency range.

In the spirit of Kohn et al. [86], a so-called *near cloak* is presented in chapter 7. In particular, four trapezoids surrounding a square of semi-width $\varepsilon$ are mapped to four narrower trapezoids such that the semi-width of the square is enlarged to $a \gg \varepsilon > 0$. The mapping is continuous and piecewise smooth everywhere on the closure of the trapezoids which form the cloak surrounding the square inclusion. Since the map used in the present thesis is non-singular on both the interior and boundary of the cloak, all material parameters are continuous and, indeed, piecewise smooth.

Chapter 7 also contains detailed analysis of wave propagation through the cloak using both numerical simulations and analytical methods based on the ray equations obtained through a WKB-type approximation. In addition, a novel illustration of the efficacy of the cloak is presented, which provides an interesting link with Quantum Mechanics. A recent paper by Greenleaf et al. [54] also raises interesting questions regarding the link between Quantum Mechanics and cloaking. The paper [54] presents a class of invisible reservoirs and amplifiers for fields governed by Schrödinger's equation. In the final part of chapter 7, a possible avenue toward the physical realisation of the cloak is presented. In particular, a relatively simple discrete metamaterial cloak formed from point masses connected via massless springs is discussed. It is shown that this lattice cloak is effective in reducing the scattered field, particularly for low frequencies. The work reported in chapter 7 has recently been published by Colquitt et al. [28].

To summarise, the structure of the present thesis is as follows. Chapter 3 is devoted to the study of the dispersive properties of elastic lattice structures and, in particular, their homogenised properties in the low frequency range. The behaviour of scalar and vector lattices in the frequency range where the response of the material is strongly anisotropic is discussed in chapter 4. It is demonstrated that this *dynamic anisotropy* is linked to, and can be predicted from, the dispersive properties of the microstructure. The problem of localised defect modes associated with eigenmodes generated by finite and infinite defects in infinite two-dimensional square lattices is considered in chapter 5. The problem of a thermally striped discrete elastic lattice is considered in chapter 6. The thermally striped discrete system is analysed and compared with the corresponding problem for the continuum. The final chapter of the main body of the present thesis is devoted to the development of invisibility cloaks for electromagnetic, out-of-plane shear elastic, and acoustic waves. Chapter 8 briefly summarises the problems studied in the present thesis and also includes a discussion of the common themes linking the physical problems presented herein. Before considering the problems summarised above, some preliminary results which

ease exposition in the main body of the thesis are presented in chapter 2.

# *Chapter Two*

# Lattice preliminaries

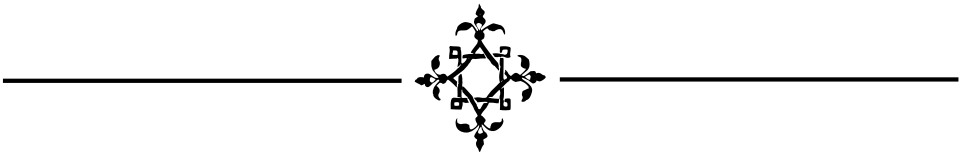

This chapter introduces some prerequisite results, theory and techniques, and establishes some common notation that will be used throughout this thesis. The emphasis of this chapter will be on brevity rather than detailed commentary.

## 2.1 Lattice equations

The following framework and analysis applies to one-, two-, and three-dimensional problems. Consider a regular array of particles in $d$-dimensional Euclidean space, $\mathbb{R}^d$, where $d = 1, 2, 3$. Each particle within the lattice may then be labelled by a multi-index $\boldsymbol{m} = (m_1, m_2, \ldots, m_d) \in \mathbb{Z}^d$ and a scalar $n \in \mathbb{N}_0$, where $\mathbb{Z}$ and $\mathbb{N}_0$ are the sets of all integers and all non-negative integers respectively. The multi-index $\boldsymbol{m}$ refers to the unit cell in which the particle is located, whereas the scalar $n$ distinguishes between different particles in the same elementary cell. The position of each particle within the lattice is then denoted by $\boldsymbol{x}_{\boldsymbol{m},n} = \mathcal{T}\boldsymbol{m} + \boldsymbol{x}_{\boldsymbol{0},n}$, where $\boldsymbol{x}_{\boldsymbol{0},n}$ is the position of the $n^{\text{th}}$ particle in the unit cell and $\mathcal{T}$ is the $d \times d$ matrix $\mathcal{T} = [\boldsymbol{t}_1, \boldsymbol{t}_2, \ldots, \boldsymbol{t}_d]$. It is emphasised that sub-script commas do not indicate differentiation, but simply separate the indices for clarity. The column vectors $\boldsymbol{t}_i$ are the direct lattice vectors, which describe the principal directions of the lattice. For example, the direct lattice vectors for a planar diatomic triangular lattice are shown in figure 3.1 on page 25. The parallelogram defined by the direct lattice vectors (and shaded in grey in figure 3.1) is the elementary cell of the lattice. For the special case of a uniform lattice, that is, lattices where all particles are the same, $\boldsymbol{x}_{\boldsymbol{0},n} = \boldsymbol{0}$ and the position of each particle is simply $\boldsymbol{x}_{\boldsymbol{m}} = \mathcal{T}\boldsymbol{m}$. It should be emphasised that both $\boldsymbol{x}_{\boldsymbol{m},n} = \mathcal{T}\boldsymbol{m} + \boldsymbol{x}_{\boldsymbol{0},n}$ and $\boldsymbol{x}_{\boldsymbol{m}} = \mathcal{T}\boldsymbol{m}$ will be used throughout this work and it is important to distinguish between the two. The former refers to the position of particle $(\boldsymbol{m}, n)$ within the lattice, whereas the latter denotes the position of the $\boldsymbol{m}^{\text{th}}$ elementary cell of the lattice. Throughout this thesis, the notation $A_{\boldsymbol{m},n}$ will be used to denote some property $A$, of node $n$ in the $\boldsymbol{m}^{\text{th}}$ unit cell.

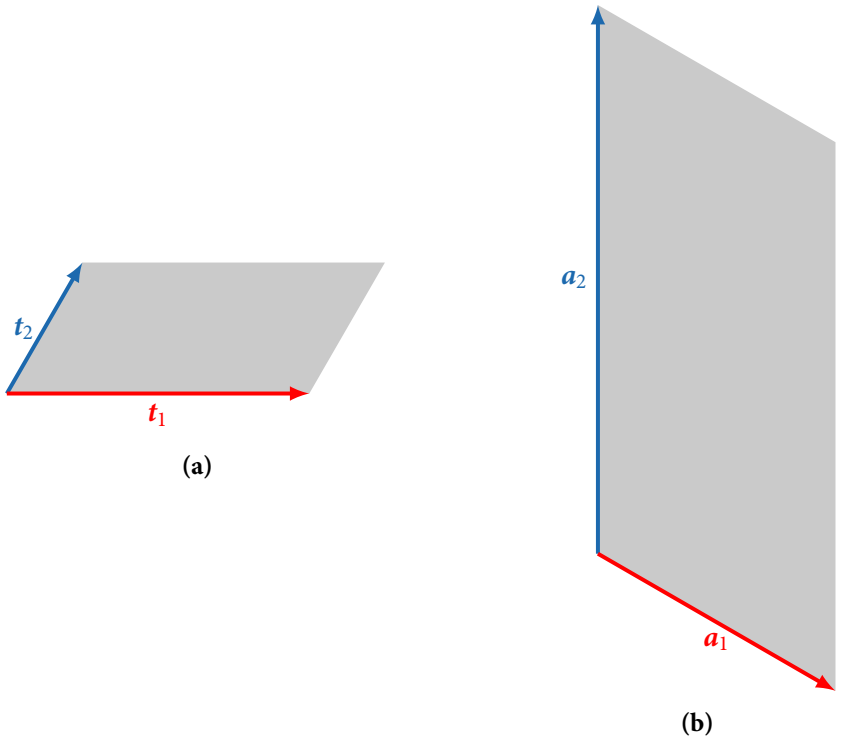


**Figure 2.1:** The direct (a) and reciprocal (b) lattice vectors for the diatomic triangular lattice shown in figure 3.1 on page 25. The corresponding elementary cells are shaded in grey.

For the physical problems presented in this thesis, the interactions between lattice points will be linear in the sense that the dynamic equations governing the potential of node $(\boldsymbol{m}, n)$ has the form

$$\sum_{(\boldsymbol{p},q)\in\mathcal{N}_n} C_{\boldsymbol{p},q}\boldsymbol{U}_{\boldsymbol{p},q}(t) - \mathcal{I}_n \frac{\mathrm{d}^s}{\mathrm{d}t^s}\boldsymbol{U}_{\boldsymbol{m},n}(t) = \boldsymbol{F}_{\boldsymbol{m},n}(t). \tag{2.1}$$

In equation (2.1), $\boldsymbol{U}_{\boldsymbol{m},n}(t)$ and $\boldsymbol{F}_{\boldsymbol{m},n}(t)$ are the potential of, and the load on, the particle $(\boldsymbol{m}, n)$ respectively; and both are continuous functions of time $t$. The parameter $s \in \mathbb{N}$ is determined by the type of interaction considered. In particular, for the mechanical lattices considered in chapters 3-7, $s = 2$ and equation (2.1) is simply Newton's Second Law; and for the heat conduction problem on a lattice as considered in chapter 6, $s = 1$. The square diagonal "*inertia matrix*"[1] is denoted by $\mathcal{I}_n$ and describes the inertial properties of the lattice point. The (square) *interaction matrix* $C_{\boldsymbol{p},q}$ characterises the interaction between node $(\boldsymbol{m}, n)$ and node $(\boldsymbol{m}+\boldsymbol{p}, n+q)$. In other words, $C_{\boldsymbol{p},q}$ describes the load on node $(\boldsymbol{m}, n)$ as a result of a change in potential of $(\boldsymbol{m}+\boldsymbol{p}, n+q)$. Finally, the set $\mathcal{N}_n$ enumerates the nodes $(\boldsymbol{m}+\boldsymbol{p}, n+q)$ interacting with node $(\boldsymbol{m}, n)$. Typically, $\mathcal{N}_n$ will be the set of nearest neighbours such that $\mathcal{N}_n = \{(\boldsymbol{p}, q) : |\boldsymbol{x}_{\boldsymbol{p},q}| \leq L\}$, where $L > 0$ is some distance chosen appropriately such that $\mathcal{N}_n$ contains only the nearest neighbours of node $(\boldsymbol{m}, n)$. The reader's attention is drawn to the fact that $(\boldsymbol{m}, n) \in \mathcal{N}_n$, that is, a lattice node belongs to the set of its nearest neighbours.

This thesis is concerned with the propagation of time-harmonic disturbances through lattices. Therefore, solutions of the form $\boldsymbol{U}_{\boldsymbol{m},n}(t) = \boldsymbol{u}_{\boldsymbol{m},n}e^{i\omega t}$ are sought and $\boldsymbol{F}_{\boldsymbol{m},n}(t)$ is restricted to the

[1] It is emphasised that the term "*inertia matrix*" is used purely for convenience and $\mathcal{I}$ need not correspond to physical inertia. For mechanical lattices (chapters 3-7), $\mathcal{I}$ is the matrix of nodal masses. For the heat conduction problem (chapter 6), the matrix $\mathcal{I}$ describes the heat capacity of the nodes.

class of functions such that $\boldsymbol{F}_{\boldsymbol{m},n}(t) = \boldsymbol{f}_{\boldsymbol{m},n}e^{i\omega t}$, where $\omega$ is the radian frequency. The functions $\boldsymbol{u}_{\boldsymbol{m},n} : \mathbb{Z}^2 \times \mathbb{N}_0 \mapsto \mathbb{C}^d$ and $\boldsymbol{f}_{\boldsymbol{m},n} : \mathbb{Z}^2 \times \mathbb{N}_0 \mapsto \mathbb{C}^d$ are the potential and load complex amplitudes respectively. It is understood that the physical fields are given by the real parts of $\boldsymbol{U}_{\boldsymbol{m},n}(t)$ and $\boldsymbol{F}_{\boldsymbol{m},n}(t)$. For time-harmonic potentials, (2.1) reduces to

$$\sum_{(\boldsymbol{p},q)\in\mathcal{N}_n} C_{\boldsymbol{p},q}\boldsymbol{u}_{\boldsymbol{p},q} - (i\omega)^s\mathcal{I}_n\boldsymbol{u}_{\boldsymbol{m},n} = \boldsymbol{f}_{\boldsymbol{m},n}. \tag{2.2}$$

Upon application of the discrete Fourier transform, which may be defined as

$$\mathcal{F}\left[\boldsymbol{u}_{\boldsymbol{m},n}\right] = \boldsymbol{u}_n^{\mathrm{FF}}(\boldsymbol{\xi}) = \sum_{\boldsymbol{m}\in\mathbb{Z}^d} \boldsymbol{u}_{\boldsymbol{m},n}\exp\left(-i\boldsymbol{\xi}\cdot\boldsymbol{x}_{\boldsymbol{m}}\right), \tag{2.3}$$

equation (2.2) takes the form

$$\sum_{(\boldsymbol{p},q)\in\mathcal{N}_n}\left[C_{\boldsymbol{p},q}e^{-i\boldsymbol{x}_{\boldsymbol{p}}\cdot\boldsymbol{\xi}} - (i\omega)^s\mathcal{I}_n\delta_{n,q}\right]\boldsymbol{u}_q^{\mathrm{FF}}(\boldsymbol{\xi}) = \boldsymbol{f}_n^{\mathrm{FF}}(\boldsymbol{\xi}), \tag{2.4}$$

where $\delta_{nq}$ is the Kronecker delta. Here, the Fourier variables are restricted to the unit cell in the reciprocal space, $\boldsymbol{\xi} \in \Xi$. In particular, the unit cell in the reciprocal space is the $d$-parallelotope spanned by the reciprocal lattice vectors, $\boldsymbol{a}_i$, where $[\boldsymbol{a}_1, \boldsymbol{a}_2, \ldots, \boldsymbol{a}_d] = 2\pi\mathcal{T}^{-\mathrm{T}}$, where $(\cdot)^{-\mathrm{T}}$ denotes the inverse and transpose of the parenthesised quantity. For the planar diatomic triangular lattice shown in figure 3.1 on page 25, the direct and reciprocal lattice vectors and associated elementary cells are shown in figure 2.1. Introducing the block matrices

$$\sigma_{nq}(\omega,\boldsymbol{\xi}) = \sum_{\boldsymbol{p}\in\mathcal{N}_n}\left[C_{\boldsymbol{p},q}e^{-i\boldsymbol{x}_{\boldsymbol{p}}\cdot\boldsymbol{\xi}} - (i\omega)^s\mathcal{I}_n\delta_{nq}\right], \tag{2.5a}$$

together with the vectors

$$\mathbf{U}^{\mathrm{FF}}(\boldsymbol{\xi}) = \begin{bmatrix}\boldsymbol{u}_1^{\mathrm{FF}}(\boldsymbol{\xi})\\ \boldsymbol{u}_2^{\mathrm{FF}}(\boldsymbol{\xi})\\ \vdots\\ \boldsymbol{u}_Q^{\mathrm{FF}}(\boldsymbol{\xi})\end{bmatrix} \quad \text{and} \quad \mathbf{F}^{\mathrm{FF}}(\boldsymbol{\xi}) = \begin{bmatrix}\boldsymbol{F}_1^{\mathrm{FF}}(\boldsymbol{\xi})\\ \boldsymbol{F}_2^{\mathrm{FF}}(\boldsymbol{\xi})\\ \vdots\\ \boldsymbol{F}_Q^{FF}(\boldsymbol{\xi})\end{bmatrix}, \tag{2.5b}$$

where $Q$ is the number of nodes in the elementary cell, equation (2.4) may be written compactly as

$$\boldsymbol{\sigma}(\omega,\boldsymbol{\xi})\mathbf{U}^{\mathrm{FF}}(\boldsymbol{\xi}) = \mathbf{F}^{\mathrm{FF}}(\boldsymbol{\xi}). \tag{2.6}$$

For the unforced problem in mechanical lattices ($s = 2$) one may set $\mathbf{F}^{\mathrm{FF}}(\boldsymbol{\xi}) = \mathbf{0}$ and immediately obtain the dispersion equation for Bloch-Floquet waves: $\det\boldsymbol{\sigma}(\omega,\boldsymbol{\xi}) = 0$. The potential field then has the well known form $\boldsymbol{u}_{\boldsymbol{m},n} = u_{\mathbf{0},n}e^{i\boldsymbol{x}_{\boldsymbol{m}}\cdot\boldsymbol{\xi}}$. For non-trivial $\mathbf{F}^{\mathrm{FF}}$, the potential field can be obtained by means of the inverse Fourier transform

$$\mathbf{U}_{\boldsymbol{m}} = \frac{1}{\|\mathcal{R}\|}\int_{\mathcal{R}}\mathbf{F}^{\mathrm{FF}}(\boldsymbol{\xi})\boldsymbol{\sigma}^{-1}(\omega,\boldsymbol{\xi})e^{i\boldsymbol{\xi}\cdot\boldsymbol{x}_{\boldsymbol{m}}}\mathrm{d}\boldsymbol{\xi}, \tag{2.7}$$

where $\mathcal{R} = \{\boldsymbol{\xi} : -\pi < \xi_i\boldsymbol{x}_{\mathbf{0},n}\cdot\boldsymbol{e}_i \le \pi\}$ and $\boldsymbol{e}_i$ is the unit vector along the $i^{\text{th}}$ axis; the symbol $\|\cdot\|$

denotes the Lebesgue measure.

## 2.2 Lattice interactions

With the exception that $C_{\boldsymbol{p},q}$ should be square, no restrictions have been placed on the form of the interaction matrices. The precise form of the interaction matrices depend on the type of lattice link considered. It is remarked that the interaction matrices may not only depend on the parameters $\boldsymbol{p}$ and $q$, but will also depend on the physical and geometrical properties of the lattice. The physical lattices consider later in this thesis will be restricted to two-dimensional planar lattices. For such lattices, it is convenient to construct *fundamental interaction matrices* $\boldsymbol{A}$ and $\boldsymbol{B}$ which describe the behaviour of a single lattice link oriented along $\boldsymbol{e}_1$ as shown in figure 2.2. It is emphasised that the shape of the links in figure 2.2 is purely illustrative. Indeed, the specific shape of the lattice links will depend on the type of physical interaction considered. Using the matrices $\boldsymbol{A}$ and $\boldsymbol{B}$, together with appropriate rotation matrices one may then construct the interaction matrix $C_{\boldsymbol{n},p}$ for any two lattice points. For example, consider a single mechanical lattice link oriented along the $\boldsymbol{e}_1$ axis as illustrated in figure 2.2. If $\boldsymbol{u}_0$ and $\boldsymbol{u}_\ell$ are the displacements at the ends of the link, then the force at $\boldsymbol{x} = \boldsymbol{0}$ can be written in the form

$$\boldsymbol{f}_0 = \boldsymbol{A}\boldsymbol{u}_0 + \boldsymbol{B}\boldsymbol{u}_\ell. \tag{2.8}$$

If $\boldsymbol{f}_0$, $\boldsymbol{u}_0$, $\boldsymbol{u}_\ell \in \mathbb{C}^n$, then $\boldsymbol{A}$ and $\boldsymbol{B}$ are $n \times n$ matrices. The force at $\boldsymbol{x} = [\ell, 0]^{\mathrm{T}}$ can be determined by applying a sequence of rotations to the system. In particular, the force at $\boldsymbol{x} = [\ell, 0]^{\mathrm{T}}$ can be expressed as

$$\boldsymbol{f}_\ell = \boldsymbol{R}\boldsymbol{A}\boldsymbol{R}^{\mathrm{T}}\boldsymbol{u}_\ell + \boldsymbol{R}\boldsymbol{B}\boldsymbol{R}^{\mathrm{T}}\boldsymbol{u}_0, \tag{2.9}$$

where $\boldsymbol{R} \in \mathrm{SO}(n, \mathbb{R})$ is a rotation matrix such that $\boldsymbol{R}\boldsymbol{e}_1 = -\boldsymbol{e}_1$. The reader is referred to section 2.2.7 for a more detailed discussion of the rotation matrices. Hence, the interaction matrices have the form $C_{\boldsymbol{0},1} = \boldsymbol{A} = \boldsymbol{R}\boldsymbol{A}\boldsymbol{R}^{\mathrm{T}}$, $C_{\boldsymbol{e}_1,1} = \boldsymbol{B}$, $C_{-\boldsymbol{e},1} = \boldsymbol{R}\boldsymbol{B}\boldsymbol{R}^{\mathrm{T}}$.

In this section, the fundamental interaction matrices required in later chapters will be introduced with the emphasis on brevity rather than exposition. Discussion of the significance and physical interpretation of these interactions is deferred to later chapters. The full interaction matrices will depend on the geometry and physical problem considered, and therefore, will be constructed as needed in later chapters. The following is not intended to represent a complete list of all possible interactions, nor is any particular significance attached to these particular models beyond that they will be required later in the thesis. For all except *heat conduction*, in which $s = 1$, one should set $s = 2$ in equations (2.1)-(2.4) in the previous section.

### 2.2.1 Out-of-plane shear

Out-of-plane shear is, perhaps, the simplest mechanical interaction possible. In this case the blue lattice link illustrated in figure 2.2 corresponds to a massless bond of stiffness $k$, for which the load is $f = u'(x)$ and the displacement field satisfies (see, for example, [53])

$$\frac{\mathrm{d}^2 u}{\mathrm{d}x^2} = 0, \qquad u(\boldsymbol{0}) = u_0,\ u(\ell, 0) = u_\ell. \tag{2.10}$$

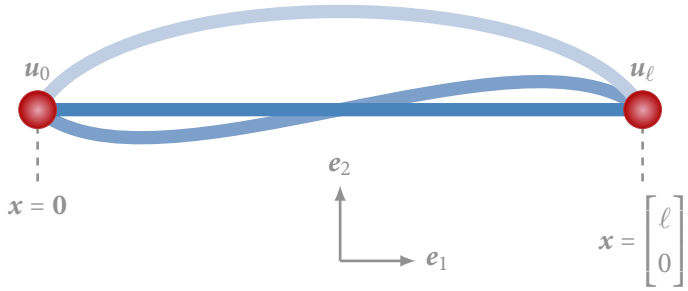


**Figure 2.2:** Two lattice nodes separated by a distance $\ell$. A range of "interactions" are illustrated in blue; it is emphasised that the shape of the lattice link will depend on the type of interaction considered.

Here, $u_0$ and $u_\ell$ denotes the out-of-plane (into and out of the page in figure 2.2) displacements of ends of the spring ($\boldsymbol{x} = 0$ and $\boldsymbol{x} = [\ell, 0]^{\mathrm{T}}$ respectively). The force at $\boldsymbol{x} = \mathbf{0}$ is then

$$\boldsymbol{f}_0 = k\frac{u_\ell - u_0}{\ell}\boldsymbol{e}_3. \tag{2.11}$$

In this case, the fundamental interaction matrices are, in fact, scalars

$$A^{\mathrm{S}} = -\frac{k}{\ell} \qquad \text{and} \qquad B^{\mathrm{S}} = \frac{k}{\ell}. \tag{2.12}$$

The superscript S is used to emphasise that these fundamental interaction matrices refer to the out-of-plane shear interaction.

### 2.2.2 Heat conduction

In this case the lattice nodes are connected by thin massless rod of thermal conductivity $k$ and uniform cross-sectional area $S$. If the lateral surface of the rod is thermally isolated from the surroundings, the temperature distribution along the rod is then

$$\theta(x) = \Theta_0 + \frac{\Theta_\ell - \Theta_0}{\ell}x, \tag{2.13}$$

where $x$ is distance along the rod, and $\Theta_\ell$ and $\Theta_0$ are the temperatures at $\boldsymbol{x} = [\ell, 0]^{\mathrm{T}}$ and $\boldsymbol{x} = \mathbf{0}$ respectively. According to Fourier's law, the local rate of heat flow through the cross section of the rod is

$$\frac{\partial Q}{\partial t} = \frac{kS}{\ell}(\Theta_\ell - \Theta_0). \tag{2.14}$$

Hence, for this simple model of heat conduction the fundamental interaction matrices are again scalars and of a similar form as the out-of-plane shear interaction

$$A^{\mathrm{H}} = -\frac{kS}{\ell} \qquad \text{and} \qquad B^{\mathrm{H}} = \frac{kS}{\ell}. \tag{2.15}$$

### 2.2.3 Elastic in-plane motion: Central interactions

Returning to mechanical interactions, let $\boldsymbol{u}_n$ and $\boldsymbol{u}_p$ denote the displacement amplitudes of the end-points of a thin elastic rod of length $\ell$, Young's modulus $E$, uniform density $\rho$, and constant cross-sectional area $S$. For central interactions, that is interactions that only depend on the distance between two points and not the relative orientation, only the longitudinal vibrations of the rod need to be considered. The time harmonic longitudinal displacement amplitude $u(x)$

then satisfies (see, for instance, [53])

$$\left(\frac{\mathrm{d}^2}{\mathrm{d}x^2}+\frac{\omega^2}{c^2}\right)u(x)=0,\quad u(0)=\boldsymbol{u}_0\cdot\boldsymbol{e}_1,\quad u(\ell)=\boldsymbol{u}_\ell\cdot\boldsymbol{e}_1, \tag{2.16}$$

where $c^2=E/\rho$ and $\omega^2$ is the angular frequency of the vibrations. The force at $\boldsymbol{x}=\boldsymbol{0}$ is then

$$\boldsymbol{f}_n=ES\left.\frac{\mathrm{d}u}{\mathrm{d}x}\right|_{x=0}\boldsymbol{e}_1=ES\lambda\left(\frac{\boldsymbol{u}_1\cdot\boldsymbol{e}_1-\boldsymbol{u}_0\cdot\boldsymbol{e}_1\cos(\omega\ell/c)}{\sin(\omega\ell/c)}\right)\boldsymbol{e}_1, \tag{2.17}$$

whence the fundamental interaction matrices have the form

$$\boldsymbol{A}^{\mathrm{C}}=-\frac{\omega ES}{c}\begin{pmatrix}\cot(\omega\ell/c) & 0\\ 0 & 0\end{pmatrix}\qquad\text{and}\qquad\boldsymbol{B}^{\mathrm{C}}=\frac{\omega ES}{c}\begin{pmatrix}\csc(\omega\ell/c) & 0\\ 0 & 0\end{pmatrix}. \tag{2.18}$$

The fundamental interaction matrices for a non-inertial lattice link can be obtained from (2.18) by taking the limit as $c\to\infty$ ($\rho\to 0$). In this case the fundamental interaction matrices take the particularly simple form

$$\boldsymbol{A}^{\mathrm{C}}=-\frac{ES}{\ell}\begin{pmatrix}1 & 0\\ 0 & 0\end{pmatrix}\qquad\text{and}\qquad\boldsymbol{B}^{\mathrm{C}}=\frac{ES}{\ell}\begin{pmatrix}1 & 0\\ 0 & 0\end{pmatrix}. \tag{2.19}$$

### 2.2.4 Elastic in-plane motion: Central and torsional interactions

Consider the thin elastic rod discussed in section 2.2.3 connecting the two end points. In addition, located at each end point is a torsional spring of stiffness $\tau$. If the elastic rod is rigid in the transverse direction ($\boldsymbol{e}_2$) and connected to the nodes at $\boldsymbol{x}=\boldsymbol{0}$ and $\boldsymbol{x}=[\ell,0]^{\mathrm{T}}$ by pin joints, then for small transverse displacements $\boldsymbol{u}_0\cdot\boldsymbol{e}_2$, the torsional spring exerts a torque $T=-\tau\boldsymbol{u}_0\cdot\boldsymbol{e}_2/\ell$ on the rod. Thus,the fundamental interaction matrices are then

$$A^{\mathrm{TS}}=-\begin{pmatrix}\omega ES\cot(\omega\ell/c)/c & 0\\ 0 & -\tau/\ell\end{pmatrix}\qquad\text{and}\qquad B^{\mathrm{TS}}=\begin{pmatrix}\omega ES\csc(\omega\ell/c)/c & 0\\ 0 & \tau/\ell\end{pmatrix}. \tag{2.20}$$

This type of interaction has been examined in previous works in the frameworks of homogenisation theory, see [102, 107, 111] among others, and is studied here in contrast to the Euler-Bernoulli interaction which follows this section.

### 2.2.5 Elastic in-plane motion: Euler-Bernoulli interactions

Consider the longitudinal and flexural vibrations of the thin rod discussed in the previous section. The longitudinal displacement amplitude $u(x)$ is still governed by the time-harmonic wave equation (2.16). The transverse amplitude $w(x)$ is governed by the Euler-Bernoulli beam equation (see [53], among many others)

$$\left(\frac{\mathrm{d}^4}{\mathrm{d}x^4}-\frac{\omega^2}{\alpha^2}\right)w(x)=0 \tag{2.21a}$$

$$w(0)=\boldsymbol{u}_0\cdot\boldsymbol{e}_2,\quad w(\ell)=\boldsymbol{u}_\ell\cdot\boldsymbol{e}_2,\quad w''(0)=\boldsymbol{u}_0\cdot\boldsymbol{e}_3,\quad w''(\ell)=\boldsymbol{u}_\ell\cdot\boldsymbol{e}_3, \tag{2.21b}$$

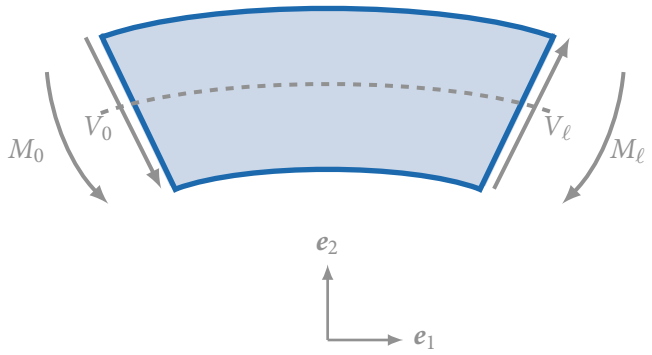


**Figure 2.3:** A segment of an Euler-Bernoulli beam, subjected to shear forces and bending moments. Notice the relationship between the directions of the forces and moments.

where, in this case, $\alpha^2 = EI/(\rho S)$. The displacement amplitudes at the end points are denoted by $\boldsymbol{u}_n$, $\boldsymbol{u}_p \in \mathbb{C}^3$ respectively. In particular, $\boldsymbol{u}_a = [u(a), w(a), w''(a)]^{\mathrm{T}}$. The second derivative of the transverse displacement represents the curvature of the beam about $\boldsymbol{e}_3$. Hence, the first two components of the vector are the rectilinear displacement along $\boldsymbol{e}_1$ and $\boldsymbol{e}_2$, whilst the third component is the rotation about $\boldsymbol{e}_3$. The bending moment (about $\boldsymbol{e}_3$) at $\boldsymbol{x} = \boldsymbol{0}$ is then

$$\begin{aligned} EIw''(0) = {} & EI\lambda^2 \frac{\cos\lambda\ell - \cosh\lambda\ell}{\cos\lambda\ell\cosh\lambda\ell - 1}\boldsymbol{u}_p \cdot \boldsymbol{e}_2 + EI\lambda^2 \frac{\sinh\lambda\ell - \sin\lambda\ell}{\cos\lambda\ell\cosh\lambda\ell - 1}\boldsymbol{u}_p \cdot \boldsymbol{e}_3 \\ & + EI\lambda^2 \frac{\sin\lambda\ell\sinh\lambda\ell}{\cos\lambda\ell\cosh\lambda\ell - 1}\boldsymbol{u}_n \cdot \boldsymbol{e}_2 + EI\lambda \frac{\cosh\lambda\ell\sin\lambda\ell - \sinh\lambda\ell\cos\lambda\ell}{\cos\lambda\ell\cosh\lambda\ell - 1}\boldsymbol{u}_n \cdot \boldsymbol{e}_3, \end{aligned} \tag{2.22a}$$

with $\lambda = \sqrt{\omega/\alpha}$. Similarly, the shear force (along $\boldsymbol{e}_2$) at $\boldsymbol{x} = \boldsymbol{0}$ is

$$\begin{aligned} EIw'''(0) = {} & -EI\lambda^3 \frac{\sin\lambda\ell + \sinh\lambda\ell}{\cos\lambda\ell\cosh\lambda\ell - 1}\boldsymbol{u}_p \cdot \boldsymbol{e}_2 + EI\lambda^2 \frac{\cosh\lambda\ell - \cos\lambda\ell}{\cos\lambda\ell\cosh\lambda\ell - 1}\boldsymbol{u}_p \cdot \boldsymbol{e}_3 \\ & + EI\lambda^3 \frac{\cosh\lambda\ell\sin\lambda\ell + \cos\lambda\ell\sinh\lambda\ell}{\cos\lambda\ell\cosh\lambda\ell - 1}\boldsymbol{u}_n \cdot \boldsymbol{e}_2 + EI\lambda^2 \frac{\sinh\lambda\ell\sin\lambda\ell}{\cos\lambda\ell\cosh\lambda\ell - 1}\boldsymbol{u}_n \cdot \boldsymbol{e}_3. \end{aligned} \tag{2.22b}$$

For lattices with Euler-Bernoulli links where the shear forces and bending moments couple, it is important to understand the orientation of the loads. In particular, the application of a positive (negative) bending moment to an element of the rod generates a negative (positive) shear load, as illustrated in figure 2.3. A more detailed discussion of the relationship between bending moments and shear forces in Euler-Bernoulli beams can be found in [53] and other classical textbooks. Formally, the bending moment and shear forces at $\boldsymbol{x} = \boldsymbol{\ell}$ can be computed and compared with those at $\boldsymbol{x} = \boldsymbol{0}$ (see equations (2.22)) to confirm the direction of the forces. In particular,

$$\begin{aligned} EIw''(\ell) = {} & EI\lambda^2 \frac{\cosh\lambda\ell - \cos\lambda\ell}{\cos\lambda\ell\cosh\lambda\ell - 1}\boldsymbol{u}_n \cdot \boldsymbol{e}_2 + EI\lambda^2 \frac{\sinh\lambda\ell - \sin\lambda\ell}{\cos\lambda\ell\cosh\lambda\ell - 1}\boldsymbol{u}_n \cdot \boldsymbol{e}_3 \\ & + EI\lambda^2 \frac{\sin\lambda\ell\sinh\lambda\ell}{\cos\lambda\ell\cosh\lambda\ell - 1}\boldsymbol{u}_p \cdot \boldsymbol{e}_2 + EI\lambda \frac{\cosh\lambda\ell\sin\lambda\ell - \sinh\lambda\ell\cos\lambda\ell}{\cos\lambda\ell\cosh\lambda\ell - 1}\boldsymbol{u}_p \cdot \boldsymbol{e}_3, \end{aligned} \tag{2.23}$$

and

$$\begin{aligned} EIw'''(\ell) = {} & -EI\lambda^3 \frac{\sin\lambda\ell + \sinh\lambda\ell}{\cos\lambda\ell\cosh\lambda\ell - 1}\boldsymbol{u}_n \cdot \boldsymbol{e}_2 + EI\lambda^2 \frac{\cos\lambda\ell - \cosh\lambda\ell}{\cos\lambda\ell\cosh\lambda\ell - 1}\boldsymbol{u}_n \cdot \boldsymbol{e}_3 \\ & + EI\lambda^2 \frac{\sinh\lambda\ell\sin\lambda\ell}{\cos\lambda\ell\cosh\lambda\ell - 1}\boldsymbol{u}_p \cdot \boldsymbol{e}_2 + EI\lambda^3 \frac{\cosh\lambda\ell\sin\lambda\ell + \cos\lambda\ell\sinh\lambda\ell}{\cos\lambda\ell\cosh\lambda\ell - 1}\boldsymbol{u}_p \cdot \boldsymbol{e}_3. \end{aligned} \tag{2.24}$$

The fundamental interaction matrices are shown in equation (2.26) on page 21. It is remarked that, as in section 2.2.3, one may obtain the classical interaction matrix for massless links by taking the limit of (2.26) as $\rho \to 0$. For the case of non-inertial links, the fundamental interaction matrices are

$$\boldsymbol{A}^{\mathrm{EB}} = -\begin{pmatrix} SE/\ell & 0 & 0 \\ 0 & 12EI/l^3 & 6EI/l^2 \\ 0 & 6EI/l^2 & 4EI/l \end{pmatrix} \quad \text{and} \quad \boldsymbol{B}^{\mathrm{EB}} = \begin{pmatrix} sE/\ell & 0 & 0 \\ 0 & 12EI/l^3 & -6EI/l^2 \\ 0 & 6EI/l^2 & -EI/l \end{pmatrix}. \tag{2.25}$$

$$\boldsymbol{A}^{\mathrm{EB}} = \begin{pmatrix} -\omega ES\cot(\omega\ell/c)/c & 0 & 0 \\ 0 & EI\lambda^3 \dfrac{\cosh\lambda\ell\sin\lambda\ell + \cos\lambda\ell\sinh\lambda\ell}{\cos\lambda\ell\cosh\lambda\ell - 1} & EI\lambda^2 \dfrac{\sinh\lambda\ell\sin\lambda\ell}{\cos\lambda\ell\cosh\lambda\ell - 1} \\ 0 & EI\lambda^2 \dfrac{\sin\lambda\ell\sinh\lambda\ell}{\cos\lambda\ell\cosh\lambda\ell - 1} & EI\lambda \dfrac{\cos\lambda\ell\sinh\lambda\ell - \sin\lambda\ell\cosh\lambda\ell}{\cos\lambda\ell\cosh\lambda\ell - 1} \end{pmatrix} \tag{2.26a}$$

and

$$\boldsymbol{B}^{\mathrm{EB}} = \begin{pmatrix} \omega ES\csc(\omega\ell/c)/c & 0 & 0 \\ 0 & -EI\lambda^3 \dfrac{\sin\lambda\ell + \sinh\lambda\ell}{\cos\lambda\ell\cosh\lambda\ell - 1} & EI\lambda^2 \dfrac{\cosh\lambda\ell - \cos\lambda\ell}{\cos\lambda\ell\cosh\lambda\ell - 1} \\ 0 & EI\lambda^2 \dfrac{\cos\lambda\ell - \cosh\lambda\ell}{\cos\lambda\ell\cosh\lambda\ell - 1} & EI\lambda^2 \dfrac{\sinh\lambda\ell - \sin\lambda\ell}{\cos\lambda\ell\cosh\lambda\ell - 1} \end{pmatrix}. \tag{2.26b}$$

### 2.2.6 Thermoelastic lattices

Consider the central interaction for elastic in-plane motion discussed in section 2.2.3 in combination with the heat conduction interaction introduced in section 2.2.2. Let the two ends of a thin elastic massless conducting rod of length $\ell$ be exposed to two temperatures $\Theta_0$ and $\Theta_\ell$. The thermal strain in the rod as a result of temperature distribution $\theta(x)$ is $\varepsilon_{\mathrm{T}} = \alpha\theta(x)$, where $\alpha$ is the linear coefficient of thermal expansion. The subscript T denotes thermal, as opposed to elastic, strain. In absence of constraint forces, the axial elongation of the rod will be

$$u = \alpha \int_0^\ell \theta(x)\,\mathrm{d}x, \tag{2.27}$$

or more explicitly

$$u = \alpha\ell\frac{\Theta_0 + \Theta_\ell}{2}. \tag{2.28}$$

Thus the compressive force required to maintain equilibrium is

$$f = \alpha ES\ell\frac{\Theta_0 + \Theta_\ell}{2}, \tag{2.29}$$

Combining this thermal interaction with the elastic response of a thin rod (2.19), the fundamental interaction matrices are

$$\boldsymbol{A}^{\mathrm{TE}} = -\frac{ES[1-\alpha\ell^2(\Theta_n+\Theta_p)]}{2\ell}\begin{pmatrix}1 & 0\\ 0 & 0\end{pmatrix} \text{ and } \boldsymbol{B}^{\mathrm{TE}} = \frac{ES[1-\alpha\ell^2(\Theta_n+\Theta_p)]}{2\ell}\begin{pmatrix}1 & 0\\ 0 & 0\end{pmatrix}. \tag{2.30}$$

### 2.2.7 The rotation matrices

Consider a regular distribution of lattice points in $\mathbb{R}^2$ at positions $\boldsymbol{x}_{\boldsymbol{m},n}$, connected by lattice links. The load-potential relationship between a lattice point at $\boldsymbol{x}_{\boldsymbol{m},n}$ and its nearest neighbours is governed by equation (2.2). The potential amplitudes in equation (2.2) are stated in some global basis, whereas the fundamental interaction matrices are written in local coordinates, with the first component of the potential vectors being aligned along the link axis. Let $\boldsymbol{R}(\boldsymbol{p},q) \in \mathrm{SO}(n,\mathbb{R})$ be a rotation matrix, where $n$ is the dimension of the potential vector $\boldsymbol{u}_{\boldsymbol{p},q}$, such that

$$\frac{\boldsymbol{x}_{\boldsymbol{p},q}}{|\boldsymbol{x}_{\boldsymbol{p},q}|} = \boldsymbol{R}(\boldsymbol{p},q)\boldsymbol{e}_1. \tag{2.31}$$

In other words, $\boldsymbol{R}(\boldsymbol{p},q)$ sends the Cartesian unit vector $\boldsymbol{e}_1$ to the unit vector which is directed along the lattice link from $\boldsymbol{x}_{\boldsymbol{m},n}$ to $\boldsymbol{x}_{\boldsymbol{m}+\boldsymbol{p},n+q}$. If $\boldsymbol{u}_{\boldsymbol{p},q}$ is the potential in global coordinates, then

$$\boldsymbol{R}^{\mathrm{T}}(\boldsymbol{p},q)\boldsymbol{u}_{\boldsymbol{p},q} \tag{2.32}$$

is potential in local coordinates. Furthermore, the load on node $(\boldsymbol{m},n)$ as a result of potential $\boldsymbol{u}_{\boldsymbol{p},q}$ in local coordinates is

$$[\boldsymbol{A}\delta_{\boldsymbol{p},\boldsymbol{0}}\delta_{nq} + \boldsymbol{B}(1-\delta_{\boldsymbol{p},\boldsymbol{0}}\delta_{nq})]\boldsymbol{R}^{\mathrm{T}}(\boldsymbol{p},q)\boldsymbol{u}_{\boldsymbol{p},q}, \tag{2.33}$$

where $\delta_{\boldsymbol{p},\boldsymbol{m}}$ is the two-dimensional Kronecker delta for indices $\boldsymbol{p}$, $\boldsymbol{m} \in \mathbb{Z}^2$ such that $\delta_{\boldsymbol{p},\boldsymbol{m}} = \delta_{p_1 m_1}\delta_{p_2 m_2}$. Finally, in global coordinates the load becomes

$$\boldsymbol{R}(\boldsymbol{p},q)[\boldsymbol{A}\delta_{\boldsymbol{p},\boldsymbol{0}}\delta_{nq} + \boldsymbol{B}(1-\delta_{\boldsymbol{p},\boldsymbol{0}}\delta_{nq})]\boldsymbol{R}^{\mathrm{T}}(\boldsymbol{p},q)\boldsymbol{u}_{\boldsymbol{p},q}, \tag{2.34}$$

whence equation (2.2) may be written as

$$\sum_{(\boldsymbol{p},q)\in\mathcal{N}_n} \boldsymbol{R}(\boldsymbol{p},q)[\boldsymbol{A}\delta_{\boldsymbol{p},\boldsymbol{0}}\delta_{nq} + \boldsymbol{B}(1-\delta_{\boldsymbol{p},\boldsymbol{0}}\delta_{nq})]\boldsymbol{R}^{\mathrm{T}}(\boldsymbol{p},q)\boldsymbol{u}_{\boldsymbol{p},q} - (i\omega)^s\mathcal{I}_n\boldsymbol{u}_{\boldsymbol{m},n} = \boldsymbol{f}_{\boldsymbol{m},n}. \tag{2.35}$$

The coefficient of $\boldsymbol{u}_{\boldsymbol{p},q}$ in equation (2.34) represents the interaction matrix $C_{\boldsymbol{p},q}$ defined in (2.2).

It is remarked that if the fundamental interaction matrix is a scalar multiple of the identity matrix, then since $\boldsymbol{R}^{\mathrm{T}}(\boldsymbol{p},q)\boldsymbol{R}(\boldsymbol{p},q) = \mathbb{I}$ by definition, and hence the full interaction matrix will also be a scalar multiple of the identity matrix. Such cases occur for uniform scalar lattices, where all lattice points are the same and the potentials are scalar.

With the necessary notation and preliminary results established, the following chapter will be concerned with the dispersive properties of an elastic triangular lattice and in particular, examination of the effect of distributed inertia on the effective group velocities of elastic waves.

# *Chapter Three*

# Elastic lattices with distributed inertia

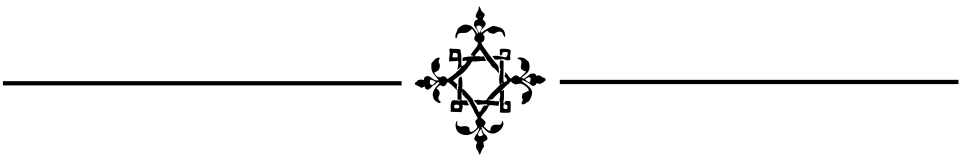

Classically, mechanical lattices can be thought of as a regular array of point masses connected by massless springs, thin rods, or beams so that all of the mass of the lattice is concentrated at the nodal points. In this sense, that the lattices are said to have non-inertial links. The primary focus of the present chapter is to examine the behaviour of lattices where the inertia is distributed over the lattice links in addition to at the nodal points. The addition of inertial links brings many interesting features not present in the lattices with non-inertial links. In particular, for lattices with inertial links the deformation of the links are no longer simply functions of the displacements at the lattice points, but also depend on the frequency of excitation. Moreover, in contrast to massless links, inertial links have their own spectrum of fundamental modes, which contribute to the overall dispersive properties of the lattice.

In the present chapter, the effect of dynamic micro-polar interactions on the response of discrete inertial systems outside the standard homogenisation regime is be examined. Several types of interaction are considered and a comparison with the earlier work of Maz'ya *et al.* [102] and Morozov [107] is made. Explicit analytical formulae are derived for the effective group velocities in the long wavelength limit. The chapter begins with an introduction of the lattice geometry and governing equations. Although only one particular lattice geometry is considered, the ideas and methods presented herein are entirely general and can equally be applied to other regular lattice geometries and higher dimensional lattices. The dispersion equation is then examined with particular emphasis placed on the low-frequency, quasi-static limit. Effective group velocities are derived and homogenised Lamé coefficients are deduced for different types of interactions. Several types of lattice interactions are considered where the lattice links correspond to: thin rods (§ 2.2.3), thin rods with rotational springs (§ 2.2.4) and Euler-Bernoulli beams (§ 2.2.5).

## 3.1 The geometry and governing equations

The diatomic triangular lattice in $\mathbb{R}^2$ consider in this chapter is shown in figure 3.1. The diatomic elements consist of the red and blue masses (see figure 3.1) having contrasting inertial proper-

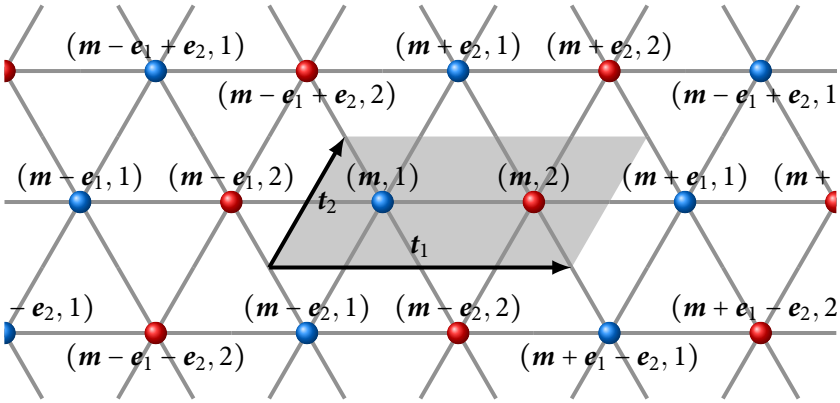


**Figure 3.1:** The diatomic triangular lattice and its elementary cell shaded in grey. The lattice vectors $\boldsymbol{t}_1$ and $\boldsymbol{t}_2$ are also indicated. The vectors $\boldsymbol{e}_1 = [1,0]^{\mathrm{T}}$ and $\boldsymbol{e}_2 = [0,1]^{\mathrm{T}}$ are counting indices.

ties. This particular lattice, whilst relatively simple, can be used to illustrate a range of interesting phenomena. For example, the static response of such a lattice is isotropic; however, as will be shown later in the thesis, at higher frequencies this lattice exhibits strong dynamic anisotropy. Moreover, the diatomic nature of the lattice allows the dynamic effects of multi-atomic lattices to be investigated, whilst not greatly overcomplicating the exposition. More importantly, the triangular geometry permits investigation of not only lattices with Euler-Bernoulli links (§ 2.2.5), but also the case of purely central interactions (§ 2.2.3). The triangular geometry also allows convenient investigation of monatomic lattices. For other lattice geometries in $\mathbb{R}^2$, the system is either degenerate if bending moments are neglected (e.g. square lattices), or cannot accommodate monatomic structures (e.g. hexagonal lattices).

This chapter will deal exclusively with in-plane elastic motion, with forces as applied loads and elastic displacements as potentials. In this case, the interaction matrices are correspond to stiffnesses. For mechanical lattices, $s = 2$ and (2.1) is simply Newton's second law. It is convenient to work with non-dimensional units. Therefore, the length of the lattice links as well as the mass of the blue nodes and the longitudinal stiffness of the lattice links ($ES/\ell$) are taken as natural units. Other natural units will be introduced when convenient. With this in mind, the direct lattice vectors are $\boldsymbol{t}_1 = [2,0]^{\mathrm{T}}$ and $\boldsymbol{t}_2 = [1/2, \sqrt{3}/2]^{\mathrm{T}}$. The position of particle $(\boldsymbol{m}, n)$ is

$$\boldsymbol{x}_{\boldsymbol{m},n} = \begin{pmatrix} 2m_1 + m_2/2 + \delta_{2,n} \\ m_2\sqrt{3}/2 \end{pmatrix}, \tag{3.1}$$

and the sets of nearest neighbours are

$$\mathcal{N}_1 = \{(\boldsymbol{0},0), (\boldsymbol{0},1), (\boldsymbol{e}_2,0), (-\boldsymbol{e}_1+\boldsymbol{e}_2,1), (-\boldsymbol{e}_1+\boldsymbol{e}_2,1), (-\boldsymbol{e}_1,1), (-\boldsymbol{e}_2,0)\}, \tag{3.2a}$$

and

$$\mathcal{N}_2 = \{(\boldsymbol{0},0), (\boldsymbol{e}_1,-1), (\boldsymbol{e}_2,0), (\boldsymbol{e}_2,-1), (\boldsymbol{0},-1), (-\boldsymbol{e}_2,0), (\boldsymbol{e}_1-\boldsymbol{e}_2,-1)\}. \tag{3.2b}$$

For the unforced problem, $\boldsymbol{f}_n = \mathbf{0}$, whence the Fourier transformed equations of motion and the dispersion equation are

$$\boldsymbol{\sigma}(\omega, \boldsymbol{\xi})\mathbf{U}^{\mathrm{FF}}(\boldsymbol{\xi}) = \mathbf{0}, \tag{3.3a}$$

and

$$\det \boldsymbol{\sigma}(\omega, \boldsymbol{\xi}) = 0, \tag{3.3b}$$

where the matrix $\boldsymbol{\sigma}(\omega, \boldsymbol{\xi})$ has $nq$-block entries

$$\sigma_{nq}(\omega, \boldsymbol{\xi}) = \sum_{\boldsymbol{p}\in\mathcal{N}_n} \left\{ \omega^2 \mathcal{I}_n \delta_{nq} + \boldsymbol{R}(\boldsymbol{p}, q)[\boldsymbol{A}\delta_{\boldsymbol{p},\mathbf{0}}\delta_{nq} + \boldsymbol{B}(1 - \delta_{\boldsymbol{p},\mathbf{0}}\delta_{nq})]\boldsymbol{R}(\boldsymbol{p}, q)^{\mathrm{T}} e^{-i\boldsymbol{x}_{\boldsymbol{p}}\cdot\boldsymbol{\xi}} \right\}. \tag{3.4}$$

### 3.1.1 The dispersion equation and the quasi-static group velocity

Plotting the $(\omega, \boldsymbol{\xi})$ solutions of (3.3b) results in a two-dimensional dispersion surface. The gradient[1] of the dispersion surface yields the group velocity of Bloch waves travelling through the lattice, $\boldsymbol{v}(\omega, \boldsymbol{\xi}) = \nabla_{\boldsymbol{\xi}} \det \boldsymbol{\sigma}(\omega, \boldsymbol{\xi})$. Later in this chapter the quasi-static group velocity, that is $\boldsymbol{v}(\omega, \boldsymbol{\xi})$ for small $\omega$ and $|\boldsymbol{\xi}|$, will be evaluated. In particular, for small $\omega$ and $|\boldsymbol{\xi}|$ the dispersion equation may be formally expanded in a Taylor series

$$0 = \sum_{|\alpha|\geq 0} [\partial^\alpha \det \boldsymbol{\sigma}(\omega, \boldsymbol{\xi})]|_{(0,\mathbf{0})} \frac{(\omega, \boldsymbol{\xi})^\alpha}{\alpha!}, \quad \text{where} \quad \partial^\alpha = \frac{\partial^{\alpha_1}}{\partial\omega^{\alpha_1}} \frac{\partial^{\alpha_2}}{\partial\xi_1^{\alpha_2}} \frac{\partial^{\alpha_3}}{\partial\xi_3^{\alpha_3}}, \tag{3.5}$$

and the multi-index $\alpha = (\alpha_1, \alpha_2, \alpha_3)$ has been introduced. It is clear from (3.4) and the fundamental interaction matrices (2.18), (2.20), and (2.26) that for $\omega = 0$ the only solution to the dispersion equation (3.3b) is $\boldsymbol{\xi} = \mathbf{0}$. Thus, there is no constant term in (3.5). Moreover, (3.4), (2.18), (2.20), and (2.26) are symmetric about the origin with respect to $\omega$. Hence, the coefficients of $\omega^{2n-1}$ (where $n \in \mathbb{N}$) in the expansion (3.5) must vanish. With the view of obtaining two quasi-static dispersion surfaces, that is the two conical acoustic dispersion surfaces near the origin, terms of order up to and including $|\alpha| = 4$ are kept in (3.5) yielding

$$0 \sim a_0(\boldsymbol{\xi}) + a_2(\boldsymbol{\xi})\omega^2 + a_4(\boldsymbol{\xi})\omega^4, \tag{3.6}$$

where $a_n(\boldsymbol{\xi})$ are polynomials in $\boldsymbol{\xi}$ of, at most, degree $4 - n$. Equation (3.6) is the quasi-static dispersion equation, whose positive solutions $\omega^{(i)}$ yield the frequency as a function of wave vector. The quasi-static group velocities may then be found by taking the gradient of $\omega^{(i)}$ with respect to the wave vector $\boldsymbol{\xi}$.

In the following sections, three types of interaction are considered. The dispersion surfaces are presented and the dispersive properties of the lattice examined. Expressions for the quasi-static group velocities are derived, from which Lamé parameters corresponding to a homogenised plane strain system can be deduced.

[1] It should be understood that all operators herein are expressed in terms of natural units. That is, the gradient is non-dimensionalised by multiplication by the length of the lattice links $\ell$.

### 3.1.2 A note on numerical solutions of the dispersion equation

Although this thesis is not focussed on numerical analysis, it is appropriate to briefly discuss the nature of equation (3.3b) and the difficulties associated with finding solutions of the dispersion equation numerically.

In general, for fixed $\boldsymbol{\xi}$, equation (3.3b) is a transcendental equation in $\omega$, the real solutions of which yield the frequencies of propagating waves for a given Bloch vector $\boldsymbol{\xi}$. These roots may have a non-unitary multiplicity and may coincide with removable singularities, both of which present significant challenges when searching for roots numerically. The former property prevents classical root bracketing, and hence those root finding algorithms which require bracketing. The latter property presents the obvious difficulty of dealing with removable singularities numerically.

For the interactions considered here, the dispersion equation is sufficiently smooth to be amenable to approximation by polynomial expansion. In particular, using the MATLAB library CHEBFUN [142] equation (3.3b) may be approximated by an expansion in Chebyshev polynomials over a specified interval, allowing the roots to be found efficiently. For the Euler-Bernoulli interaction, the commercial finite element software Comsol Multiphysics® is also used to solve the dispersion equation using finite elements. This allows independent verification of the CHEBFUN approximation for the Euler-Bernoulli interaction.

For the case of non-inertial links, the dispersion equation (3.3b) $\det \boldsymbol{\sigma}(\omega, \boldsymbol{\xi}) = 0$ need not be solved directly. From a numerical point of view, it is far more efficient and convenient to solve the eigenvalue problem by, for example, Schur decomposition. However, for the case of inertial links it is necessary to solve the dispersion equation directly.

Consider the block entries of $\boldsymbol{\sigma}(\omega, \boldsymbol{\xi})$ as introduced in (3.4) for non-inertial matrices and fixed $\boldsymbol{\xi}$. Introducing the square auxiliary matrices $\boldsymbol{G} = \operatorname{diag}[\mathcal{I}_1, \mathcal{I}_2, \ldots, \mathcal{I}_Q]$[2] and $\boldsymbol{H}(\omega, \boldsymbol{\xi})$, with $nq$-block entries

$$H_{nq}(\omega, \boldsymbol{\xi}) = -\sum_{\boldsymbol{p} \in \mathcal{N}_n} \left\{ \boldsymbol{R}(\boldsymbol{p}, q)[\boldsymbol{A}\delta_{\boldsymbol{p},\boldsymbol{0}}\delta_{nq} + \boldsymbol{B}(1 - \delta_{\boldsymbol{p},\boldsymbol{0}}\delta_{nq})]\boldsymbol{R}^{\mathrm{T}}(\boldsymbol{p}, q)e^{-i\boldsymbol{x}_{\boldsymbol{p}}\cdot\boldsymbol{\xi}} \right\}, \tag{3.7}$$

the equations of motion (3.3a) may be written as

$$\omega^2 \boldsymbol{G}\mathbf{U}^{\mathrm{FF}}(\boldsymbol{\xi}) = \boldsymbol{H}(\omega, \boldsymbol{\xi})\mathbf{U}^{\mathrm{FF}}(\boldsymbol{\xi}). \tag{3.8}$$

The hermitian transpose of $H_{n,q}(\omega, \boldsymbol{\xi})$ is

$$H^{\dagger}_{nq}(\omega, \boldsymbol{\xi}) = -\sum_{\boldsymbol{p} \in \mathcal{N}_n} \left\{ \left[\boldsymbol{R}^{\mathrm{T}}(\boldsymbol{p}, q)\right]^{\dagger} [\boldsymbol{A}^{\dagger}\delta_{\boldsymbol{p},\boldsymbol{0}}\delta_{nq} + \boldsymbol{B}^{\dagger}(1 - \delta_{\boldsymbol{p},\boldsymbol{0}}\delta_{nq})]\boldsymbol{R}^{\dagger}(\boldsymbol{p}, q)e^{i\boldsymbol{x}_{\boldsymbol{p}}\cdot\boldsymbol{\xi}} \right\}. \tag{3.9}$$

The rotation matrices are real hence,

$$H_{nq}(\omega, \boldsymbol{\xi}) = -\sum_{\boldsymbol{p} \in \mathcal{N}_n} \left\{ \boldsymbol{R}(\boldsymbol{p}, q)[\boldsymbol{A}^{\dagger}\delta_{\boldsymbol{p},\boldsymbol{0}}\delta_{nq} + \boldsymbol{B}^{\dagger}(1 - \delta_{\boldsymbol{p},\boldsymbol{0}}\delta_{nq})]\boldsymbol{R}^{\mathrm{T}}(\boldsymbol{p}, q)e^{i\boldsymbol{x}_{\boldsymbol{p}}\cdot\boldsymbol{\xi}} \right\}, \tag{3.10}$$

If $\boldsymbol{p} \in \mathcal{N}_n$ then it follows immediately that $-\boldsymbol{p} \in \mathcal{N}_q$ and further it is clear that $\boldsymbol{x}_{-\boldsymbol{p}} = -\boldsymbol{x}_{\boldsymbol{p}}$. Physi-

[2] In this case, $Q = 2$.

cally, this means that node $(\boldsymbol{m}, n)$ is connected to node $(\boldsymbol{m}+\boldsymbol{p}, n+q)$ by a lattice link along $\boldsymbol{x}_{\boldsymbol{p}}$ and, equally, node $(\boldsymbol{m}+\boldsymbol{p}, n+q)$ is connected to node $(\boldsymbol{m}, n)$ by a lattice link along $-\boldsymbol{x}_{\boldsymbol{p}}$. Hence,

$$H^{\dagger}_{nq}(\omega, \boldsymbol{\xi}) = -\sum_{\boldsymbol{p}\in\mathcal{N}_q} \left\{ \boldsymbol{R}(-\boldsymbol{p}, q)[\boldsymbol{A}^{\dagger}\delta_{\boldsymbol{p},\boldsymbol{0}}\delta_{nq} + \boldsymbol{B}^{\dagger}(1-\delta_{\boldsymbol{p},\boldsymbol{0}}\delta_{nq})]\boldsymbol{R}^{\mathrm{T}}(-\boldsymbol{p}, q)e^{-i\boldsymbol{x}_{\boldsymbol{p}}\cdot\boldsymbol{\xi}} \right\}, \tag{3.11}$$

where it is emphasised that the summation is now over $\mathcal{N}_q$, that is the set of nodes connected to node $(\boldsymbol{m}+\boldsymbol{p}, n+q)$ in the elementary cell, rather than $\mathcal{N}_n$ (the set of nodes connected to node $(\boldsymbol{m}, n)$). For planar rotations (rotations about the $x_3$ axis), $\boldsymbol{R}(-\boldsymbol{p}, q) = \boldsymbol{R}(\boldsymbol{p}, q)\tilde{\boldsymbol{R}}$, where $\tilde{\boldsymbol{R}}\boldsymbol{x} = -\boldsymbol{x}$, i.e. a rotation by $\pi$ about the $x_3$ axis. For the fundamental interaction matrices considered in the previous section, $\tilde{\boldsymbol{R}}\boldsymbol{A}^{\dagger}\tilde{\boldsymbol{R}}^{\mathrm{T}} = \boldsymbol{A}^{\dagger} = \boldsymbol{A}$ and $\tilde{\boldsymbol{R}}\boldsymbol{B}^{\dagger}\tilde{\boldsymbol{R}}^{\mathrm{T}} = \boldsymbol{B}$, whence

$$H^{\dagger}_{nq}(\omega, \boldsymbol{\xi}) = -\sum_{\boldsymbol{p}\in\mathcal{N}_q} \left\{ \boldsymbol{R}(\boldsymbol{p}, q)[\boldsymbol{A}\delta_{\boldsymbol{p},\boldsymbol{0}}\delta_{nq} + \boldsymbol{B}(1-\delta_{\boldsymbol{p},\boldsymbol{0}}\delta_{nq})]\boldsymbol{R}^{\mathrm{T}}(\boldsymbol{p}, q)e^{-i\boldsymbol{x}_{\boldsymbol{p}}\cdot\boldsymbol{\xi}} \right\} = H_{qn}(\omega, \boldsymbol{\xi}). \tag{3.12}$$

Thus, for fixed $\boldsymbol{\xi}$, the square matrix $\boldsymbol{H} = \boldsymbol{H}(\boldsymbol{\xi})$ is normal and has $N$ real eigenvalues (eigenfrequencies) and $N$ linearly independent eigenvectors (eigenmodes), where $N$ is the dimension of $\boldsymbol{H}$.

## 3.2 Central interactions

For central lattice interactions, as in section 2.2.3, the in-plane elastic displacement amplitude of particle $(\boldsymbol{m}, n)$ is denoted by $\boldsymbol{u}_{\boldsymbol{m},n} \in \mathbb{C}^2$. The rotation matrix is the $2\times 2$ skew-symmetric matrix

$$R(\boldsymbol{p}, q) = \begin{pmatrix} \cos\theta_{\boldsymbol{p},q} & -\sin\theta_{\boldsymbol{p},q} \\ \sin\theta_{\boldsymbol{p},q} & \cos\theta_{\boldsymbol{p},q} \end{pmatrix}, \tag{3.13}$$

where $\theta_{\boldsymbol{p},q}$ is the angle between $\boldsymbol{x}_{\boldsymbol{p},q}$ and $\boldsymbol{e}_1$. At this point, it is convenient to introduce the non-dimensional parameter $\eta = \omega\sqrt{\rho}$, which characterises the natural frequency of longitudinal vibrations in the lattice links[3]. Indeed, $\eta$ is the eigenvalue of the wave equation (2.16) which governs the longitudinal vibration of a thin prismatic rod. The elements of the diagonal blocks $\sigma_{11}$ and $\sigma_{22}$ of matrix $\boldsymbol{\sigma}(\omega, \boldsymbol{\xi})$ are as follows:

$$\left.\begin{aligned} \left[\sigma_{jj}\right]_{11} &= m_j\omega^2 - 3\eta\cot\eta + \frac{\eta}{2}\cos\varphi\csc\eta \\ \left[\sigma_{jj}\right]_{12} &= \left[\sigma_{jj}\right]_{21} = \eta\frac{\sqrt{3}}{2}\cos\varphi\csc\eta \\ \left[\sigma_{jj}\right]_{22} &= m_j\omega^2 - 3\eta\cot\eta + \eta\frac{3}{2}\cos\varphi\csc\eta \end{aligned}\right\}, \tag{3.14a}$$

where $\varphi = \boldsymbol{k}\cdot\mathcal{T}\boldsymbol{e}_2 = (\xi_1 + \sqrt{3}\xi_2)/2$, $\mathcal{T} = [\boldsymbol{t}_1, \boldsymbol{t}_2]$ is the translation matrix, and $m_j = \delta_{1j} + m\delta_{2j}$. Similarly, the off-diagonal blocks $\sigma_{12} = \sigma^{\dagger}_{21}$, where $(\cdot)^{\dagger}$ indicates the Hermitian transpose, have

[3] In the current system of natural units, the frequency $\omega$ and density of the lattice links $\rho$ are themselves non-dimensional. For definiteness, the corresponding quantities expressed in dimensional form are $\bar{\omega} = \omega\sqrt{ES/(m_1\ell)}$ and $\bar{\rho} = \rho m_1/(S\ell)$, where $m_1$ is the mass of the blue lattice points in figure 3.1.

the entries

$$\left.\begin{aligned}[\sigma_{12}]_{11} &= \left[\left(e^{-2i\xi_1 l}+\frac{e^{-i\varphi}+e^{-i\psi}}{4}\right)+1\right]\eta\csc\eta\\ [\sigma_{12}]_{12} &= [\sigma_{12}]_{21} = -\sqrt{3}\frac{e^{-i\varphi}+e^{-i\psi}}{4}\eta\csc\eta,\\ [\sigma_{12}]_{22} &= \frac{e^{-i\psi}+e^{-i\varphi}}{4}3\eta\csc\eta\end{aligned}\right\}, \tag{3.14b}$$

where $\psi = \boldsymbol{\xi}\cdot\mathcal{T}(\boldsymbol{e}_1-\boldsymbol{e}_2) = (3\xi_1-\sqrt{3}\xi_2)/2$. The corresponding entries for the case of massless links can be recovered by taking the limit of (3.14) as $\eta\to 0$. Doing so yields

$$\left.\begin{aligned}[\sigma_{11}]_{11} &= -3+\frac{\cos\varphi}{2}\\ [\sigma_{11}]_{12} &= [\sigma_{11}]_{21} = \frac{\sqrt{3}\cos\varphi}{2}\\ [\sigma_{11}]_{22} &= -3+\frac{3\cos\varphi}{2}\end{aligned}\right\}, \tag{3.15a}$$

and

$$\left.\begin{aligned}[\sigma_{12}]_{11} &= \left[\left(e^{-2i\xi_1 l}+\frac{e^{-i\varphi}+e^{-i\psi}}{4}\right)+1\right]\\ [\sigma_{12}]_{12} &= [\sigma_{12}]_{21} = -\sqrt{3}\frac{e^{-i\varphi}+e^{-i\psi}}{4},\\ [\sigma_{12}]_{22} &= 3\frac{e^{-i\psi}+e^{-i\varphi}}{4}\end{aligned}\right\}. \tag{3.15b}$$

From (3.6), the following equation is obtained for the quasi-static (i.e. small $\omega$ and $|\boldsymbol{\xi}|$) dispersion surfaces

$$3(1+m+3\rho)^2\omega^4 - 9|\boldsymbol{\xi}|^2(1+m+3\rho)\omega^2 + \frac{81}{16}|\boldsymbol{\xi}|^4 = 0, \tag{3.16}$$

whence the positive solutions are

$$\omega_{\mathrm{C}}^{(1)} = \frac{3}{2}\frac{|\boldsymbol{\xi}|}{\sqrt{1+m+3\rho}}, \tag{3.17a}$$

$$\omega_{\mathrm{C}}^{(2)} = \frac{\sqrt{3}}{2}\frac{|\boldsymbol{\xi}|}{\sqrt{1+m+3\rho}}, \tag{3.17b}$$

where $m$ is the mass of the red nodes (see figure 3.1). The corresponding quasi-static effective group velocities are then

$$\boldsymbol{v}_{\mathrm{C}}^{(1)} = \frac{3}{2}\frac{\hat{\boldsymbol{\xi}}}{\sqrt{1+m+3\rho}}, \tag{3.18a}$$

$$\boldsymbol{v}_{\mathrm{C}}^{(2)} = \frac{\sqrt{3}}{2}\frac{\hat{\boldsymbol{\xi}}}{\sqrt{1+m+3\rho}}, \tag{3.18b}$$

where $\hat{\boldsymbol{\xi}} = \boldsymbol{\xi}/|\boldsymbol{\xi}|$. The first observation that may be drawn from (3.18) is that the quasi-static group velocities are isotropic. In other words, in the low frequency limit, the wave speeds of elastic waves travelling through the triangular lattice with central interactions do not depend on the direction of propagation. Secondly, in this low frequency regime, the group velocities

coincide with the phase velocities ($\omega_C^{(i)}\hat{\boldsymbol{\xi}}/|\boldsymbol{\xi}|$).

The neighbourhood of the quasi-static limit $(\omega, \boldsymbol{\xi}) \to \mathbf{0}$, also referred to as the *long wavelength* limit, is the region in which classical homogenisation is applied. In this regime, the dynamic response of a micro-structured solid may be treated as a continuum with appropriately chosen elastic moduli and densities. Typically, these effective moduli are determined from the static response of the lattice (see [27, 50, 100, 123]among others).

Consider the well known wave speeds for elastic waves in a linear homogeneous isotropic elastic medium

$$v_p = \sqrt{\frac{\lambda + 2\mu}{\varrho}}, \tag{3.19a}$$

$$v_s = \sqrt{\frac{\mu}{\varrho}}, \tag{3.19b}$$

where $\lambda$, $\mu$ and $\varrho$ are the Lamé constants and density respectively. The subscript $p$ and $s$ in (3.19) denote the pressure and shear wave speeds respectively. It is observed that $\boldsymbol{v}_{\mathrm{C}}^{(1)} > \boldsymbol{v}_{\mathrm{C}}^{(2)}$, hence, comparing (3.18) and (3.19) it can be inferred that $\boldsymbol{v}_{\mathrm{C}}^{(1)}$ corresponds to pressure waves and $\boldsymbol{v}_{\mathrm{C}}^{(2)}$ corresponds to shear waves in the quasi-static limit. Moreover, equating $\boldsymbol{v}_{\mathrm{C}}^{(1)} = v_p$ and $\boldsymbol{v}_{\mathrm{C}}^{(2)} = v_s$ implies $\lambda = \mu$ and hence $\nu = 1/4$. Further, treating $\varrho$ as the *quasi-static effective density* of the lattice, that is taking $\varrho = (1 + m + 3\rho)/\sqrt{3}$, equations (3.18) and (3.19) imply

$$\lambda = \mu = \frac{\sqrt{3}}{4}. \tag{3.20}$$

In the long wavelength limit, the macroscopic density $\varrho$ (sometimes known as the relative density) is usually determined by computing the microscopic density of the elementary cell, as done in [50,127]. The total density of the elementary cell is $(1+m+6\rho)/\sqrt{3}$ (refer to figure 3.1), that is the mass of the two particles and six lattice links, with the area of the elementary cell being $\sqrt{3} = |\boldsymbol{t}_1 \times \boldsymbol{t}_2|$. However, considering equations (3.19) and (3.18) one is lead to the conclusion that $\varrho = (1 + m + 3\rho)/\sqrt{3}$. Thus, the macroscopic density obtained from taking the static limit of the dynamic system is different to the macroscopic density obtain by purely considering the distribution of mass in the lattice. In this sense, there is said to be a *morphological change* to the static group velocity of elastic waves in the lattice.

The morphological change to the group velocity is a result of the distribution of mass along the lattice links. For the case of non-inertial links ($\rho = 0$), the macroscopic density obtained from the limit case of the dynamic system is identical to the so-called relative density obtained from the static analysis. However, for a lattice with inertial links ($\rho > 0$), the effective macroscopic density obtained from the quasi-static limit case of the dynamic system is not equivalent to the density obtained from the static analysis. In particular, consider two diatomic triangular lattices, identical in every way, except that one lattice has massless links connecting alternating nodes of unit mass and $m = 9$ as illustrated in figure 3.1, and the second lattice has links of unit density connecting alternating masses of unit mass and $m = 3$. In both cases the total mass in the elementary cell is identical. According to the static analysis, both lattices have the same elastic moduli and relative densities and therefore have the same group velocities. However, according to (3.19) and the previous discussion, the quasi-static limit of the dynamic system predicts dif-

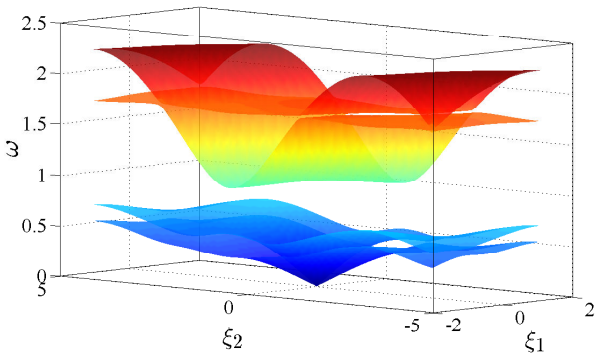


**Figure 3.2:** The four dispersion surfaces for the diatomic triangular lattice with non-inertial links ($\rho = 0$) and $m = 10$.

ferent effective group velocities. From the dynamic system, the effective group velocities *even in the quasi-static limit* depend on the distribution of inertia in the elementary cell, not simply the total mass. Qualitatively, the effect of distributing the mass of the lattice over the lattice links is to increase the quasi-static group velocities, i.e. the higher the proportion of mass in the lattice links, the higher the group velocity.

For the case of massless links ($\varrho = 0$), the effective material properties in the quasi-static limit agree with those already in the literature for static systems (see, for example, [123]).

### 3.2.1 A remark on central interactions and square lattices

At the outset of this chapter it was remarked that for some other planar lattice geometries, considering only central interactions leads to a degenerate system for in-plane mechanical motion. For the square lattice, $\theta_{\boldsymbol{p},q}$ in the rotation matrix (3.13) are integer multiples of $\pi/2$ which, for a monatomic square lattice with massless links, leads to an interaction matrix of the form

$$\sigma(\omega, \boldsymbol{\xi}) = \begin{pmatrix} \omega^2 - 4\sin^2\left(\frac{\xi_1}{2}\right) & 0 \\ 0 & \omega^2 - 4\sin^2\left(\frac{\xi_2}{2}\right) \end{pmatrix}. \tag{3.21}$$

Thus, the system decouples and degenerates into a model of the one-dimensional wave propagation in two non-interacting chains. In particular, the lattice permits Bloch waves of amplitude $\boldsymbol{u}_{\boldsymbol{m}}^{(i)} = [\delta_{i,1}, \delta_{i,2}]^{\mathrm{T}} e^{i\xi_i m_i}$ with angular frequencies $\omega^{(i)} = 2\sin\xi_i/2$ and $\xi_i \in [0, \pi)$. Analysis of a square lattice with inertial links yields a less concise, but still diagonal, interaction matrix. Hence, the square lattice with inertial links is also degenerate when only central interactions are considered.

### 3.2.2 Dispersion properties and standing waves

Figures 3.2–3.4 show dispersion diagrams for the diatomic triangular lattice with central interactions for a range of parameter values. The dispersion surfaces are the zero $(\omega, \boldsymbol{\xi})$ isosurfaces

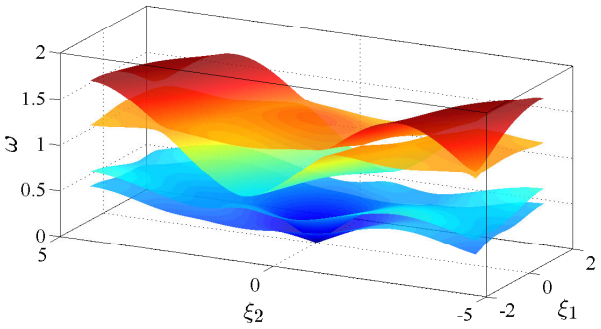


**Figure 3.3:** The first four dispersion surfaces for the diatomic triangular lattice with inertial links, for $\rho = 1$ and $m = 10$.

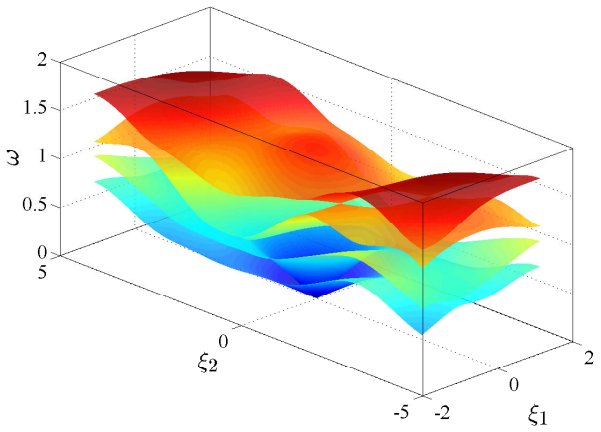


**Figure 3.4:** The first four dispersion surfaces for the diatomic triangular lattice with inertial links, for $\rho = 1$ and $m = 4$.

of the dispersion equation (3.3b), that is the set $\{(\omega, \boldsymbol{\xi}) : \det \boldsymbol{\sigma}(\omega, \boldsymbol{\xi}) = 0\}$. Formally, the elementary cell in the reciprocal lattice is the parallelogram spanned by the principle lattice vectors $\boldsymbol{b}_1 = \pi[1, -1/\sqrt{3}]^{\mathrm{T}}$ and $\boldsymbol{b}_2 = 4\pi[0, 1/\sqrt{3}]^{\mathrm{T}}$. However, it is convenient to plot the dispersion surfaces of the rectangular region $\boldsymbol{\xi} = [-\pi, \pi] \times [-5\pi/(2\sqrt{3}), 5\pi/(2\sqrt{3})]$, which contains an elementary cell of the reciprocal lattice.

Figure 3.2 shows the dispersion surfaces for lattice with non-inertial links. For this particular configuration (diatomic triangular lattice with non-inertial links and central interactions), the dispersion equation is a quadratic polynomial in $\omega^2$ and as such has closed form solutions $\omega = \omega(\boldsymbol{\xi})$. However, these solutions are cumbersome when expressed in the form $\omega = \omega(\boldsymbol{\xi})$. Furthermore, for the configurations examined later it is not possible to obtain closed form solutions. Nevertheless, relevant information may be extracted from the dispersion equation itself. Since the dispersion equation is quadratic in $\omega^2$ and symmetric about $\omega = 0$, there exists at most four distinct positive solutions and hence not more than four dispersion surfaces. Figure 3.2 shows the two acoustical dispersion surfaces and the two optical dispersion surfaces separated by a band gap of finite width. The characteristic semi-infinite band gap for discrete structures exists above the highest dispersion surface.

In the vicinity of the origin, the two acoustic dispersion surfaces are conical with circular cross-sections. Hence, in the quasi-static limit the response of the lattice is isotropic, as expected from the analysis in section 3.2. The finite-width band gap is bounded from below by an acoustic dispersion surface and from above by an optical surface. On the boundary of the band gap, the dispersion surfaces have local maxima and minima characterising standing waves (waves with zero group velocity). The presence of these stationary points allow the width of the stop band to be estimated.

*Some features of the dispersion surfaces may by difficult to discern in the static 2D representations presented here. Therefore, 3D MATLAB figure files corresponding to these dispersion surfaces are provided at* `http://dx.doi.org/`10.6084/`m`9.`figshare`.746915.

The maxima of the upper acoustic surface bounding the band gap from below lies at the edge of the elementary cell of the reciprocal lattice along $\boldsymbol{b}_2 - \boldsymbol{b}_1$, where $\boldsymbol{b}_1$ and $\boldsymbol{b}_2$ are the basis vectors of the reciprocal lattice. At this point, $\boldsymbol{\xi} = (\boldsymbol{b}_2 - \boldsymbol{b}_1)/2$, the off-diagonal block matrices $\sigma_{12}$ and $\sigma_{21}$ vanish (see equations (3.15)) and the dispersion equation reduces to

$$[(7 - 2\omega_O^2)(9 - 2\omega_O^2) - 3][(7 - 2m\omega_A^2)(9 - 2m\omega_A^2) - 3] = 0, \tag{3.22}$$

with solutions $\omega_A^2$ corresponding to acoustic modes and $\omega_O^2$ corresponding to optical modes, where $\omega_A^2 \leq \omega_O^2$. It has been assumed, without loss of generality, that $m \geq 1$. The lower bound of the band gap is then given by $\max\{\omega_A\}$: $\omega_l = \sqrt{5/m}$ where $\omega_A \leq \omega_l$. Similarly, the minima of the optical surfaces bounding the stop band from above occurs at the boundary of the elementary cell in the reciprocal lattice along the vector $\boldsymbol{b}_1$. Again, the off-diagonal block entries $\sigma_{12}$ and $\sigma_{21}$ vanish at $\boldsymbol{\xi} = \boldsymbol{b}_1/2$, whence the dispersion equation becomes

$$[(5 - 2\omega_O^2)(3 - 2\omega_O^2) - 3][(5 - 2m\omega_A^2)(3 - 2m\omega_A^2) - 3] = 0. \tag{3.23}$$

In this case, the upper bound of the band gap is then $\min\{\omega_O\}$: $\omega_u = 1$. Thus, the finite width band gap is defined by the interval $\max\{\omega_A\} < \omega < \min\{\omega_O\}$, or more explicitly

$$\sqrt{\frac{5}{m}} < \omega < 1. \tag{3.24}$$

For the numerical values used to produce figure 3.2, in particular $m = 10$, the interval is $1/\sqrt{2} < \omega < 1$, which agrees with the position of the band gap in figure 3.2. Thus, the width of the finite band gap may be controlled by adjusting the parameter $m$. The position of the band gap is determined by the sum of the nodal masses. It is observed that the band gap interval becomes the empty set if $m \leq 5$. Thus, a minimum contrast in mass is required to maintain a finite-width band gap.

The lower bound of the semi-infinite band gap may be obtained by taking $\max\{\omega_O\}$ from equation (3.22) to obtain $\omega_l^* = \sqrt{5}$, which again agrees with the position of the band edge on the dispersion surface.

Figures 3.3 and 3.4 show the first four dispersion surfaces for the diatomic lattice with inertial links. It is emphasised that, in contrast with the non-inertial lattices, there is an infinite number of dispersion surfaces and only the first four are shown here. The parameter values are $\rho = 1$ and $m = 10$, and $\rho = 1$, $m = 4$ for figures 3.3 and 3.4 respectively. The lattice corresponding to figure 3.3 has the same distribution of mass at the junctions as the non-inertial lattice considered previously. However, the macroscopic density of the lattice is increased as a result of the lattice links having unitary density. Figure 3.4 corresponds to a lattice with the same macroscopic density as the non-inertial lattice, but with a different contrast in mass at the nodes to account for the additional mass contribution from the links with unitary density. In both figures 3.3 and 3.4, it is observed that the finite band gap of figure 3.2 is no longer present.

## 3.3 Central and torsional interactions

This class of interaction is similar to the central interactions presented in the previous section, and was considered in [102, 107, 111]. As in 3.2, the potential $\boldsymbol{u}_{\boldsymbol{m},n}$ corresponds to the in-plane elastic displacement amplitudes and the associated rotation matrix is as defined in (3.13). The distinction between this and the previous interaction is characterised by an additional torsional interaction between the links. In particular, each link resists transverse motion at the nodes. Physically the interaction may be understood in terms of massless Hookean torsional springs which retard changes in angle between the lattice links (cf. § 2.2.4). In the works of Maz'ya *et al.* [102], Morozov [107], and Nazarov and Paukschto [111], this resistance to transverse motion is referred to as *"transverse rigidity"* where the force per unit mass between points $\boldsymbol{x}$ and $\boldsymbol{y}$ is

$$\boldsymbol{F}(\boldsymbol{x},\boldsymbol{y}) = K\left\langle \boldsymbol{u}(\boldsymbol{y}) - \boldsymbol{u}(\boldsymbol{x}), \boldsymbol{y}-\boldsymbol{x}\right\rangle \frac{\boldsymbol{y}-\boldsymbol{x}}{\|\boldsymbol{y}-\boldsymbol{x}\|^2} + L\left\langle \boldsymbol{u}(\boldsymbol{y}) - \boldsymbol{u}(\boldsymbol{x}), (\boldsymbol{y}-\boldsymbol{x})^{\perp}\right\rangle \frac{(\boldsymbol{y}-\boldsymbol{x})^{\perp}}{\|\boldsymbol{y}-\boldsymbol{x}\|^2}, \tag{3.25}$$

where $(\boldsymbol{y}-\boldsymbol{x})^{\perp}$ denotes the vector perpendicular (in the right-handed sense) to $\boldsymbol{y}-\boldsymbol{x}$. The first term corresponds to the central interaction, whilst the second is the transverse interaction. It should be emphasised that this *"transverse rigidity"* is not equivalent to the flexural rigidity (i.e.

Euler-Bernoulli flexural stiffness) as it is understood in the engineering literature. Rather, *"transverse rigidity"* refers to the torsional spring type interaction discussed in section 2.2.4.

Returning to the present work, the elements of the diagonal blocks $\sigma_{11}$ and $\sigma_{22}$ of matrix $\boldsymbol{\sigma}(\omega, \boldsymbol{\xi})$ are

$$\left.\begin{aligned} \left[\sigma_{jj}\right]_{11} &= m_j\omega^2 - 3(\tau + \eta\cot\eta) + \frac{3\tau + \eta\cos\varphi\csc\eta}{2} \\ \left[\sigma_{jj}\right]_{12} &= \left[\sigma_{jj}\right]_{21} = \frac{\sqrt{3}\cos\varphi(\eta\csc\eta - \tau)}{2} \\ \left[\sigma_{jj}\right]_{22} &= m_j\omega^2 - 3(\tau + \eta\cot\eta) + \frac{\tau + 3\eta\cos\varphi\csc\eta}{2} \end{aligned}\right\}. \tag{3.26a}$$

The off-diagonal blocks $\sigma_{12} = \sigma_{21}^*$ have the entries

$$\left.\begin{aligned} \left[\sigma_{12}\right]_{11} &= \left[\left(e^{-2i\xi_1 l} + \frac{e^{-i\varphi} + e^{-i\psi}}{4}\right) + 1 + \frac{3\tau\sin\eta}{\eta}\right]\eta\csc\eta \\ \left[\sigma_{12}\right]_{12} &= \left[\sigma_{12}\right]_{21} = -\sqrt{3}\frac{e^{-i\varphi} + e^{-i\psi}}{4}(\eta\csc\eta - \tau), \\ \left[\sigma_{12}\right]_{22} &= \frac{e^{-i\psi} + e^{-i\varphi}}{4}(3\eta\csc\eta + \tau) \end{aligned}\right\}, \tag{3.26b}$$

where $\varphi$, $m_j$, and $\psi$ have the same definitions as in (3.14). It is remarked that the elements of $\boldsymbol{\sigma}(\omega, \boldsymbol{\xi})$ are written in (3.26) are equivalent to those for the central interaction (3.14) if $\tau = 0$, that is if the stiffness of the torsional springs is neglected. The quasi-static dispersion equation is

$$(1 + m + 3\rho)^2(3 + 10\tau + \tau^2)\omega^4 - 3|\boldsymbol{\xi}|^2(1 + m + 3\rho)(3 + 13\tau + 13\tau^2 + 3\tau^3)\omega^2 + \frac{9}{16}|\boldsymbol{\xi}|^4(3 + 10\tau + 3\tau^2)^2 = 0, \tag{3.27}$$

which has the positive solutions

$$\omega_{\mathrm{TS}}^{(1)} = \frac{\sqrt{3}}{2}\sqrt{\frac{3 + \tau}{1 + m + 3\rho}}|\boldsymbol{\xi}|, \tag{3.28a}$$

and

$$\omega_{\mathrm{TS}}^{(2)} = \frac{\sqrt{3}}{2}\sqrt{\frac{1 + 3\tau}{1 + m + 3\rho}}|\boldsymbol{\xi}|. \tag{3.28b}$$

The corresponding quasi-static group velocities are then

$$\boldsymbol{v}_{\mathrm{TS}}^{(1)} = \frac{\sqrt{3}}{2}\sqrt{\frac{3 + \tau}{1 + m + 3\rho}}\hat{\boldsymbol{\xi}}, \tag{3.29a}$$

and

$$\boldsymbol{v}_{\mathrm{TS}}^{(2)} = \frac{\sqrt{3}}{2}\sqrt{\frac{1 + 3\tau}{1 + m + 3\rho}}\hat{\boldsymbol{\xi}}, \tag{3.29b}$$

where $\hat{\boldsymbol{\xi}} = \boldsymbol{\xi}/|\boldsymbol{\xi}|$. Comparing equations (3.18) and (3.29), it is evident that in the quasi-static limit the qualitative effect of the torsional springs is a stiffer structure than that with only central interactions. Assuming, without loss of generality, that $0 \leq \tau < 1$ gives $1 + 3\tau < 3 + \tau$ and equations (3.29a) and (3.29b) may be associated with quasi-static pressure and shear waves

respectively. The Lamé parameters may then be determined as

$$\lambda = \frac{\sqrt{3}}{4}(1 - 5\tau) \qquad \text{and} \qquad \mu = \frac{\sqrt{3}}{4}(1 + 3\tau), \tag{3.30}$$

with the macroscopic density defined as $\varrho = 1 + m + 3\rho$ as before. For the special case of a fine isotropic triangular lattice, Maz'ya et al. [102, ch. 20] determined the effective Lamé parameters for the static case (as opposed to the quasi-static case considered here) as $\lambda = 3(K - 5L)/8$ and $\mu = 3(K + 3L)/8$, where $K$ and $L$ are the longitudinal and transverse rigidities per unit area respectively. The Lamé coefficients derived in [102, ch. 20] are consistent with those derived here once the difference in normalisation has been accounted for.

Again, as was the case for the central interactions, it is evident from equations (3.29) that redistributing the inertia over the lattice links results in a *morphological change* in the effective group velocities in the quasi-static limit. The dispersive properties are similar to those of the central interaction. Therefore, the dispersion diagrams and analysis of the dispersive properties for this interaction are omitted.

## 3.4 Euler-Bernoulli interactions

For the Euler-Bernoulli interaction introduced in section 2.2.5, the three-dimensional vector $\boldsymbol{u}_{\boldsymbol{m},n} \in \mathbb{C}^3$ now denotes the displacement amplitude with the first two components corresponding to the in-plane elastic displacement amplitudes, whilst the third component corresponds to in-plane rotations about the axis perpendicular to the plane of motion. In this case, the rotation matrix is an augmented matrix representing rotation about a single axis in three dimensions

$$\boldsymbol{R}(\boldsymbol{p}, q) = \begin{pmatrix} \cos\theta_{\boldsymbol{p},q} & -\sin\theta_{\boldsymbol{p},q} & 0 \\ \sin\theta_{\boldsymbol{p},q} & \cos\theta_{\boldsymbol{p},q} & 0 \\ 0 & 0 & 1 \end{pmatrix}. \tag{3.31}$$

The elements of the block matrices $\sigma_{nq}$ are not stated here explicitly. Instead, the reader is referred to equations (2.26) and (3.4) for the form of the block entries for $\boldsymbol{\sigma}(\omega, \boldsymbol{\xi})$.

With reference to equation (3.6), the quasi-static dispersion equation is

$$\beta^2(1 + 2\beta)(1 + 18\beta)\left[9(1 + 2\beta)|\boldsymbol{\xi}|^2 - 4\omega^2(1 + m + 6\rho)\right] \times \left[3(1 + 6\beta)|\boldsymbol{\xi}|^2 - 4\omega^2(1 + m + 6\rho)\right] = 0, \tag{3.32}$$

whence the positive solutions are immediately apparent

$$\omega_{\mathrm{EB}}^{(1)} = \frac{3}{2}\sqrt{\frac{1 + 2\beta}{1 + m + 6\rho}}|\boldsymbol{\xi}|, \tag{3.33a}$$

$$\omega_{\mathrm{EB}}^{(2)} = \frac{\sqrt{3}}{2}\sqrt{\frac{1 + 6\beta}{1 + m + 6\rho}}|\boldsymbol{\xi}|, \tag{3.33b}$$

where the non-dimensional parameter $\beta = 2I/(s\ell^2)$ has been introduced. The quasi-static effec-

tive group velocities are then

$$\boldsymbol{v}_{\mathrm{EB}}^{(1)} = \frac{3}{2}\sqrt{\frac{1+2\beta}{1+m+6\rho}}\hat{\boldsymbol{\xi}}, \tag{3.34a}$$

$$\boldsymbol{v}_{\mathrm{EB}}^{(2)} = \frac{\sqrt{3}}{2}\sqrt{\frac{1+6\beta}{1+m+6\rho}}\hat{\boldsymbol{\xi}}. \tag{3.34b}$$

In contrast to the quasi-static group velocities for the central interaction (3.18), and the central and torsional interaction (3.29), the effective density of lattice is equal to the macroscopic density $1 + m + 6\rho$. In other words, redistributing the inertia over the lattice links does not result in a *morphological change* in the quasi-static group velocities for lattices with the Euler-Bernoulli interaction.

It is also observed that setting $\beta = 0$ does not recover the case of central interactions. However, if one considers the governing equation (2.21a), it is immediately apparent that the differential equation is singularly perturbed for small $\beta$ (large $\lambda$). Thus, one would not necessarily expect the Euler-Bernoulli interaction to correspond to the central interaction for the case of $\beta = 0$. Moreover, with reference to (2.22) it can be deduced that the elements of $\boldsymbol{\sigma}$ do not converge as $\beta \to 0^+$ (or, equivalently, $\lambda \to \infty$). However for massless links ($\lambda \to 0$), the governing equation (2.21a) is regularly perturbed ($w^{(\mathrm{iv})} = 0$) and the Euler-Bernoulli does indeed correspond to the central interaction if both $\lambda$ and $\beta$ vanish. Hence, the equivalence of the effective group velocities for the central interaction (3.18) and the Euler-Bernoulli interaction (3.34) when both $\beta$ and $\rho$ vanish.

### 3.4.1 Dispersion properties and standing waves

As in section 3.2.2, figures 3.5 and 3.7 show examples dispersion diagrams for the diatomic triangular lattice with the Euler-Bernoulli interaction. Figure 3.5 shows the dispersion diagram for the case of a diatomic triangular lattice with non-inertial links. The dispersion diagrams for the case of a triangular lattice with inertial links is shown in figure 3.7. Again, the dispersion surfaces are plotted over the rectangular region $\boldsymbol{\xi} = [-\pi, \pi] \times [-5\pi/(2\sqrt{3}), 5\pi/(2\sqrt{3})]$, which contains the elementary cell in the reciprocal space.

Comparing figures 3.2 and 3.5, the most striking difference between the two is the presence of two relatively flat low frequency dispersion surfaces in 3.5. These surfaces correspond to modes dominated by rotational motion. An example of one of these *micopolar* mode is shown in figure 3.6; this mode corresponds to a periodic solution ($\boldsymbol{\xi} = \mathbf{0}$) for the case of non-inertial links. It is apparent from figure 3.6 that the translational displacements of the nodes are much smaller than the rotational components. Hence, for a simple estimate, the translational displacement of the nodes may be neglected. For periodic, purely rotational motion, the equations of motion for the nodes in the elementary cell of the lattice reduce to

$$J_i \partial_{tt}\theta^{(i)} = \tau^{(i)} - \left(14\beta\theta^{(i)} + 4\beta\theta^{(3-i)}\right), \quad i = 1, 2. \tag{3.35}$$

Here, the superscript indices label particles within the elementary cell and it is emphasised that repeated indices are not summed over. The symbols $\theta^{(i)}$and $\tau^{(i)}$ represent the non-dimensional angular displacement and torque respectively. For time-harmonic waves $\partial_{tt}\theta^{(i)} = -\omega^2\theta^{(i)}$ and

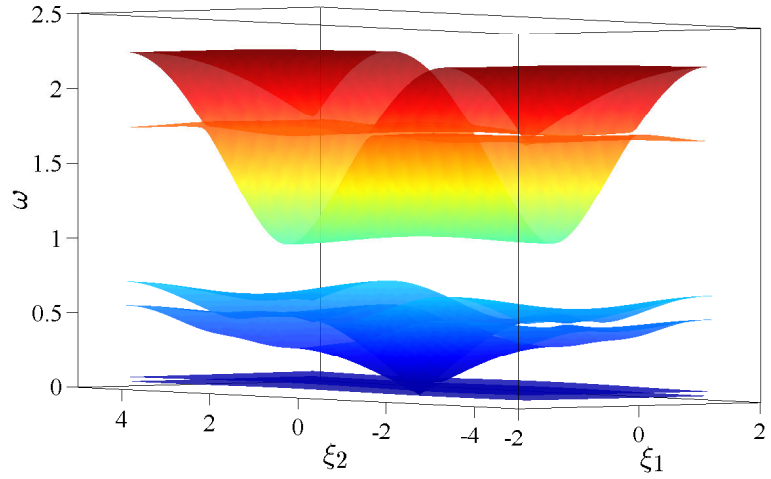


**Figure 3.5:** The six dispersion surfaces for the diatomic triangular lattice with non-inertial Euler-Bernoull links ($\rho = 0$) and $m = 10$.

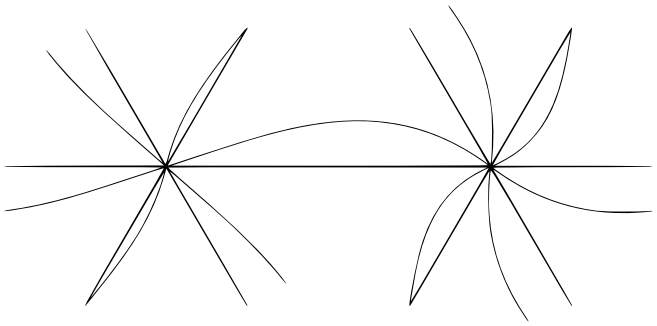

**Figure 3.6:** An example of a micopolar mode, superimposed on the undeformed structure.

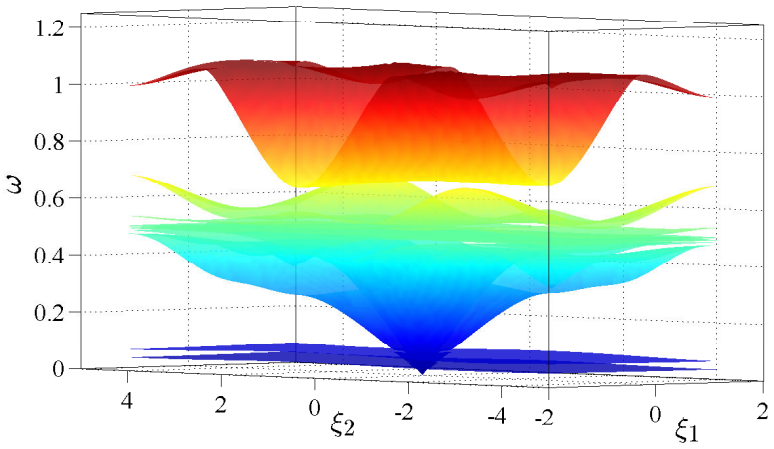


**Figure 3.7:** A range of dispersion surfaces for the diatomic triangular lattice with Euler-Bernoull inertial links for $\rho = 1$ and $m = 10$.

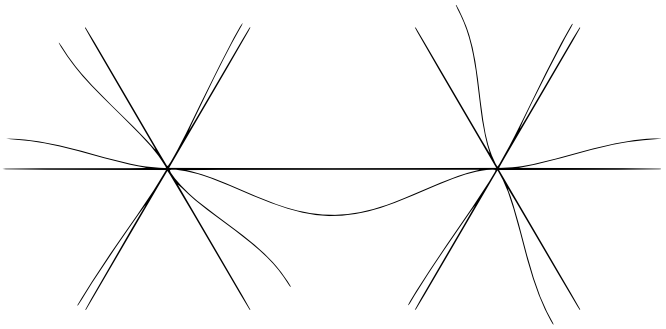

**Figure 3.8:** An example of an eigenmode where the beams vibrate at their fundamental frequency and the nodal displacements are small.

in the absence of external loads $\tau^{(i)} = 0$; the system (3.35) has non-trivial solutions if and only if

$$\det\begin{pmatrix} 14\beta - \omega^2 J_1 & 4\beta \\ 4\beta & 14\beta - \omega^2 J_2 \end{pmatrix} = 0. \tag{3.36}$$

The positive solutions for $\omega$ then yield the estimates for the frequencies of the standing rotational modes:

$$\omega_R^{\pm} = \left(\frac{\beta}{J_1 J_2}\left(7J_1 + 7J_2 \pm \sqrt{49\left(J_1^2 + J_2^2\right) - 82J_1J_2}\right)\right)^{1/2}. \tag{3.37}$$

Taking the parametric values used to produced figure 3.5: $J_1 = 2$, $J_2 = 6$, $\beta = 0.001$ yields numerical estimates of $\omega_R^+ = 0.0853$ and $\omega_R^- = 0.0454$, which are in good agreement with the numerical solutions to the full spectral problem. In the case of lattices with inertial links, for low frequencies and sufficiently small values of $2\varrho/\beta$, the equations of motion for pure rotations take the form (3.35) to leading order. For the values of the parameters used in figure 3.5 the results of the finite element computations are in good agreement with the estimates, $\omega_R^{\mathrm{FE}+} = 0.0845$ and $\omega_R^{\mathrm{FE}-} = 0.0452$. Usually, triangular lattices are treated as so-called *truss structures* where the flexural rigidity of the links is considered negligible and only central interactions are taken into account. However, if the flexural rigidity of the lattice links is neglected, then these low-frequency micro-polar modes are also neglected. Thus, it is important to take into account the flexural rigidity of the lattice links of triangular lattices, even in the low-frequency regime.

With reference to the dispersion diagram of figure 3.5, there exists a finite-width stop band for the diatomic lattice with non-inertial links. Using the same approach as employed in section 3.2.2, the width of the stop band may be determined. Similarly to the case of central interactions, the maxima of the upper acoustic surface bounds the stop band from below and lies at the edge of the elementary cell of the reciprocal lattice along the vector $\boldsymbol{b}_2 - \boldsymbol{b}_1$. At this point, $\boldsymbol{\xi} = (\boldsymbol{b}_2 - \boldsymbol{b}_1)/2$, the off-diagonal block matrices are sparse

$$\sigma_{12} = \begin{pmatrix} 0 & 0 & -3\sqrt{3}\beta \\ 0 & 0 & 3\beta \\ 3\sqrt{3}\beta & -3\beta & 0 \end{pmatrix} = \sigma_{21}^{\dagger}, \tag{3.38}$$

and the diagonal blocks are

$$\sigma_{jj} = \begin{pmatrix} m_j\omega^2 - 7/2 - 27\beta & \sqrt{3}(1-6\beta)/2 & 0 \\ \sqrt{3}(1-6\beta)/2 & m_j\omega^2 - 9/2 - 21\beta & 0 \\ 0 & 0 & J_j\omega^2 - 10\beta \end{pmatrix}, \qquad \text{for } j = 1, 2, \tag{3.39}$$

where $m_j = \delta_{1j} + m\delta_{2j}$ and $J_j = \delta_{1j} + J\delta_{2j}$. Assuming that $\sigma_{11}$ and $\sigma_{22}$ are not simultaneously singular[4], the eigenvalue problem may be recast thus[5]:

$$(\sigma_{ii} - \sigma_{12}\sigma_{jj}^{-1}\sigma_{12}^{\dagger})\boldsymbol{u}_i^{\mathrm{FF}} = \mathbf{0}, \qquad \text{for } i = 1,2 \text{ and } i \neq j, \tag{3.40}$$

and where $j$ is chosen such that $\det \sigma_{jj} \neq 0$. It is emphasised that repeated indices are not summed over. The matrix product $\sigma_{12}\sigma_{jj}^{-1}\sigma_{12}^{\dagger}$ has the same distribution of zeros as (3.39). Hence, the translational and micropolar modes decouple and the frequencies of the two micropolar modes can immediately be obtained from the equation $[\sigma_{ii} - \sigma_{12}\sigma_{jj}^{-1}\sigma_{12}^{\dagger}]_3 = 0$. Explicitly, the equation for the frequency of these micropolar modes is

$$J_j\omega^2 - 2\beta\left(5 + \frac{18\beta}{m_i\omega^2 - 3 - 30\beta}\right) = 0, \qquad \text{for } i = 1,2 \text{ and } i \neq j. \tag{3.41}$$

For thin beams, the typical bending stiffness is much smaller than the longitudinal stiffness of the links; in the notation used herein this corresponds to $0 < \beta \ll 1$. For example, for a beam of unit length and circular cross-section with slenderness ratio[6] $r/l = 0.1$, the parameter $\beta = 0.0025$. Hence, for small $\beta$ equation (3.41) has the solution $\omega \approx \sqrt{10\beta/J_j}$. Thus, these standing waves correspond to the low frequency micropolar modes mentioned earlier.

Having established that the rotational and translational modes decouple, that is $[\boldsymbol{u}_i^{\mathrm{FF}}]_j$ is independent of $[\boldsymbol{u}_i^{\mathrm{FF}}]_3$ for $i, j = 1, 2$, it is sufficient to consider the problem for the reduced block matrices $\tilde{\sigma}_{ij}$, which have elements $[\tilde{\sigma}_{ij}]_{kl}$, for $k, l = 1, 2$. In this case, the reduced off-diagonal matrices vanish and the dispersion equation reduces to $\det \sigma_{11} \det \sigma_{22} = 0$, or more explicitly

$$(5 + \beta - \omega^2)(3 + 30\beta - \omega^2)(5 + \beta - m\omega^2)(3 + 30\beta - m\omega^2) = 0. \tag{3.42}$$

Assuming, without loss of generality, that $m > 1$ the parenthesised terms involving $m$ correspond to the acoustic modes; whence the lower bound of the band gap is

$$\omega_l = \max\{\sqrt{(5 + 18\beta)/m}, \sqrt{(3 + 30\beta)/m}\}. \tag{3.43}$$

The minima of the optical dispersion surface bounding the finite band gap from above occurs at the edge of the Brillouin zone along $\boldsymbol{b}_1$. At $\boldsymbol{\xi} = \boldsymbol{b}_1/2$, the block matrix entries of $\boldsymbol{\sigma}$ have the same structure as above, although the values are indeed different. Hence, following the same procedure the upper bound of the finite band gap is

$$\omega_u = \min\left\{\sqrt{1 + 18\beta}, \sqrt{3 + 6\beta}\right\}. \tag{3.44}$$

For small $\beta$, specifically for $0 < \beta < 1/6$, the width of the finite band gap is defined by the interval

$$\sqrt{\frac{5 + 18\beta}{m}} < \omega < \sqrt{1 + 18\beta}. \tag{3.45}$$

[4]Equivalently $m \neq 1$ and/or $J_1 \neq J_2$.
[5]Since $\sigma_{11}$ and $\sigma_{22}$, and hence their inverses, are hermitian, the product $\sigma_{12}\sigma_{jj}^{-1}\sigma_{12}^{\dagger}$ is also hermitian.
[6]The ratio of beam radius to length.

Comparing inequalities (3.24) and (3.45), it is observed that (for small $\beta$) the band gaps are of approximately the same width and occur at the same frequencies as for the case of central interactions.

Figure 3.7 shows the dispersion diagram for the triangular diatomic lattice with inertial links. The dispersion diagram shares many features with the diagram for the lattice with non-inertial links (figure 3.5). However, figure 3.7 is distinguished from figure 3.5 by the presence of several densely packed, relatively flat surfaces in what was the band gap in figure 3.5. These surfaces correspond to modes where the nodal displacements are small, or indeed zero; an example of such a mode is shown in figure 3.8. These flat dispersion surfaces are associated with the fundamental modes of the lattice links; an estimate of their location can be obtained by considering an isolated Euler-Bernoulli beam with clamped ends. Such systems have been treated extensively in the literature (see the book by Graff [53], among others); a brief discussion is included here for completeness.

Consider the boundary value problem for the non-dimensional time-harmonic deflection of an Euler-Bernoulli beam of unit length, clamped at both ends

$$\left(\frac{\mathrm{d}^4}{\mathrm{d}x^4} - \lambda^4\right) y(x) = 0, \qquad x \in [0,1], \tag{3.46a}$$

and

$$y(0) = y(1) = y'(0) = y'(1) = 0, \tag{3.46b}$$

where $\lambda^4 = 2\omega^2\rho/\beta$. The well known family of solutions is $y_n = A_1[\cos(\lambda_n x) - \cosh(\lambda_n x)] + A_2[\sin(\lambda_n x) - \sinh(\lambda_n x)]$, where $\lambda_n$ satisfy the transcendental equation $\cos\lambda_n \cosh\lambda_n = 1$, with $\lambda_n \neq 0$. The first eigenfrequency is then

$$\omega^{(1)}_{\text{beam}} \approx 4.730^2 \sqrt{\frac{\beta}{2\rho}}, \tag{3.47}$$

which for the parameter values used to produce figure 3.7 yields $\omega^{(1)}_{\text{beam}} \approx 0.5$. In figure 3.7 there are several approximately flat surfaces which lie between $\omega = 0.4932$ and $\omega = 0.5044$.

Consider the Dirichlet boundary value problem for the non-dimensional time-harmonic longitudinal displacement amplitude of a thin rod of unit length

$$\left(\frac{\mathrm{d}^2}{\mathrm{d}x^2} - \frac{\omega^2}{\rho}\right) y(x) = 0, \qquad x \in [0,1], \tag{3.48a}$$

and

$$y(0) = y(1) = 0. \tag{3.48b}$$

In this case, the spectrum is $\omega_n = n\pi/\sqrt{\rho}$ for $n \in \mathbb{N}$. Thus, for the parameter values used here ($\rho = 1$ and $0 < \beta \ll 1$), the lowest frequency resonant longitudinal mode is much higher than the first flexural mode. Indeed, the resonant frequency for the first longitudinal mode of a thin rode lies beyond the frequency range shown in figures 3.2-3.5, and 3.7.

## 3.5 Remarks

Conventionally, triangular lattices are treated as so-called *truss structures* where flexural deformations are neglected and only central interactions are considered. However, the analysis presented in this chapter indicates that care is required if important features are not to be neglected. If the flexural rigidity of the links is small compared with their longitudinal stiffness, then accounting for flexural deformations offers a small correction to the width of the finite band gap (see inequalities (3.24) and (3.45)). However, if the lattice links are inertial then the band gap becomes populated with flexural standing modes. Moreover, for inertial links in the low frequencies regime, neglecting flexural deformations results in erroneous estimates for the long wavelength group velocities. Finally, the two low frequency micropolar modes (evidenced by the flat low frequency surfaces in figures 3.5 and 3.7) will be absent if flexural deformations are neglected.

# *Chapter Four*

# Dynamic anisotropy and focusing in discrete media

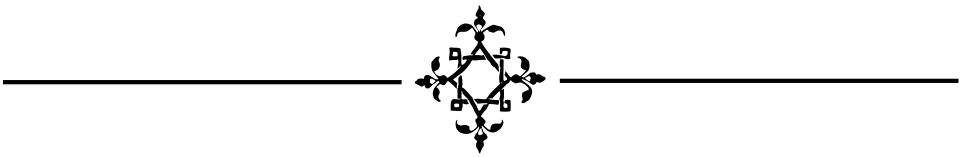

The previous chapter was concerned with the low frequency response of two dimensional lattices. In the current chapter, the finite frequency response is considered. In particular, where in the previous chapter it was demonstrated that the quasi-static response of the triangular lattice was isotropic, it is demonstrated that for higher frequencies the response is strongly anisotropic. It is in this sense that lattices are said to posses *dynamic anisotropy*. The present chapter examines the diffraction of time harmonic fields by an infinite lattice in $\mathbb{R}^2$ and is developed as follows. First, the dynamic response of both square and triangular scalar lattices will be analysed, with emphasis on Green's functions and the diffraction patterns generated by a point load. The current chapter is also concerned with the dynamic anisotropy of discrete elastic structures in the full vector setting of planar elasticity. The analysis is focused on the directionally localised waveforms, which correspond to saddle points on the dispersion surfaces. Here, the term "localised" is used in a similar sense to that used in several papers (see, for example [5, 121]) to describe an effect where the field is predominantly confined to one or more finite width "beams" with differing orientations. Finally, a design for a structured elastic slab of finite width, which possesses focusing properties for waves within a certain frequency range, is developed.

## 4.1 Primitive waveforms in scalar lattices

Consider the out-of-plane displacement of a regular array of uniform point masses in $\mathbb{R}^2$ connected by massless Hookean springs and loaded at a single lattice point. The governing equations of motion are those described in section 2.1 with the fundamental interaction matrix given in section 2.2.1. In this section, two different monatomic lattice geometries will be considered: square and triangular.

### 4.1.1 The square monatomic lattice

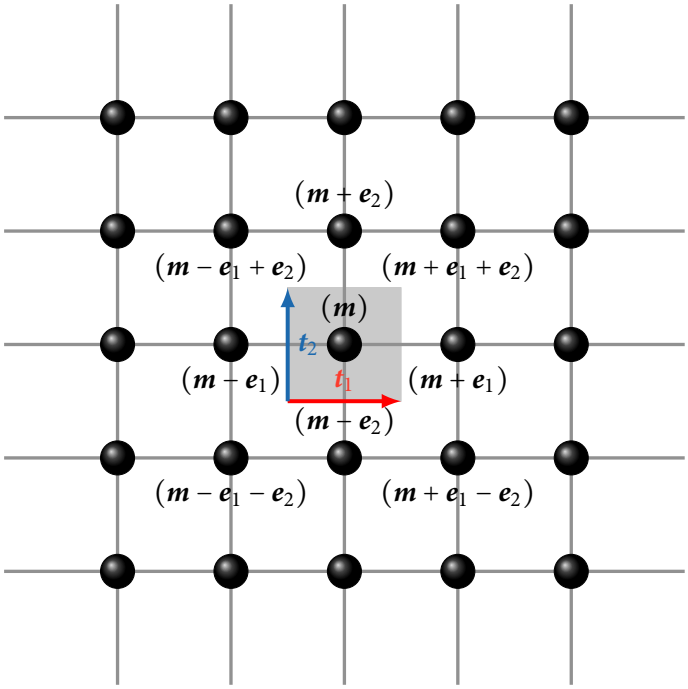


**Figure 4.1:** The monatomic square lattice and its elementary cell (shaded in grey). The lattice vectors $\boldsymbol{t}_1$ (in red) and $\boldsymbol{t}_2$ (in blue) are also indicated. The vectors $\boldsymbol{e}_i$ are defined as follows: $\boldsymbol{e}_1 = [1,0]^{\mathrm{T}}$ and $\boldsymbol{e}_2 = [0,1]^{\mathrm{T}}$.

Consider first, the uniform square lattice as illustrated in figure 4.1. The lattice consists of a regular array of unitary point masses connected by linear springs of unit stiffness. The assumption of uniformity is purely for convenience and may be weakened without significant additional work. The lattice is uniform and the particles are indistinguishable; the lattice nodes are labelled by the double index $\boldsymbol{m} \in \mathbb{Z}^2$ (see § 2.1). Let the lattice be forced harmonically at a single point. Given the uniformity of the lattice, the forcing point is chosen as the origin $\boldsymbol{m} = \boldsymbol{0}$ for convenience and without loss of generality. The displacement field is then given by the Fourier Integral (see equation (2.7) in § 2.1)

$$u_{\boldsymbol{m}} = \frac{1}{\|\mathcal{R}\|} \iint_{\mathcal{R}} \frac{\exp(i\boldsymbol{m}\cdot\boldsymbol{\xi})}{\sigma(\omega,\boldsymbol{\xi})} \mathrm{d}\boldsymbol{\xi}, \tag{4.1}$$

where $\sigma(\omega,\boldsymbol{\xi}) = \omega^2 - 4 + 2(\cos\xi_1 + \cos\xi_2)$. The scalar $\sigma$ is even with respect to $\boldsymbol{\xi}$ and the region $\mathcal{R}$ is symmetric about $\xi_i = 0$ $(i = 1,2)$, hence the odd terms in $\exp(i\boldsymbol{m}\cdot\boldsymbol{\xi})$ do not contribute to the integral and the Lattice Green's Function may be expressed as

$$u_{\boldsymbol{m}} = \frac{1}{\pi^2} \iint_{[0,\pi]^2} \frac{\cos(m_1\xi_1)\cos(m_2\xi_2)}{\sigma(\omega,\boldsymbol{\xi})} \mathrm{d}\boldsymbol{\xi}. \tag{4.2}$$

Alternative representations of the Lattice Green's function and detailed analysis in various frequency regimes may be found in many texts, including [32, 97, 99, 109], in addition to later in the present text. For certain restrictions of $\omega$ one, but not both, of the integrals in (4.2) may be evaluated in closed form; alternatively, the integral may be converted to a semi-infinite integral

over the positive semi-axis. However, for the purposes of this chapter it suffices to consider the Lattice Green's function in the form (4.2).

The dispersion surface (the zero isosurface $\{(\omega, \boldsymbol{\xi}) : \sigma(\omega, \boldsymbol{\xi}) = 0\}$) is shown in figure 4.2a and has a number of interesting features. In particular, it is observed that within the Brillouin zone the surface has one maximum, with the four points at the corners of the Brillouin zone each contributing one quarter of a maximum, and two saddle points, with the four points labelled $\pm A$ and $\pm B$ each contributing one half of a saddle point. The saddle points all lie at the frequency $\omega = 2$, for which the slowness contour is shown in figure 4.2b in addition to its representation on the dispersion diagram 4.2a. The saddle points lie at the vertices of the rhombic slowness contour. Figure 4.2 is fully consistent with those figures presented in [5, 121].

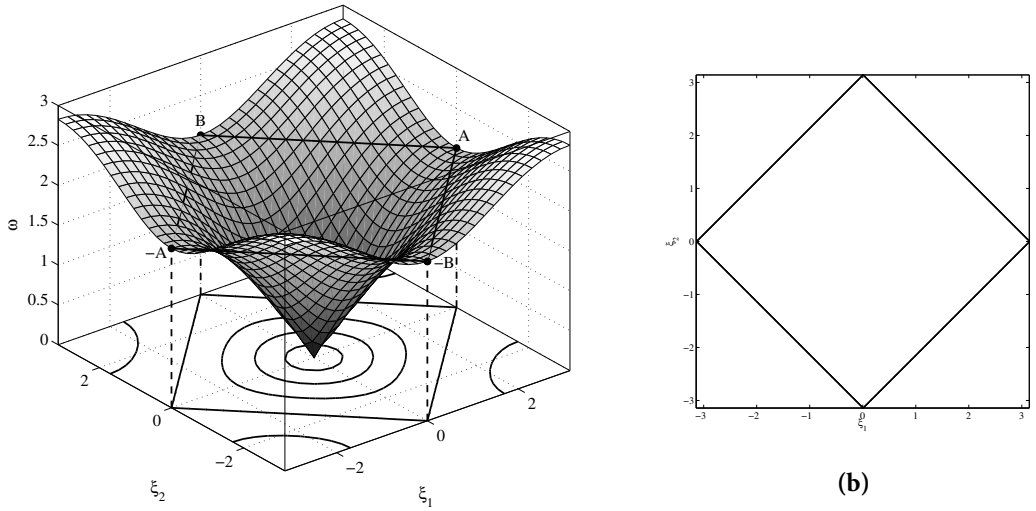


**Figure 4.2:** (a) The dispersion surface for the square cell lattice together with the projections of the level curves onto the $\omega = 0$ plane. (b) The slowness contour at the frequency coinciding with the saddle points, $\omega = 2$. The saddle points lie at the vertices of the rhombic slowness contour.

The optical analogue of (4.2) is the so-called diffraction integral [10, 52, 118]. In optics, the term *aberration* is used to describe perturbation of the wave front away from its ideal shape as a result of a lens or diffraction grating [10, 52]. The *aberration function* is used to quantitatively characterize the phase perturbation at the exit pupil plane. The distinction is often made between two types of aberration: *chromatic* and *monochromatic*. The latter is attributed to the geometry of the lens or grating whilst the former results from the dispersive properties of the lens. In the case of a uniform mechanical (or conductive) lattice, there is no such distinction since the dispersive properties arise as a result of the geometry of the medium. Hereinafter, the term *aberration* is used to describe the features of the field resulting from the dispersive properties of the lattice.

The displacement field for the square cell lattice when the forcing frequency coincides with the frequency of the saddle points $\omega = 2$ is shown in figure 4.3. The field is determined by computing (4.2) numerically using the Gauss-Kronrod quadrature algorithm in MATLAB® for each $\boldsymbol{m}$ in a given range. The displacement field is consistent with the *star shaped contours* observed in

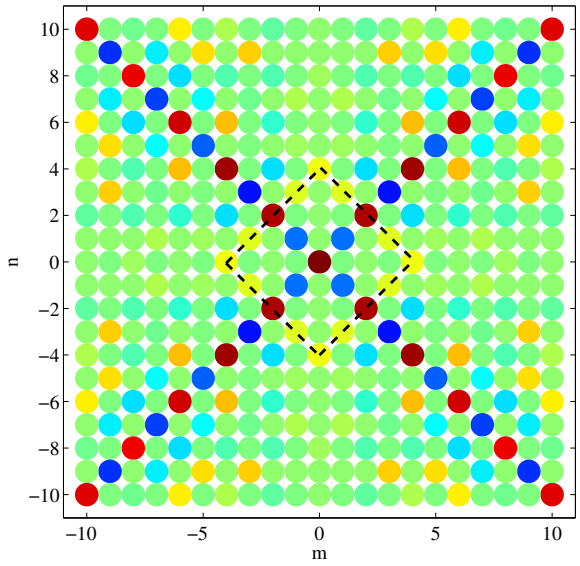


**Figure 4.3:** The displacement field of the square cell lattice for a forcing frequency of $\omega = 2$. The colour represents the anti-plane displacements of the masses, from blue (minimal) through green (zero) to red (maximal)

references [5, 90, 91, 121]. However, a novel feature is observed: the rhombic aberration in the vicinity of the point source. This feature was not apparent in the previous publications as only equi-displacement contours were plotted in the case of references [5, 90, 91] or all points over a given threshold were plotted with equal weight [121]. The effect is sensitive to perturbations in the frequency around the saddle points $\pm A$ and $\pm B$ in figure 4.2a. For example, changing the frequency by as little as 0.01 significantly alters the diffraction pattern shown in figure 4.3. This sensitivity can be understood in terms of the group velocity which varies rapidly in the vicinity of the saddle points. Moreover, the phenomena of *star shaped contours* and *aberrations* is closely linked with the nature of the slowness contours. In particular, consider the slowness contour in figure 4.2b. It is observed that the direction (but not the magnitude) is piecewise constant over the Brillouin zone. These constant directions, corresponding to the normals of the sides of the rhombus, are precisely those of the four rays shown in figure 4.3. The group speed is maximal at the centre of each side of the rhombus and is zero at the vertices.

### A stationary point of a different kind

Consider the dispersion equation $\sigma(\omega, \boldsymbol{\xi}) = \omega^2 - 4 + 2(\cos\xi_1 + \cos\xi_2) = 0$. Since $|\cos\xi_1 + \cos\xi_2| \leq 2 \;\forall\; \boldsymbol{\xi}$, there exist no solutions for $\omega^2 > 8$; hence the square lattice possesses a semi-infinite stop band for frequencies $\omega^2 > 8$ where no propagating solutions exist. For the case of free oscillations, Martin [99] found that there exist solutions of the form $u_{\boldsymbol{m}} = (-1)^{m_1+m_2}$. These so-called *lattice waves* exist at the *resonant frequency* $\omega = 2\sqrt{2}$ which demarcates the pass band and the stop band, i.e. these are the maxima in figure 4.2a. A similar phenomenon is observed in the case of forced excitation. In particular, figure 4.4 shows a plot of the field for such a resonant frequency. The white (black) nodes indicate maximal positive (negative) displacement. In direct

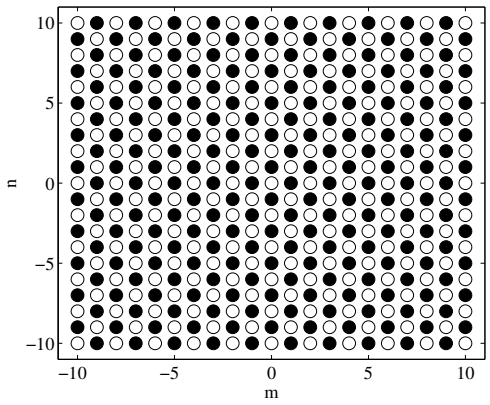


**Figure 4.4:** *Lattice waves* where the origin of the lattice is forced at the resonant frequency $\omega = 2\sqrt{2}$. White nodes indicate maximal positive displacement, while black nodes correspond to maximal negative displacement.

analogy to the lattice waves described in [99], the displacement of the nodes can be approximately described by $u(\boldsymbol{m}) \approx (-1)^{m_1+m_2}u(\boldsymbol{0})$. Here, no preferential direction of propagation is observed.

### 4.1.2 The triangular cell lattice

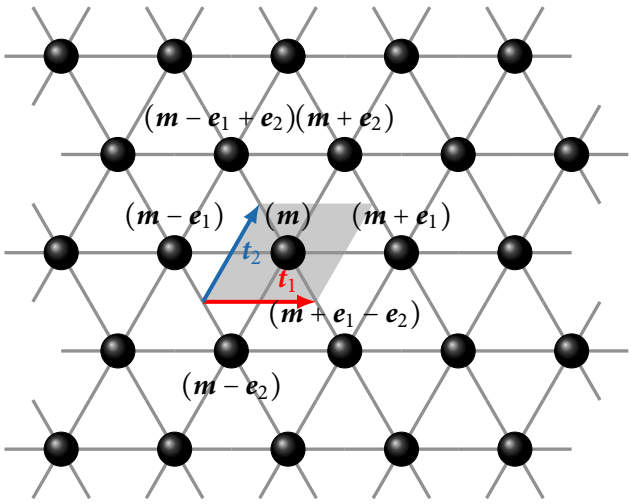


**Figure 4.5:** The monatomic triangular lattice and its elementary cell (shaded in grey). The lattice vectors $\boldsymbol{t}_1$ (in red) and $\boldsymbol{t}_2$ (in blue) are also indicated. The vectors $\boldsymbol{e}_i$ are defined thus: $\boldsymbol{e}_1 = [1,0]^{\mathrm{T}}$ and $\boldsymbol{e}_2 = [0,1]^{\mathrm{T}}$.

As a further example, the triangular lattice with basis vectors $\boldsymbol{t}_1 = [1,0]^{\mathrm{T}}$ and $\boldsymbol{t}_2 = [1/2, \sqrt{3}/2]^{\mathrm{T}}$ as illustrated in figure 4.5 is considered. In this case, the physical field has the representation

$$u_{\boldsymbol{m}} = \frac{\sqrt{3}}{4\pi^2} \iint_{\mathcal{R}} \cos[(m_1 + m_2/2)\xi_1] \cos[n\sqrt{3}\xi_2/2]\sigma^{-1}(\boldsymbol{\xi};\omega)\mathrm{d}\boldsymbol{\xi}\,, \tag{4.3}$$

where $\sigma(\boldsymbol{\xi};\omega) = \omega^2 - 6 + 2\cos\xi_1 + 4\cos(\xi_1/2)\cos(\sqrt{3}\xi_2/2)$ and $\mathcal{R} = [0, 2\pi] \times [0, 2\pi/\sqrt{3}]$. The dispersion surface, together with the slowness contour for the frequency $\omega = 2\sqrt{2}$ correspond-

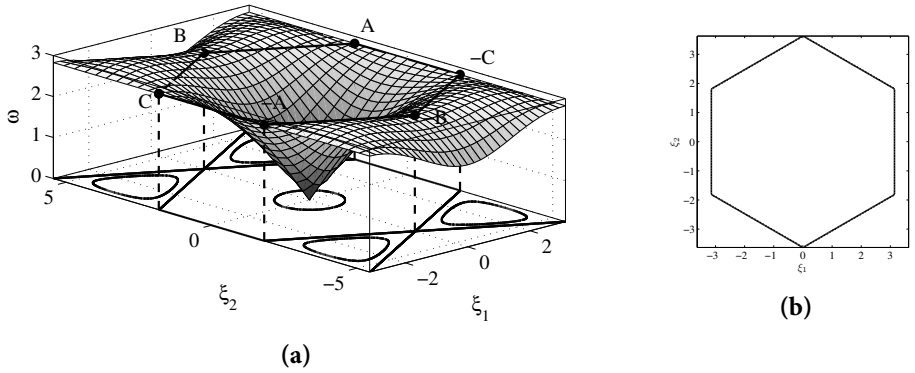


**Figure 4.6:** (a) The dispersion surface for the triangular cell lattice and (b) the slowness contour at the frequency coinciding with the saddle points, $\omega = 2\sqrt{2}$. The saddle points lie at the vertices of the hexagon.

ing to the position of the saddle points ($\pm A$, $\pm B$ and $\pm C$), is shown in figure 4.6. As in the case of the square lattice, the direction of the group velocity is piecewise constant along the sides of the hexagon, with the saddle points located at the vertices. Here, six preferential directions of propagation (directions of maximal group velocity) corresponding to the perpendicular bisectors of the six sides are clearly identifiable. The displacement field for the triangular lattice when the forcing frequency is $\omega = 2\sqrt{2}$ is shown in figure 4.7. As expected, the star shaped waveforms with the six rays corresponding to the six discrete directions of group velocity, as indicated by the slowness contour in figure 4.6b, are evident. Figure 4.7 is consistent with the star shaped contours shown in [5, 121].

The determination of the position of the semi-infinite stop band requires a little more attention than in the case of a square lattice. With reference to the dispersion equation $\omega^2 - 6 + 2\cos\xi_1 + 4\cos(\xi_1/2)\cos(\sqrt{3}\xi_2/2) = 0$, the band edge corresponds to the global minimum of the function $f(\boldsymbol{\xi}) = 2\cos\xi_1 + 4\cos(\xi_1/2)\cos(\sqrt{3}\xi_2/2)$. Since the dispersion equation is periodic with respect to the elementary cell of the reciprocal lattice, $\boldsymbol{\xi}$ may be restricted to the parallelogram spanned by the two primitive vectors $\boldsymbol{b}_1 = \pi[2, -2/\sqrt{3}]^{\mathrm{T}}$ and $\boldsymbol{b}_2 = [0, 4\pi/\sqrt{3}]^{\mathrm{T}}$ in the reciprocal lattice. The first partial derivatives, Hessian determinant, and second partial derivative with respect to $\xi_1$ are then

$$\nabla f(\boldsymbol{\xi}) = -2\begin{pmatrix} \sin\xi_1 + \cos(\sqrt{3}\xi_2/2)\sin(\xi_1/2) \\ \sqrt{3}\cos(\xi_1/2)\sin(\sqrt{3}\xi_2/2) \end{pmatrix}, \tag{4.4a}$$

$$H(\boldsymbol{\xi}) = \frac{3}{2}\left\{\cos\xi_1 + \cos(\sqrt{3}\xi_2) + 2\left[\cos\left(\frac{\xi_1}{2}\right) + \cos\left(\frac{3\xi_2}{2}\right)\right]\right\}, \tag{4.4b}$$

and

$$\frac{\partial^2 f}{\partial \xi_1^2} = -2\cos\xi_1 - \cos\left(\frac{\xi_1}{2}\right)\cos\left(\frac{\sqrt{3}\xi_2}{2}\right). \tag{4.4c}$$

Within the irreducible Brillouin zone, the function $f(\boldsymbol{\xi})$ has stationary points at the following positions

$$\Xi = \{[0,0]^{\mathrm{T}}, [\pi, \pi/\sqrt{3}]^{\mathrm{T}}, [4\pi/3, 0]^{\mathrm{T}}\}. \tag{4.5}$$

Analysis of the signs of the Hessian determinant and second derivatives at the stationary points

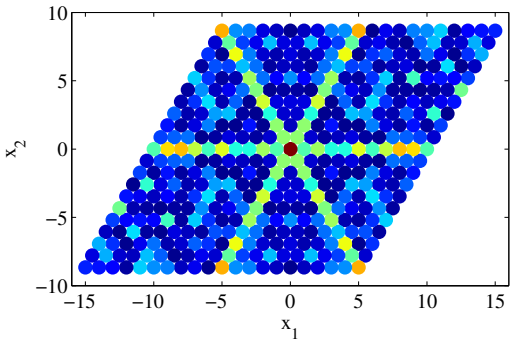


**Figure 4.7:** The magnitude of the out-of-plane displacement field of the triangular cell lattice for a forcing frequency of $\omega = 2\sqrt{2}$. The colour scale runs from blue (zero) to red (maximal).

reveal that the first is a local maximum of $f(\boldsymbol{\xi})$, the second is a saddle point, whilst the third is a local minimum. Indeed, since these are the only stationary points in the irreducible Brillouin zone of the reciprocal lattice, the local extrema are global extrema. Thus, the maximum value of $\omega$ which corresponds to the minima of $f(\boldsymbol{\xi})$ is $\omega = 3$. Hence, there exists a semi-infinite stop band for frequencies $\omega > 3$, whilst propagating solutions are supported for $0 < \omega \leq 3$. The saddle point frequency, corresponding to the saddle points of $f(\boldsymbol{\xi})$, is $\omega = 2\sqrt{2}$ as stated earlier. Finally, as expected, the minimum value of $\omega$, corresponding to the maxima of $f(\boldsymbol{\xi})$ is $\omega = 0$.

## 4.2 Diffraction in elastic lattices

The section is devoted to the analysis of the vector elasticity analogue of the problems presented in the previous section. The in-plane elasticity problem is distinct from the scalar system and presents a number of novel features and challenges. In particular, it is demonstrated that the orientation of the applied force can be used to select one or more of the preferential directions defined by the dispersive properties of the lattice. In the scalar case, the papers [5, 121] have focused on the preferential directions, *primitive waveforms*, and star shaped contours at resonant (saddle point) frequencies. As mentioned in the previous section, these primitive waveforms and associated effects are sensitive to perturbation in the frequency around the saddle points. In contrast to the scalar problem, when working in the framework of vector elasticity it will be shown that similar star shaped waveforms exist at frequencies other than resonant frequencies. In other words, the presence of star shaped waveforms is not necessarily linked to the existence and position of stationary points on the dispersion surfaces.

The concept of preferential directions of propagation in discrete elastic structures has been demonstrated in [29], which built on the earlier work for the structured continuum [81] and for the discrete interface embedded within the continuum [16]. The three papers [16, 29, 81] also illustrate the effects of filtering and focusing of plane elastic waves and the formation of image points.

Consider a regular triangular array of uniform point masses arranged in $\mathbb{R}^2$ as depicted in figure 4.5. The point masses are connected by Euler-Bernoulli beams of constant density (see § 2.2.5 and 3.4). In this case, the $3 \times 3$ Hermitian matrix $\boldsymbol{\sigma}(\omega, \boldsymbol{\xi})$ is as introduced in section 3.4 using equations (2.26) and (3.4). The displacement amplitude $\boldsymbol{u_m} \in \mathbb{C}^3$ is a three-dimensional vector with the first two components corresponding to translational motion and the third describing micropolar rotations. The field has the same representation as (4.3) and the dispersion

| Property | Value |
|---|---|
| Young's Modulus ($E$) | 200 GPa |
| Second Moment of Inertia ($I$) | $349 \times 10^{-8}$ m$^4$ |
| Cross Sectional Area ($S$) | $2.12 \times 10^{-3}$ m$^2$ |
| Beam Density ($\bar{\varrho}$) | 7850 kg m$^{-2}$ |
| Beam Length ($\ell$) | 1 m |
| Nodal Mass ($m$) | 91.531 kg |
| Polar Mass Moment of Inertia ($\bar{J}$) | 66.568 kg m$^2$ |

**Table 4.1:** The material and geometrical parameters used to produce the dispersion surfaces and finite element computations.

equation is $\det \boldsymbol{\sigma}(\omega, \boldsymbol{\xi}) = 0$.

### 4.2.1 Dispersive properties

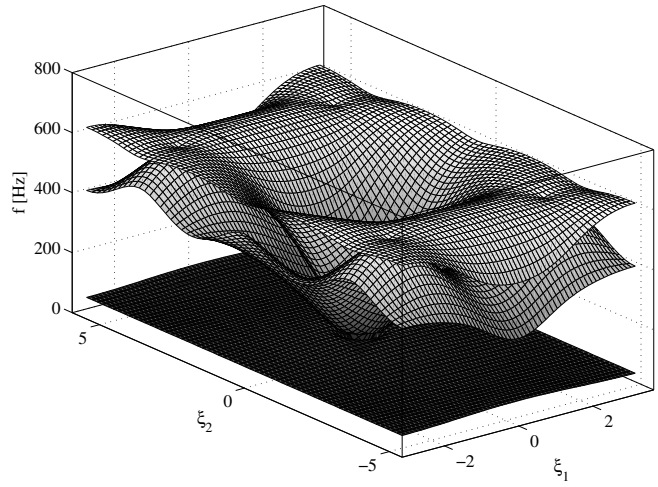


**Figure 4.8:** The first three dispersion surfaces for the triangular lattice of masses connected by Euler-Bernoulli beams in $\mathbb{R}^2$.

The dispersion surfaces for the infinite lattice system are shown in figure 4.8. In this case, it is convenient to work with dimensional units. The material parameters used to produce the dispersion surfaces are detailed in table 4.1. The first surface, which is relatively flat, is associated with micropolar modes (see § 3.4.1 and in particular p. 37). Here the focus will be on the second and third surfaces, which contain saddle points. Figure 4.9e shows the slowness contour for the resonant frequency $f = 615$ Hz. The contour exhibits the same characteristic hexagonal shape as the slowness contour of the scalar triangular lattice (see figure 4.6b) suggesting that the characteristic shape of the slowness contours are a feature of the geometry of the lattice. It is emphasised that the governing equations for vector elasticity are significantly different from those of scalar problems. As in the scalar case, the six preferential directions can be identified as the normals to the edges of the hexagon, although here, the slowness contour is rotated by $\pi/2$ compared with the scalar case. Now consider figure 4.9b, which shows the slowness contours for the frequency $f = 323$ Hz. Here a similar hexagonal slowness contour is observed, with the

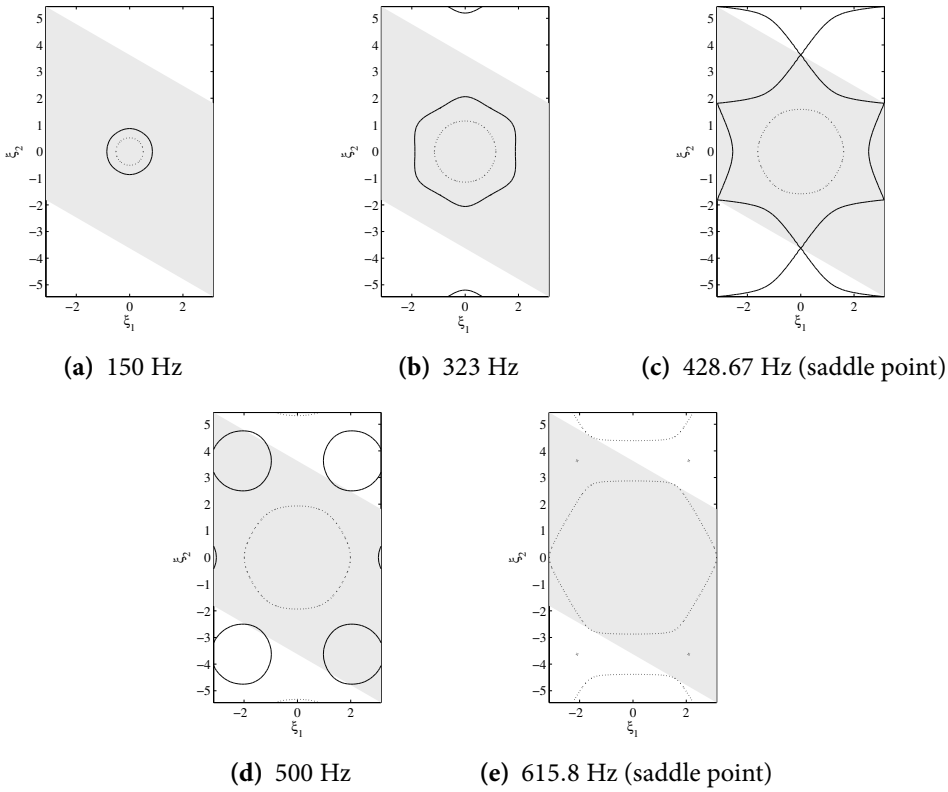

**(a)** 150 Hz **(b)** 323 Hz **(c)** 428.67 Hz (saddle point)

**(d)** 500 Hz **(e)** 615.8 Hz (saddle point)

**Figure 4.9:** The slowness contours for a range of frequencies starting at 150 Hz (a) and ending at the saddle point frequency near the band edge (e). The solid lines correspond to the lower conical surface, whilst the dotted lines correspond to the upper conical surface. The elementary cell in the reciprocal space is shaded in grey.

same orientation as for the scalar case. However, $f = 323$ Hz does not correspond to a resonant frequency, that is there are no saddle points on the dispersion surfaces which coincide with $f = 323$ Hz. Nevertheless, the six preferential directions of propagation are clearly visible. This is in contrast to the scalar problems considered earlier in this chapter (§ 4.1) and in the papers [5,121], where these polygonal-like slowness contours were associated exclusively with saddle points.

**The forced problem in elastic structured media.**

Following the structure of the previous section on scalar lattices, the forced in-plane problem is now considered. In particular, the monatomic uniform triangular lattice described above is subjected to a concentrated load (either linear or torsional) at a single lattice point. The triangular lattice is chosen because it is isotropic in the long wavelength limit [29]. Here, the emphasis is on the dynamic anisotropy at higher frequencies and in particular on the existence of localised primitive waveforms, in direct analogy to the scalar case previously considered. The finite element software COMSOL Multiphysics® is used to determine the displacement field. The lattice nodes on the boundary are fixed and PML-like absorbing boundary conditions are applied to the lattice links in the vicinity of the boundary nodes in order to reduce reflection. The harmonic disturbance is generated in a similar fashion as in the scalar case: by prescribing a time-harmonic displacement of magnitude $10^{-6}$ m in a given direction or a time-harmonic rotation at node $(0, 0)$. The material parameters are as detailed in table 4.1. A selection of the displace-

ment amplitude fields for various forcing orientations and frequencies are shown in figure 4.10. Figures 4.10a, 4.10c and 4.10e correspond to an excitation frequency of 323 Hz for which the slowness contours are shown in figure 4.9b. Similarly, figures 4.10b, 4.10d and 4.10f correspond to a excitation frequency of 615.8 Hz for which the slowness contours are shown in figure 4.9e. It is observed that the slowness contours of figure 4.9e correspond to the saddle point on the upper dispersion surface of figure 4.8. The other frequency of 323 Hz (see figure 4.9b) is not a saddle point frequency. However, the slowness contour corresponding to the lower dispersion surface has six segments with almost zero curvature, and the normal vector to this slowness contour shows the preferential directions at this particular frequency. The slowness contours for the saddle point at 428.67 Hz on the lower dispersion surface are shown in figure 4.9c; the contour corresponding to the lower dispersion surface contains corner points but the curvature of the smooth parts of the boundary is large.

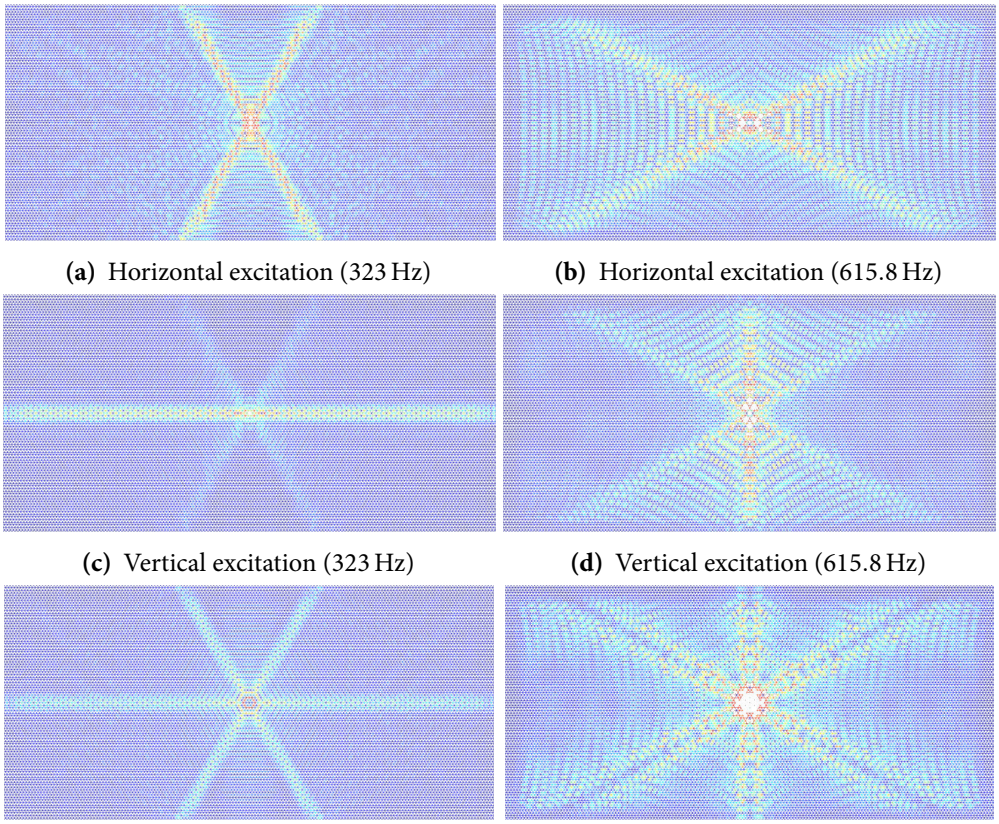

**(a)** Horizontal excitation (323 Hz) **(b)** Horizontal excitation (615.8 Hz)

**(c)** Vertical excitation (323 Hz) **(d)** Vertical excitation (615.8 Hz)

**(e)** Torsional excitation (323 Hz) **(f)** Torsional excitation (615.8 Hz)

**Figure 4.10:** Finite element computations showing the magnitude of the [real] displacement amplitude fields for different types of applied load. For figures (a),(c) & (e), the excitation frequency is 323 Hz and 615.8 Hz in (b),(d) & (f). The colours indicate the magnitude of the displacement field from blue (zero) to red (maximal). The white regions are those regions where the displacement field is outside the range.

The displacement fields have a number of interesting features. Firstly, one may observe the so-called *primitive waveforms* already demonstrated in the scalar case [5, 90, 91, 121]. However, in contrast to the scalar case, the presence of these star shaped contours (or localised waveforms) is not associated with the resonant frequencies as identified in [5, 121]. In the present problem, the localised waveforms are associated with frequencies where the slowness contours exhibit strong

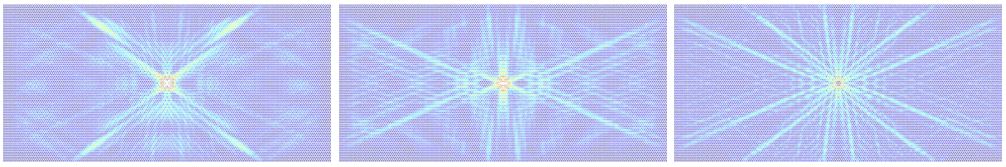

**(a)** Horizontal excitation **(b)** Vertical excitation **(c)** Torsional excitation

**Figure 4.11:** Finite element computations showing the magnitude of the displacement amplitude fields for different types of the applied force. The excitation frequency is 428.67 Hz, which coincides with the saddle point frequency for which the slowness contours are shown in figure 4.9c. The colours indicate the magnitude of the displacement field from blue (zero) to red (maximal). The white regions are those regions where the displacement field is above the range.

preferential directions (see figure 4.9). For the two frequencies considered, the six preferential directions of propagation corresponding to the outward unit normals may be identified. It is emphasised that only figures 4.9c and 4.9e correspond to a resonant frequency and yet the localised waveforms persist at the non-resonant frequency of 323 Hz due to the shape of slowness contour in figure 4.9b. In contrast to the scalar lattice, where the applied loading was anti-planar and hence isotropic, the in-plane elasticity problem allows the freedom to choose any in-plane direction (and type) of the applied loading. As can be observed from the computations shown in figure 4.10, the orientation of the applied force has a significant effect on the resultant field. The effect is strongest in directions that have a component of the group velocity perpendicular to the applied force. The hexagonal aberrations and wave envelopes, are evident at the resonant frequency (see figures 4.10b, 4.10d and 4.10f).

For comparison, figure 4.11 also shows the displacement amplitude at the saddle point frequency of 428.67 Hz, with the slowness contours shown in figure 4.9c. Three types of loading, similar to those of figure 4.10, are shown. Although the directional preference is clearly visible, the aberration is more pronounced for this case compared to figure 4.10.

The different orientations of the hexagonal slowness contours and hence, the different preferential directions of propagation for different frequencies are a novel feature of the elastic lattice, which are absent in the scalar cases. One may envisage applications in shielding and focusing of elastic waves where this "switch" in preferential direction coupled with the ability to "select" a given direction via the applied force could be useful. The frequency at which this switching of preferential direction occurs is exactly the saddle point frequency of 428.67 Hz. This saddle point also marks the frequency at which a similar rotation in the hexagonal-like contours occurs. As can be seen from figure 4.9c, this is also the frequency at which the slowness contours intersect at two corners and the centre of each side of the elementary cell in the reciprocal lattice.

## 4.3 A discrete structural interface: shielding, negative refraction, and focusing

In this section, applications of the dispersive properties of Bloch-Floquet waves in discrete systems are considered. In particular, applications relating to the effects of filtration and focusing of elastic waves by a *"metamaterial flat lens"* for certain frequencies are presented. The effects of

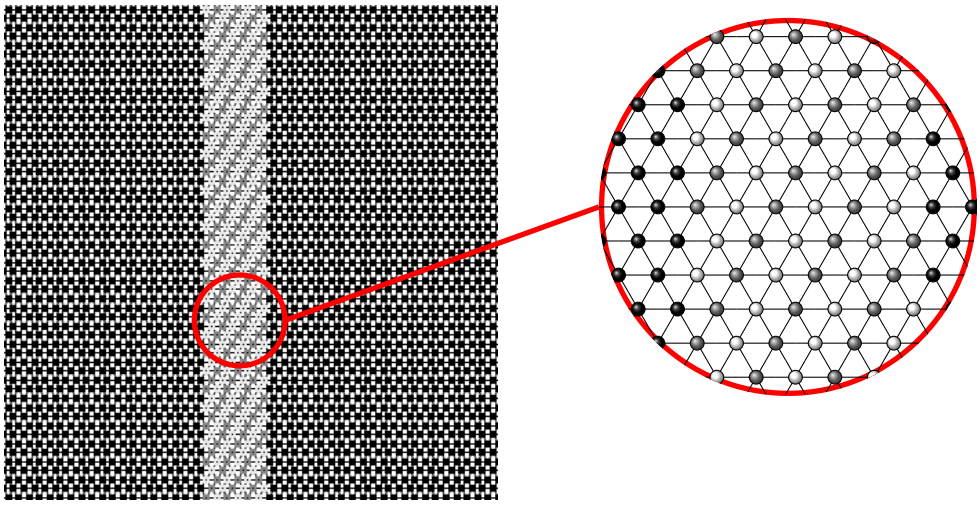

**Figure 4.12:** A schematic diagram of the lattice system with the heterogeneous diatomic interface (highlighted). The regions to the left and to the right of the interface consist of homogeneous monatomic lattices.

| Property | Value |
|---|---|
| Young's Modulus | 200 GPa |
| Second Moment of Inertia | $349 \times 10^{-8}$ m$^4$ |
| Cross Sectional Area | $2.12 \times 10^{-3}$ m$^2$ |
| Beam Density | 7850 kg m$^{-2}$ |
| Beam Length | 1 m |
| Nodal Mass (Ambient) | 91.531 kg |
| Nodal Mass (Interface $m_1$) | 16.642 kg |
| Nodal Mass (Interface $m_2$) | 166.42 kg |
| Polar Mass Moment of Inertia (Ambient) | 66.568 kg m$^2$ |
| Polar Mass Moment of Inertia (Interface $J_1$) | 633.284 kg m$^2$ |
| Polar Mass Moment of Inertia (Interface $J_2$) | 99.852 kg m$^2$ |

**Table 4.2:** The material and geometrical parameters for the ambient and interface lattices. The parameters of the ambient and interface nodes are links are differentiated where required and are uniform otherwise.

focussing and filtering for solutions of the Helmholtz equation have already been demonstrated in the literature, see for example [103]. More recently, Jones et al. [81] analysed similar effects for the case of vector elasticity in a structured continuum. Here, the effects of focussing and filtration of elastic waves in discrete structures are discussed.

Consider a finite triangular lattice, of the same geometry as in section 4.2. Let the ambient lattice be monatomic and homogeneous. Within the ambient lattice a finite slab of heterogeneous diatomic lattice of the same geometry is embedded. Both the ambient lattice and interface lattice (finite slab) are lattices with inertial links, formed from Euler-Bernoulli beams. The material and geometrical parameters of the lattices are detailed in table 4.2. A schematic diagram of the ambient and interface lattices is shown in figure 4.12.

Consider the time-harmonic propagation of elastic in-plane waves through the ambient lattice and structural interface as shown in figure 4.13b. The wave is generated by a single point source: a time-harmonic displacement of amplitude $10^{-6}$ m in the horizontal direction is prescribed at

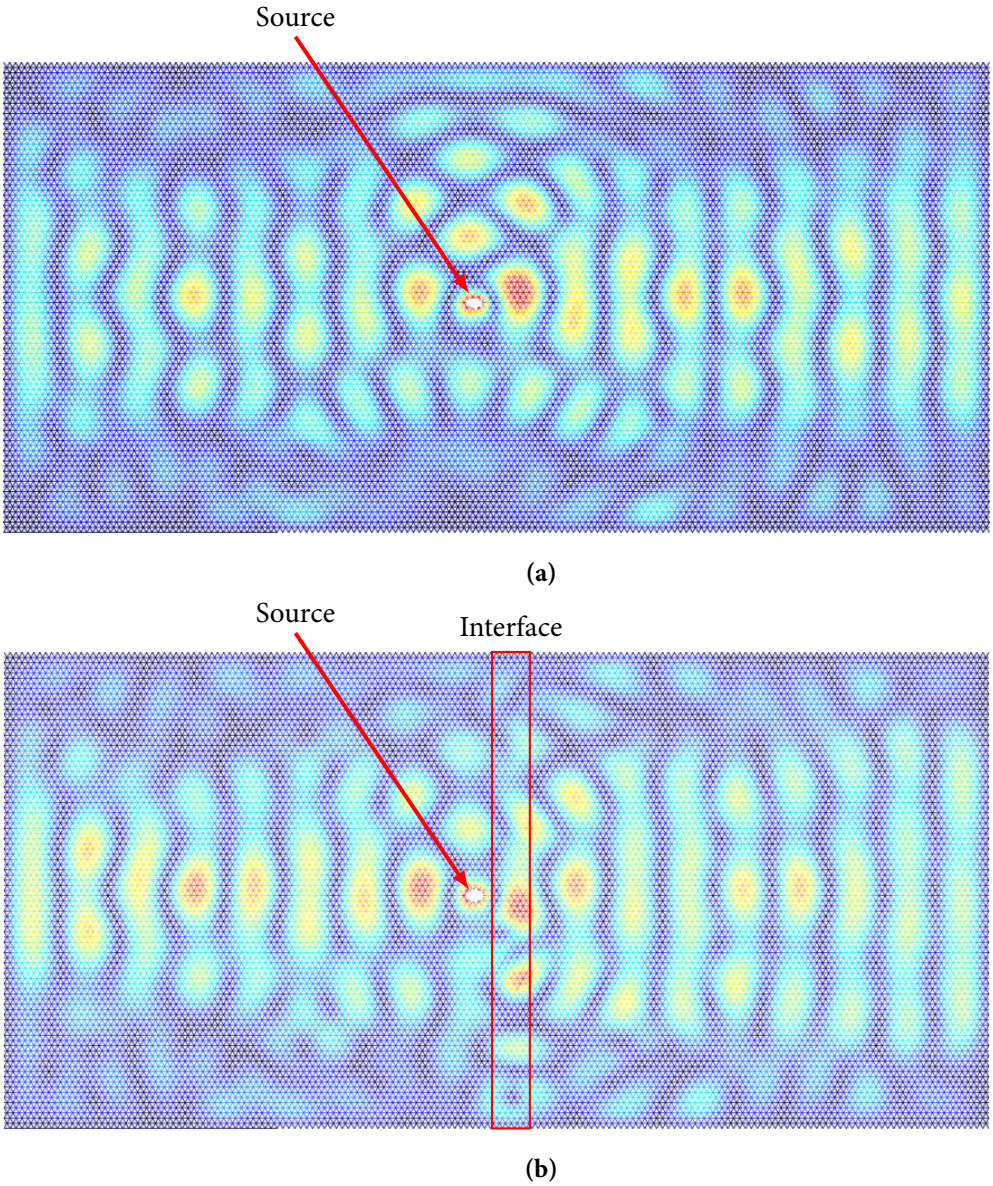


**Figure 4.13:** Part (a) shows a harmonic wave propagating through the ambient lattice. Part (b) shows a harmonic wave interacting with the structured interface. This figure is for the same configuration as part (b), except that the structured interface has been embedded in the ambient lattice. The magnitude of the displacement field is plotted. It is observed that the displacement field is essentially unaffected by the presence of the interface. In both cases, the forcing frequency is 100 Hz.

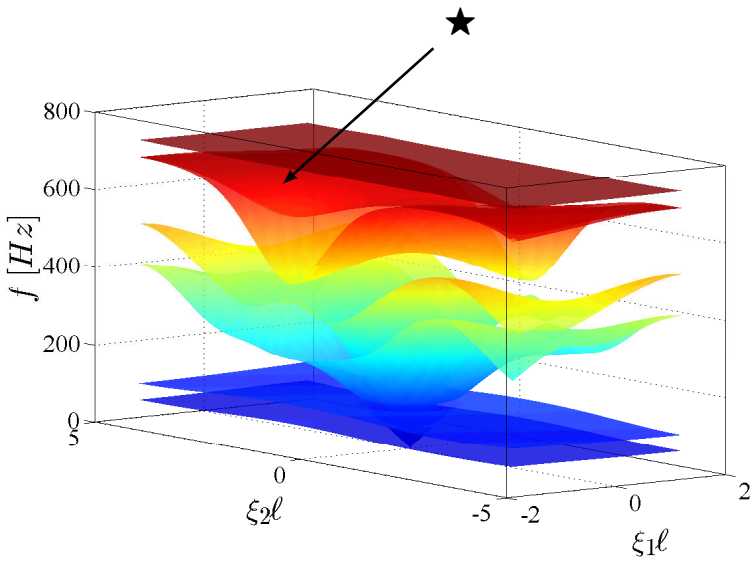


**Figure 4.14:** The dispersion surfaces corresponding to heterogeneous diatomic interface lattice. Of particular interest, in addition to the band gap at 700 Hz, is the surface labelled ★, which possesses saddle points.

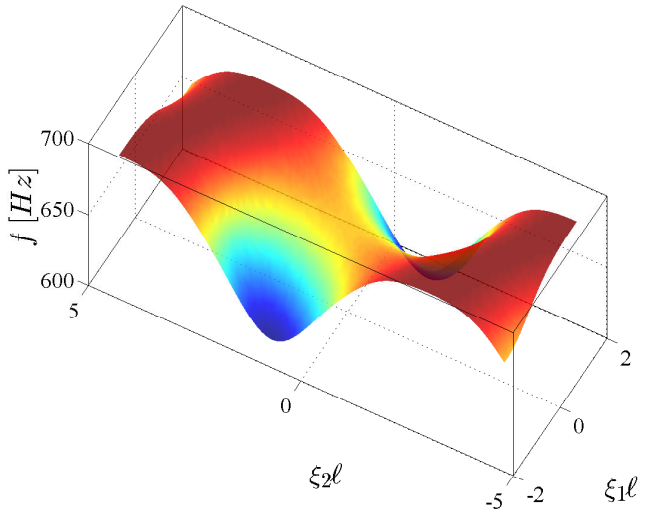


**Figure 4.15:** The sixth dispersion surface, labelled ★ in figure 4.14, possessing the saddle point of interest.

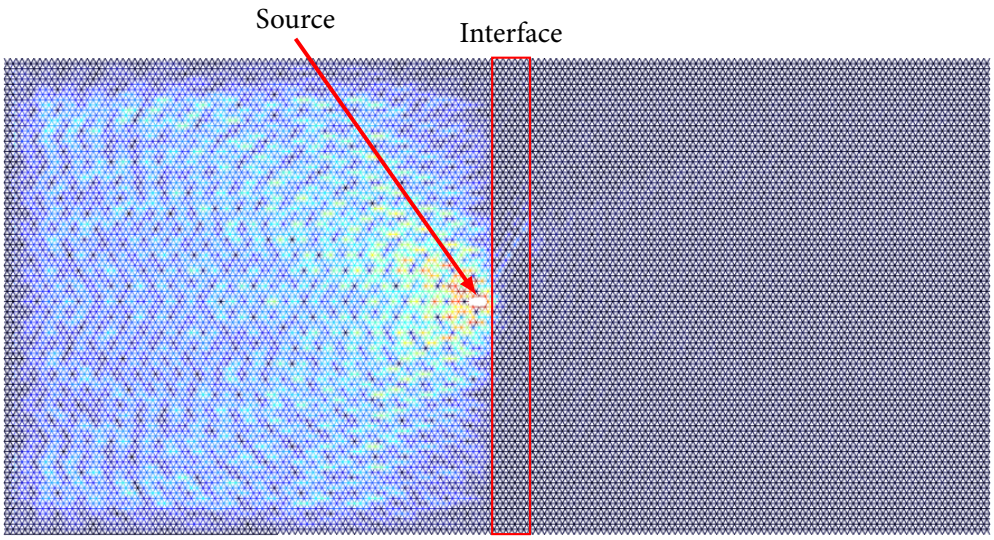


**Figure 4.16:** The same configuration as in figure 4.13b, but with a forcing frequency of 700 Hz, which lies in the band gap of the dispersion diagram for the interface lattice. The wave is reflected from the interface as would be expected for frequencies within the stop band for the interface.

one of the lattice nodes. Damping is applied to the lattice links in the neighbourhood of the fixed boundary nodes in order to reduce reflection from the boundary of the computational domain.

Consider now the dispersion surfaces for the elementary cell of the structured interface, shown in figure 4.14. The transmission problem is formally distinct from the Bloch-Floquet spectral problem. Nevertheless, the dispersion diagram may be used in order to predict the reflection and transmission patterns. Figure 4.13b shows the magnitude of the displacement amplitude[1] when the forcing frequency is 100 Hz. A similar wave pattern can clearly be observed on both sides of the interface layer, indicating that the low frequency response of the structured interface is very close to that of the ambient medium. A resembling wave pattern can also be seen in figure 4.13a where the structured interface has been removed entirely. In contrast, figure 4.16 shows the magnitude of the displacement field when the forcing frequency is 700 Hz, which lies in the stop band of figure 4.14. In this case, the incoming wave is reflected, with very little transmission.

It has been suggested that the phenomenon of focusing by a flat interface is linked to the presence of saddle points and regions of negative group velocities (see, for example, [81, 103]). Referring to the dispersion surfaces for the heterogeneous interface lattice (figure 4.14), it is observed that the surface labelled ★ and shown in figure 4.15 possesses a saddle point and regions where the group velocity is negative. In particular, for small perturbations around the saddle point it is observed that the components of the group velocity $(\partial\omega/\partial\boldsymbol{\xi})$ will have opposing signs. Figure 4.17 shows a plot of the magnitude of the displacement field when the forcing frequency is 642.5 Hz. The frequency was chosen in the vicinity of the saddle point on the corresponding dispersion surface. The effect described here is typical for neighbourhoods of saddle points. A clear directional preference can be observed within the interface. In addition, the *secondary source* on the right hand side of the interface can also be observed. Figure 4.17

[1] That is, $\|\boldsymbol{u}(\boldsymbol{x})\|$.

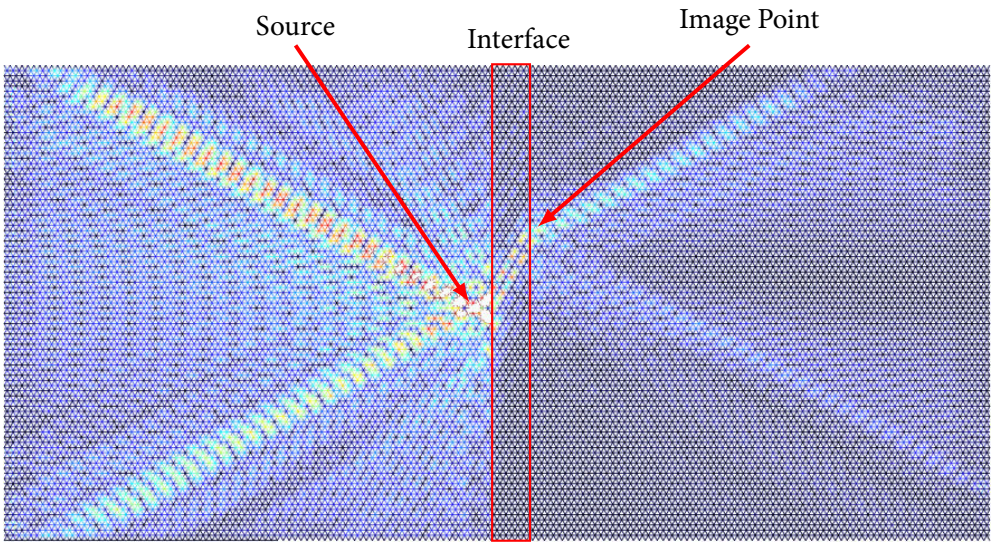


**Figure 4.17:** The same configuration as in figure 4.13b, but with a forcing frequency of 642.5 Hz. The image point is visible on the right hand side of the interface. The image point is shifted along the direction of preferential propagation of the interface lattice.

shows the preferential direction of propagation and the effect of focusing. This feature of the waves persists in a small interval containing the saddle point.

Finally, in figure 4.18 a simulation where the source has been shifted away from the interface region is presented. In this case, the forcing frequency is 654.4 Hz, which again is in the vicinity of the saddle point and within the region where there is a preferential direction of propagation. Moreover, where the beams intersect on the right hand side, we can see the formation of the *image point*. This effect is strongly frequency dependent and, as was the case with the primitive waveforms discussed earlier, is sensitive to perturbation in the frequency.

## 4.4 Remarks

In contrast to the previous chapter, which primarily dealt with the low frequency response of discrete metamaterial structures, the discussion in the present chapter has been focused on the finite frequency response. It has been demonstrated that, even uniform, structured media may exhibit vastly different behaviour at higher frequencies compared with the low frequency response. In particular, strongly anisotropic wave propagation associated with polygonal slowness contours is exhibited at higher frequencies.

The dynamic anisotropy of both scalar and elastic discrete systems has been examined. In particular, extending the previous work with scalar lattices, the presence of directionally localised waveforms in elastic lattices which are isotropic in the long wavelength limit have been demonstrated. These waveforms are identified with regions on the dispersion surfaces and slowness contours with several preferential directions of propagation. The presence of aberrations in the displacement fields, corresponding to the shape of the slowness contours have been observed and connection has been made with the notion of aberration in optics.

In addition, it has been demonstrated that the dispersive properties of Bloch-Floquet waves in an infinite lattice structure can be used in problems of optimal design for finite size micro-

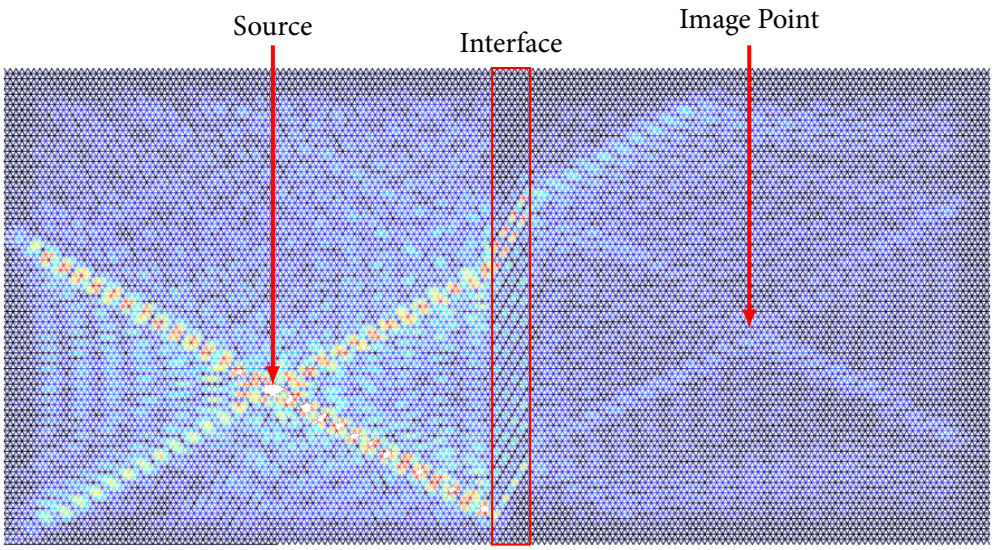


**Figure 4.18:** In this case the source has been shifted further away from the interface. Correspondingly, this leads to a shift in the image point due to the preferential direction within the layer. Here, the forcing frequency is 654.5 Hz.

structures. In particular, the interaction of waves with a heterogeneous diatomic lattice of finite width was considered. Special attention is drawn to the range of frequencies in the neighbourhood of saddle points on the dispersion diagram. The corresponding regime shows directional preferences for waves interacting with the structured medium. The apparent focussing and creation of an *image point*, by a flat elastic 'lens' is one of the interesting outcomes of this work.

Having consider the low frequency response of discrete metamaterial structures in chapter 3, and the behaviour around resonant frequencies in the present chapter, the next chapter examines the behaviour of such structured media at even higher frequencies in the stop band.

# *Chapter Five*

# Localised modes for rectilinear defects in a square lattice

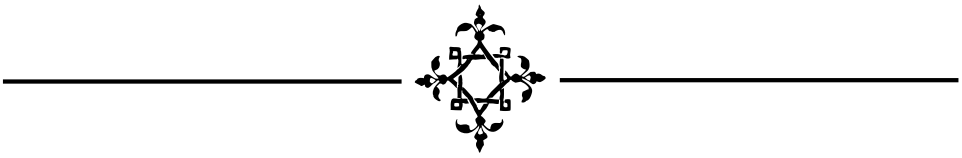

A well-known and interesting feature of discrete media is the existence of pass and stop bands, as demonstrated in chapters 3 and 4. In the present chapter, localised defect modes associated with the eigenmodes of a finite line of defects in an infinite square lattice are examined.

The present chapter is developed as follows. In section 5.1, the problem of a finite line of defects (created by a perturbation of point masses) embedded in an infinite square lattice is considered. Several representations for the Green's matrix are presented, including integral forms and representation in terms of generalised hypergeometric functions. Localised defect modes for the finite line are analysed in section 5.1.1. Therein, the necessary and sufficient condition for the existence of localised modes is formulated, and asymptotic expansions in the far field are also presented. Band edge expansions are constructed using an analytic continuation of the Green's function. Illustrative examples for a finite number of defects are given in section 5.2, where eigenfrequencies and eigenmodes are presented and compared with the asymptotic results from the previous section. Here, the defects a characterised by one or more lattice nodes having a mass smaller than the nodes in the ambient lattice. For one- and three-dimensional multi-atomic lattices, there exists some lower bound on the difference in mass between the defect and ambient nodes such that a localised mode may be initiated [98]. However, in the present chapter, it is demonstrated that this is not the case for two-dimensional lattices: there is no lower bound on the mass that should be removed from a defect node in order to initiate a localised mode. The analysis of a finite-sized defect region is accompanied by the waveguide modes that may exist in a lattice containing an infinite chain of point masses. A brief discussion of the infinite waveguide problem is presented, for completeness, in section 5.3. Finally, in section 5.4, a numerical simulation illustrates that the solution for the problem of the infinite chain can be used to predict the range of eigenfrequencies of localised modes for a finite but sufficiently long array of masses representing a rectilinear defect in a square lattice.

## 5.1 A finite inclusion in an infinite square lattice

Consider a square meshing of $\mathbb{R}^2$ such that each node is labelled by the double index $\boldsymbol{n} \in \mathbb{Z}^2$, where $\boldsymbol{n} = (n_1, n_2)$. Let there be $N > 0$ defects (with $N \in \mathbb{N}$) distributed along $n_2 = 0$ as shown in figure 5.1. The defects are characterised by a non-dimensional mass $0 < r < 1$, where the mass of the ambient nodes is taken as a natural unit. The stiffness and lengths of the lattice bonds are uniform and taken as further natural units. All physical quantities, such as the frequency and displacement, have been normalized according to these natural units and are therefore dimensionless. Let $u_{\boldsymbol{n}}$ denote the complex amplitude of the time-harmonic out-of-plane displacement

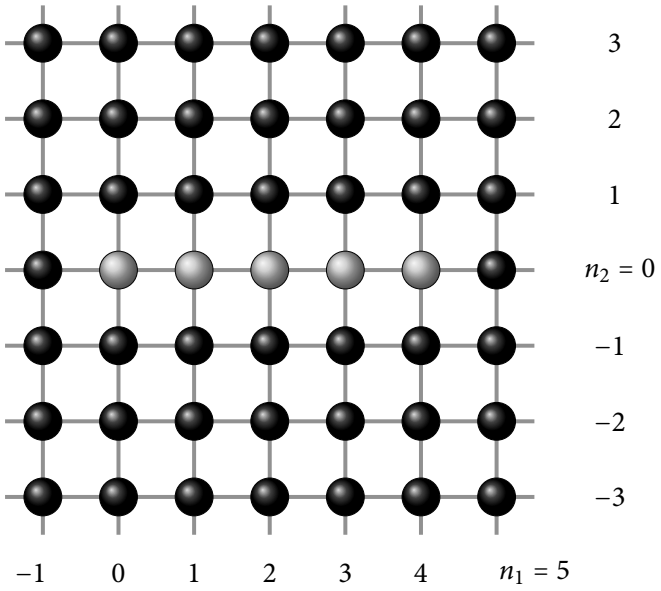


**Figure 5.1:** A finite line of defects in an infinite square lattice. The length of the links, the stiffness of the bonds and the mass of the black nodes are taken as natural units.

of node $\boldsymbol{n}$. Then, the equation of motion is (see § 2.1 and 2.2.1)

$$u_{\boldsymbol{n}+\boldsymbol{e}_1} + u_{\boldsymbol{n}-\boldsymbol{e}_1} + u_{\boldsymbol{n}+\boldsymbol{e}_2} + u_{\boldsymbol{n}-\boldsymbol{e}_2} + (\omega^2 - 4)u_{\boldsymbol{n}} = (1-r)\omega^2 \delta_{0,n_2} \sum_{p=0}^{N-1} u_{\boldsymbol{n}} \delta_{p,n_1}, \tag{5.1}$$

where $\omega$ is the radian frequency, $\boldsymbol{e}_i = [\delta_{1,i}, \delta_{2,i}]^{\mathrm{T}}$, and $\delta_{i,j}$ is the Kronecker Delta. By means of the discrete Fourier Transform the governing equation (5.1) may be written

$$(\omega^2 - 4 + 2\cos\xi_1 + 2\cos\xi_2)u^{\mathrm{FF}}(\boldsymbol{\xi}) = (1-r)\omega^2 \sum_{p=0}^{N-1} u_{p,0} \exp(-ip\xi_1). \tag{5.2}$$

In the notation of section 2.1 the parenthesised term on the left hand side is $\sigma(\omega, \boldsymbol{\xi})$ and the right hand side of equation (5.2) is the Fourier Transform of the load $f_{N-1}(\xi_1)$. The positive root of the parenthesised term represents the dispersion equation for the ambient lattice. As mentioned earlier in section 4.1.1, it is observed that for $\omega^2 > 8$ there exist no real solutions to the dispersion equation. Hence, the ambient lattice possesses a semi-infinite stop band: $\omega^2 \in (8, \infty)$. Inverting the transform yields the discrete field

$$u_{\boldsymbol{n}}(\omega) = (1-r)\omega^2 \sum_{p=0}^{N-1} u_{p,0}\, g(\boldsymbol{n}, p; \omega), \tag{5.3}$$

where $g(\boldsymbol{n}, p; \omega)$ is the shifted Green's matrix defined as:

$$g(\boldsymbol{n}, p; \omega) = \frac{1}{\pi^2} \int_0^\pi \int_0^\pi \frac{\cos\left([n_1 - p]\xi_1\right)\cos(n_2\xi_2)}{\omega^2 - 4 + 2\cos\xi_1 + 2\cos\xi_2} \mathrm{d}\xi_1 \mathrm{d}\xi_2. \tag{5.4}$$

For the purposes of numerical evaluation and asymptotic analysis in the stop band of the ambient lattice ($\omega^2 > 8$), it is convenient to rewrite the Green's matrix as a single integral

$$g(\boldsymbol{n}, p; \omega) = \frac{1}{2\pi} \int_0^\pi \frac{\left(\sqrt{a^2 - 1} - a\right)^{|n_1 - p|}}{\sqrt{a^2 - 1}} \cos\left(n_2\xi_2\right) \mathrm{d}\xi_2, \tag{5.5}$$

where $a(\xi_2; \omega) = \omega^2/2 - 2 + \cos\xi_2$. Reversing the order of integration yields the same result, but with $n_1 - p$ and $n_2$ interchanged, and $\xi_1$ interchanged with $\xi_2$. An alternative representation can be found in the book by van der Pol [143] as

$$g(\boldsymbol{n}, p; \omega) = \frac{(-1)^{n_1 - p + n_2}}{2} \int_0^\infty I_{n_1 - p}(x) I_{n_2}(x) e^{-\alpha x} \mathrm{d}x, \tag{5.6}$$

where $I_m(x)$ is the modified Bessel function of the first kind, $\alpha = \omega^2/2 - 2 > 2$. The integral is symmetric about $n_1 - p = 0$ and $n_2 = 0$ and therefore it may be assumed, without loss of generality, that $n_1 \geq p$ and $n_2 \geq 0$. The integral (5.6) may then be represented in terms of regularised generalised hypergeometric functions (see [131], section 3.15.6, equation 8)

$$g(\boldsymbol{n}, p; \omega) = \frac{(-1)^{m+n_2}}{(2\alpha)^{1+m+n_2}} \left((m + n_2)!\right)^2 {}_4\mathbf{F}_3\left[\begin{matrix} a_1, & a_1, & a_2, & a_2 \\ b_1, & b_2, & b_1 + b_2 - 1 & \end{matrix}; \frac{4}{\alpha^2}\right], \tag{5.7}$$

where $m = n_1 - p$, $a_1 = (1 + m + n_2)/2$, $a_2 = (2 + m + n_2)/2$, $b_1 = 1 + m$, and $b_2 = 1 + n_2$. The series (5.7) is convergent for $\alpha^2 > 4$ (see [120]), that is, everywhere in the stop band of the ambient lattice. It is observed that along the ray $m = n_2$, the Green's matrix may be written in terms of Gauss' hypergeometric function. In particular, equation (5.7) reduces to

$$g(n, n, 0; \omega) = \frac{\left((2n)!\right)^2}{(2\alpha)^{1+2n}} {}_2\mathbf{F}_1\left[\begin{matrix} 1/2 + n, & 1/2 + n \\ & 1 + 2n \end{matrix}; \frac{4}{\alpha^2}\right]. \tag{5.8}$$

The function (5.8) is strictly positive in the region $n \geq 0$ and $\alpha > 2$. Hence, for a single defect, the lattice nodes along the diagonal rays do not oscillate relative to each other.

Furthermore, for the case of $m = n_2 = 0$, the integral representation (5.4) reduces to the 2-fold Watson integral (see, for example, [82] and [150]). Using a simple change of variables (5.4) can be written in terms of an elliptic integral, or alternatively, one can use (5.8) and observe that

$$g(\mathbf{0}, 0; \omega) = \frac{1}{2\alpha} {}_2\mathbf{F}_1\left[\begin{matrix} 1/2, & 1/2 \\ & 1 \end{matrix}; \frac{4}{\alpha^2}\right] = \frac{1}{\alpha\pi} K\left(\frac{4}{\alpha^2}\right), \tag{5.9}$$

where $K(x)$ is the complete elliptical integral of the first kind. Together with equation (5.9), the representation (5.6) is particularly useful since, by repeated integration by parts and use of the identity $I_n(x) = 2I'_{n-1}(x) - I_{n-2}(x)$, one can iterate from $g(\mathbf{0}, 0; \omega)$ to a general $g(\boldsymbol{n}, p; \omega)$.

### 5.1.1 Localised modes

Of primary interest are localised modes, that is, modes of vibration at frequencies that are not supported by the ambient lattice and therefore decay rapidly away from the defect. Introducing the vector $\boldsymbol{\mathcal{U}} = [u_{0,0}, u_{2,0}, \ldots, u_{N-1,0}]^{\mathrm{T}}$ and choosing $n_2 = 0$ in equation (5.3) yields the eigenvalue problem

$$\boldsymbol{\mathcal{U}} = (1-r)\omega^2 \mathcal{G}(\omega)\boldsymbol{\mathcal{U}}, \tag{5.10}$$

where the matrix entries $[\mathcal{G}(\omega)]_{ij} = g(i-1, 0, j-1; \omega)$. Clearly, $\mathcal{G}$ is symmetric and Toeplitz (and hence bisymmetric and centrosymmetric)

$$\mathcal{G} = \begin{pmatrix} \mathcal{G}_{11} & \mathcal{G}_{12} & \mathcal{G}_{13} & \cdots & \mathcal{G}_{1(N-1)} & \mathcal{G}_{1N} \\ & \mathcal{G}_{11} & \mathcal{G}_{12} & \cdots & \mathcal{G}_{1(N-2)} & \mathcal{G}_{1(N-1)} \\ & & \mathcal{G}_{11} & \cdots & \mathcal{G}_{1(N-3)} & \mathcal{G}_{1(N-2)} \\ & & & \ddots & \vdots & \vdots \\ & & & & \mathcal{G}_{11} & \mathcal{G}_{12} \\ & & & & & \mathcal{G}_{11} \end{pmatrix}, \tag{5.11}$$

which greatly reduces the number of required computations. Indeed, for $N$ defects the matrix $\mathcal{G}$ has $N$ independent elements. The solvability condition of the spectral problem (5.10) yields a transcendental equation in $\omega$,

$$\det\left[\mathbb{I}_N - (1-r)\omega^2\mathcal{G}\right] = 0, \tag{5.12}$$

where $\mathbb{I}_N$ is the $N \times N$ identity matrix. Equation (5.12) is the necessary and sufficient condition for the existence of localised modes. Symmetry implies that there exists an orthonormal set of $N$ eigenvectors of $\mathcal{G}$ and hence, $N$ eigenvalues (frequencies). The centrosymmetry of $\mathcal{G}$ allows the number of symmetric and skew-symmetric modes to be determined (see, for example, [21]). Introducing the $N \times N$ exchange matrix

$$\mathbb{J}_N = \begin{pmatrix} 0 & 0 & 0 & 1 \\ 0 & 0 & 1 & 0 \\ 0 & \iddots & 0 & 0 \\ 1 & 0 & 0 & 0 \end{pmatrix}, \tag{5.13}$$

an eigenmode is said to be symmetric if $\boldsymbol{\mathcal{U}} = \mathbb{J}_N\boldsymbol{\mathcal{U}}$ and skew-symmetric if $\boldsymbol{\mathcal{U}} = -\mathbb{J}_N\boldsymbol{\mathcal{U}}$. For a system of $N$ defects there exist $\lceil N/2 \rceil$ symmetric modes and $\lfloor N/2 \rfloor$ skew-symmetric modes, where $\lceil\cdot\rceil$ and $\lfloor\cdot\rfloor$ are the ceiling and floor operators respectively. Of course here, symmetry refers to the symmetry of the eigenmodes in the $n_1$ direction about the centre of the defect line. Due to the symmetry of the system, all modes are symmetric about the line $n_2 = 0$.

Consider the total force on an inclusion containing $N$ defects

$$F = \sum_{p=0}^{N-1} \left(u_{p-1,0} + u_{p+1,0} + 2u_{p,1} - 4u_{p,0}\right). \tag{5.14}$$

By definition, for a skew-symmetric mode $u_{p,0} = -u_{N-1-p,0}$ and further $u_{p,q} = -u_{N-1-p,q}$. Hence, for all skew-symmetric modes the inclusion is self-balanced (i.e. $F = 0$) and therefore, all skew-symmetric localised modes can be considered as multipole modes.

For the illustrative examples presented later, the eigenvalue problem (5.10) will be solved for the unit eigenvectors ($\|\boldsymbol{\mathcal{U}}\| = 1$).

### 5.1.2 Asymptotic expansions in the far field

Here, asymptotic expansions in the far field are considered for some particular cases. Asymptotic expansions for an isolated Green's matrix in various configurations have been considered in [109] and the approach detailed therein is used here.

**Far field, along the line of defects.** The case of $n_1 \to \infty$, $n_2 = 0$ and finite $N$ is considered. Introducing the small parameter $\varepsilon = p/n_1$, the kernel of (5.5) may be expanded for small $|\varepsilon| \ll 1$. In particular,

$$\left(\sqrt{a^2-1}-a\right)^{|n_1-p|} \sim \left(\sqrt{a^2-1}-a\right)^{|n_1|}\left[1-\varepsilon\log\left(\sqrt{a^2-1}-a\right)\right]^{|n_1|}. \tag{5.15}$$

It is observed that at large $n_1$ and sufficiently small $N$, the dominant contribution to the integral (5.5) comes from a small region in the vicinity of $\xi_2 = \pi$. Therefore,

$$\left(\sqrt{a^2-1}-a\right)^{|n_1-p|} \sim \left(\sqrt{c^2-1}-c\right)^{|n_1|}\left[1-\frac{(\pi-\xi_2)^2}{2\sqrt{c^2-1}}\right]^{|n_1|} \times\left[1-\varepsilon\log\left(\sqrt{c^2-1}-c\right)+\varepsilon\frac{(\pi-\xi_2)^2}{2\sqrt{c^2-1}}\right]^{|n_1|}, \tag{5.16}$$

where $c = \omega^2/2 - 3$. Thus,

$$\left(\sqrt{a^2-1}-a\right)^{|n_1-p|} \sim \left(\sqrt{c^2-1}-c\right)^{|n_1-p|}\exp\left[-|n_1-p|\frac{(\pi-\xi_2)^2}{2\sqrt{c^2-1}}\right]. \tag{5.17}$$

In addition, $1/\sqrt{a^2-1} \sim 1/\sqrt{c^2-1}$. Hence, for $0 < \varepsilon \ll 1$ and making use of (5.5)

$$g(n_1,0,p;\omega) \sim \frac{\left(\sqrt{c^2-1}-c\right)^{|n_1-p|}}{2\pi\sqrt{c^2-1}}\int_{\pi-\varepsilon}^{\pi}\exp\left[-|n_1-p|\frac{(\pi-\xi_2)^2}{2\sqrt{c^2-1}}\right]\mathrm{d}\xi_2. \tag{5.18}$$

Making the substitution $x = (\pi-\xi_2)\sqrt{|n_1-p|/(2\sqrt{c^2-1})}$, and performing the resulting integration yields

$$g(n_1,0,p;\omega) \sim \frac{\left(\sqrt{c^2-1}-c\right)^{|n_1-p|}}{\sqrt{8\pi\sqrt{c^2-1}}}\frac{1}{\sqrt{|n_1-p|}} \quad \text{as} \quad n_1 \to \infty. \tag{5.19}$$

Thus from (5.3), the physical field has the following approximate representation for $n_1 \to \infty$

$$u_{n_1,0}(\omega) \sim (1-r)\omega^2 \sum_{p=0}^{N-1} \frac{\left(\sqrt{c^2-1}-c\right)^{|n_1-p|}}{\sqrt{8\pi\sqrt{c^2-1}}} \frac{u_{p,0}(\omega)}{\sqrt{|n_1-p|}}, \tag{5.20}$$

where $u_{p,0}(\omega)$ should be determined from (5.10). It is observed that when $N = 1$ equation (5.20) is consistent with equation (4.17) of [109] up to a change in sign.

**Far field, perpendicular to the line of defects.** Here, the case considered is $n_1 = p'$, $n_2 \to \infty$ with $N$ and $p'$ finite. The method used here follows the same general procedure as in the previous case. However in this case, the kernel is oscillatory and is therefore approximated as a product of decaying and oscillatory functions. For sufficiently small $|p'-p|$ and large $n_2$, the non-oscillatory part of the integrand in (5.5) is approximated as before, leading to

$$g(p', n_2, p; \omega) \sim \frac{\left(\sqrt{c^2-1}-c\right)^{|n_2|}}{2\pi\sqrt{c^2-1}} \int_{\pi-\varepsilon}^{\pi} \exp\left[-|n_2|\frac{(\pi-\xi_1)^2}{2\sqrt{c^2-1}}\right] \cos\left([p'-p]\xi_1\right) \mathrm{d}\xi_1. \tag{5.21}$$

Making a similar change of variable, $x = (\pi-\xi_1)\sqrt{|n_2|/(2\sqrt{c^2-1})}$, and integrating, it is found that

$$g(p', n_2, p; \omega) \sim (-1)^{(p'-p)} \frac{\left(\sqrt{c^2-1}-c\right)^{|n_2|}}{\sqrt{8\pi\sqrt{c^2-1}}} \frac{1}{\sqrt{|n_2|}} \exp\left[-(p'-p)^2\frac{\sqrt{c^2-1}}{2|n_2|}\right]. \tag{5.22}$$

Hence, for $n_2 \to \infty$ the physical field in (5.3) may be approximated by

$$u_{p',n_2}(\omega) \sim (1-r)\omega^2 \frac{\left(\sqrt{c^2-1}-c\right)^{|n_2|}}{\sqrt{8\pi\sqrt{c^2-1}}} \sum_{p=0}^{N-1} (-1)^{(p'-p)} \exp\left[-(p'-p)^2\frac{\sqrt{c^2-1}}{2|n_2|}\right] \frac{u_{p,0}(\omega)}{\sqrt{|n_2|}}. \tag{5.23}$$

It is observed that for $N = 1$ and $p' = p$, the above equation (5.23) is consistent with equation (4.17) of [109] up to a change in sign. Moreover, for the case of $p' = p$, (5.23) reduces to (5.20).

### 5.1.3 Band edge expansions

The representations of Green's matrix (5.5)-(5.7) are valid in the stop band. However, given that the hypergeometric function in the representation (5.7) is zero balanced, that is, the sum of the bottom parameters minus the sum of the top parameters vanishes: $2(b_1+b_2)-1-2(a_1+a_2) = 0$, the stop band Green's matrix can be extended to the boundary of the pass band by analytic

continuation[1]. In particular, the analytical continuation of the function (5.7) has the form

$$g(\boldsymbol{n},p;\omega)=\frac{(-4)^{m+n_2}}{\pi(2\alpha)^{1+m+n_2}}\sum_{j=0}^{\infty}\left(\frac{([1+m+n_2]/2)_j}{j!}\right)^2\left(1-\frac{4}{\alpha^2}\right)^j \times\left\{\sum_{k=0}^{j}\frac{(-j)_k}{\left\{([1+m+n_2]/2)_j\right\}^2}\,\mathcal{H}(m,n_2,k)\Big[\quad\psi(1+j-k) +\psi(1+j)-\psi\left(\frac{1+m+n_2}{2}+j\right)-\log\left(1-\frac{4}{\alpha^2}\right)\Big] +(-1)^j(j)!\sum_{k=j+1}^{\infty}\frac{(k-j-1)!}{\{([1+m+n_2]/2)_k\}^2}\,\mathcal{H}(m,n_2,k)\right\} \tag{5.24}$$

where the reader is reminded that $m = n_1 - p$, $(\cdot)_j$ is the Pochhammer symbol, $\psi(x)$ is the Digamma function, and

$$\mathcal{H}(m,n,k)=\frac{(m)_k(n)_k}{k!}\,{}_3\mathrm{F}_2\left[\begin{matrix}(m+n_2)/2,\ (m+n_2)/2,\ -k\\ m,\ n\end{matrix};1\right]. \tag{5.25}$$

The symbol ${}_p\mathrm{F}_q[\ldots]$ denotes the generalised hypergeometric function, which is related to the regularised generalised hypergeometric function thus:

$${}_p\mathrm{F}_q[a_1,\ldots,a_p;b_1,\ldots b_q;z]=\{\Gamma(b_1)\ldots\Gamma(b_q)\}\,{}_p\mathbf{F}_q[a_1,\ldots,a_p;b_1,\ldots b_q;z].$$

In this case, the continuation (5.24) holds for $\alpha^2 \geq 4$, which in terms of frequency corresponds to $\omega^2 \geq 8$. It is emphasised that in this section, the term "*vicinity of the band edge*" refers to a small interval $8 \leq \omega^2 < 8+\varepsilon$, where $0 < \varepsilon \ll 1$.

Hence, choosing $j = 0$ yields the leading order behaviour of (5.7) as $\alpha^2 \to 4^+$ ($\omega^2 \to 8^+$), that is, as $\omega$ approaches the boundary of the pass band from the stop band:

$$g(\boldsymbol{n},p;\omega)\sim\frac{(-4)^{m+n_2}}{\pi(2\alpha)^{1+m+n_2}}\left\{\left[-2\gamma-\psi\left(\frac{1+m+n_2}{2}\right)-\log\left(1-\frac{4}{\alpha^2}\right)\right] +\sum_{k=1}^{\infty}\frac{(k-1)!}{\{([1+m+n_2]/2)_k\}^2}\,\mathcal{H}(m,n_2,k)\right\}, \tag{5.26}$$

where $\gamma$ is the Euler-Mascheroni constant. Alternative representations of the leading order continuations for general zero-balanced ${}_{q+1}\mathrm{F}_q$ were derived by Saigo and Srivastava [135]. Since $k > 0$, the series representation of the hypergeometric function in (5.25) has a finite number of terms and therefore may be computed exactly. The convergence condition for the infinite sums in (5.24) and (5.26) is $2 + m + n_2 + j > 0$, and is automatically satisfied since it was assumed (without loss of generality) at the outset that $m \geq 0$ and $n_2 \geq 0$.

The asymptotic expression (5.26) is particularly interesting as it elucidates the nature of the singularity of the lattice Green's matrix at the band edge. In particular, the asymptotic representation (5.26) captures the logarithmic singularity as $\omega^2 \to 8^+$. This logarithmically singular

[1] Indeed, for any integer balanced hypergeometric function ${}_{q+1}\mathrm{F}_q$ there exists an analytic continuation to the boundary of the unit disk (see [19], among others, for details).

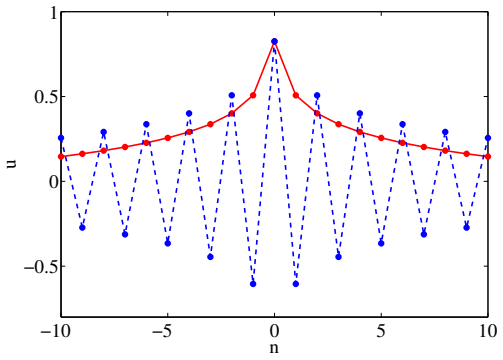


**Figure 5.2:** The solid curve shows the asymptotic expression for the displacement field along the diagonal ($n_1 = n_2$ with $p = 0$) in the vicinity of the band edge (see equation (5.27b)). The dashed curve shows the corresponding asymptotic expression for the field along the bond line (see equation (5.27a)). The frequency chosen is $\omega = 2.829$.

behaviour near the band edge is not obvious from the original representations presented earlier (see equations (5.5)-(5.7)).

For some particular cases, equation (5.26) reduces to the following simplified forms. Along the rays[2] $m = 0$ (i.e. $n_1 = p$):

$$g(p, n_2, p; \omega) \sim \frac{(-4)^{1+n_2}}{\pi(2\alpha)^{1+n_2}} \left[ 2\gamma + \psi\left(\frac{1+n_2}{2}\right) + \log\left(1 - \frac{4}{\alpha^2}\right) \right] \triangleq \tilde{g}^{(\text{bond})}(n_2; \omega), \tag{5.27a}$$

and along the diagonal rays $m = n_2$:

$$g(n_1, m, p; \omega) \sim -\frac{16^m}{\pi(2\alpha)^{1+2m}} \left[ 2\gamma + \psi\left(\frac{1}{2} + m\right) + \log\left(1 - \frac{4}{\alpha^2}\right) \right] \triangleq \tilde{g}^{(\text{diag})}(m; \omega), \tag{5.27b}$$

The Digamma function grows logarithmically as $m \to \infty$ and the term $2\gamma + \psi(1/2 + m)$ is strictly positive for $m > 0$. Therefore, for sufficiently small $m$ the bracketed term in equations (5.27) is negative in the neighbourhood of $\alpha = 2$. Hence, in the vicinity of the band edge, the stop band Green's matrix exhibits fundamentally different behaviour along the bond lines compared with the diagonal rays. In particular, along the bond lines the masses will oscillate out of phase, whereas for the diagonal ray lines the masses will oscillate in phase, as illustrated in figure 5.2. In the far field, equations (5.27) further reduce to

$$g(p, n_2, p; \omega) \sim \frac{(-4)^{1+n_2}}{\pi(2\alpha)^{1+n_2}} \left[ 2\gamma + \log\left(\frac{n_2}{2}\right) + \log\left(1 - \frac{4}{\alpha^2}\right) \right], \text{ as } n_2 \to \infty, \tag{5.28a}$$

$$g(m, m, p; \omega) \sim -\frac{16^m}{\pi(2\alpha)^{1+2m}} \left[ 2\gamma + \log m + \log\left(1 - \frac{4}{\alpha^2}\right) \right], \text{ as } m \to \infty. \tag{5.28b}$$

Using equations (5.3) and (5.27) the out-of-plane displacement for a lattice with $N$ defects has the following asymptotic representation in the vicinity of the band edge

$$u_{n_1,0}(\omega) \sim (1-r)\omega^2 \sum_{p=0}^{N-1} u_{p,0}\, \tilde{g}^{(\text{bond})}(n_1 - p; \omega), \text{ as } \omega^2 \to 8^+, \tag{5.29a}$$

$$u_{n_1,n_2-p}(\omega) \sim (1-r)\omega^2 \sum_{p=0}^{N-1} u_{p,0}\, \tilde{g}^{(\text{diag})}(n_1 - p; \omega), \text{ as } \omega^2 \to 8^+, \tag{5.29b}$$

along the rays $n_2 = 0$ and $n_2 = n_1 - p$ respectively.

[2]Equivalently, one may substitute $n_2$ by $n_1 - p$ in (5.27a) to obtain expansions of $g$ along $n_2 = 0$

## 5.2 Illustrative examples

Several particular cases are considered here corresponding to relatively short defects with $N \in [1, 3]$. The solid curves in figure 5.3 show the $i^{\text{th}}$ solution, $r_{N,i}(\omega)$, of the solvability condition (5.12) for a line of $N$ defects. The shaded region indicates the stop band ($\omega^2 > 8$) of the ambient lattice. For frequencies in this region, waves in the ambient lattice will decay exponentially away from the defect or source.

It is interesting to note that, for one- and three-dimensional multi-atomic lattices, there exists some lower bound on the amount of mass that should be removed from the defect nodes such that a localised mode may be initiated (see, for instance, [98]). However, here the image of $r_{N,N}(\omega)$, indicated by the solid curves in figure 5.3, is $(0, 1)$. In other words, there is no lower bound on the mass that should be removed from a defect node in order to initiate a localised mode. As $r \to 1$, that is, as the lattice approaches a homogeneous lattice, the frequency of the localised mode approaches the band edge ($\omega^2 \to 8^+$). It is also observed that for $N > 1$, the solid curves intersect the band edge at several distinct values of $r$. This suggests that for a given number of defects, there exists a maximum value of $r$ below which all possible localised eigenmodes may be initiated. Above this value of $r$ it is only possible to initiate a subset of the possible eigenmodes with the lower frequency eigenmodes being filtered out. In all cases, the highest frequency eigenmode persists for all possible values of $r$ on $(0, 1)$. For fixed $\omega$, the solvability condition (5.12) for a system of $N$ defects is a polynomial in $r$ of at most degree $N$. Therefore, there exist no more than $N$ solutions for a given frequency $\omega$.

The dashed curves correspond to the problem of an isolated chain of $N$ particles of non-dimensional mass $r^*$, connected by springs to two nearest neighbours and surrounded by rigid foundations. For such a problem, the out-of-plane displacement of mass $n \in \mathbb{Z}$ satisfies

$$\mathcal{L}[v_0, v_1, \cdots, v_{N-1}]^{\mathrm{T}} = 0, \tag{5.30}$$

where the matrix $\mathcal{L}$ has elements

$$[\mathcal{L}]_{ij} = (r^*\omega^2 - 4)\delta_{ij} + \delta_{i-1,j} + \delta_{i,j-1}. \tag{5.31}$$

The dashed curves in figure 5.3 represent the solutions $r^*_{N,i}(\omega)$ of the solvability condition: $\det \mathcal{L} = 0$. It is observed that as $\omega \to \infty$, the dashed curves approach the solid curves from below.

### 5.2.1 A single defect

For the case of a single defect located at the origin, the quantity $\mathcal{G}$ in (5.10) is a scalar:

$$\mathcal{G}(\omega) = \frac{1}{\alpha\pi} K\left(\frac{4}{\alpha^2}\right), \tag{5.32}$$

where $K(x)$ is the complete elliptical integral of the first kind. The solvability condition may be written as

$$r_{1,1} = 1 + \pi\left(\frac{2}{\omega^2} - \frac{1}{2}\right)\left[K\left(\frac{16}{(\omega^2-4)^2}\right)\right]^{-1}, \tag{5.33}$$

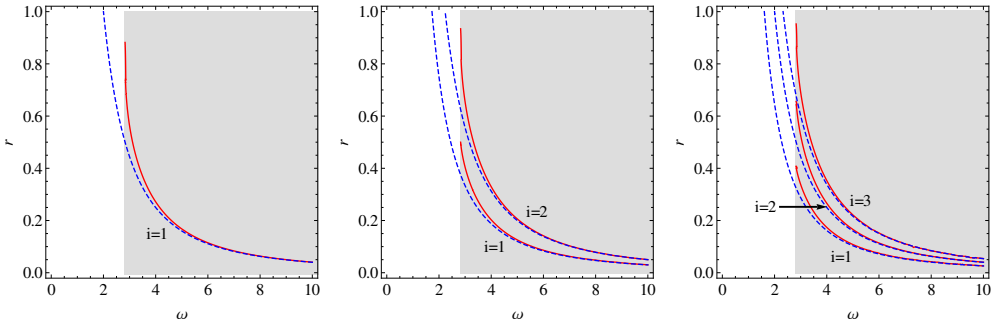


**(a)** A single defect ($N = 1$) **(b)** A pair defects ($N = 2$) **(c)** A triplet of defects ($N = 2$)

**Figure 5.3:** The solid curves show the $i^{\text{th}}$ solution, $r_{N,i}(\omega)$, of the solvability condition (5.12) for a system of $N$ defects embedded in the square lattice. The shaded region ($\omega^2 > 8$) indicates the stop band of the ambient lattice. The dashed curves show the corresponding $i^{\text{th}}$ solution, $r^*_{N,i}(\omega)$, of the solvability condition for an isolated system of $N$ defects (see equation (5.30)).

which has the leading order asymptotic representation

$$r_{1,1} \sim \frac{4}{\omega^2}, \qquad \text{as} \qquad \omega \to \infty. \tag{5.34}$$

It is observed that the solvability condition for equation (5.30) with $N = 1$ agrees precisely with the leading order high frequency asymptotic expansion, hence, the observed coalescence of the solid and dashed curves in figure 5.3a.

The localised defect mode is shown in figure 5.4a, together with field along the line $n_2 = 0$ and the associated asymptotic field as $n_1 \to \infty$ in figure 5.4b. Figures 5.4c and 5.4d show the field (solid line) and the band edge asymptotics (dashed line) for a value of $\alpha = 2.006$. The asymptotic expansions show good agreement with the computed field, even for the far field asymptotics in the neighbourhood of the defect.

### 5.2.2 A pair of defects

In the case of a pair of defects, $\mathcal{G}(\omega)$ is a $2 \times 2$ matrix with the diagonal elements given by (5.32). The off-diagonal elements have the form

$$[\mathcal{G}(w)]_{12} = \frac{1}{4} - \frac{1}{2\pi} K\left(\frac{4}{\alpha^2}\right). \tag{5.35}$$

The solutions of the solvability condition are

$$r_{2,1} = 1 - \frac{4\pi(\omega^2 - 4)}{\pi\omega^2(\omega^2 - 4) - 2\omega^2(\omega^2 - 8)K\left(\dfrac{16}{(\omega^2 - 4)^2}\right)}, \tag{5.36}$$

$$r_{2,2} = 1 + \frac{4\pi(\omega^2 - 4)}{\pi\omega^2(\omega^2 - 4) - 2\omega^4 K\left(\dfrac{16}{(\omega^2 - 4)^2}\right)}, \tag{5.37}$$

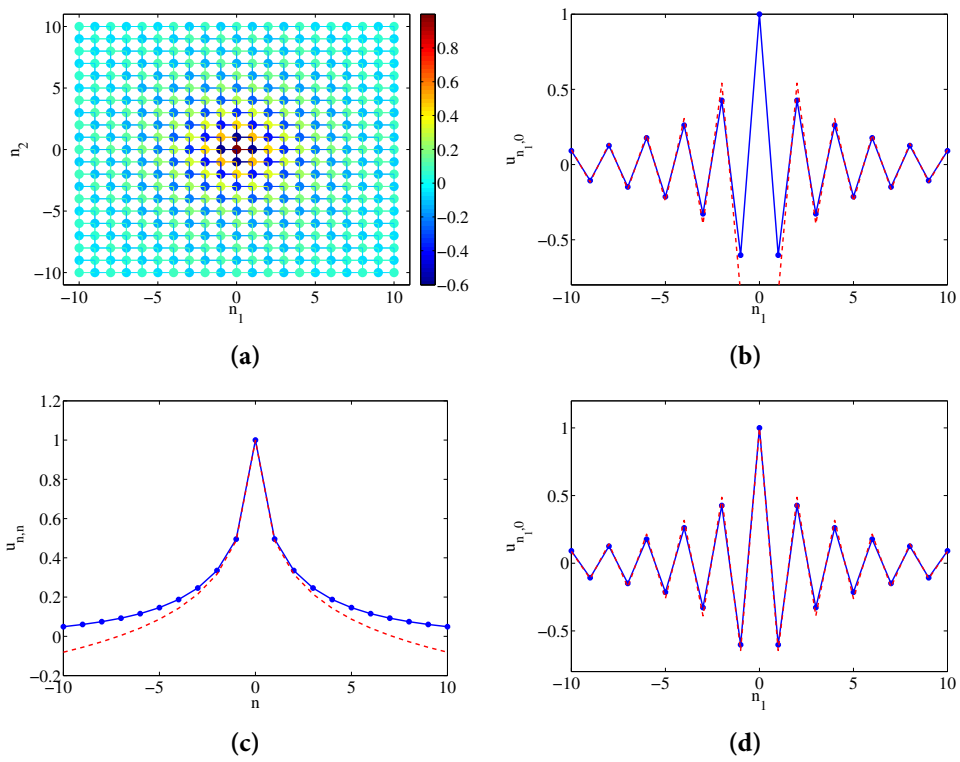


**Figure 5.4:** (a) The localised defect mode for a single defect with $r = 0.8$ and $\omega = 2.83$. (b) The solid curve is the out-of-plane displacement along the line $n_2 = 0$ and the dashed curve is the asymptotic expansion for $n_1 \to \infty$ (see equation (5.20)). (c) The out-of-plane displacement along the line $n_1 = n_2$ (solid curve) with the corresponding asymptotic expansion (5.27b) for the band edge (dashed curve). (d) As for (b), but the dashed curve represents the band edge expansion along $n_2 = 0$ (see equation (5.29a)).

whence the leading order high frequency asymptotic expansions are

$$r_{2,1} \sim \frac{3}{\omega^2} \qquad \text{and} \qquad r_{2,2} \sim \frac{5}{\omega^2} \quad \text{as} \quad \omega \to \infty, \tag{5.38}$$

which agree with the solvability condition of the isolated system (5.30) for $N = 2$, hence, the observed coalescence of the solid and dashed curves in figure 5.3.

Figure 5.5 shows the two defect modes together with the field along the lines $n_1 = 0$, and $n_2 = 0$ and the associated asymptotic field at infinity. In addition, the dash-dot line in figure 5.5c shows the band edge expansion in the vicinity of $\alpha = 2$. In this case, figure 5.5c corresponds to value of $\alpha \approx 2.025$. Once again, the asymptotics are in good agreement with the computed field. Due to the symmetry, the field along the line $n_1 = 1$ is identical to that in figure 5.5e for the symmetric case and identical up to a reflection in the line $u_{0,n_2} = 0$ in figure 5.5f for the skew-symmetric case.

The lower solid curve in figure 5.3b corresponds to $r_{2,1}$ as defined in (5.36). The maximum value of the lower solid curve is given by

$$r_{2,1}^{(\max)} = \lim_{\omega^2 \to 8^+} r_{2,1} = \frac{1}{2}. \tag{5.39}$$

Hence for a pair of defects, a symmetric localised mode cannot be initiated for $r \geq 1/2$.

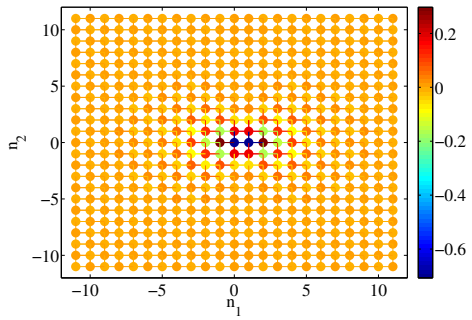


**(a)** Symmetric mode at $\omega = 2.84$

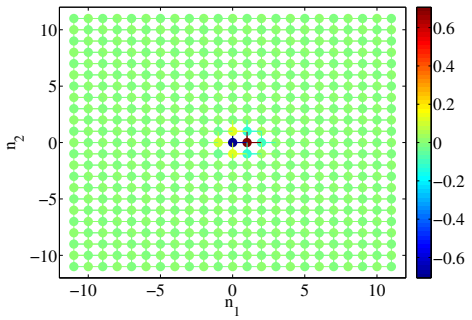


**(b)** Skew-symmetric mode at $\omega = 3.35$

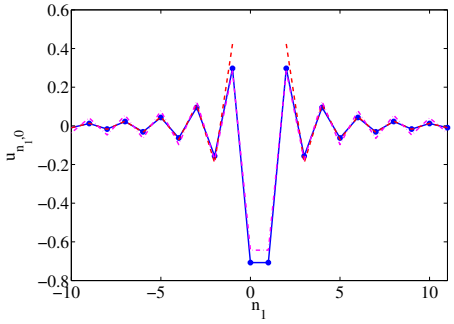


**(c)** The field along the line $n_2 = 0$ for the symmetric mode

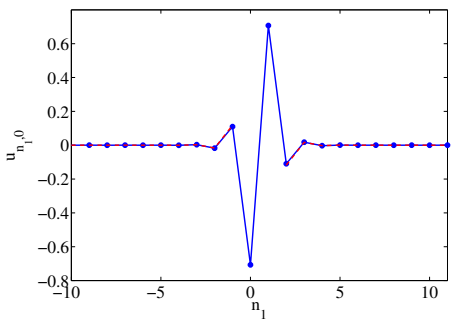


**(d)** The field along the line $n_2 = 0$ for the skew-symmetric mode

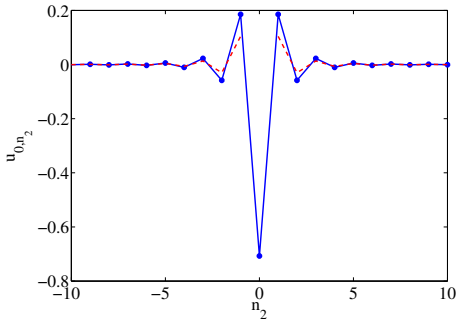


**(e)** The field along the line $n_1 = 0$ for the symmetric mode

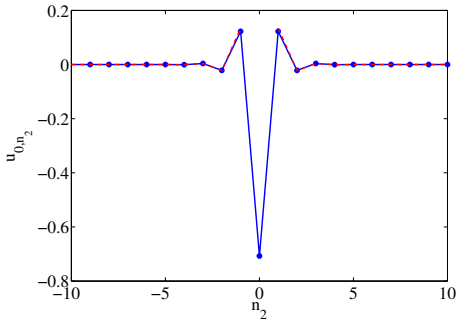


**(f)** The field along the line $n_1 = 0$ for the skew-symmetric mode

**Figure 5.5:** The localised defect mode for a pair of defects with $r = 0.49$. The solid curves show the out-of-plane displacement along the indicated line, and the dashed curves are the associated asymptotic expansions in the far field (see equations (5.20) and (5.23) as appropriate). The dash-dot curve in figure 5.5c shows the band edge expansion (see equation (5.29a)).

### 5.2.3 A triplet of defects

For the case of three defects, the $3 \times 3$ matrix $\mathcal{G}(\omega)$ has the $[\mathcal{G}]_{11}$ and $[\mathcal{G}]_{12}$ elements as defined in equations (5.32) and (5.35). The remaining independent component is

$$[\mathcal{G}(w)]_{13} = [\mathcal{G}(\omega)]_{11} - \frac{\alpha}{2} + \frac{\alpha}{\pi} E\left(\frac{4}{\alpha^2}\right), \tag{5.40}$$

where $E(x)$ is the complete Elliptic Integral of the second kind. The solutions of the solvability condition are of similar form to the previous two cases and are omitted for brevity. The high

frequency asymptotics for $r(\omega)$ are

$$r_{3,1} \sim \frac{4-\sqrt{2}}{\omega^2}, \qquad r_{3,2} \sim \frac{4}{\omega^2}, \qquad \text{and} \qquad r_{3,3} \sim \frac{4+\sqrt{2}}{\omega^2} \qquad \text{as} \qquad \omega \to \infty, \tag{5.41}$$

which again coincide with the solvability condition for (5.30) for the case of a particle triplet ($N = 3$). The maximum values of $r_{3,i}(\omega)$ are $r_{3,1}^{(\max)} = 1 - 3\pi/16$, $r_{3,2}^{(\max)} = 7/8 - (8 - 4\pi)^{-1}$, and $r_{3,3}^{(\max)} = 1$.

The three localised eigenmodes, along with plots of the associated asymptotic expressions are shown in figures 5.6–5.8 for a contrast ratio of $r = 0.4$. Plots of the displacement field along the lines $n_2 = 0$, $n_1 = 1$ and $n_1 = 0$ are also provided together with their associated asymptotic fields. In each case, the solid curves show the displacement field, whilst the dashed curves show the associated asymptotics in the far field. The dash-dot line in figure 5.6b shows the band edge expansion in the vicinity of $\alpha = 2$. In this case, figure 5.6b corresponds to value of $\alpha \approx 2.017$. There are two symmetric modes (the lowest and highest frequency modes) and a single skew-symmetric mode, as expected from the properties of $\mathcal{G}$ discussed in the previous subsection. However, for defects of mass $r \geq r_{3,1}^{(\max)}$, it is not possible to initiate the lower frequency symmetric eigenmode and only a further symmetric mode and a skew-symmetric mode persist. For values of $r \geq r_{3,2}^{(\max)}$, it is only possible to initiate the highest frequency symmetric mode.

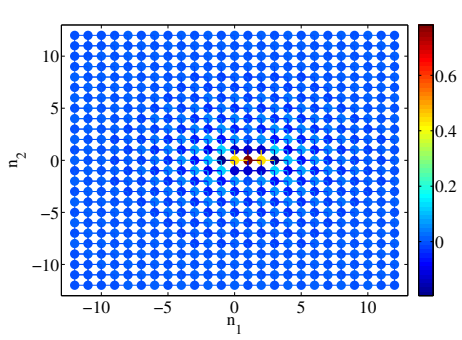


**(a)** Symmetric mode at $\omega = 2.83$

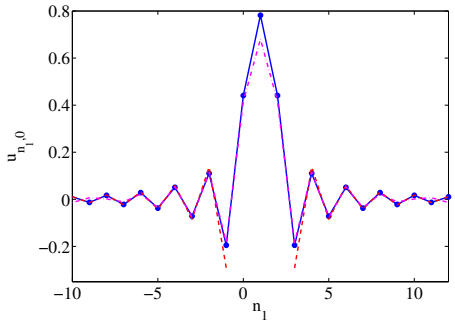


**(b)** The field along the line $n_2 = 0$ for the symmetric mode

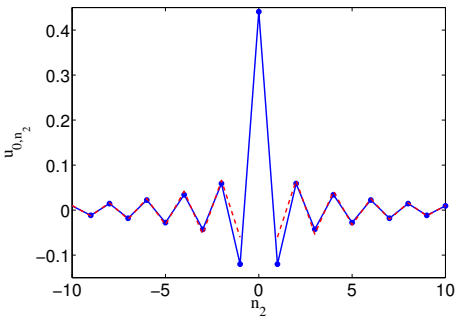


**(c)** The field along the line $n_1 = 0$ for the symmetric mode

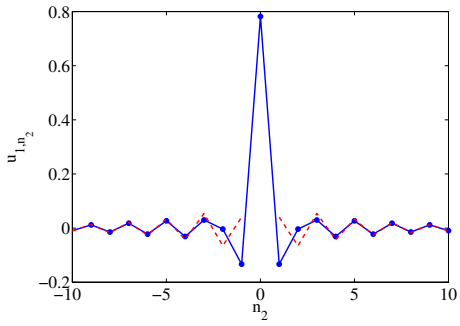


**(d)** The field along the line $n_1 = 1$ for the symmetric mode

**Figure 5.6:** The first localised defect mode for a triplet of defects with $r = 0.4$. The solid curves show the out-of-plane displacement along the indicated line, and the dashed curves are the associated asymptotic expansions in the far field (see equations (5.20) and (5.23) as appropriate). The dash-dot line in (b) corresponds to the band edge expansion (see equation (5.29a)).

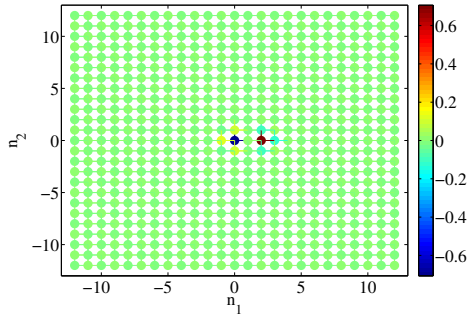


**(a)** Skew-symmetric mode at $\omega = 3.33$

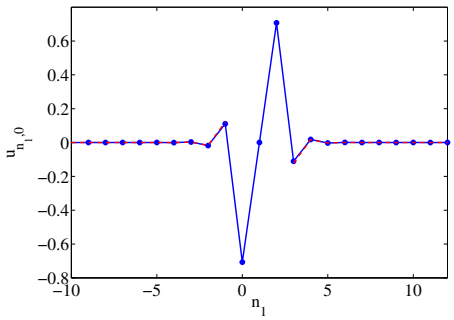


**(b)** The field along the line $n_2 = 0$ for the skew-symmetric mode

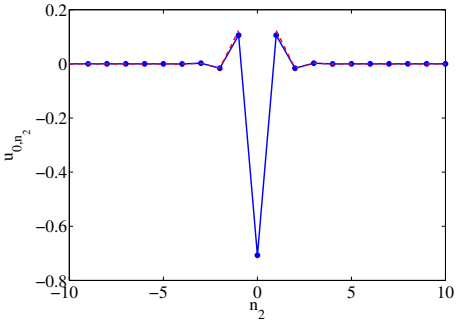


**(c)** The field along the line $n_1 = 0$ for the skew-symmetric mode

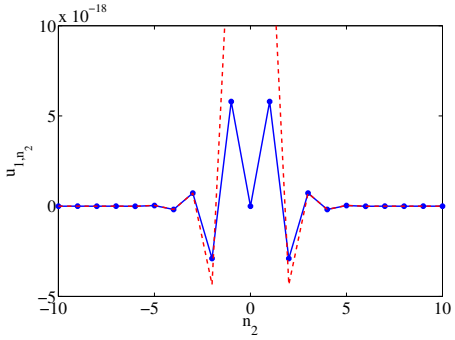


**(d)** The field along the line $n_1 = 1$ for the skew-symmetric mode

**Figure 5.7:** The second localised mode for a triplet of defects. The solid curves show the out-of-plane displacement along the indicated line, and the dashed curves are the associated asymptotic expansions in the far field (see equations (5.20) and (5.23) as appropriate).

## 5.3 An infinite inclusion in an infinite square lattice

The section will be devoted to the discussion of an infinite line of defects embedded in an infinite square lattice, as shown in figure 5.9. As in the previous section, the defects are characterised by a non-dimensional mass $0 < r < 1$. A recent paper by Osharovich and Ayzenberg-Stepanenko [122] studied the waveguide problem for an infinite linear defect embedded in a square lattice. More recently, Colquitt *et al.* [32] studied in detail this precise problem. It should be emphasised that the work reported in section 4 of [32] was primarily carried out by Dr Michael Nieves and not the present author. Therefore, the work detailed in [32, §4] is be briefly recounted here in section 5.3 purely in order to provide context for the following section.

### 5.3.1 The equations of motion

Given the symmetry of the system about the line $n_2 = 0$ (see figure 5.9), it is convenient to reduce the problem to a half-plane system, which may be formulated as follows. The displacement amplitude field for time-harmonic disturbances in the upper-half plane, $\boldsymbol{n} \in \mathbb{Z} \times \mathbb{Z}^+$ is

$$u_{\boldsymbol{n}+\boldsymbol{e}_1} + u_{\boldsymbol{n}-\boldsymbol{e}_1} + u_{\boldsymbol{n}+\boldsymbol{e}_2} + u_{\boldsymbol{n}-\boldsymbol{e}_2} + (\omega^2 - 4)u_{\boldsymbol{n}} = 0, \tag{5.42a}$$

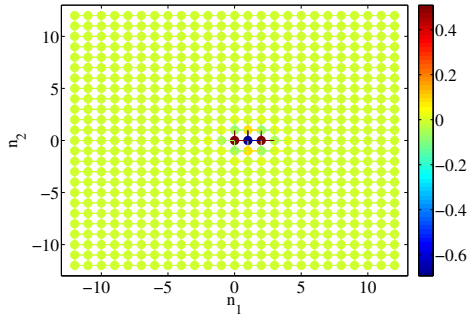


**(a)** The second symmetric mode at $\omega = 3.77$

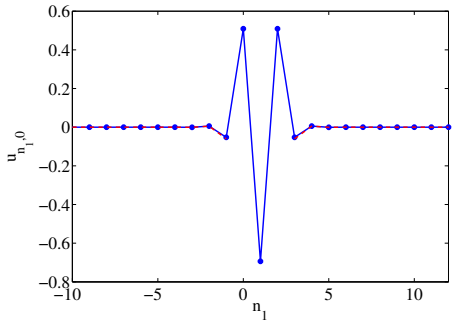


**(b)** The field along the line $n_2 = 0$ for the second symmetric mode

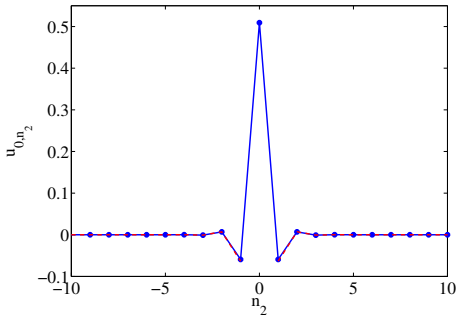


**(c)** The field along the line $n_1 = 0$ for the second symmetric mode

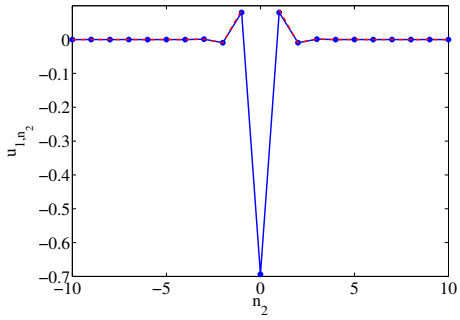


**(d)** The field along the line $n_1 = 1$ for the second symmetric mode

**Figure 5.8:** The third localised defect mode for a triplet of defects. The solid curves are the out-of-plane displacement along the indicated line, and the dashed curves are the associated asymptotic expansions in the far field (see equations (5.20) and (5.23) as appropriate).

and for $n_1 \in \mathbb{Z}$, $n_2 = 0$ is

$$u_{n_1+1,0} + u_{n_1-1,0} + u_{n_1,1} + u_{n_1,-1} + (r\omega^2 - 4)u_{n_1,0} = 0. \tag{5.42b}$$

Taking the discrete Fourier Transform in the $n_1$ direction yields

$$u^{\mathrm{F}}_{n_2+1} + u^{\mathrm{F}}_{n_2-1} - 2\Omega_1(\xi,\omega)u^{\mathrm{F}}_{n_2} = 0, \tag{5.43a}$$

and

$$u^{\mathrm{F}}_{1} + u^{\mathrm{F}}_{-1} - 2\Omega_r(\xi,\omega)u^{\mathrm{F}}_{0} = 0, \tag{5.43b}$$

where

$$\Omega_\beta(\xi,\omega) = 1 + 2\sin^2\left(\frac{\xi}{2}\right) - \frac{\beta\omega^2}{2} \tag{5.44}$$

and $\xi$ is the Fourier parameter. For $n_2 > 1$ a solution of the form

$$u^{\mathrm{F}}_{n_2} = \lambda^{n_2} u^{\mathrm{F}}_{1}, \quad \text{with } |\lambda| \leq 1, \tag{5.45}$$

is sought. The case of $|\lambda| = 1$ corresponds to a displacement field which propagates sinusoidally, with constant amplitude, away from the defect along $n_2 = 0$. The condition $|\lambda| < 1$ corresponds to a localised mode, the amplitude of which, decays exponentially away from the waveguide along

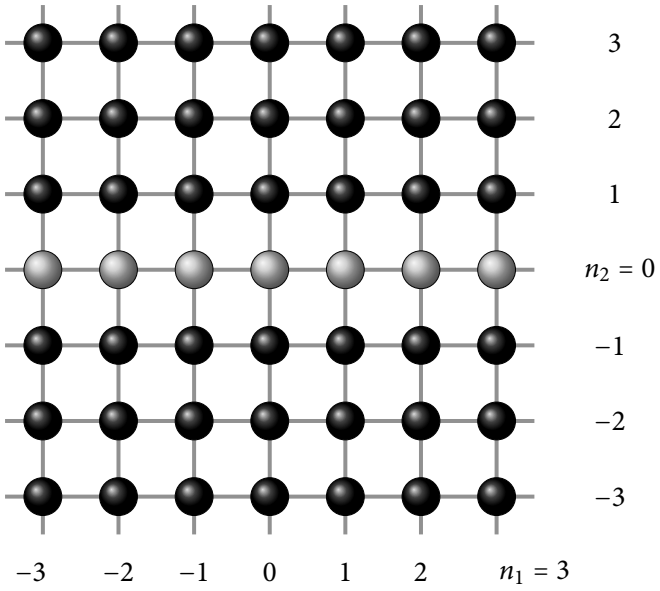


**Figure 5.9:** A square cell lattice containing an infinite chain of defects with non-dimensional mass $r$ along $n_2 = 0$, and an ambient lattice composed of particles with unit mass. As before, the stiffness and length of the links are taken as natural units.

$n_2 = 0$. The primary focus of this chapter is localised modes, therefore the following discussion will be devoted to the latter case of $|\lambda| < 1$. For a detailed analysis of the system, the reader is referred to [32, §4]. Together, equations (5.43a) and (5.45) yield an expression for the factor $\lambda$ corresponding to localised modes

$$\lambda = 1 + 2\sin^2\left(\frac{\xi}{2}\right) - \frac{r\omega^2}{2}. \tag{5.46}$$

**Skew-symmetric solutions.** Consider solutions that are skew-symmetric about the line $n_2 = 0$. These modes satisfy the symmetry condition $u_{n_1,n_2} = -u_{n_1,-n_2}$, whence $u_{n_1,0} = 0$ and hence $u_{\boldsymbol{n}} = 0$. In other words, the only skew-symmetric solution is the trivial one.

**Symmetric solutions.** For the case when symmetry conditions are imposed about $n_2 = 0$, that is $u_{n_1,n_2} = u_{n_1,-n_2}$, the dispersion equation for localised defect modes supported by the infinite line defect is given by

$$\omega^{(-)}(\xi) = \left\{\frac{2}{r(2-r)}\left[1 + 2\sin^2(\xi/2) + \sqrt{1 + 4(1-r)^2\sin^2(\xi/2)(1+\sin^2(\xi/2))}\right]\right\}^{1/2}. \tag{5.47}$$

This dispersion relation is determined in two parts. First, the symmetry conditions are imposed about the line $n_2 = 0$ and a linear system is derived which links the displacements along the rows $n_2 = 0$ and $n_2 = 1$. Then, the solvability of this system is considered for various cases of $\lambda$, and (5.47) is deduced. The reader is referred to [32, §4] for a detailed discussion and derivation of (5.47). In figure 5.10, the dispersion relation (5.47) is plotted for several values of $r$. The in-phase standing wave solution, of the form (5.45), is always given when $\xi = 0$ and corresponds to the minima of the dispersion curves. The frequency of the in-phase standing wave is

$$\omega = \sqrt{\frac{4}{r(2-r)}}, \tag{5.48}$$

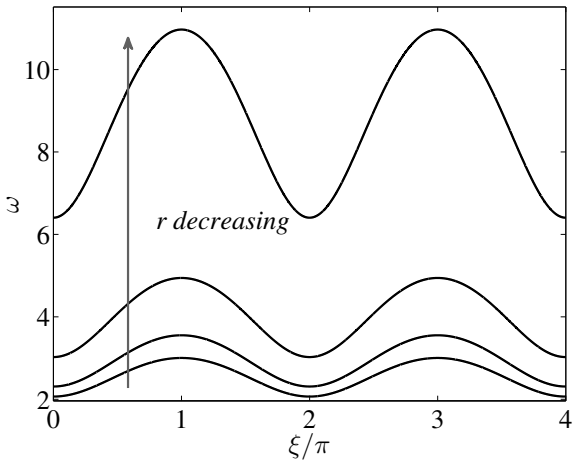


**Figure 5.10:** The quantity $\omega^{(-)}$, given in equation (5.47), plotted as a function of the normalised Bloch parameter $\xi/\pi$ for $r = 0.05, 0.25, 0.5$ and $0.75$.

whereas for the out-of-phase solution, at $\kappa = \pi$ corresponding to the maxima of the dispersion curves, is

$$\omega = \sqrt{\frac{2}{r(2-r)}\left[3 + \sqrt{1 + 8(1-r)^2}\right]}\,. \tag{5.49}$$

## 5.4 From an infinite inclusion to a large finite defect: The case of large $N$

In this section, it will be demonstrated that the range of eigenfrequencies for which localised eigenmodes exist for the model of finite inclusions described in section 5.1, can be predicted using the model of an infinite chain of defects considered in section 5.3. The motivation for this is as follows. In order to determine the frequencies of localised modes, according to the analysis presented in section 5.1, it is required to solve a transcendental equation (e.g. equation (5.33)) for $\omega$. Hence, one must resort to numerical methods. Moreover, the equation in question (the solvability condition (5.12)) is obtained by setting the determinant of a matrix system to zero. For a system of $N$ defects the matrix system is $N \times N$; hence, for a large system of defects, this becomes computationally intensive. However, as will be shown in the current section, if one is merely interested in the range of permitted localised frequencies, this information may be obtained from the dispersion equation of the infinite system.

As an illustrative example, a defect with $N = 20$ particles of non-dimensional mass $r = 0.25$ is embedded within an infinite square lattice. The eigenfrequencies of the finite defect are computed using the method described in section 5.1 and are shown as dash-dot, and dashed, lines in figure 5.11. In this figure, the eigenfrequency $\omega_{\min} = 3.0374$ corresponds to an in-phase standing wave solution, whereas the frequency $\omega_{\max} = 4.9344$ represents the out-of-phase solution. The maximum and minimum eigenfrequencies are indicated by the dashed lines in figure 5.11.

Since $N$ is large, it is useful to consider the model of an infinite chain embedded in a square lattice. Expressions (5.48) and (5.49) predict the values of the frequency $\omega$ for which there exist such solutions. For the numerical values above, the in-phase solution occurs when $\xi = 0$ and $\omega = 3.0237$ and the out-of-phase solution occurs when $\xi = \pi$ and $\omega = 4.9432$. These values of the frequency are close to those encountered in the problem of the finite defect for $N = 20$.

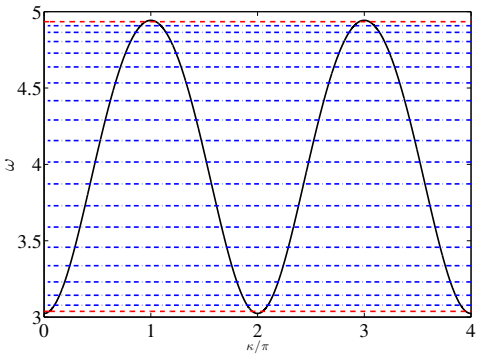


**Figure 5.11:** The dispersion equation (5.47), for the infinite chain, plotted as a function of the normalised Bloch parameter, for $r = 0.25$, represented by the solid curve. Also shown are the blue dash-dot lines corresponding to the eigenfrequencies computed for a finite defect containing $N = 20$ masses. The red dashed lines correspond to $\omega_{\min}$ and $\omega_{\max}$.

Moreover, all the eigenfrequencies computed for the finite defect lie within the passband for the infinite defect, as shown in figure 5.11.

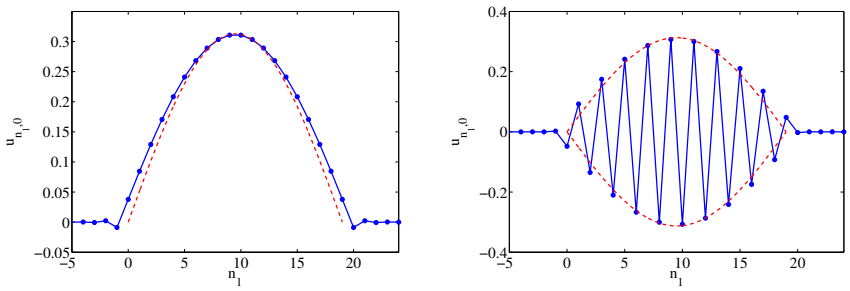


**(a)** In-phase mode at $\omega = 3.037$ **(b)** Out-of-phase mode at $\omega = 4.934$

**Figure 5.12:** The blue solid lines are the eigenmodes for the maximum and minimum eigenfrequencies for a finite line containing 20 defects. The envelope functions defined in (5.56) are shown by the red dashed lines.

Figure 5.12 shows the plot of the eigenmodes for the maximum and minimum eigenfrequencies computed for the line defect containing 20 masses. The maximum eigenfrequency $\omega_{\max}$ corresponds to the out-of-phase mode, whereas the minimum eigenfrequency $\omega_{\min}$ gives the in-phase mode.

It is remarked that both the field in figure 5.12a, and the envelope of the field in figure 5.12b resemble the first eigenmode of an homogenised rectilinear inclusion. Using this motivation, the difference operator

$$\mathcal{D}_{\boldsymbol{p}}\left(\cdot\right)_{\boldsymbol{p}} = \left(\cdot\right)_{\boldsymbol{p}+\boldsymbol{e}_1} + \left(\cdot\right)_{\boldsymbol{p}-\boldsymbol{e}_1} + \left(\cdot\right)_{\boldsymbol{p}+\boldsymbol{e}_2} + \left(\cdot\right)_{\boldsymbol{p}-\boldsymbol{e}_2} - 4\left(\cdot\right)_{\boldsymbol{p}}, \tag{5.50}$$

is introduced. Making use of (5.3), it is found that

$$\left(\frac{\mathcal{D}_{n_1,0}}{\omega^2} + 1\right) u_{n_1,0} = (1-r) \sum_{p=0}^{N-1} u_{p,0} \left(\mathcal{D}_{n_1,0} + \omega^2\right) g(n_1, 0, p; \omega), \tag{5.51}$$

where $\boldsymbol{n} = (n_1, n_2)$ has been restricted to $\{\boldsymbol{n} : 0 \le n_1 \le N-1,\ n_2 = 0\}$. Since the lattice Green's matrix is a difference kernel (i.e. depends on the difference $|n_1 - p|$),

$$\left(\frac{\mathcal{D}_{n_1,0}}{\omega^2} + 1\right) u_{n_1,0} = (1-r) \sum_{p=0}^{N-1} u_{p,0} \left(\mathcal{D}_{p,0} + \omega^2\right) g(n_1, 0, p; \omega), \tag{5.52}$$

whence, and recalling from (5.1) that $(\mathcal{D}_{\boldsymbol{n}} + \omega^2)g(\boldsymbol{n}, p, \omega) = \delta_{n_1,p}\delta_{n_2,0}$, it is found that

$$(\mathcal{D}_{\boldsymbol{n}} + r\omega^2)u_{\boldsymbol{n}} = 0, \quad \text{for} \quad \boldsymbol{n} \in \{\boldsymbol{n} : 0 \leq n_1 \leq N-1,\ n_2 = 0\}. \tag{5.53}$$

It is observed that for a sufficiently large inclusion, the field above and below the inclusion behaves as $u_{n_1,1} = u_{n_1,-1} \approx \lambda u_{n_1,0}$, with $|\lambda| < 1$, in a similar manner to the infinite inclusion. Hence, using (5.53) together with the aforementioned approximation yields

$$u_{n_1+1,0} + u_{n_1-1,0} - 2u_{n,0} + \left[r\omega^2 - 2\left(1-\lambda\right)\right]u_{n_1,0} = 0, \tag{5.54}$$

for $0 \leq n_1 \leq N-1$. The first three terms on the left hand side of (5.54) correspond to the second order central difference operator. Hence, introducing the continuous variable $\eta = n_1$ (where the reader is reminded that the length of the lattice links has been normalised to unity) equation (5.54) is written as

$$\left[\frac{d^2}{d\eta^2} + r\omega^2 - 2\left(1-\lambda\right)\right]u(\eta) = 0. \tag{5.55}$$

The form of equation (5.55) suggests that the homogenised system is analogous to a string on an elastic foundation, with the constant $2\left(1-\lambda\right)$ characterising the effective stiffness of the foundation. It is emphasised that $|\lambda| < 1$ and as such, the stiffness of the elastic foundation is positive.

Consider the problem of an infinite inclusion. According to equation (5.46), the value of $\lambda$ corresponding to the lowest eigenmode is $\lambda = 1 - r\omega^2/2$. For this value of $\lambda$, the second order derivative vanishes according to equation (5.55). Moreover, for the displacement at infinity to be finite, $u(\eta)$ must be constant for all $\eta$. In this case, the solution of the infinite waveguide problem (5.42) (i.e. $u_{n_1,0} = \text{const.}$) is obtained.

For the finite inclusion, it is observed that the displacements at the endpoints are small (see figure 5.12a). Hence, for a simple estimate it suffices to impose $u(0) = u(N-1) = 0$ whence the solution to (5.55) is

$$u(\eta) = u_0 \sin\left(\eta\sqrt{r\omega^2 - 2(1-\lambda)}\right), \text{ with } \lambda = 1 + \frac{1}{2}\left[\left(\frac{q\pi}{N-1}\right)^2 - r\omega^2\right], \tag{5.56}$$

where $q$ is an odd number and $u_0$ an arbitrary scaling constant. The first eigenmode corresponds to $\lambda = -0.1396$, which is close to the mean value of $\lambda$ obtained from the full numerical computation ($\lambda = -0.1426$). The approximation (5.56) for $\lambda = -0.1396$ is shown in figure 5.12a by the red dashed line. The same approximation is used to produce the envelope function shown by the dashed lines in figure 5.12b. One can observe that this, relatively simple, homogenised model predicts the envelope of the field very well.

## 5.5 Remarks

In this chapter the problem of localised vibrations around a finite rectilinear defect embedded in an infinite square lattice has been discussed in detail. The waveguide problem for an infinite defect has also been briefly described and a comparative analysis of the two classes of problems

has been presented.

Although the physical configurations and the methods of analysis of these problems are different, one can observe remarkable properties of solutions, which can be used to make a strong connection. As illustrated in figure 5.11, the pass band for frequencies of waveguide modes, localised around an infinite chain of masses in a square lattice, contains all eigenmodes describing vibrations localised around a rectilinear defect built of a finite number of masses embedded into the lattice.

In particular, the reader's attention is drawn to the band edges of the dispersion diagram for the infinite defect: figure 5.11 shows that the frequencies of the eigenmodes for a finite line defect are distributed non-uniformly and they cluster around the edges of the pass band identified for the infinite waveguide. Furthermore the limit, as one approaches the band edge frequency, corresponds to a homogenisation approximation of the linear defect as an inclusion embedded into a homogenised ambient system. The illustrative numerical simulation is produced for an array of 20 masses. It is emphasised that the effect shown is generic and, with an increased number of masses, the density of frequencies of localised modes near the band edges increases.

Symmetric and skew-symmetric modes have been constructed and analysed for a rectilinear "*inclusion*" built of a finite number of masses embedded into the lattice. It has also been shown that the total force exerted on the ambient by the vibrating discrete inclusion is zero for all skew-symmetric modes. Consequently, the displacement fields, associated with skew-symmetric modes, decay at infinity like dipoles, vanishing faster than the displacements corresponding to symmetric modes. This follows from the analytical representations for the solutions and illustrated in figures 5.5 and 5.6 where the skew-symmetric modes appear to be localised to a much higher degree than symmetric modes. In the aforementioned numerical simulations, the skew-symmetric and symmetric modes appear in pairs, and the frequency of the skew-symmetric mode is higher than the frequency of the corresponding symmetric mode. With reference to figure 5.3 it is also observed that, in contrast to the one- and three-dimensional multi-atomic cases, there is no lower bound on the perturbation of mass required to initiate a localised mode.

Finally, the reader's attention is drawn to the symmetric and skew-symmetric eigenmodes for a chain of 20 masses shown in figure 5.12. The corresponding frequencies are the maximum and minimum values in the array of frequencies associated with horizontal lines of figure 5.11. The envelope curves for both diagrams in figure 5.12 represent the first eigenmode of a homogenised rectilinear inclusion. The simple homogenised model presented in section 5.4 provides the envelope curves for the finite inclusion. The form of the homogenised system suggests that, macroscopically, the inclusion behaves as a string on an elastic foundation. As expected, the skew-symmetric mode of figure 5.12b has the higher frequency than the symmetric mode of figure 5.12a.

# *Chapter Six*

# Thermal striping of a micro-structured edge-cracked solid

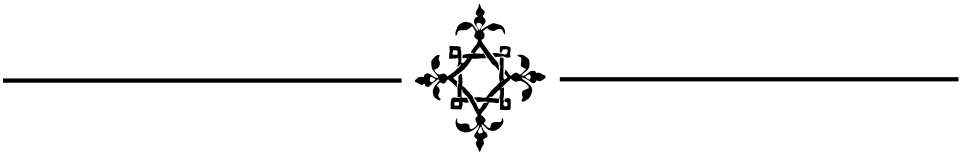

Having studied static inclusions in scalar lattices, the current chapter will be devoted to the analysis of the response of a triangular lattice and a continuum containing a conducting finite edge crack under sinusoidal thermal loading. The material parameters of the continuum are chosen such that they correspond to the homogenised lattice. The response of the lattice to the uncoupled thermoelastic problem is examined and the notion of an *"effective stress intensity factor"* is introduced using the crack opening displacements behind the crack tip. The *"effective stress intensity factor"* is then compared with the stress intensity factor for an edge-cracked continuum obtained by use of a J-integral derived for formulations of uncoupled thermoelasticity.

## 6.1 Crack-tip fields and the J-integral

For the purpose of the present chapter, it will be necessary to evaluate the stress intensity factor for an edge crack in a two-dimensional elastic body under the assumptions of plane strain. The stress intensity factor provides a convenient measure of the stress state in the vicinity of the crack tip. Indeed, stress intensity factors are often incorporated into fracture criteria. One such fracture criteria is Paris' law [124], which has found extensive use in problems related crack growth under fatigue. The scholarly literature on fracture mechanics, and particularly fracture in linear elasticity, is very well developed. For a more detailed discussion of fracture mechanics, the reader is referred to [6, 15, 59, 64, 146] and references therein.

Consider a semi-infinite crack $\gamma = \{\boldsymbol{x} : -\infty < x_1 < 0,\, x_2 = 0\}$ in $\mathbb{R}^2$ as shown in figure 6.1. The stresses in the vicinity of the crack-tip ($\boldsymbol{x} = \boldsymbol{0}$) are singular. In particular, to leading order the stresses in the vicinity of the crack tip are of the form (see, for example, [15, 124])

$$\sigma_{ij} \sim \frac{f_{ij}(\theta)}{\sqrt{r}}, \tag{6.1}$$

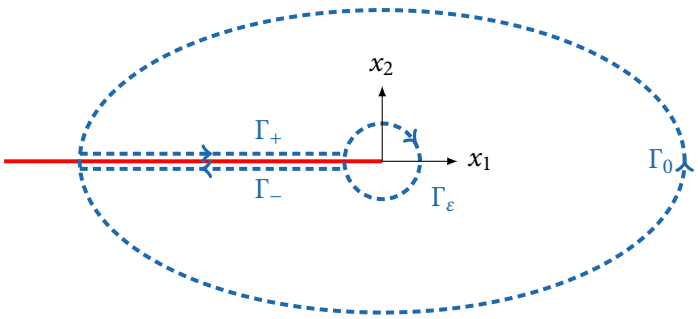


**Figure 6.1:** A semi-infinite crack (solid red line) defined by the set $\gamma = \{\boldsymbol{x} : -\infty < x_1 < 0,\ x_2 = 0\}$ embedded in an elastic body. The dashed blue lines indicate the contours of integration.

where $r$ and $\theta$ are the polar distance and angle respectively. In the present chapter, it will be sufficient to consider mode I loading. Under mode I loading, the crack opening displacements are odd with respect to $x_2$ [65] such that $u_2(x_1, x_2) = -u_2(x_1, -x_2)$; the displacements parallel to the crack are even: $u_1(x_1, x_2) = u_1(x_1, -x_2)$. According to the definition given by Irwin [64], the mode I stress intensity factor is

$$K_I = \lim_{r\to 0} \sqrt{2\pi r}\sigma_{\theta\theta}(r, 0). \tag{6.2}$$

To leading order, the normal stress ahead of the crack tip can then be written as

$$\sigma_{\theta\theta}|_{\theta=0} \sim \frac{K_I}{\sqrt{2\pi r}}. \tag{6.3}$$

In general the leading order stresses can be expressed as

$$\sigma_{rr} \sim \frac{K_I}{\sqrt{2\pi r}} \cos\frac{\theta}{2}\left(1 + \sin^2\frac{\theta}{2}\right), \quad \sigma_{\theta\theta} \sim \frac{K_I}{\sqrt{2\pi r}} \cos^3\frac{\theta}{2}, \quad \sigma_{r\theta} \sim \frac{K_I}{\sqrt{2\pi r}} \sin\frac{\theta}{2}\cos^2\frac{\theta}{2}, \tag{6.4}$$

with $\sigma_{zz} = \nu(\sigma_{rr} + \sigma_{\theta\theta})$.

### 6.1.1 The J-integral

The J-integral provides a convenient method through which the stress intensity factor for a notch or crack may be evaluated. The J-integral is a path independent energetic contour integral and was developed independently by Cherepanov [26] and Rice [134] in the late 1960's. A detailed development of the J-integral may be found, for example, in the initiating two papers [26, 134] or classical reference texts such as [15] among many others.

Consider a crack, defined by the set $\gamma = \{\boldsymbol{x} : -\infty < x_1 < 0,\ x_2 = 0\}$, embedded in a linearly elastic medium and oriented as illustrated in figure 6.1. The J-intgeral introduced by Rice can be written in the form

$$J_i = \int_\Gamma \left(Wn_i - \sigma_{jk}n_j u_{k,i}\right) \mathrm{d}s, \tag{6.5}$$

where $W$ is the strain energy density functional, $n_i$ is the $i^{\text{th}}$ component of the outward unit normal to some arbitrary closed contour $\Gamma$, index summation notation is used and subscript commas followed by indices indicate differentiation. Here, $J_i$ represents the $i^{\text{th}}$ component of

the J-integral, corresponding to crack opening displacements in the $x_i$ direction. Application of Green's theorem yields integration over the region enclosed by $\Gamma$

$$J_i = \int_\Omega \frac{\partial}{\partial x_j}\left(W\delta_{ij} - \sigma_{jk}u_{k,i}\right)\mathrm{d}A. \tag{6.6}$$

In the absence of body forces the equilibrium equation is $\sigma_{ji,j} = 0$, whence $\left(\sigma_{jk}u_{k,i}\right)_{,j} = \sigma_{jk}u_{k,ij}$. Moreover, for sufficiently smooth $\boldsymbol{u}$, $\sigma_{kl}\varepsilon_{kl,i} = \frac{1}{2}\left(\sigma_{kl}u_{k,li} + \sigma_{lk}u_{k,li}\right) = \sigma_{kl}u_{l,ik}$ since $\boldsymbol{\sigma}$ is symmetric. Thus,

$$J_i = \int_\Omega \left(W_{,j}\delta_{ij} - \sigma_{kl}\varepsilon_{kl,i}\right)\mathrm{d}A. \tag{6.7}$$

For elastic material the stress is related to the energy strain functional by $\sigma_{kl} = \frac{\partial W}{\partial \varepsilon_{kl}}$, hence $\frac{\partial W}{\partial x_i} = \frac{\partial W}{\partial \varepsilon kl}\varepsilon_{kl,i}$ and finally

$$J_i = \int_\Omega \left(\sigma_{kl}\varepsilon_{kl,i} - \sigma_{kl}\varepsilon_{kl,i}\right)\mathrm{d}A = 0. \tag{6.8}$$

Thus, the J-integral vanishes around any closed contour which encloses a simply connected region without any stress singularities[1]. Moreover, it may be shown that if the crack faces are traction free, then the J-integral is path-independent.

The fact that the J-integral vanishes over an appropriate contour allows convenient determination of the stress intensity factor. Consider now the contour $\Gamma = \Gamma_0 \cup \Gamma_+ \cup \Gamma_- \cup \Gamma_\varepsilon$ as shown in figure 6.1. In particular, let $\Gamma_\varepsilon = \{\boldsymbol{x} : |\boldsymbol{x}| < \varepsilon\}$, where $\varepsilon \to 0$ but $\Gamma_0$ be arbitrary. Since the J-integral vanishes over $\Gamma$

$$\int_{\Gamma_0}\left(Wn_i - \sigma_{jk}n_ju_{k,i}\right)\mathrm{d}s + \int_{\Gamma_+}\left(Wn_i - \sigma_{jk}n_ju_{k,i}\right)\mathrm{d}s + \int_{\Gamma_-}\left(Wn_i - \sigma_{jk}n_ju_{k,i}\right)\mathrm{d}s + \int_{\Gamma_\varepsilon}\left(Wn_i - \sigma_{jk}n_ju_{k,i}\right)\mathrm{d}s = 0. \tag{6.9}$$

Evaluating the integral over $\Gamma_\varepsilon$ it is found that, in the case of plane strain and mode I loading (setting $i = 1$),

$$K_I^2 = \frac{E}{1-\nu^2}\int_{\Gamma_0}\left(Wn_1 - \sigma_{jk}n_ju_{k,1}\right)\mathrm{d}s - \frac{E}{1-\nu^2}\int_{\Gamma_+\cup\Gamma_-}\sigma_{jk}n_ju_{k,1}\mathrm{d}s, \tag{6.10}$$

where the fact that the contribution of $n_1$ vanishes over $\Gamma_+ \cup \Gamma_-$ has already been used. Hence, the stress intensity factor for mode I loading can be determined by evaluating the integral over the remote contour $\Gamma_0$ and an integral involving the tractions and derivative of displacements over the crack faces. Moreover, if the crack faces are traction free such that $\sigma_{ji}n_j = 0$, then the final integral vanishes and the *J* integral becomes path-independent.

[1]Hereinafter *appropriate contour*.

**Modifying the J-integral**

In the present chapter, the J-integral method is used to compute the stress intensity factor for a quasi-static[2] thermoelastic problem. However, care is required when treating thermoelastic problems using the J-integral. In particular, it was demonstrated by Wilson and Yu [147] that the J-integral as defined by Rice [134] does not vanish around an appropriate contour for thermoelastic problems. The non-trivial nature of the J-integral may be easily demonstrated by noting that, for a two-dimensional linearly elastic isotropic body under a quasi-static thermal load, the stress-strain relationship in plane strain is

$$\sigma_{ij} = \lambda\varepsilon_{ii}\delta_{ij} + 2\mu\varepsilon_{ij} - \frac{E\alpha}{1-2\nu}T\delta_{ij}, \tag{6.11}$$

where $T(\boldsymbol{x};t)$ is the temperature field and $\alpha$ is the coefficient of linear thermal expansion. The first and second Lamé parameters are denoted by $\lambda$ and $\mu$ respectively and are related to Young's modulus and Poisson's ratio by $\lambda = \frac{E\nu}{(1+\nu)(1+2\nu)}$ and $\mu = \frac{E}{2(1+\nu)}$. The first two terms in the expression are the standard expressions for plane strain linear isotropic homogeneous elasticity and the analysis presented in the previous section leading to equation (6.8) follows through exactly. However, the final term on the right hand side of (6.11) yields an area integral leading to a non-vanishing J-integral

$$J_i = \frac{E\alpha}{1-2\nu}\int_{\Omega}\left[T_{,i}\varepsilon_{jj} - \frac{1}{2}(T\varepsilon_{jj})_{,i}\right]\mathrm{d}A. \tag{6.12}$$

Thus, in contrast to the standard elastic case, the stress intensity factor cannot be determined by a line integral over an appropriate remote contour. Instead, an additional area integral must be evaluated. In this case, equation (6.10) takes the form

$$K_I^2 = \frac{E}{1-\nu^2}\int_{\Gamma_0}\left(Wn_1 - \sigma_{jk}n_j u_{k,1}\right)\mathrm{d}s + \frac{E^2\alpha}{(1-\nu^2)(1-2\nu)}\int_{\Omega}\left[T_{,i}\varepsilon_{jj} - \frac{1}{2}(T\varepsilon_{jj})_{,i}\right]\mathrm{d}A, \tag{6.13}$$

where the crack faces are assumed to be traction free for convenience. By means of Green's theorem equation (6.13) may be written

$$K_I^2 = \frac{E}{1-\nu^2}\int_{\Gamma_0}\left(Wn_1 - \frac{E\alpha}{2(1-2\nu)}T\varepsilon_{jj} - \sigma_{jk}n_j u_{k,1}\right)\mathrm{d}s + \frac{E^2\alpha}{(1-\nu^2)(1-2\nu)}\int_{\Omega}\varepsilon_{jj}\frac{\partial T}{\partial x_1}\mathrm{d}A. \tag{6.14}$$

The first integral on the right hand side of equation (6.14) is the so-called *J*-integral* introduced by Wilson and Yu [147].

It should be emphasised that here, $\sigma_{ij}$ is the thermoelastic stress tensor (6.11) and $W$ is the corresponding energy density functional; $\Omega$ is the area enclosed by $\Gamma_0$. The integral in (6.13) as well as the alternative integrals presented by Wilson and Yu [147] require evaluation of the derivatives of strain, which may be numerically challenging, particularly in the vicinity of the crack tip. However, the representation (6.14) requires only derivatives of the temperature field,

[2]Quasi-static in the sense that no inertia term appears in the equations of motion, but the temperature field may depend, parametrically, on time

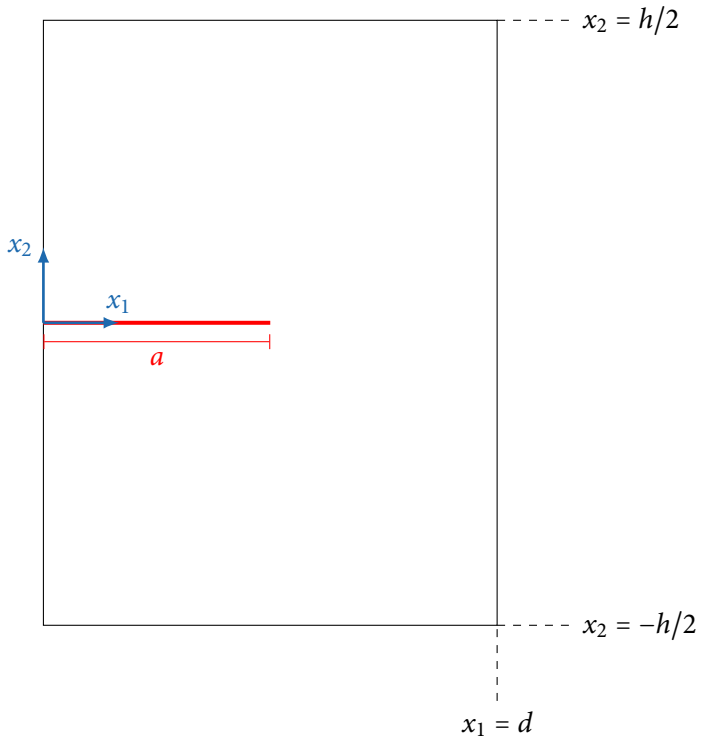


**Figure 6.2:** A finite edge-crack (solid red line) defined by the set $M_a = \{\boldsymbol{x} : 0 \le x_1 \le a,\ x_2 = 0\}$ embedded in an elastic body $\Omega = \{\boldsymbol{x} : 0 < x_1 < d,\ |x_2| < h/2\}$.

which for the present application, are known analytically and are smooth.

## 6.2 The uncoupled thermoelastic problem

In the continuum, the thermal striping problem for the rectangle $\Omega = \{\boldsymbol{x} : 0 < x_1 < d,\ |x_2| < h/2\}$, containing a finite edge crack $M_a = \{\boldsymbol{x} : 0 \le x_1 \le a,\ x_2 = 0\}$, with the crack faces $M_a^{\pm}$ (see figure 6.2), satisfies the following problem for the elastic displacement field $\boldsymbol{U}(\boldsymbol{x}; t)$:

$$\mathcal{L}\boldsymbol{U}(\boldsymbol{x}; t) = \alpha(3\lambda + 2\mu)\nabla T(\boldsymbol{x}; t), \qquad \boldsymbol{x} \in \Omega \setminus M_a, \tag{6.15a}$$

$$\boldsymbol{\sigma}^{(\boldsymbol{n})}[\boldsymbol{U}](\boldsymbol{x}; t) = \alpha(3\lambda + 2\mu)\boldsymbol{n}T(\boldsymbol{x}; t), \qquad \boldsymbol{x} \in B_0 \cup B_d \cup M_a^{+} \cup M_a^{-}, \tag{6.15b}$$

$$\boldsymbol{U}(\boldsymbol{x}; t) = \boldsymbol{0}, \qquad \boldsymbol{x} \in \{\boldsymbol{x} : 0 < x_1 < d, |x_2| = h/2\}, \tag{6.15c}$$

where $\mathcal{L}\boldsymbol{U} = \mu\Delta\boldsymbol{U} + (\lambda + \mu)\nabla\nabla\cdot\boldsymbol{U}$, $B_r = \{\boldsymbol{x} : x_1 = r,\ |x_2| < h/2\}$, $\lambda$ and $\mu$ are the Lamé coefficients and $\alpha$ is the coefficient of linear thermal expansion. The differential operator of tractions is denoted by $\boldsymbol{\sigma}^{(\boldsymbol{n})}[\boldsymbol{U}] = \{\lambda(\nabla\cdot\boldsymbol{U})\mathbb{I} + \mu\{\nabla\boldsymbol{U} + (\nabla\boldsymbol{U})^{\mathrm{T}}\}\}\boldsymbol{n}$, with $\boldsymbol{n}$ being the outward unit normal and $\mathbb{I}$ being the $2 \times 2$ identity matrix. Physically, system (6.15) corresponds to the uncoupled thermoelastic problem on a finite plate of width $d$ and height $h$. The plate is clamped on the horizontal boundaries ($|x_2| = h/2$) and mechanically free on the lateral boundaries ($x_1 = 0,\ d$). The solution $\boldsymbol{U}(\boldsymbol{x}; t)$ is then the elastic displacement for a given temperature field $T(\boldsymbol{x}; t)$. The problem is uncoupled in the sense that, in the elastic problem, the time $t$ is treated as a parameter and $T(\boldsymbol{x}; t)$ is the solution of an appropriate heat conduction problem (see (6.19)).

Consider a uniform triangular meshing of $\mathbb{R}^2$ with nodes at discrete positions $\boldsymbol{x}_{\boldsymbol{m}} = \ell\mathcal{T}\boldsymbol{m}$,

where $\boldsymbol{m} \in \mathbb{Z}^2$ labels the nodes separated by distance $\ell$ and

$$\mathcal{T} = \begin{pmatrix} 1 & 1/2 \\ 0 & \sqrt{3}/2 \end{pmatrix}. \tag{6.16}$$

The reader is referred to section 2.1 for further details and clarification of notation. It is convenient to introduce the following sets of nodes

Interior nodes: $$\Gamma = \left\{ \boldsymbol{m} : 0 < x_1(\boldsymbol{m}) < d,\ |x_2(\boldsymbol{m})| < \frac{h}{2} \right\},$$

Lateral boundaries: $$\gamma_0 = \left\{ \boldsymbol{m} : 0 \le x_1(\boldsymbol{m}) \le \frac{\ell}{2}, |x_2(\boldsymbol{m})| \le \frac{h}{2} \right\},$$

$$\gamma_d = \left\{ \boldsymbol{m} : d - \frac{\ell}{2} \le x_1(\boldsymbol{m}) \le d, |x_2(\boldsymbol{m})| \le \frac{h}{2} \right\},$$

Horizontal boundaries: $$\gamma_h = \left\{ \boldsymbol{m} : \ell/2 < x_1(\boldsymbol{m}) < d - \frac{\ell}{2}, |x_2(\boldsymbol{m})| = \frac{h}{2} \right\}.$$

In addition, the set containing the lattice nodes on the crack faces is denoted as $M_a^L = \{\boldsymbol{m} : 0 \le x_1(\boldsymbol{m}) \le a,\ -\sqrt{3}\ell/2 \le x_2(\boldsymbol{m}) \le 0\}$, and the set of nodes connected to node $\boldsymbol{m}$ is written $\mathcal{N}_{\boldsymbol{m}} = \{\boldsymbol{q} : |\boldsymbol{x}(\boldsymbol{m}+\boldsymbol{q}) - \boldsymbol{x}(\boldsymbol{m})| = \ell\} \setminus M_a^L$. The problem for the in-plane elastic displacement $\boldsymbol{u}_{\boldsymbol{m}}$ of a thermally striped lattice with a finite edge crack is then (see § 2.2.6)

$$\sum_{\boldsymbol{q}\in\mathcal{N}_{\boldsymbol{m}}} \boldsymbol{B}(\boldsymbol{q}) \left\{ \boldsymbol{u}_{\boldsymbol{m}+\boldsymbol{q}}(t) - \boldsymbol{u}_{\boldsymbol{m}}(t) \right\} = \frac{\alpha\ell}{2} \sum_{\boldsymbol{q}\in\mathcal{N}(\boldsymbol{m})} \boldsymbol{b}(\boldsymbol{q}) \left\{ \Theta_{\boldsymbol{m}+\boldsymbol{q}}(t) + \Theta_{\boldsymbol{m}}(t) \right\}, \boldsymbol{p} \in \Gamma, \tag{6.17a}$$

$$\boldsymbol{u}_{\boldsymbol{m}}(t) = \boldsymbol{0}, \boldsymbol{m} \in \gamma_h, \tag{6.17b}$$

where $\Theta_{\boldsymbol{m}}(t)$ is the temperature at node $\boldsymbol{m}$ at time $t$. The matrices $\boldsymbol{B}(\boldsymbol{q})$ and vectors $\boldsymbol{b}(\boldsymbol{q})$ describe the direction of interaction between lattice nodes $\boldsymbol{m}+\boldsymbol{q}$ and $\boldsymbol{m}$. In particular

$$\boldsymbol{B}(\boldsymbol{q}) = \begin{pmatrix} \cos^2\varphi & \cos\varphi\sin\varphi \\ \cos\varphi\sin\varphi & \sin^2\varphi \end{pmatrix}, \quad \boldsymbol{b}(\boldsymbol{q}) = \begin{pmatrix} \cos\varphi \\ \sin\varphi \end{pmatrix}, \tag{6.18}$$

where $\varphi$ is the angle between the point $\mathcal{T}\boldsymbol{q}$ and the positive $x_1$-axis. Physically, problem (6.17) corresponds to a triangular array of thin conducting rods connected via pin-joints. In the language of earlier sections, the lattice nodes interact via the central interaction (see § 2.2.3). The variation of temperature from some "stress free" reference configuration creates elastic strains within the rods.

It is remarked that in problem (6.17), the equation of motion is independent of the stiffness of the lattice links. This may, initially, appear to be counter-intuitive. However, it is emphasised that this is a quasi-static problem, that is, there is no inertia term. The variation in temperature between two lattice nodes generates a strain in the lattice link connecting the two nodes. The stress generated by the thermal strain and the stress generated by the nodal displacements are both proportional to the stiffness of the link, hence, the absence of any elastic parameters in the equilibrium equation (6.17a).

## 6.3 The heat conduction problem

Time-harmonic fluctuations in temperature are studied in the present section. Therefore, it is convenient to formulate the heat conduction problem in terms of the complex amplitudes: $\theta(\boldsymbol{x})$ for the continuum and $\vartheta_{\boldsymbol{m}}$ for the lattice. The continuum amplitude satisfies the following problem on the rectangle $\Omega = \{\boldsymbol{x} : 0 < x_1 < d,\ |x_2| < h/2\}$

$$\kappa\Delta\theta(\boldsymbol{x}) = i\omega\theta(\boldsymbol{x}), \qquad \boldsymbol{x} \in \Omega, \tag{6.19a}$$

$$\theta(\boldsymbol{x}) = T_0, \qquad \boldsymbol{x} \in \{\boldsymbol{x} : x_1 = 0,\ |x_2| \le h/2\}, \tag{6.19b}$$

$$\theta(\boldsymbol{x}) = 0, \qquad \boldsymbol{x} \in \{\boldsymbol{x} : x_1 = d\,|x_2| \le h/2\}, \tag{6.19c}$$

$$\nabla[\theta(\boldsymbol{x})] \cdot \boldsymbol{n} = 0, \qquad \boldsymbol{x} \in \{\boldsymbol{x} : 0 < x_1 < d,\ |x_2| = h/2\}, \tag{6.19d}$$

where $\omega$ is the radian frequency of the thermal load and $\kappa$ is the thermal diffusivity of $\Omega$. Physically (6.19) corresponds to the time-harmonic thermal striping of a finite conducting rectangle by a sinusoidal load applied to the left face $x_1 = 0$. The right face $x_1 = d$ is isothermal, whilst the upper and lower faces $x_2 = \pm h/2$ are adiabatic. The crack is perfectly conducting. The boundary value problem (6.19) has the following unique solution

$$\theta(x_1) = T_0 \frac{\sinh[(1+i)\beta(d-x_1)]}{\sinh[(1+i)\beta d]}, \tag{6.20}$$

where $\beta^2 = \omega/2\kappa$.

Similarly, the time-harmonic heat conduction problem on a finite lattice can be written in terms of the discrete complex amplitude $\vartheta_{\boldsymbol{m}}$ (see §2.2.2)

$$\vartheta_{\boldsymbol{m}} = \frac{1}{i\omega\Xi + |\mathcal{N}(\boldsymbol{m})|} \sum_{\boldsymbol{q}\in\mathcal{N}(\boldsymbol{m})} \vartheta_{\boldsymbol{m}+\boldsymbol{q}}, \qquad \boldsymbol{m} \in \Gamma, \tag{6.21a}$$

$$\vartheta_{\boldsymbol{m}} = T_0, \qquad \boldsymbol{m} \in \gamma_0, \tag{6.21b}$$

$$\vartheta_{\boldsymbol{m}} = 0, \qquad \boldsymbol{m} \in \gamma_d, \tag{6.21c}$$

$$\vartheta_{\boldsymbol{m}} = \frac{1}{|\mathcal{N}(\boldsymbol{m})|} \sum_{\boldsymbol{q}\in\mathcal{N}(\boldsymbol{m})} \vartheta_{\boldsymbol{m}+\boldsymbol{q}}, \qquad \boldsymbol{m} \in \gamma_h, \tag{6.21d}$$

here $\Xi = C\ell/(S\lambda)$ and $\mathcal{N}(\boldsymbol{p}) = \{\boldsymbol{q} : |\boldsymbol{x}(\boldsymbol{p}+\boldsymbol{q}) - \boldsymbol{x}(\boldsymbol{p})| = \ell\}$ denotes the set of nodes connected to node $\boldsymbol{p}$, with $\boldsymbol{q} \in \mathbb{Z}^2$. Physically, problem (6.21) describes heat conduction through an array of masses of heat capacity $C$ connected by massless conducting links of thermal conductivity $\lambda$, cross-sectional area $S$ and length $\ell$. Neglecting the mass of the conducting links (equivalently the heat capacity of the links) results in a constant temperature gradient along the rods. The reader is referred to section 2.2.2 for discussion of the fundamental interaction matrices for heat conduction. For a direct comparison with the continuum solution (6.20) the ratio $\Xi$ should be chosen such that the homogenised problem corresponds to the continuum heat conduction problem (6.19). In particular, choosing $\Xi = \ell^2\sqrt{3}/\kappa$ means that the homogenised limit of the lattice problem (6.21), corresponds to the continuum problem (6.19).

The lattice conduction problem (6.21) is formally equivalent to a finite difference problem on a triangular mesh and is therefore amenable to the associated numerical techniques. The Gauss-

Seidel iterative method is used to solve (6.21). The numerical solution reveals that the heat flow is approximately one-dimensional. Indeed, for the frequency range in question, the variation in the solution with $x_2$ is below 1% of the striping amplitude. Figure 6.3 shows a comparison of the temperature solution as a function of distance from the striped face for three characteristic striping frequencies. The three striping frequencies chosen characterise the typical range found in a model test rig of a prototype fast reactor [77]. The comparison indicates that the temperature distribution on lattice approximates the continuum temperature distribution very well. Therefore, for the current regime, it is appropriate to impose the continuum temperature distribution (6.20) for the uncoupled thermoelastic problem in both the continuum and a sufficiently refined lattice.

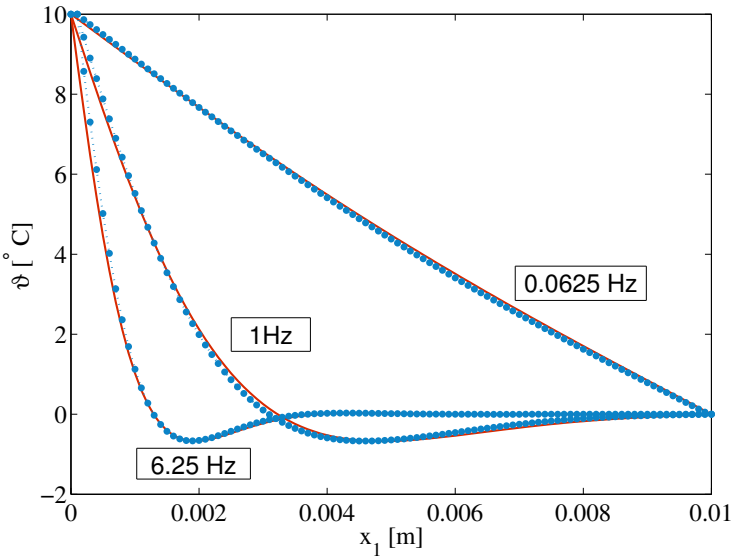


**Figure 6.3:** The solutions to the heat conduction problem in the continuum (6.19) (solid red curve) and the heat conduction problem in the lattice (6.21) (dashed blue curve) as a function of $x_1$ (depth through the plate). The lattice links are of length $\ell = 1 \times 10^{-4}$m.

| Parameter | | |
|---|---|---|
| Symbol | Description | Numerical Value |
| $S/\ell$ | Ratio of the length of the lattice links to cross-sectional area (m) | $10^{-4}$ |
| $T_0$ | Amplitude of thermal striping load (°C) | 10 |
| $\kappa$ | Thermal diffusivity (m$^2$/s) | $2.29 \times 10^{-5}$ |
| $h$ | Block height (m) | $1.16\sqrt{3} \times 10^{-2}$ |
| $d$ | Block width (m) | $10^{-2}$ |
| E | Young's Modulus (GPa) | 163.5 |
| $\nu$ | Poisson's ratio | 1/4 |
| $\alpha$ | Linear thermal expansion coefficient (1/°C) | $2 \times 10^{-5}$ |

**Table 6.1:** The parametric values used for the purposes of numerical computations.

## 6.4 Numerical simulations: the displacement fields and the stress intensity factor

Both the continuum (6.15) and the lattice (6.17) problems are solved using the finite element method for a plate of height $1.16\sqrt{3} \times 10^{-2}$m and width $1 \times 10^{-2}$m. The commercial package Comsol Multiphysics® is used to simulate the thermal striping problem for three characteristic striping frequencies and different crack lengths. The problem is solved using a transient solver with the continuum temperature field being imposed as an external time-harmonic load with complex amplitude as given in (6.20). For the continuum, one half of the plate is modelled with the mode I symmetry condition applied to the uncracked boundary ahead of the crack and the zero displacement condition applied to the horizontal boundary $x_2 = h/2$. The triangular lattice possesses no vertical symmetry and therefore the entire plate must be modelled. Two lattices of varying refinements are considered: (a) a *sparse* lattice with links of length $\ell = 2 \times 10^{-4}$m and cross-sectional area of $S = 2 \times 10^{-8}$m$^2$; and (b) a *fine* lattice with links of length $\ell = 1 \times 10^{-4}$m and cross-sectional area of $S = 1 \times 10^{-8}$m$^2$. The material and geometric parameters are chosen such that the homogenised limit of both lattices correspond to the continuum parameters, as discussed in section 3.2. The numerical values are summarised in table 6.1 and are chosen to correspond to typical values for steel.

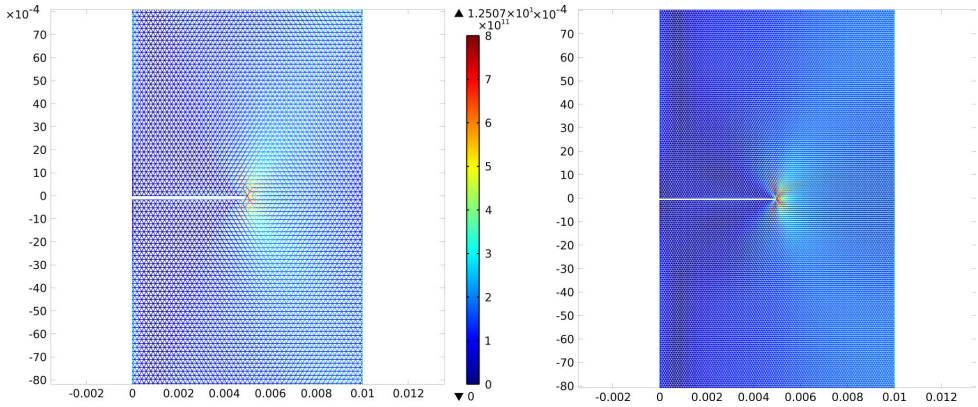


**(a)** The sparse lattice **(b)** The fine lattice

**Figure 6.4:** The axial stresses in the sparse and fine lattices.

Figure 6.4 shows the absolute values of the axial stresses in the two lattices. In contrast to the continuum, all the stresses in the lattice are finite. However, figure 6.4 does show a concentration of stress in the vicinity of the crack tip. In order to define an *"effective stress intensity factor"* for the lattice, it is assumed that for a sufficiently refined lattice the vertical displacements behind the crack tip exhibit similar asymptotic behaviour to the continuum. Indeed, for mode I loading of a semi-infinite crack in a triangular lattice excited by a remote load, it has been shown (see, for example, [115] and [139]) that in the long wavelength limit, the $u_2$ displacement behaves in the same way as the continuum, that is, $u_2(x_1) \sim a_0|a - x_1|^{1/2}$. For the present work, it is assumed that for a sufficiently refined lattice

$$u_2(\boldsymbol{m}) \sim \frac{K_I}{(1-k^2)\mu}\sqrt{\frac{a - x_1(\boldsymbol{m})}{2\pi}} + b_1\left[a - x_1(\boldsymbol{m})\right] + b_2\left[a - x_1(\boldsymbol{m})\right]^{3/2} + b_3\left[a - x_1(\boldsymbol{m})\right]^2, \quad (6.22)$$

for $\boldsymbol{m} \in \{\boldsymbol{p} : x_1(\boldsymbol{p}) < a,\ x_2(\boldsymbol{p}) = 0\}$; here $k = 3 - 4\nu$ and $\mu$ is the shear modulus corresponding to the homogenised continuum. It should be understood that the coefficients $K_I$ and $b_i$ depend on $t$. In direct analogy to the displacement extrapolation method for the continuum (see [63, 124] among others), the stress intensity factor at a particular time can be determined by fitting the expansion (6.22) to the displacements behind the crack tip. Figure 6.5 shows that the expansion (6.22) is sufficient to accurately capture the behaviour of the $u_2$ displacements behind the crack tip and that the displacements exhibit the same qualitative behaviour as in the continuum. Of primary interest is the peak-to-peak amplitude of the stress intensity factor

$$\Delta K_I = \max_{t_0 \le t < t_0 + 2\pi/\omega} K_I(t) \quad - \min_{t_0 \le t < t_0 + 2\pi/\omega} K_I(t). \tag{6.23}$$

Data is taken from the region $\boldsymbol{x} \in \{\boldsymbol{x} : a - 1 \times 10^{-3} \le x_1 \le a - \ell, x_2 = 0\}$, that is, along the upper face of the crack from the node adjacent to the crack tip node for a distance of $1 \times 10^{-3}$m, behind the crack tip (see figure 6.2). Here, $a \ge 0.01$ is the crack length and $0 < \ell < a$ is the length of a lattice link.

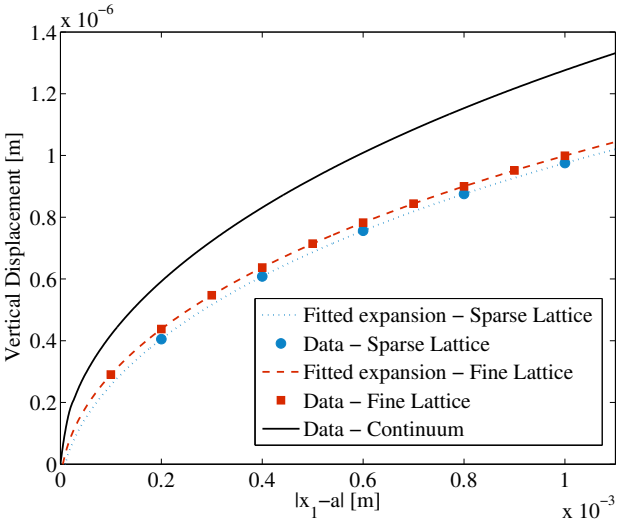


**Figure 6.5:** The $u_2$ displacements for the two lattices and the continuum against distance from the crack tip, together with the fitted expansion curves (see equation (6.22)) for a representative crack depth and time.

For the continuum, it is convenient to use a J-integral type approach to compute the stress intensity factor for the edge-cracked plate. In particular, equation (6.14) is used to determine the stress intensity factor. The line and area integrals in (6.14) are computed from the finite element results using fourth order quadrature over three contours in the vicinity of the crack tip. The positions of the contours are varied to ensure path independence.

Figure 6.6 shows the maximum $\Delta K_I$ values for the thermally striped continuum and the two lattices at three striping frequencies: 0.0625Hz, 1Hz and 6.25Hz. The continuum curves show similar behaviour to that observed in [72, 77], with the local maxima of $\Delta K_I$ increasing and shifting further to the right for lower frequencies. For sufficiently long cracks, the lattice curves exhibit the same qualitative behaviour as the continuum. Compared with the continuum, the lattices have a reduced stress intensity factor, except for shorter cracks at higher frequencies. It

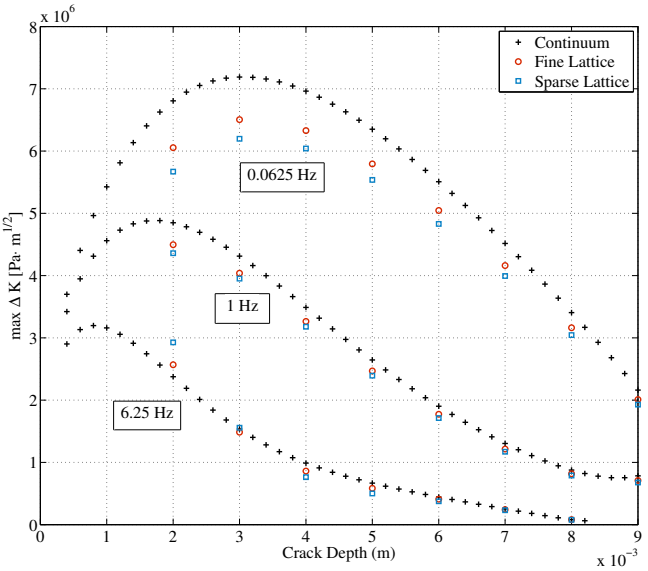


**Figure 6.6:** The maximum $\Delta K_I$ for the continuum and the two lattices against crack depth for three characteristic frequencies.

is also apparent that the more "refined" the lattice, the closer the stress intensity factor is to the continuum value. For shorter edge cracks (smaller than $2 \times 10^{-3}$m) the nodal displacements no longer exhibit the square root asymptotic behaviour (see equation (6.22)).

## 6.5 Remarks

This chapter has examined the effect of a discrete microstructure on quasi-static crack growth in a thermally striped plate for in-plane elasticity. The heat conduction problem on a triangular lattice was formulated and solved numerically. It was demonstrated that the thermal field in the lattice can be approximated by the analytical solution to the heat conduction problem on the corresponding continuous plate. The thermal striping problem, for both the continuum and triangular lattice, was solved using the finite element method. It was shown that, although there is no singularity in the lattice, there is a stress concentration in the neighbourhood of the crack tip. Moreover, the crack face displacements were shown to exhibit the same characteristic square root behaviour, consistent with earlier works (see [115, 139] among others). The notion of an *"effective stress intensity factor"* was introduced via the crack face displacements in direct analogy to the continuum displacement extrapolation method [63, 124] and compared with the stress intensity factor for a corresponding continuum obtained via a modified J-integral. The *"effective stress intensity factor"*, and the stress intensity factor itself, were shown to exhibit the same qualitative properties. In particular, the local maxima of $\Delta K_I$ increases and shifts further to the right for lower frequencies. In physical terms, this means that in the quasi-static regime cracks will tend to grow further for lower striping frequencies. For a sufficiently long crack and low frequency, the *"effective stress intensity factor"*for the lattice is lower than the corresponding continuum. Moreover, the more refined lattice, the closer the *"effective stress intensity factor"* is to the stress intensity factor for the corresponding continuum.

# *Chapter Seven*

# A microstructured invisibility cloak

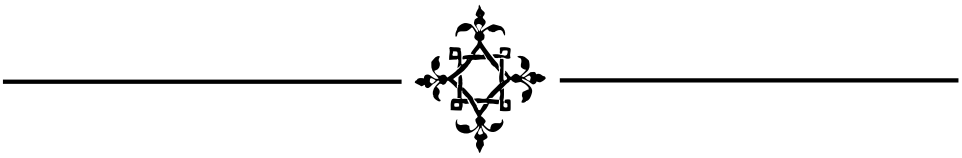

The present chapter is devoted to the development of a square invisibility cloak for fields governed by the Helmholtz equation. The Helmholtz equation arises in a wide variety of fields including electromagnetism, elasticity, and acoustics. Therefore, solutions to the cloaking problem for the Helmholtz equation have a wide range of potential applications. However, for definiteness and ease of exposition the language of elasticity will be used throughout this chapter.

The current chapter is structured as follows. A description of the regularised cloak in the continuum model of out-of-plane shear elastic waves follows the introduction. This also includes the discussion of the essential and natural interface conditions on the boundaries of the cloak. An explicit analytical ray algorithm is developed, and the phenomenon of negative refraction on the interface boundaries is explained. Numerical scattering measures are included, with detailed simulations. The analysis also incorporates Neumann and Dirichlet boundary conditions on the inner contour of the cloak. As a demonstration of the effectiveness of the regularised cloak, a Young's double slit experiment is presented. A recent paper by Greenleaf et al. [54] considers an application of cloaking via transformation optics in quantum mechanics. In particular, Greenleaf et al. present a class of invisible reservoirs and amplifiers for waves and particles. The issues discussed in the present chapter, which are raised by this linkage between cloaking and quantum mechanics, are in some ways similar to those discussed by Greenelaf et al. It is also shown that one of the undeniable advantages of such an approximate cloak is the straightforward connection with the discrete lattice structures. These connections are analysed in detail, and accompanied by a range of physical simulations.

## 7.1 The regularised continuum cloak

The classical approach to cloaking via transformation geometry involves deforming a region such that a point is mapped to a finite region corresponding to the inner boundary of the cloak. Indeed, the square *push out* transformation proposed by Rahm et al. [132] maps a point to a

square. The mapping is non-singular everywhere except at the inner boundary of the cloak. In the present paper, a regularised version of the square *push out* transformation is used. In particular, the trapezoids $\chi^{(i)}$ are mapped to the trapezoids $\Omega_-^{(i)}$ as illustrated in figure 7.1 with continuity, but not smoothness, imposed on the interfaces between the four trapezoids. The mapping is non-singular on the closure of the cloak, and hence, all corresponding material properties are finite. It will be shown that this regularised transformation yields an effective broadband cloak, with finite material properties which may easily be approximated by a regular lattice.

### 7.1.1 The transformation

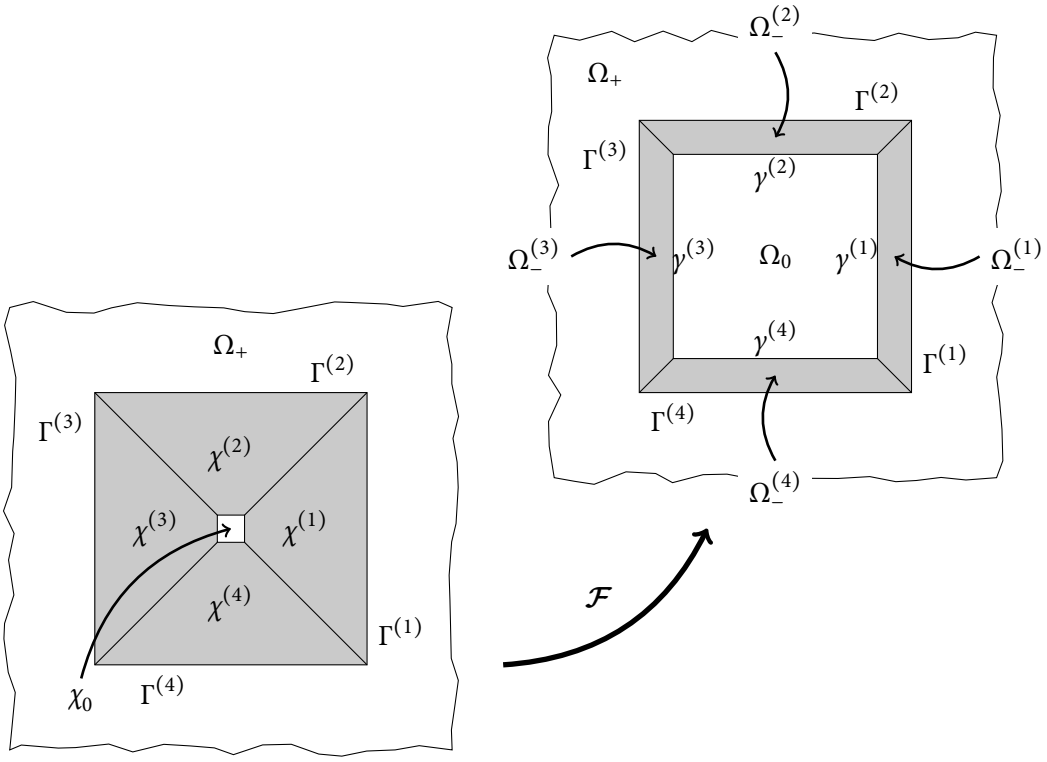


**Figure 7.1:** The transformation $\boldsymbol{\mathcal{F}}$ maps the undeformed region $\chi = \chi^{(1)} \cup \chi^{(2)} \cup \chi^{(3)} \cup \chi^{(4)}$ to the deformed configuration $\Omega_- = \Omega_-^{(1)} \cup \Omega_-^{(2)} \cup \Omega_-^{(3)} \cup \Omega_-^{(4)}$. The boundary between $\Omega_+$ and $\Omega_-^{(i)}$ is denoted $\Gamma^{(i)}$, while the interface between $\Omega_0$ and $\Omega_-^{(i)}$ is denoted $\gamma^{(i)}$. The corresponding boundaries in the undeformed configuration are denoted by $\Gamma^{(i)}$ and $\sigma^{(i)}$ respectively.

Consider a small square $\chi_0 = \{\boldsymbol{X} : |X_1| < \varepsilon, |X_2| < \varepsilon\} \subset \mathbb{R}^2$, which via the transformation $\boldsymbol{\mathcal{F}}$ is mapped to the square $\Omega_0 = \{\boldsymbol{x} : |x_1| < a, |x_2| < a\} \subset \mathbb{R}^2$. The exterior of the cloak remains unchanged by the map, that is, $\boldsymbol{X} = \boldsymbol{\mathcal{F}}(\boldsymbol{X})$ for $\boldsymbol{X} \in \bar{\Omega}_+$, where the bar denotes the closure of the domain. Physically $w$ is the thickness of the cloak, $a$ is the semi-width of the inclusion $\Omega_0$, and $\varepsilon$ is the initial semi-width of the square $\chi_0$ where $0 < \varepsilon/a \ll 1$. In this case, it is convenient to decompose the cloak into four sub-domains $\chi = \chi^{(1)} \cup \chi^{(2)} \cup \chi^{(3)} \cup \chi^{(4)}$, as illustrated in figure 7.1. Formally, $\boldsymbol{\mathcal{F}}$ defines a pointwise map from $\boldsymbol{X} \in \chi = \chi^{(1)} \cup \chi^{(2)} \cup \chi^{(3)} \cup \chi^{(4)}$ to $\boldsymbol{x} = \boldsymbol{\mathcal{F}}(\boldsymbol{X}) \in \Omega_- = \Omega_-^{(1)} \cup \Omega_-^{(2)} \cup \Omega_-^{(3)} \cup \Omega_-^{(4)}$. The mapping is continuous and non-linear on $\chi$,

and defined in a piecewise fashion such that $\boldsymbol{\mathcal{F}} = \boldsymbol{\mathcal{F}}^{(i)}(\boldsymbol{X})$ for $\boldsymbol{X} \in \chi^{(i)}$, where

$$\boldsymbol{\mathcal{F}}^{(1)}(\boldsymbol{X}) = \begin{bmatrix} \alpha_1 X_1 + \alpha_2 \\ \alpha_1 X_2 + \alpha_2 X_2/X_1 \end{bmatrix}, \qquad \boldsymbol{\mathcal{F}}^{(2)}(\boldsymbol{X}) = \begin{bmatrix} \alpha_1 X_1 + \alpha_2 X_1/X_2 \\ \alpha_1 X_2 + \alpha_2 \end{bmatrix}$$

$$\boldsymbol{\mathcal{F}}^{(3)}(\boldsymbol{X}) = \begin{bmatrix} \alpha_1 X_1 - \alpha_2 \\ \alpha_1 X_2 - \alpha_2 X_2/X_1 \end{bmatrix}, \qquad \boldsymbol{\mathcal{F}}^{(4)}(\boldsymbol{X}) = \begin{bmatrix} \alpha_1 X_1 - \alpha_2 X_1/X_2 \\ \alpha_1 X_2 - \alpha_2 \end{bmatrix},$$

with $\alpha_1 = w/(a + w - \varepsilon)$ and $\alpha_2 = (a + w)(a - \varepsilon)/(a + w - \varepsilon)$. The Jacobian matrices and determinants are then

$$\boldsymbol{J}^{(1)} = \begin{pmatrix} \alpha_1 & 0 \\ \dfrac{x_2\alpha_1\alpha_2}{x_1(\alpha_2 - x_1)} & \dfrac{x_1\alpha_1}{x_1 - \alpha_2} \end{pmatrix}, \qquad \boldsymbol{J}^{(2)} = \begin{pmatrix} \dfrac{x_2\alpha_1}{x_2 - \alpha_2} & \dfrac{x_1\alpha_1\alpha_2}{x_2(\alpha_2 - x_2)} \\ 0 & \alpha_1 \end{pmatrix},$$

$$\boldsymbol{J}^{(3)} = \begin{pmatrix} \alpha_1 & 0 \\ \dfrac{x_2\alpha_1\alpha_2}{x_1(\alpha_2 + x_1)} & \dfrac{x_1\alpha_1}{x_1 + \alpha_2} \end{pmatrix}, \qquad \boldsymbol{J}^{(4)} = \begin{pmatrix} \dfrac{x_2\alpha_1}{x_2 + \alpha_2} & \dfrac{x_1\alpha_1\alpha_2}{x_2(\alpha_2 + x_2)} \\ 0 & \alpha_1 \end{pmatrix},$$

$$J^{(1)} = \frac{x_1\alpha_1^2}{x_1 - \alpha_2}, \qquad J^{(2)} = \frac{x_2\alpha_1^2}{x_2 - \alpha_2}, \qquad J^{(3)} = \frac{x_1\alpha_1^2}{x_1 + \alpha_2}, \qquad J^{(4)} = \frac{x_2\alpha_1^2}{x_2 + \alpha_2}.$$

It is emphasised that $J^{(i)}(x_i) = \det \boldsymbol{J}^{(i)} = \operatorname{tr} \boldsymbol{J}^{(i)}$ is strictly positive for $\boldsymbol{x} \in \bar{\Omega}_-^{(i)}$ and $\varepsilon \neq 0$, that is, the map is continuous on both the interior and boundary of the cloak. The metric of the deformed space $\Omega_-^{(i)}$ is $\boldsymbol{g}^{(i)} = (\boldsymbol{J}^{(i)}\boldsymbol{J}^{(i)\mathrm{T}})^{-1}$.

The present section will be devoted to the propagation of time harmonic out-of-plane shear waves of radian frequency $\omega$ and displacement amplitude $u(\boldsymbol{x})$. Lemma 2.1 in [116] allows the Helmholtz equation for an isotropic homogeneous medium $\mu\nabla_{\boldsymbol{X}} \cdot (\nabla_{\boldsymbol{X}})u(\boldsymbol{X}) + \varrho\omega^2 u(\boldsymbol{X}) = 0$ for $\boldsymbol{X} \in \chi$ to be written in deformed co-ordinates as

$$[\nabla \cdot (\boldsymbol{C}^{(i)}(\boldsymbol{x})\nabla) + \rho^{(i)}(\boldsymbol{x})\omega^2]u(\boldsymbol{x}) = 0, \qquad \boldsymbol{x} \in \Omega_-^{(i)}, \tag{7.1}$$

where $\mu$ is the constant ambient stiffness, $\varrho$ is the constant ambient density, the transformed stiffness tensor may be expressed as

$$\boldsymbol{C}^{(i)}(\boldsymbol{x}) = \frac{\mu}{J^{(i)}(\boldsymbol{x})}\boldsymbol{J}^{(i)}(\boldsymbol{x})[\boldsymbol{J}^{(i)}(\boldsymbol{x})]^{\mathrm{T}}, \tag{7.2}$$

and $\rho^{(i)}(\boldsymbol{x}) = \varrho/J^{(i)}(\boldsymbol{x})$ is the scalar transformed density. The differential operator $\nabla_{\boldsymbol{X}}$ is written in the undeformed space and should be distinguished from $\nabla$ which is written in the deformed coordinates.

Since the mapping is continuous on $\bar{\Omega}_-$, the material properties of the cloak are non-singular. It is obvious from the representation (7.2) that the transformed stiffness tensor is symmetric and positive definite. Physically, the transformed material properties correspond to a heterogeneous anisotropic membrane.

### 7.1.2 Interface conditions

Without loss of generality, it is convenient to restrict the following analysis to a single side of the cloak. With reference to figure 7.1, consider a sub-domain $\Omega_-^{(i)} \subset \mathbb{R}^2$ in the absence of the inclusion and remaining three sides of the cloak. In the absence of sources, the amplitude of the out-of-plane shear deformation of an outgoing time-harmonic wave of angular frequency $\omega$ satisfies the following equation

$$\left[\nabla \cdot (\boldsymbol{A}(\boldsymbol{x})\nabla) + \rho(\boldsymbol{x})\omega^2\right] u(\boldsymbol{x}) = 0, \tag{7.3}$$

together with the Sommerfeld radiation condition at infinity. Here, $\boldsymbol{A}(\boldsymbol{x})$ and $\rho(\boldsymbol{x})$ are defined as

$$\boldsymbol{A}(\boldsymbol{x}) = \begin{cases} \boldsymbol{C}^{(i)}(\boldsymbol{x}) & \text{for } \boldsymbol{x} \in \Omega_-^{(i)} \\ \mu\mathbb{I} & \text{for } \boldsymbol{x} \in \Omega_+ \end{cases}, \qquad \rho(\boldsymbol{x}) = \begin{cases} \rho^{(i)}(\boldsymbol{x}) & \text{for } \boldsymbol{x} \in \Omega_-^{(i)} \\ \varrho & \text{for } \boldsymbol{x} \in \Omega_+ \end{cases}. \tag{7.4}$$

Let $v(\boldsymbol{x})$ be a continuous piecewise smooth solution of the Helmholtz equation in $\mathbb{R}^2$ satisfying the Sommerfeld radiation condition at infinity. Integrating the difference $u(\boldsymbol{x})[\nabla\cdot(\boldsymbol{A}(\boldsymbol{x})\nabla)+\rho(\boldsymbol{x})\omega^2]v(\boldsymbol{x}) - v(\boldsymbol{x})[\nabla\cdot(\boldsymbol{A}(\boldsymbol{x})\nabla)+\rho(\boldsymbol{x})\omega^2]u(\boldsymbol{x})$ over a disc $\mathcal{D}_r$ of radius $r$ containing $\Omega_-^{(i)}$ yields

$$\begin{aligned} 0 &= \int_{\mathcal{D}_r} \left(u\nabla\cdot\boldsymbol{A}\nabla v - v\nabla\cdot\boldsymbol{A}\nabla u\right) \mathrm{d}\boldsymbol{x}, \\ &= \int_{\partial\Omega_-^{(1)}} \left(u^-\boldsymbol{n}\cdot\boldsymbol{A}\nabla v^- - v^-\boldsymbol{n}\cdot\boldsymbol{A}\nabla u^-\right) \mathrm{d}\boldsymbol{x} - \int_{\partial\Omega_-^{(1)}} \left(u^+\boldsymbol{n}\cdot\boldsymbol{A}\nabla v^+ - v^+\boldsymbol{n}\cdot\boldsymbol{A}\nabla u^+\right) \mathrm{d}\boldsymbol{x} \\ &\qquad + \mu \int_{\partial\mathcal{D}_r} \left(u\boldsymbol{n}\cdot\nabla v + v\boldsymbol{n}\cdot\nabla u\right) \mathrm{d}\boldsymbol{x}, \end{aligned}$$

where the fact that $\nabla u \cdot \boldsymbol{A}\nabla v = \nabla v \cdot \boldsymbol{A}\nabla u$ (since $\boldsymbol{A}$ is symmetric) has already been used. Since $u(\boldsymbol{x})$ and $v(\boldsymbol{x})$ represent outgoing solutions, the integral over $\partial\mathcal{D}_r$ vanishes as $r \to \infty$. Thus, the essential interface condition is the continuity of the field

$$[u] = 0 \qquad \text{on} \qquad \partial\Omega_-^{(i)}, \tag{7.5}$$

and the natural interface condition is continuity of tractions, that is,

$$[\boldsymbol{n}\cdot\boldsymbol{A}(\boldsymbol{x})\nabla u] = 0 \qquad \text{on} \qquad \partial\Omega_-^{(i)}. \tag{7.6}$$

### 7.1.3 The cloaking problem

Consider the propagation of a time harmonic out-of-plane deformation, generated by a point source, in a homogeneous infinite elastic solid containing an inclusion surrounded by a cloak. The displacement amplitude then satisfies

$$\left[\nabla \cdot (\boldsymbol{A}(\boldsymbol{x})\nabla) + \rho(\boldsymbol{x})\omega^2\right] u(\boldsymbol{x}) = -\delta(\boldsymbol{x} - \boldsymbol{x}_0), \qquad \boldsymbol{x} \in \mathbb{R}^2 \setminus \bar{\Omega}_0, \qquad \boldsymbol{x}_0 \in \Omega_+ \tag{7.7}$$

$$\left[\mu_0\nabla\cdot(\nabla) + \varrho_0\omega^2\right] u(\boldsymbol{x}) = 0, \qquad \boldsymbol{x} \in \Omega_0, \tag{7.8}$$

with the continuity condition (7.5) for $u(\boldsymbol{x})$ and the condition (7.6) for traction on all interface boundaries. Additionally, the Sommerfeld radiation condition is imposed at infinity. The stiffness tensor $\boldsymbol{A}(\boldsymbol{x})$ and density $\rho(\boldsymbol{x})$ are

$$\boldsymbol{A}(\boldsymbol{x}) = \begin{cases} \boldsymbol{C}^{(i)}(\boldsymbol{x}) & \text{for } \boldsymbol{x} \in \Omega_-^{(i)} \\ \mu\mathbb{I} & \text{for } \boldsymbol{x} \in \Omega_+ \end{cases}, \qquad \rho(\boldsymbol{x}) = \begin{cases} \rho^{(i)}(\boldsymbol{x}) & \text{for } \boldsymbol{x} \in \Omega_-^{(i)} \\ \varrho & \text{for } \boldsymbol{x} \in \Omega_+ \end{cases}, \tag{7.9}$$

and $\mu_0$ and $\varrho_0$ are the stiffness and density of the inclusion respectively.

### 7.1.4 The ray equations

Whilst, in principle, it is possible to find the displacement field by solving the cloaking problem it is useful to consider the leading order behaviour of rays through the cloak. Consider a WKB-type expansion (see *WKB Expansions* in the appendices on page 126) of the displacement amplitude in terms of angular frequency $\omega$, and the amplitude and phase functions $U_n(\boldsymbol{x})$ and $\phi(\boldsymbol{x})$ respectively

$$u(\boldsymbol{x}) \sim e^{i\omega\phi(\boldsymbol{x})} \sum_{n=0}^{\infty} \frac{i^n U_n(\boldsymbol{x})}{\omega^n}, \qquad \text{as } \omega \to \infty. \tag{7.10}$$

The leading order equation for the phase on the interior of the cloak has the form

$$H(\boldsymbol{x}, \boldsymbol{s}) = 0, \tag{7.11}$$

where $H(\boldsymbol{x}, \boldsymbol{s}) = \mu\varrho^{-1}\boldsymbol{s} \cdot \boldsymbol{g}^{-1}\boldsymbol{s} - 1$, $\boldsymbol{s} = \nabla\phi$ is the slowness vector, $\mu$ and $\varrho$ are the stiffness and the density of the ambient medium respectively, and $\boldsymbol{g}$ is the metric of the transformation. In terms of wave propagation, the conserved quantity $H(\boldsymbol{x}, \boldsymbol{s})$ represents the first order slowness contours(see, for instance, [110]). The characteristics of the quantity $H(\boldsymbol{x}, \boldsymbol{s})$ then satisfy the following system

$$\frac{\mathrm{d}H}{dt} = 0, \qquad \frac{\mathrm{d}\boldsymbol{x}}{\mathrm{d}t} = \frac{\partial H}{\partial \boldsymbol{s}}, \qquad \frac{\mathrm{d}\boldsymbol{s}}{\mathrm{d}t} = -\frac{\partial H}{\partial \boldsymbol{x}}, \tag{7.12}$$

where $t$ is the ray (time-like) parameter. At this point, it is convenient to introduce index summation notation where summation from 1 to 2 over repeated indices is assumed. The system (7.12) may then be expressed as follows

$$\frac{\mathrm{d}s_i}{\mathrm{d}t} = -2\varrho^{-1}\mu\, s_m\, s_n\, J_{nl}\, \frac{\partial J_{ml}}{\partial x_i}, \qquad \frac{\mathrm{d}x_i}{\mathrm{d}t} = 2\varrho^{-1}\mu\, J_{il}\, J_{jl}\, s_j, \tag{7.13}$$

where $J_{ij} = (\boldsymbol{J})_{ij}$ are the components of the Jacobian matrix and should be distinguished from the $J$, the Jacobian determinant. The superscript labels have been omitted for brevity, but $J_{ij}$ and $J$ should be understood as $J_{ij}^{(k)}$ and $J^{(k)}$ for $k = 1, \ldots 4$, corresponding to the four sides of the cloak. Written in terms of wave normals $\boldsymbol{n}$ and the phase velocity $v$, equation (7.11) takes the form

$$\mu\varrho^{-1}\boldsymbol{n} \cdot \boldsymbol{g}^{-1}\boldsymbol{n} - v^2 = 0. \tag{7.14}$$

The representation (7.14) is obtained by assuming a plane wave solution to the Helmholtz equation (see, for example [110])[1].

From (7.11) and (7.14) the slowness vector can be expressed in terms of the original material properties (through $\varrho$ and $\mu$) and the map (through $\boldsymbol{J}$) as

$$\boldsymbol{s} = \frac{\boldsymbol{n}}{v} = \frac{\boldsymbol{n}}{|\boldsymbol{J}^{\mathrm{T}}\boldsymbol{n}|}\sqrt{\frac{\varrho}{\mu}}, \tag{7.15}$$

Further, in the undeformed configuration, the equivalent conserved quantities are $\mu\varrho^{-1}\boldsymbol{S}\cdot\boldsymbol{S}-1 = 0$ and $\mu\varrho^{-1} = V^2$. Together with (7.11) and (7.14), these two equations imply that

$$\boldsymbol{s} = \boldsymbol{J}^{-\mathrm{T}}\boldsymbol{S} = \frac{\boldsymbol{J}^{-\mathrm{T}}\boldsymbol{N}}{V} = \boldsymbol{J}^{-\mathrm{T}}\boldsymbol{N}\sqrt{\frac{\varrho}{\mu}}, \tag{7.16}$$

where $\boldsymbol{J}^{-\mathrm{T}} = (\boldsymbol{J}^{\mathrm{T}})^{-1}$ denotes the inverse and transpose of $\boldsymbol{J}$.

Now, consider a ray (i.e. a line) in the ambient medium, in direction $\boldsymbol{N}$ passing through $\boldsymbol{X}_0$ and parameterised by $t$. The corresponding curve in the cloak is $\boldsymbol{x}(t) = \boldsymbol{\mathcal{F}}(\boldsymbol{X}_0 + t\boldsymbol{N})$, whence

$$\frac{\mathrm{d}x_i}{\mathrm{d}t} = J_{ij}N_j,$$

which using (7.16) can be rewritten in the form

$$\frac{\mathrm{d}x_i}{\mathrm{d}t} = J_{il}J_{jl}s_j\sqrt{\frac{\mu}{\varrho}}. \tag{7.17}$$

Taking the derivative of (7.16) for constant $\boldsymbol{N}$ yields

$$\frac{\mathrm{d}s_i}{\mathrm{d}t} = s_k s_n J_{kj}J_{lm}J_{nm}\frac{\partial J^{-1}{}_{ji}}{\partial x_l}\sqrt{\frac{\mu}{\varrho}}.$$

Here is it emphasised that $J^{-1}_{ji} = (\boldsymbol{J}^{-1})_{ij}$ as opposed to $1/J_{ij}$. Using the compatibility condition, that is, the deformation gradient should be irrotational under finite deformation $\varepsilon_{jk\ell}\partial J^{-1}{}_{ik}/\partial x_j = 0_{\ell i}$, the partial derivative above can be written as $\partial J^{-1}{}_{jl}/\partial x_i$, whence

$$\frac{\mathrm{d}s_i}{\mathrm{d}t} = -s_m s_n J_{n\ell}\frac{\partial J_{ml}}{\partial x_i}\sqrt{\frac{\mu}{\varrho}}, \tag{7.18}$$

where $\varepsilon_{jk\ell}$ is the permutation tensor and the equality $J_{lm}\partial J^{-1}_{jl}/\partial x_i = -J^{-1}_{jl}\partial J_{lm}/\partial x_i$ has been used.

Consider the characteristic equations for the waves in the cloak (7.13), together with the equations of the transformed rays (7.17) and (7.18). The system (7.17) and (7.18) are the equations of characteristics in the cloak, up to an arbitrary scaling constant $2\sqrt{\mu/\varrho}$. Thus, to leading order, rays (or straight lines) in the ambient medium map directly to rays in the cloak.

[1] Alternatively, seeking a solution of the full wave equation in the form of the leading term in a WKB expansion

$$u(\boldsymbol{x},t) \sim e^{i\omega\phi(\boldsymbol{x},t)}\sum_{n=0}^{\infty}\frac{i^n U_n(\boldsymbol{x},t)}{\omega^n}, \qquad \text{as } \omega\to\infty,$$

yields the same result with $\partial\phi/\partial t = v$.

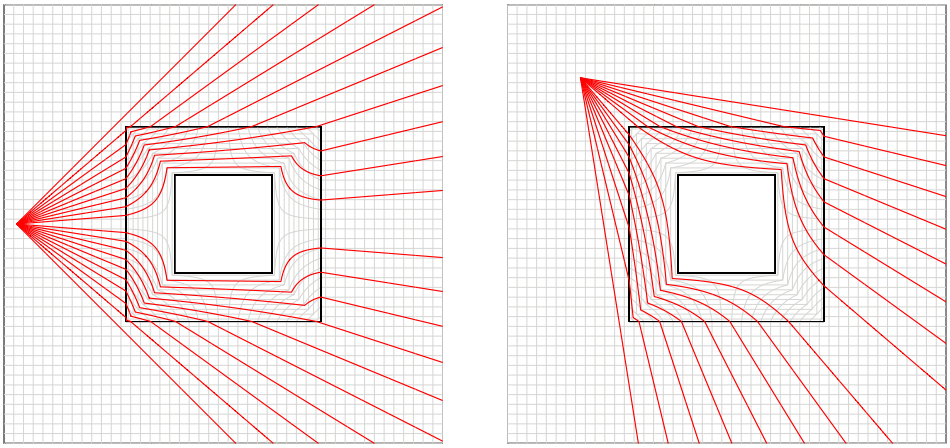

(a) (b)

**Figure 7.2:** Plots of the ray paths through the cloak for a cylindrical source. The grey lines indicate the deformation of the space inside the cloak. (Animated versions of these figures may be found in the supplementary material [30].)

Figure 7.2 shows rays emanating from a point source, passing through the cloak and emerging from the cloak along their original trajectory. In this sense, the object is "invisible" to an observer outside the cloaking region. Figure 7.2 clearly illustrates how wave propagation in the cloak is related to the map. Animated versions of figure 7.2 can be found in the supplementary material [30].

An interesting alternative perspective is apparent if figure 7.2 is viewed, not as rays diverging from a source, but as rays converging to a focal point. It is observed that the rays converge to the focal point around the inclusion. One can envisage several applications where such an effect can be useful. For example, image distortion from the mirror mounts in telescopes could be reduced by cloaking the mounts. In addition, apparatus and mounting structures on microwave receivers could be cloaked to improve the quality of the signal. One could also conceive of cloaking mounting points and the surrounding structures in laser cutting machines to protect them from accidental damage.

### Negative refraction

It is evident from figure 7.2 that, whilst the rays are continuous, they are not necessarily smooth. In particular, at the interfaces of the cloak, refraction occurs characterised by the discontinuity of the first order spatial derivatives of the rays. Of particular interest are the regions on the outer boundary of the cloak where negative refraction occurs.

Consider figure 7.2a. Negative refraction occurs on the right hand interface between the cloak and the ambient medium. A ray exiting the right hand side of the cloak with gradient $M$ at point $\boldsymbol{X}^{(0)} = \boldsymbol{x}^{(0)}$ can be described by the equation $X_2^{(s)} - X_2^{(0)} = M(X_1^{(s)} - X_1^{(0)})$ in the ambient medium, where $\boldsymbol{X}^{(s)}$ is the position of the source. The behaviour of the ray at the interface is characterised by the position of the source relative to the interface, its initial gradient and the properties of the cloak. Therefore, without loss of generality, the following analysis is restricted to the right hand side of the cloak. On the interior of the right hand side of the cloak, the ray exiting the cloak at

$\boldsymbol{x}^{(0)}$ is characterised by

$$x_2 = x_1\left(M + \frac{\alpha_1(x_2^{(0)} - Mx_1^{(0)})}{x_1 - \alpha_2}\right).$$

The gradient of the ray as it approaches the exterior boundary from the interior of the cloak is then

$$m^* = \lim_{x_1\to(a+w)^-}\frac{\mathrm{d}x_2}{\mathrm{d}x_1} = \frac{M(a+w-\varepsilon)(a+w) - x_2^{(0)}(a+\varepsilon)}{w(a+w)}.$$

Thus, the gradient is discontinuous at the exterior interface. For negative refraction it is required that $m^*M < 0$. This inequality is satisfied when either

$$0 < M < x_2^{(0)}\frac{a+\varepsilon}{(a+w)(a+w-\varepsilon)}, \qquad \text{or} \qquad x_2^{(0)}\frac{a+\varepsilon}{(a+w)(a+w-\varepsilon)} < M < 0. \tag{7.19}$$

For a source located on the line $X_2 = 0$ as in figure 7.2a, the above inequalities reduce to the single inequality

$$X_1^{(s)} < -\frac{(a+w)(w-2\varepsilon)}{a+\varepsilon},$$

which is satisfied for all sources outside the cloak $X_1^{(s)} < -(a+w)$, provided $w < a + 3\varepsilon$. Thus, for a sufficiently thin cloak and a cylindrical source placed along $X_2 = 0$ at any distance from the cloak, negative refraction is expected on the opposite side of cloak.

For a source located along the line $X_1 = 0$, the inequalities (7.19) become

$$0 < X_2^{(s)} < \frac{(a+w)(w-2\varepsilon)}{(a+w-\varepsilon)}, \qquad \text{or} \qquad -\frac{(a+w)(w-2\varepsilon)}{(a+w-\varepsilon)} < X_2^{(s)} < 0, \tag{7.20}$$

where the fact that $|x_2^{(0)}| < (a+w)$ has been used. Since $a, w > 0$, and $0 < \varepsilon/a \ll 1$, the above inequalities are never satisfied, hence, the lack of negative refraction on the horizontal interfaces in figure 7.2a. Similar arguments may be used in other regions to decide whether negative refraction occurs or not. It is observed that negative refraction always occurs at the interfaces between the different regions of the cloak, where the material properties (equivalently the transformation) are not smooth.

### 7.1.5 Scattering measure

It is desirable to have some quantifiable measure of the quality of the cloak with respect to shielding, rather than relying on visual observations. However, it is not obvious what "quality" means with respect to a cloak, given that there are essentially three fields involved, i.e. the ideal field in the absence of both cloak and inclusion, the uncloaked field with an inclusion present but without a cloak, and the cloaked field with both the inclusion and cloak. Previous experimental works [141] have used an $L_2$ norm computed directly from the measured fields to place a numerical value on the quality of the cloak. It is in this spirit that the following "*scattering measure*" is formally introduced as a tool to quantify the cloaking effect

$$\mathcal{E}(u_1, u_2, \mathcal{R}) = \left(\int_{\mathcal{R}} |u_1(\boldsymbol{x}) - u_2(\boldsymbol{x})|^2\,\mathrm{d}\boldsymbol{x}\right)\left(\int_{\mathcal{R}} |u_2(\boldsymbol{x})|^2\,\mathrm{d}\boldsymbol{x}\right)^{-1}, \tag{7.21}$$

where $\mathcal{R} \subset \mathbb{R}^2$ is some region outside the cloak, and $u_1(\boldsymbol{x})$ and $u_2(\boldsymbol{x})$ are any two fields. In the present chapter, the quantities $\mathcal{E}(u_u, u_0, \mathcal{R})$ and $\mathcal{E}(u_c, u_0, \mathcal{R})$ are given for a series of illustrative simulations. The field $u_0(\boldsymbol{x}) = i\,\mathrm{H}_0^{(1)}(\omega\sqrt{\varrho/\mu}|\boldsymbol{x} - \boldsymbol{x}_0|)/4$ is the Green's function for the unperturbed problem and represents the "ideal" field, $u_u(\boldsymbol{x})$ and $u_c(\boldsymbol{x})$ are the uncloaked and cloaked fields respectively. Thus, perfect cloaking corresponds to a vanishing $\mathcal{E}$. Along with the raw scattering measures an additional quantity, $Q = |\mathcal{E}(u_u, u_0, \mathcal{R}) - \mathcal{E}(u_c, u_0, \mathcal{R})|/\mathcal{E}(u_u, u_0, \mathcal{R})$, is also presented. The parameter $Q$ characterises the relative reduction of the scattering measure by the introduction of a cloak. It should be emphasised that this is only one of a number of possible measures of quality.

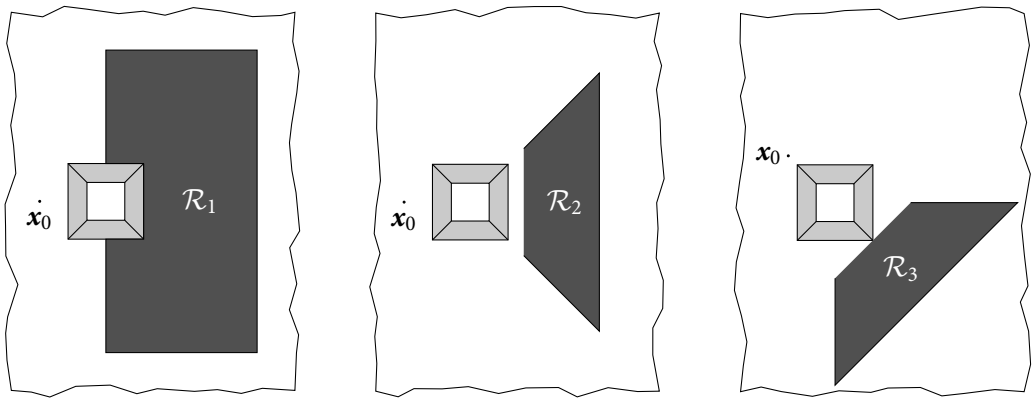


**(a)** Strict scattering region **(b)** Forward Scattering **(c)** Corner Scattering

**Figure 7.3:** The three regions used for computation of the scattering measure.

**Choice of $\mathcal{R}$.** For the purpose of illustration three different regions of integration are considered, as shown in figure 7.3. The three regions used were chosen as follows: (a) $\mathcal{R}_1$ is the most strict region used taking into account significant near field effects and a wide range of scattering angles. However, it is unlikely that this region would be measurable in practice. (b) The forward scattering region ($\mathcal{R}_2$) is relevant if the scattered field is measurable over a wide range of forward scattering angles. (c) The corner scattering region ($\mathcal{R}_3$) is employed for sources located along the diagonal of the square inclusion. It is emphasised that $\|\mathcal{R}_1\| \neq \|\mathcal{R}_2\| = \|\mathcal{R}_3\|$, and the leading edges of the regions $\mathcal{R}_2$ and $\mathcal{R}_3$ are located at the same distance from the source.

In the following section the scattering measures will be presented for a series of illustrative simulations.

### 7.1.6 Illustrative simulations

A series of illustrative simulations were created using the finite element software COMSOL Multiphysics®. Perfectly matched layers were used in the vicinity of the boundary of the computational domain in order to simulate an infinite domain. For the purposes of these computations, the following non-dimensional parameter values[2] were chosen: $a = 0.5$, $w = 0.5$, $\mu = \varrho = 1$, $\mu_0 = 0.1$, $\varrho_0 = 0, \varepsilon = 1 \times 10^{-6}$. Figures 7.4 and 7.5 show the displacement amplitude field $u(\boldsymbol{x})$ for a cylindrical source oscillating at $\omega = 5$ and $\omega = 10$ respectively. The figures clearly illustrate

[2]Throughout this chapter, all numerical parameters are normalised such $\mu = \varrho = 1$ unless otherwise stated.

| Source | | Scattering Measure $\mathcal{E}$ | | |
|---|---|---|---|---|
| Position | Frequency | Uncloaked | Cloaked | $Q$ |
| | | Scattering region $\mathcal{R}_1$ | | |
| $[-3,0]^{\mathrm{T}}$ | 5 | 0.1529 | $4.351 \times 10^{-4}$ | 0.9972 |
| $[-3,0]^{\mathrm{T}}$ | 10 | 0.1455 | $4.514 \times 10^{-4}$ | 0.9969 |
| $[-3,3]^{\mathrm{T}}/\sqrt{2}$ | 5 | 0.2002 | $3.941 \times 10^{-4}$ | 0.9980 |
| $[-3,3]^{\mathrm{T}}/\sqrt{2}$ | 10 | 0.3286 | $4.068 \times 10^{-4}$ | 0.9988 |
| | | Scattering region $\mathcal{R}_2$ | | |
| $[-3,0]^{\mathrm{T}}$ | 5 | 0.3224 | $3.664 \times 10^{-4}$ | 0.9989 |
| $[-3,0]^{\mathrm{T}}$ | 10 | 0.3093 | $1.167 \times 10^{-3}$ | 0.9962 |
| | | Scattering region $\mathcal{R}_3$ | | |
| $[-3,3]^{\mathrm{T}}/\sqrt{2}$ | 5 | 0.2988 | $3.654 \times 10^{-4}$ | 0.9988 |
| $[-3,3]^{\mathrm{T}}/\sqrt{2}$ | 10 | 0.2988 | $7.803 \times 10^{-4}$ | 0.9974 |

**Table 7.1:** The scattering measures corresponding to the simulations shown in figures 7.4 and 7.5.

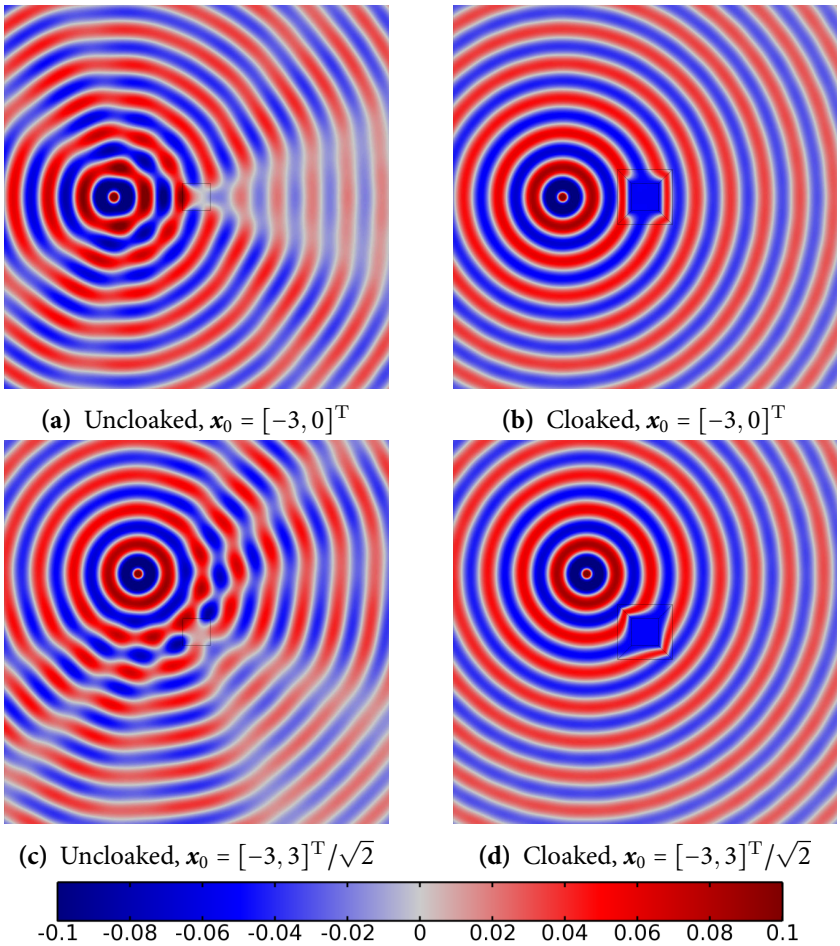


**(a)** Uncloaked, $\boldsymbol{x}_0 = [-3,0]^{\mathrm{T}}$ **(b)** Cloaked, $\boldsymbol{x}_0 = [-3,0]^{\mathrm{T}}$

**(c)** Uncloaked, $\boldsymbol{x}_0 = [-3,3]^{\mathrm{T}}/\sqrt{2}$ **(d)** Cloaked, $\boldsymbol{x}_0 = [-3,3]^{\mathrm{T}}/\sqrt{2}$

**Figure 7.4:** Plots of the field $u$ for the uncloaked and cloaked square inclusion, where the angular frequency of excitation is $\omega = 5$. The position $\boldsymbol{x}_0$ of the source is indicated under the relevant plot.

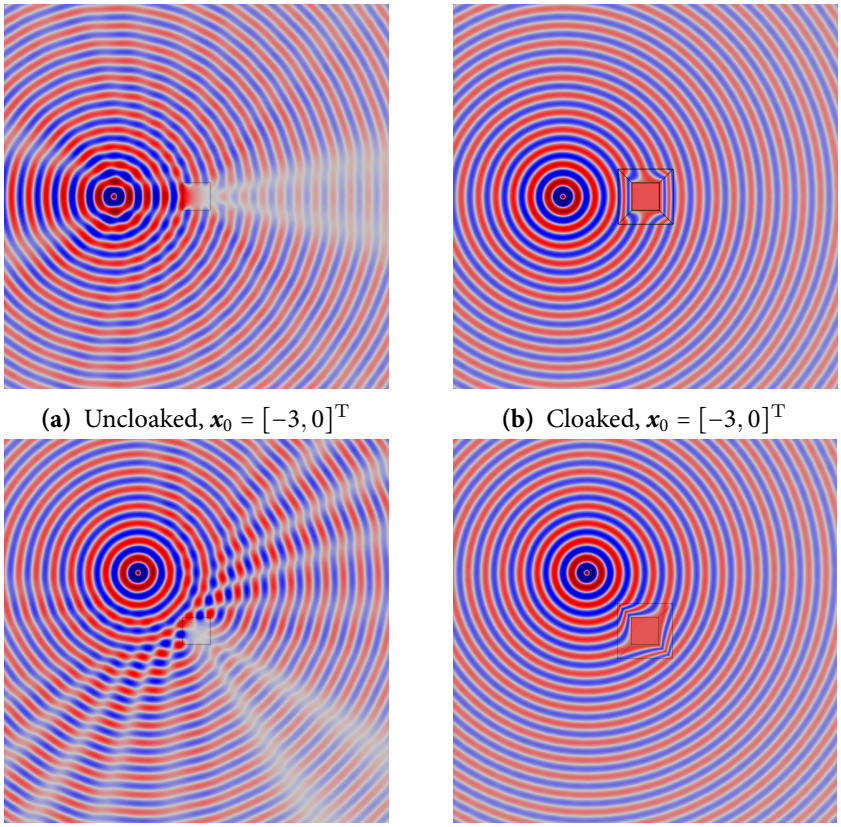

**(a)** Uncloaked, $\boldsymbol{x}_0 = [-3, 0]^{\mathrm{T}}$ **(b)** Cloaked, $\boldsymbol{x}_0 = [-3, 0]^{\mathrm{T}}$

**(c)** Uncloaked, $\boldsymbol{x}_0 = [-3, 3]^{\mathrm{T}}/\sqrt{2}$ **(d)** Cloaked, $\boldsymbol{x}_0 = [-3, 3]^{\mathrm{T}}/\sqrt{2}$

**Figure 7.5:** Plots of the field $u$ for the uncloaked and cloaked square inclusion where the angular frequency of excitation is $\omega = 10$. The position $\boldsymbol{x}_0$ of the source is indicated under the relevant plot and the inclusion is located at the centre of the image in all cases. The colour scale is as indicated in figure 7.4.

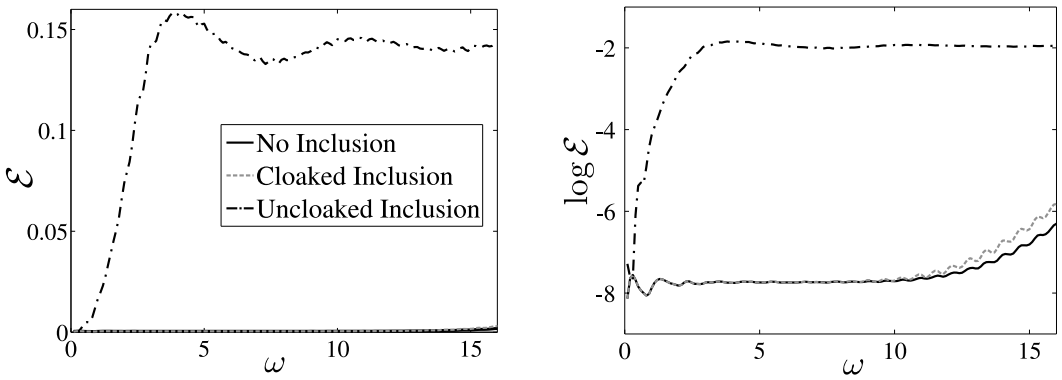


**(a)** **(b)**

**Figure 7.6:** (a) The scattering measure plotted against angular frequency. (b) The log of the scattering measure plotted against angular frequency. The solid line corresponds to the continuum in the absence of both an inclusion and cloak. The dashed line represents the cloaked inclusion and the dash-dot line corresponds to the uncloaked inclusion. The region $\mathcal{R}_1$ (see figure 7.3 and the associated text) was used to compute the error measure.

| Source Boundary Condition | Frequency | Scattering Measure $\mathcal{E}$ Uncloaked | Cloaked | $Q$ |
|---|---|---|---|---|
| | Scattering region $\mathcal{R}_1$ | | | |
| Neumann | 5 | 0.1624 | $4.351 \times 10^{-4}$ | 0.9973 |
| Neumann | 10 | 0.1558 | $4.540 \times 10^{-4}$ | 0.9971 |
| Dirichlet | 5 | 0.2931 | $1.038 \times 10^{-2}$ | 0.9646 |
| Dirichlet | 10 | 0.2553 | $7.875 \times 10^{-3}$ | 0.9692 |
| | Scattering region $\mathcal{R}_2$ | | | |
| Neumann | 5 | 0.3436 | $3.664 \times 10^{-4}$ | 0.9989 |
| Neumann | 10 | 0.3258 | $1.163 \times 10^{-3}$ | 0.9964 |
| Dirichlet | 5 | 0.4864 | $1.566 \times 10^{-2}$ | 0.9678 |
| Dirichlet | 10 | 0.5030 | $1.673 \times 10^{-2}$ | 0.9667 |

**Table 7.2:** The scattering measures for a void with Neumann and Dirichlet boundary conditions. Here the source is located at $[-3, 0]^{\mathrm{T}}$.

the efficacy of the square cloak, even at relatively high frequencies. Table 7.1 shows the corresponding scattering measures as introduced in section 7.1.5. It is clear that this square "*push out*" cloak is highly effective. Indeed, for the illustrative simulations presented here, the cloak reduces the scattering measure by not less than 99.62% compared with the uncloaked inclusion.

Figure 7.6 shows the scattering measure plotted against non-dimensional angular frequency $\omega$ (with $\mu = \varrho = 1$). The solid curve in figure 7.6 corresponds to the continuum, in the absence of both cloak and inclusion. This curve gives an indication of the numerical error in the simulation induced by, for example, the use of perfectly matched layers and the numerical discretisation. The dashed curve corresponds to the cloaked inclusion, whilst the dash-dot curve corresponds to the uncloaked inclusion. It is observed that the numerical measure of the cloaked inclusion remains close to that of the intact continuum for a large range of frequencies. Moving to dimensional quantities, suppose the simulation corresponded to a particular polarization of an electric wave travelling through glass at a speed of approximately $2 \times 10^8$ m/s. The line $\omega = 10$ on figure 7.6 then corresponds to a frequency of approximately 340 MHz.

**Boundary considerations**

Whilst cloaking via transformation geometry has been extensively treated in the literature, the sensitivity of the cloaking effect to the boundary conditions is rarely discussed. The cloak is formed by deforming a small region (a point in the case of the classical radial transformation [126]), into a larger finite region. If the region is an inclusion, then the natural interface conditions may be determined following the method outlined in section 7.1.2. If the cloaked region is a void or rigid inclusion, however, there is some freedom in choosing the boundary condition, subject to the constraints of the physical problem. Figure 7.7 shows the field $u(\boldsymbol{x})$ for a cloaked void, with Neumann (parts (a) and (b)) and Dirichlet (parts (c) (d)) conditions applied to the interior of the cloaked region. The corresponding scattering measures are shown in table 7.2.

Although the square cloak is effective in both cases, it is clear from both the figures and the table of scattering measures that the type of boundary condition imposed on the cloaked object affects the quality of the cloaking. Indeed, for a void (Neumann) the cloaking reduces the scat-

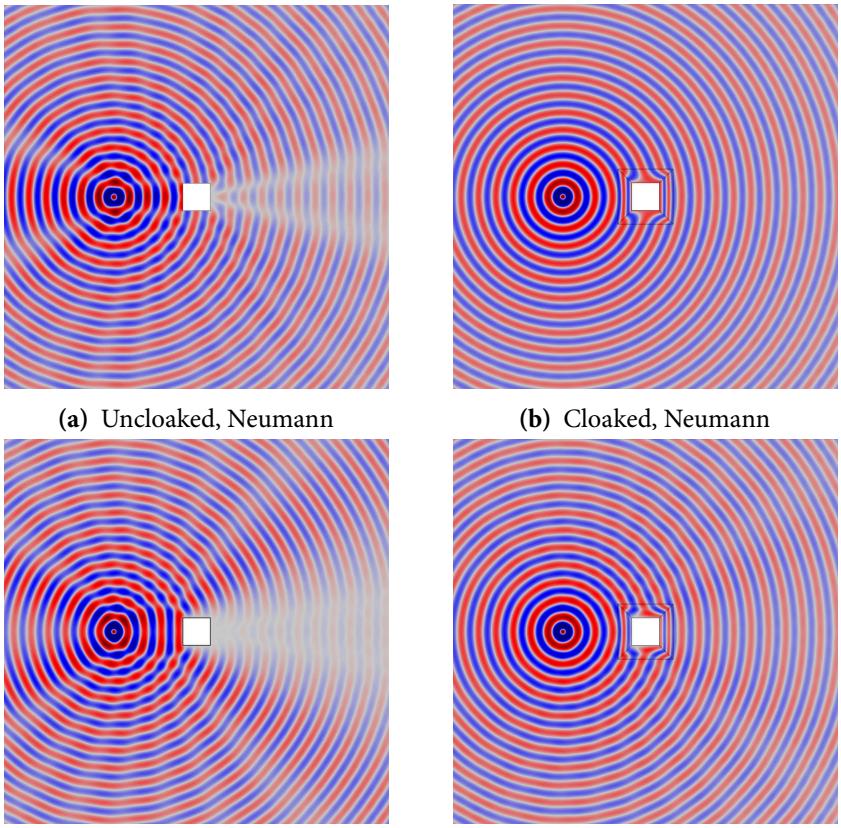

**(a)** Uncloaked, Neumann

**(b)** Cloaked, Neumann

**(c)** Uncloaked, Dirichlet

**(d)** Cloaked, Dirichlet

**Figure 7.7:** Plots of the field $u$ for the uncloaked and cloaked square inclusion with Neumann boundary conditions on the boundary of the inclusion in parts (a) and (b), and Dirichlet boundary conditions on the boundary of the inclusion in parts (c) and (d). Here the source is located at $\boldsymbol{x} = [-3, 0]^{\mathrm{T}}$ and oscillates at $\omega = 10$. The colour scale is as indicated in figure 7.4.

tering measure by between 99.7% and 99.9% for both $\omega = 5$ and $\omega = 10$. In contrast, cloaking reduces the scattering measure of a rigid inclusion (Dirichlet) by between 96.5% and 96.8% for $\omega = 5$ and between 96.7% and 96.9% for $\omega = 10$. The effect of the boundary condition may be interpreted in the following way. As a result of the transformation, the cloaked object and cloak together behave as if the void is small. In this sense, the cloaked inclusion represents a singular perturbation of the fundamental solution of the Helmholtz equation. In the case of a free void with Neumann conditions, the leading order term in the asymptotic expansion is the dipole term, which is of order $\varepsilon^2$ and decays like the first derivative of the fundamental solution. On the other hand, for a fixed void with Dirichlet conditions, the leading order term in the expansion is the monopole term which is of order $\varepsilon$ and decays like the fundamental solution. Thus, the perturbation from the free void is smaller than the perturbation from the fixed void, leading to improved cloaking

## 7.2 Cloaking path information

In recent years there has been much interest in experiments to elucidate the fundamental principles of quantum mechanics, and in particular the relationship between measurement and system behaviour. One basic experiment which with its variants features in many such experimental studies is the classical Young's double slit experiment (see, for example, [66, 67]). This suggested that it may be of interest to consider the interaction of the excellent mechanical cloaking demonstrated earlier with the foundational quantum mechanics experiment. A recent paper by Greenleaf et al. [54] considers an application of cloaking via transformation optics in quantum mechanics. In particular, Greenleaf et al. present a class of invisible reservoirs and amplifiers for waves and particles. The issues discussed below, which are raised by this linkage between cloaking and quantum mechanics, are in some ways similar to those discussed by Greenelaf et al.

Thus, a Young's double slit experiment is considered where a monochromatic plane wave is incident on a screen with two apertures. Due to the superposition of the waves passing through the two apertures, the distinctive double slit interference pattern is produced on an observation screen placed on the opposite side of the apertures to the source. The result of a simulation of the standard experiment is shown in figure 7.8a, with the diffraction pattern produced on the observation screen (in this case, a vertical line near the right hand edge of figures 7.8a-7.8c) shown as curve (a) in figure 7.8d. Placing an object (inclusion) over one slit, as in figure 7.8b, partially destroys the diffraction pattern. The corresponding pattern on the observation screen is shown as line (b) in figure 7.8d. However, coating the object with the square *push out* cloak presented earlier, as shown in figure 7.8c, restores the original diffraction pattern almost entirely. The interference pattern corresponding to the cloaked object is shown as curve (c) in figure 7.8d.

The simulation, shown in the supplementary material [30], confirms that the excellent cloaking for the inclusion position of figure 7.8c, exemplified in figure 7.8d, holds irrespective of the inclusion position. It has thus been conclusively demonstrated that the cloaking is of sufficient quality to render the interference pattern almost immune to movement in the position of the cloaked obstacle. In particular movement of the cloaked obstacle, it would seem, does not yield

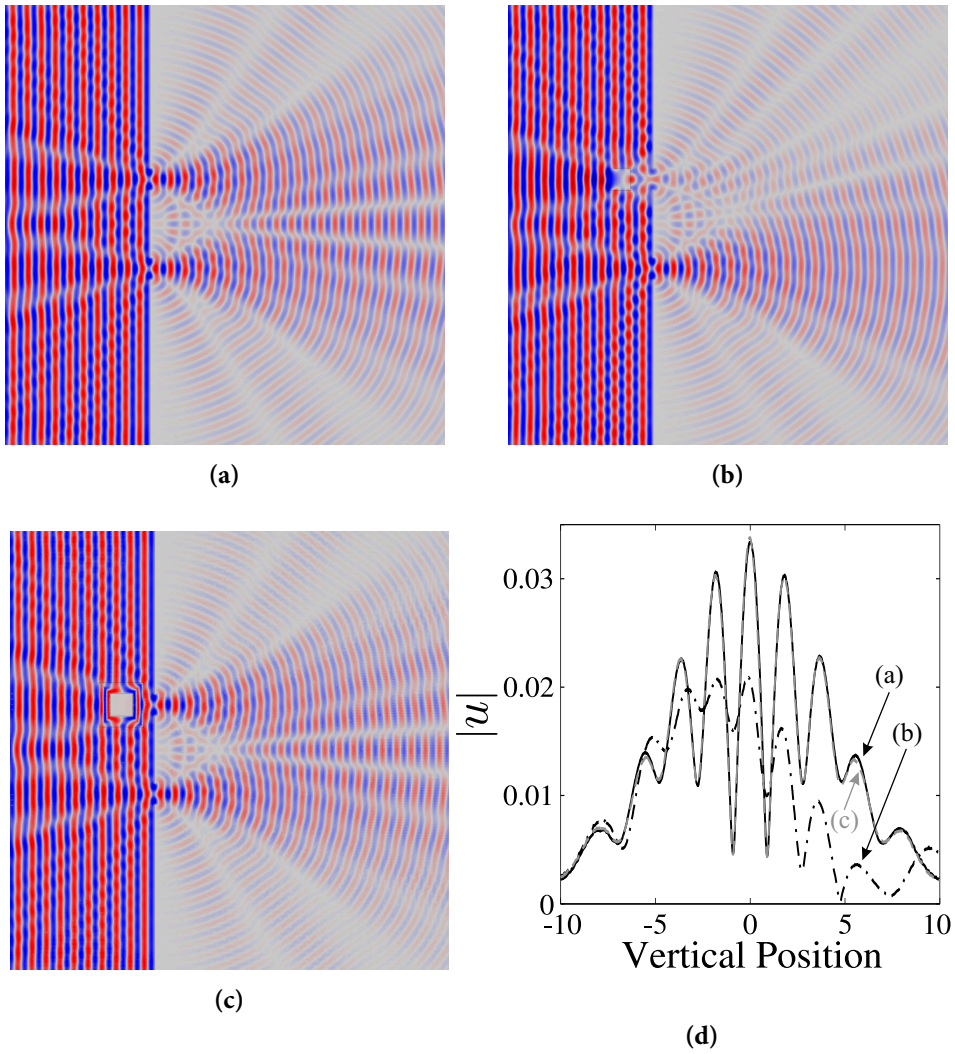


**Figure 7.8:** (a)-(c) The field $u(\boldsymbol{x})$ for the Young's double slit experiment with no inclusion, an uncloaked inclusion, and a cloaked inclusion respectively. (d) A plot of $|u(\boldsymbol{x})|$ over the observation screen illustrating the interference fringes for cases (a)-(c). (An animated version of this figure may be found in the supplementary material [30].)

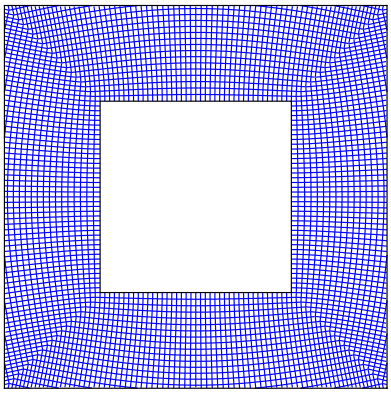

**Figure 7.9:** The lattice formed from the principal directions of the stiffness matrix for the continuum cloak.

any information about the passage of waves through one slit or the other. This consideration would be important if one were able to carry out an experiment in which single quantised elements of vibration were in the system at any given instance in time. The quantum mechanical view would be that, if no path information were available from measurements, the interference fringes behind the double slit should persist.

This proposed quantum experiment raises interesting questions if an appropriate vibration transducer were embedded within the cloak, so that information about vibrations moulded by the cloak were available to experimentalists. One would assume, in line with the results of say optical experiments of the type referred to in [66], that any path information gained in this way would be evident in a change in the fringe pattern. This suggests the interest of a comprehensive quantum mechanical treatment of the interaction between mechanical cloaks and measurement systems.

## 7.3 Cloaking with a lattice

Cloaks designed using transformation optics may have such extreme physical attributes that the requisite materials cannot be physically realised without recourse to metamaterials. It is with this motivation in mind that the following approximate cloak in the low frequency regime is developed. The cloak is constructed as an approximation to the continuum square cloak considered earlier, but is realised using a discrete lattice structure, formed from rods and point masses. The advantage of a discrete structure over a continuous material is that much higher contrasts in material properties are easily realisable using lattices. The development of an approximate cloaking material using a lattice may allow the practical construction of cloaks. In the following discussion, it is emphasised that repeated indices are not summed over.

With reference to the formulae for the Jacobian of the transformation in section 7.1.1, the symmetric stiffness tensors $\boldsymbol{C}^{(i)} = [\mu/J^{(i)}]\boldsymbol{J}^{(i)}\boldsymbol{J}^{(i)\mathrm{T}}$ are positive definite. Therefore, the stiffness matrix admits the following diagonalisation

$$\boldsymbol{C}^{(i)} = \boldsymbol{P}^{(i)\mathrm{T}}\boldsymbol{\Lambda}^{(i)}\boldsymbol{P}^{(i)}, \tag{7.22}$$

where $\boldsymbol{P}^{(i)} = [\boldsymbol{e}_1^{(i)}, \boldsymbol{e}_2^{(i)}]$ are the matrices with columns consisting of the principal directions

(eigenvectors) of $\boldsymbol{C}^{(i)}$, and $\boldsymbol{\Lambda}^{(i)} = \operatorname{diag}(\lambda_1^{(i)}, \lambda_2^{(i)})$ is the diagonal matrix of the corresponding ordered [positive] eigenvalues such that $\lambda_1^{(i)} > \lambda_2^{(i)}$. The eigenvectors yield the principal lattice vectors of the locally orthogonal lattice with homogenised stiffnesses $\lambda_j^{(i)}$ in direction $\boldsymbol{e}_j^{(i)}$. In particular, the lattice nodes lie at the intersection points of the solutions of the following non-linear system of first order differential equations

$$\frac{\mathrm{d}}{\mathrm{d}\tau}\boldsymbol{x}_j^{(i)} = \boldsymbol{e}_j^{(i)}(\boldsymbol{x}_j^{(i)}), \qquad \text{for } i = 1, \dots 4, \text{ and } j = 1, 2, \tag{7.23}$$

for some array of initial positions, where $\boldsymbol{x}_j^{(i)}$ is the position vector along the characteristic defined by $\boldsymbol{e}_j^{(i)}$ inside the $i^{\text{th}}$ side of the cloak and $\tau$ parametrises the curve. Naturally, this would lead to a lattice with curved links. However, for a sufficiently refined lattice the curved members may be replaced with linear links. The lattice links are then the linearisation of the characteristic between two neighbouring nodes on the characteristic. Figure 7.9 shows the geometry of the lattice formed from the principal vectors of the stiffness matrix. Requiring local conservation of flux allows the stiffness of the lattice link parallel to $\boldsymbol{e}_j^{(i)}$ to be determined as $\ell_{ij}\lambda_j^{(i)}$, where $\ell_{ij}$ is the length of the link along $\boldsymbol{e}_j^{(i)}$ . The distribution of nodal mass may be determined by evaluating the integral

$$m(\boldsymbol{x}_{\boldsymbol{p}}) = \int_{\mathcal{A}(\boldsymbol{x}_{\boldsymbol{p}})} \rho(\boldsymbol{x})\,\mathrm{d}\boldsymbol{x},$$

over the unit cell $\mathcal{A}(\boldsymbol{x}_{\boldsymbol{p}})$ containing the lattice node at $\boldsymbol{x}_{\boldsymbol{p}}$.

In principle, the lattice cloak may be constructed exactly as described above and illustrated in figure 7.9. However, for narrow cloaks where $w/a \ll 1$, the locally orthogonal lattice depicted in figure 7.9 may be approximated by a globally orthogonal regular square lattice. A regular square lattice is more convenient to implement compared with the non globally orthogonal lattice generated from the eigendecomposition of the stiffness matrix. Although the geometry of the approximate lattice is regular, it should be emphasised that the stiffness of the links and mass of the nodes vary with position according to the projection of $\boldsymbol{A}(\boldsymbol{x})$ and $\rho(\boldsymbol{x})$ as described above.

### 7.3.1 Geometry and governing equations for an inclusion cloaked by a lattice

Consider a square inclusion $\Omega_0 = \{\boldsymbol{x} : |x_1| < a, |x_2| < a\}$, $a > 0$, embedded in $\mathbb{R}^2$, surrounded by a cloak $\Omega_- = \{\boldsymbol{x} : a < |x_1| < a + w, a < |x_2| < a + w\} \setminus \Omega_0$, where $w > 0$ is the thickness of the cloak. The cloak consists of a discrete lattice structure with lattice points at $\boldsymbol{x} = \ell\boldsymbol{p}$, where $\boldsymbol{p} \in \mathbb{Z}^2 \cap \{\boldsymbol{n} : \ell\boldsymbol{n} \in \Omega_-\}$. The lattice is statically anisotropic with links parallel and perpendicular to the boundaries having contrasting material properties, as shown in figure 7.10.

As for the continuum cloak, solutions of the Helmholtz equation are of primary interest. In particular, the following problem for the field $u(\boldsymbol{x})$ is studied

$$[\mu\nabla\cdot(\nabla) + \varrho\omega^2]u(\boldsymbol{x}) = -\delta(\boldsymbol{x} - \boldsymbol{x}_0), \qquad \boldsymbol{x}, \boldsymbol{x}_0 \in \Omega_+, \tag{7.24}$$

$$[\mu_0\nabla\cdot(\nabla) + \varrho_0\omega^2]u(\boldsymbol{x}) = 0, \qquad \boldsymbol{x} \in \Omega_0, \tag{7.25}$$

$$m(\boldsymbol{p})\omega^2 u(\boldsymbol{p}) + \sum_{\boldsymbol{q}\in\mathcal{N}(\boldsymbol{p})} \ell\eta(\boldsymbol{q}, \boldsymbol{p})\,[u(\boldsymbol{p} + \boldsymbol{q}) - u(\boldsymbol{p})] = 0, \qquad \text{in } \Omega_-, \tag{7.26}$$

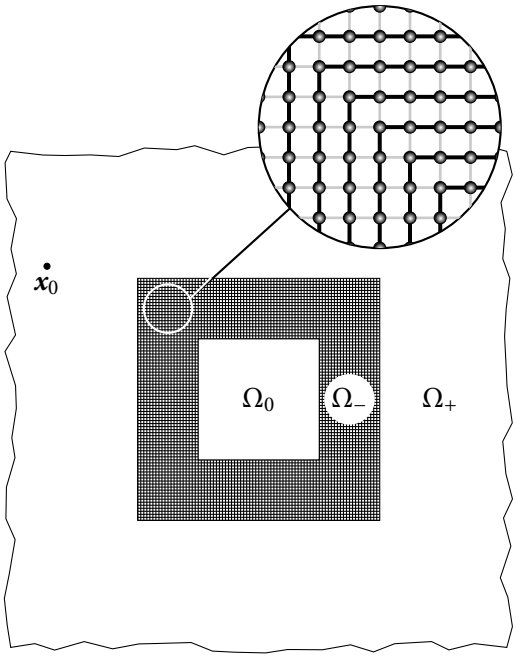


**Figure 7.10:** The lattice cloak $\Omega_-$, surrounding the square inclusion $\Omega_0$, embedded in the ambient medium $\Omega_+$. The thick black lines in the lattice cloak indicate links of high stiffness or conductivity, while the thick grey lines indicate links of low or stiffness conductivity.

where $\boldsymbol{e}_i = [\delta_{i1}, \delta_{i2}]^{\mathrm{T}}$, $\boldsymbol{p} \in \mathbb{Z}^2$, and $\mathcal{N} = \{\pm\boldsymbol{e}_1, \pm\boldsymbol{e}_2\}$ is the set of nearest neighbours. The stiffness and density of the ambient continuum are denoted by $\mu$ and $\varrho$ respectively, whilst the corresponding quantities of the inclusion are denoted by $\mu_0$ and $\varrho_0$. The stiffness of the lattice links are the restriction of the eigenvalues of the stiffness matrix to the links. In particular, for the link connecting nodes $\boldsymbol{p}$ and $\boldsymbol{p}+\boldsymbol{q}$, $\eta(\boldsymbol{q},\boldsymbol{p})$ takes the value $\lambda_1^{(i)}|_{[\ell\boldsymbol{p},\ell(\boldsymbol{p}+\boldsymbol{q})]}$ if the vector $\boldsymbol{q}$ is parallel to the exterior boundary of the cloak, $\Gamma^{(i)}$, and $\lambda_2^{(i)}|_{[\ell\boldsymbol{p},\ell(\boldsymbol{p}+\boldsymbol{q})]}$ otherwise. The corner regions are matched as illustrated in figure 7.10. Here, $\lambda_j^{(i)}|_{[\ell\boldsymbol{p},\ell(\boldsymbol{p}+\boldsymbol{q})]}$ indicates the restriction of $\lambda_j^{(i)}$ to the line $[\ell\boldsymbol{p}, \ell(\boldsymbol{p}+\boldsymbol{q})]$. The associated interface conditions corresponding to continuity of tractions are

$$\boldsymbol{n}\cdot\nabla u(\boldsymbol{x}) = \begin{cases} 0 & \text{for } \boldsymbol{x}\in\partial\Omega^- \text{ and } \boldsymbol{x}\pm\ell\boldsymbol{q}\notin\Omega_- \\ \ell\eta(\mp\boldsymbol{q},\boldsymbol{p})u(\boldsymbol{x}\pm\ell\boldsymbol{q})/\mu & \text{for } \boldsymbol{x}\in\bigcup_i\Gamma^{(i)} \text{ and } \boldsymbol{x}\pm\boldsymbol{q}\in\Omega_- \\ \ell\eta(\mp\boldsymbol{q},\boldsymbol{p})u(\boldsymbol{x}\pm\ell\boldsymbol{q})/\mu_0 & \text{for } \boldsymbol{x}\in\bigcup_i\gamma^{(i)} \text{ and } \boldsymbol{x}\pm\boldsymbol{q}\in\Omega_- \end{cases}, \qquad i=1,\ldots,4, \quad (7.27)$$

and the Sommerfeld radiation condition at infinity. The quantity $\eta(\boldsymbol{q},\boldsymbol{p})$ is the projection of the diagonalised stiffness matrix onto the lattice link connecting lattice points $\boldsymbol{p}$ and $\boldsymbol{p}+\boldsymbol{q}$.

Physically, (7.24)–(7.27) corresponds to the problem of the propagation of time-harmonic waves of angular frequency $\omega$ generated by a point load at $\boldsymbol{x}_0$. The field $u(\boldsymbol{x})$ then corresponds to the out-of-plane displacement amplitude field. The region $\Omega_-$ consists of an array of nodes of mass $m$, connected by massless rods of length $\ell$ and stiffness according to their orientation.

| Source Position | Frequency | Scattering Measure $\mathcal{E}$ Uncloaked | Cloaked | $Q$ |
|---|---|---|---|---|
| | | Scattering region $\mathcal{R}_1$ | | |
| $[-3,0]^{\mathrm{T}}$ | 3 | 0.1430 | 0.1662 | 0.1617 |
| $[-3,3]^{\mathrm{T}}/\sqrt{2}$ | 3 | 0.1113 | 0.1816 | 0.6327 |
| $[-3,0]^{\mathrm{T}}$ | 5 | 0.1529 | 0.2495 | 0.6318 |
| $[-3,3]^{\mathrm{T}}/\sqrt{2}$ | 5 | 0.2002 | 0.3538 | 0.7676 |
| | | Scattering region $\mathcal{R}_2$ | | |
| $[-3,0]^{\mathrm{T}}$ | 3 | 0.2341 | 0.3362 | 0.4363 |
| $[-3,0]^{\mathrm{T}}$ | 5 | 0.3224 | 0.4671 | 0.4489 |
| | | Scattering region $\mathcal{R}_3$ | | |
| $[-3,3]^{\mathrm{T}}/\sqrt{2}$ | 3 | 0.1578 | 0.3455 | 1.189 |
| $[-3,3]^{\mathrm{T}}/\sqrt{2}$ | 5 | 0.2988 | 0.6011 | 1.012 |

**Table 7.3:** The scattering measures corresponding to the simulations for the *basic lattice model* shown in figures 7.11 and 7.12.

### 7.3.2 Illustrative lattice simulations

The approximate lattice cloaks were examined using the finite element software Comsol Multiphysics®. Perfectly matched layers were used in the vicinity of the boundary of the computational domain in order to simulate an infinite domain. For the purpose of illustration, a square of semi-width $a = 0.5$, surrounded by a lattice cloak with $w = 0.1$ and links of length $5 \times 10^{-3}$ was used. The inclusion is located at the origin of the computational window.

#### A basic lattice cloak

Before proceeding to the illustrative simulations for the regular lattice with heterogeneous distributions of stiffness and mass, it is instructive to consider a simple approximation. Many cloaks created via transformation optics have the general characteristic of having a high phase speed parallel to the boundary of the cloak, and a low phase speed in the direction normal to the boundary (see [39] among others). Therefore, as an initial approximation, the case of a regular square lattice with a homogeneous, but orthotropic distribution of stiffness and a homogeneous distribution of mass is considered. Consider the right-hand side of the cloak $\Omega_{-}^{(1)}$. For a narrow cloak with $w/a \ll 1$, $x_1 \sim a+w$ and hence the density may be approximated by $\rho \sim 1+a/w$. The greatest contrast in stiffness occurs at $x_2 = 0$, thus the vertical links are assigned stiffness $\ell\lambda_1^{(1)}(a+w,0)$ and the horizontal links stiffness $\ell\lambda_2^{(1)}(a+w,0)$. The mass of the nodes is $\ell^2(1+a/w)$. The material properties of the remaining three sides of the cloak are adjusted accordingly.

Figures 7.11 and 7.12 show the field $u(\boldsymbol{x})$ for the uncloaked inclusion (a) and (d), and the inclusion cloaked with this *basic* cloak (b) and (e). For $\omega = 3$ figure 7.11 indicates that the *basic* cloak partially mitigates the shadow cast by the inclusion and acts to reform the cylindrical wave fronts behind the inclusion. As illustrated by figure 7.12, this partial cloaking effect deteriorates with increasing frequency. Indeed, in some cases, the presence of the lattice cloak seems to increase the shadow region. Table 7.3 details the values of the scattering measures for the fields illustrated in figure 7.11 and 7.12. The scattering measures shown in table 7.3 suggest

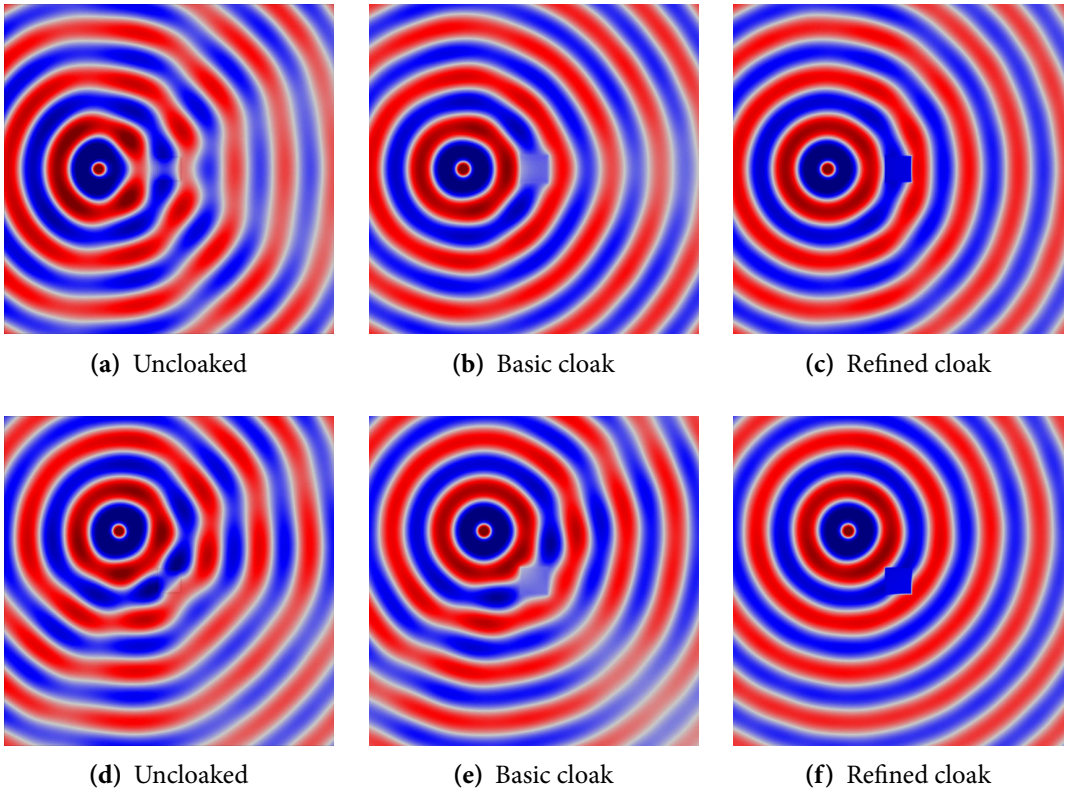

**(a)** Uncloaked **(b)** Basic cloak **(c)** Refined cloak

**(d)** Uncloaked **(e)** Basic cloak **(f)** Refined cloak

**Figure 7.11:** Plots of the field $u(\boldsymbol{x})$ for a cylindrical wave incident on a square inclusion in the absence of a cloak (parts (a) and (d)), a square inclusion coated with the *basic* lattice (parts (b) and (e)), and an inclusion coating with the refined lattice (parts (c) and (f)). Here the angular frequency of excitation is $\omega = 3$ and the source is located at $\boldsymbol{x}_0 = [-3, 0]^{\mathrm{T}}$ in (a)–(c), and at $\boldsymbol{x}_0 = [-3, 3]^{\mathrm{T}}/\sqrt{2}$ in (e)–(f). The colour scale is as indicated in figure 7.4.

that, although visually the basic lattice cloak appears to work reasonably well, this may not be the case. The fact that the basic lattice cloak increases the scattering measure compared with the uncloaked inclusion further emphasises the need for an objective measure of the quality of cloaks, rather than simply relying on visual observations.

This increase in the scattering measure by the basic lattice cloak motivates the introduction of the following refined model.

### A refined lattice cloak

Consider now the lattice described in section 7.3.1, i.e. the regular square lattice with inhomogeneous distribution of stiffness and mass. Figures 7.11 and 7.12 show the field $u(\boldsymbol{x})$ for the uncloaked inclusion and the inclusion with a lattice cloaking. With reference to the simulations for the *basic* cloak (b) and (e) the *refined* lattice cloak (c) and (f), it is observed that the efficiency of the *refined* lattice cloak, whilst not as high as that of the continuum cloak, is much greater than that of the *basic* cloak. The table of scattering measures for the approximate cloak is shown in table 7.4 and further evidences the effectiveness of the *refined* lattice cloak. Indeed, for several simulations (in particular those where the scattering measure is taken over the forward or corner scattering regions $\mathcal{R}_1$ and $\mathcal{R}_2$ respectively) the efficiency of the *refined* cloak in reducing the scattering measure approaches that of the continuum cloak.

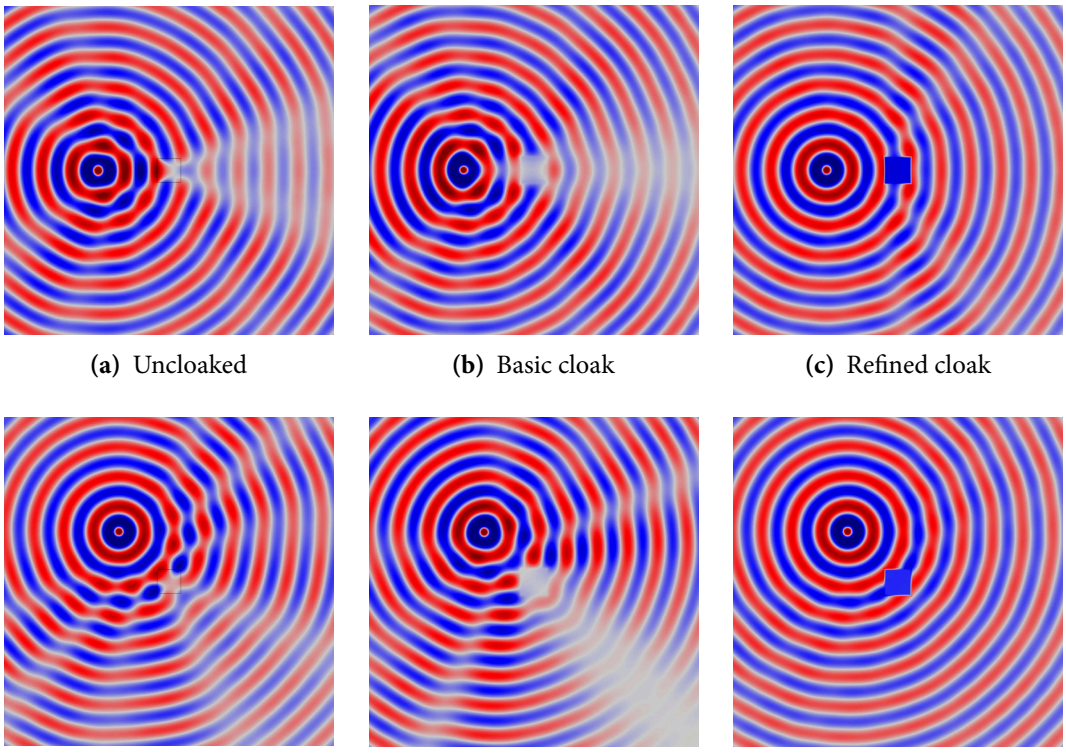

**(a)** Uncloaked **(b)** Basic cloak **(c)** Refined cloak

**(d)** Uncloaked **(e)** Basic cloak **(f)** Refined cloak

**Figure 7.12:** Plots of the field $u(\boldsymbol{x})$ for a cylindrical wave incident on a square inclusion in the absence of a cloak (parts (a) and (d)), a square inclusion coated with the *basic lattice model* (parts (b) and (e)), and an inclusion coating with the refined lattice (parts (c) and (f)). Here the angular frequency of excitation is $\omega = 5$ and the source is located at $\boldsymbol{x}_0 = [-3, 0]^{\mathrm{T}}$ in (a)–(c), and at $\boldsymbol{x}_0 = [-3, 3]^{\mathrm{T}}/\sqrt{2}$ in (e)–(f). The colour scale is as indicated in figure 7.4.

| Source | | Scattering Measure $\mathcal{E}$ | | |
|---|---|---|---|---|
| Position | Frequency | Uncloaked | Cloaked | Q |
| | | Scattering region $\mathcal{R}_1$ | | |
| $[-3, 0]^{\mathrm{T}}$ | 3 | 0.1430 | 0.01191 | 0.8929 |
| $[-3, 3]^{\mathrm{T}}/\sqrt{2}$ | 3 | 0.1113 | $3.385 \times 10^{-3}$ | 0.9763 |
| $[-3, 0]^{\mathrm{T}}$ | 5 | 0.1529 | 0.04324 | 0.7173 |
| $[-3, 3]^{\mathrm{T}}/\sqrt{2}$ | 5 | 0.2002 | 0.03125 | 0.8438 |
| | | Scattering region $\mathcal{R}_2$ | | |
| $[-3, 0]^{\mathrm{T}}$ | 3 | 0.2341 | 0.01150 | 0.9508 |
| $[-3, 0]^{\mathrm{T}}$ | 5 | 0.3224 | 0.0172 | 0.9508 |
| | | Scattering region $\mathcal{R}_3$ | | |
| $[-3, 3]^{\mathrm{T}}/\sqrt{2}$ | 3 | 0.1578 | $5.047 \times 10^{-3}$ | 0.9680 |
| $[-3, 3]^{\mathrm{T}}/\sqrt{2}$ | 5 | 0.2988 | 0.02114 | 0.9292 |

**Table 7.4:** The scattering measures corresponding to the simulations shown for the *refined lattice model* in figures 7.11 and 7.12.

As expected the effectiveness of the lattice cloaks reduce with increasing frequency. However, for sufficiently low frequencies the *refined* lattice cloak in particular, works well.

## 7.4 Remarks

The work reported in this, the final chapter of the present thesis, represents a comprehensive treatment of a non-singular cloak for a square inclusion. The significant advantage of this continuous cloak is the straightforward correspondence with a discrete metamaterial lattice structure. Such a connection may present a method through which a physical cloak may be fabricated. The material and geometric properties of the discrete cloak are directly linked to the properties of the continuum cloak, and hence, to the properties of the formal map. The effectiveness of such discrete cloaks, particularly at low frequencies, was demonstrated through numerical simulations and the use of objective scattering measures.

Particular attention was paid to the objective measurement of the quality of the cloaking effect. The quality of the cloaks was primarily assessed using a scattering measure introduced as an $L_2$ norm of the difference between the cloaked field and the ideal unperturbed field. A further demonstration of the efficacy of the square *push out* cloak was presented via the classical Young's double slit experiment. It was shown that the interference pattern on the observation screen was significantly modified when an obstacle was place in front of one of the apertures. However, if the obstacle was cloaked then the interference pattern remained almost entirely unperturbed. This numerical experiment presents a further, perhaps more interesting, method through which the quality of particular cloaks may be examined. Moreover, the experiment raises interesting questions regarding the interaction between cloaking and quantum mechanics.

# *Chapter Eight*

# Concluding remarks

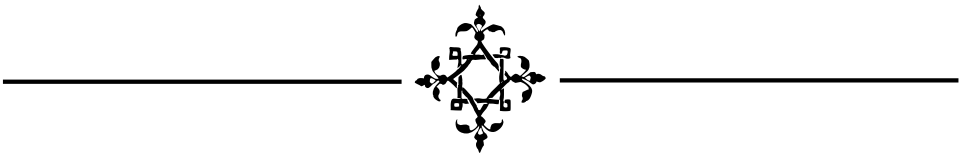

The present text represents a comprehensive study of a range of physical problems which may be described by the unified theme of *the dynamic response of metamaterial structures*. Discrete lattice models were first employed by Newton [112], who used simple mass-spring systems to study the propagation of sound. As exemplified by the present thesis and references herein, such lattice models remain both useful and interesting systems to study, providing a range of problems and many fascinating phenomena. The dynamic response of structured media depends on several factors including the geometrical and material properties of the micro-structure in addition to the external load (e.g. applied force or incident wave). For low-frequencies, the structured medium is often homogenised with the effective material properties being determined from the static response. However, as demonstrated in chapter 3, the effective material properties derived as a limiting case of the dynamic response (for small frequency and wave number) may not necessarily correspond to those derived from the purely static response. Moreover, in the finite frequency regime the response of discrete lattice systems is strongly anisotropic yielding striking *primitive waveforms* as shown in chapter 4. Such effects can be employed to create interesting systems such as flat *"metamaterial lenses"*, which exhibit the novel effects of filtering, focusing, and negative refraction for elastic media. It is also possible to control the width and position of stop bands as well as the resonant frequencies for discrete lattice structures. With this in mind, compact estimates for the widths of stop bands, and the position of saddle points, maxima and minima of the dispersion surfaces were derived in chapter 3.

The dynamic response of lattices with defects, considered in chapters 5 and 6, also brings many interesting features. In particular, for rectilinear defects in square lattices it was demonstrated that a connection can be made with the problem of a infinite line defect and a homogenised continuous inclusion. In chapter 5, the defect was created by removing some mass from a line of lattice nodes, such that their mass was smaller than those of the ambient lattice. For one- and three-dimensional multi-atomic lattices, there exists some lower bound on the amount of mass that should be removed from the defect nodes such that a localised mode may be initiated [98, 109].

However, as shown in chapter 5, this is not the case for uniform two-dimensional lattices: there is no lower bound on the mass that should be removed from a defect node to initiate a localised mode. The primary tool used to study these localised modes for finite rectilinear defects are the lattice Green's functions, which have direct connections to so-called *Watson Integrals* (see [150] and references therein). In general, the lattice Green's functions cannot be expressed in terms of elementary functions. Nevertheless, their representation in terms of hypergeometric functions allows compact asymptotic expansions to be derived for band-edge modes using analytic continuation. Discrete metamaterial structures also have wide applicability in coupled systems, such as the thermoelastic problem discussed in chapter 6. It was demonstrated that a connection can be made between the discrete problem for a thermally striped lattice and the corresponding problem for the continuum. In particular, it was shown that it is possible to define an *"effective stress intensity factor"* for the discrete thermoelastic lattice. Moreover, for sufficiently long cracks and low frequencies, the peak-to-peak amplitude of this *"effective stress intensity factor"* was shown to be lower than that of the continuum. In this sense, the discrete lattice microstructure is said to reduce the stress intensity factor of an edge-cracked plate similar to the case of micro-structured continua [114].

One novel area of research in which metamaterials have found extensive use is that of invisibility cloaks (see, for example, [89, 137, 141]). In chapter 7, a design for a square metamaterial cloak for fields governed by the Helmholtz equation was discussed. The material properties of the cloak are continuous and piecewise smooth on the closure of the cloak. Nevertheless, the contrast in principle stiffnesses required to achieve the cloaking effect is far beyond what can be realised with *"natural"* materials. However, the metamaterial lattice model presented in chapter 7 is far less restrictive. With the approximate discrete mass-spring cloak design presented in this thesis it was possible to obtain the requisite contrast in principle stiffnesses to physically realise the cloaking effect. The material and geometric properties of the lattice cloak were derived, analytically, for a continuum cloak. As demonstrated by the numerical simulations presented in chapter 7, such an approximate lattice cloak provides effective cloaking particularly in the low frequency regime.

In summary, the present thesis provides a detailed study of wave propagation and the dynamic response of metamaterial structures in the physical settings of out-of-plane and in-plane elasticity, electromagnetism, acoustics, heat conduction, and thermoelasticty. A wide range of analytical and numerical techniques have been employed to study the problems presented herein, leading to connections with other fields. To conclude, wave propagation in metamaterial structures remains an active area of research with many interesting phenomena yet to be investigated. The reader is referred to the concluding remarks at the end of each chapter for a more detailed summary of the work contained within the present thesis.

# Bibliography

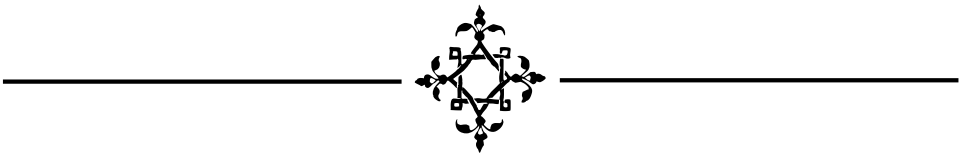


[1] Adams SD, Cherednichenko KD, Craster RV, Guenneau S, et al. (2010) High-frequency spectral analysis of thin periodic acoustic strips: theory and numerics. *European Journal of Applied Mathematics* **21**, 557–590.

[2] Antonakakis T, Craster R, Guenneau S (2013) Moulding flexural waves in elastic plates lying atop a faqir's bed of nails. *arXiv preprint arXiv:1301.7653* .

[3] Antonakakis T, Craster RV, Guenneau S (2013) Asymptotics for metamaterials and photonic crystals. *Proceedings of the Royal Society A: Mathematical, Physical and Engineering Science* **469**.

[4] Askar A, Cakmak AS (1968) A structural model of a micropolar continuum. *International Journal of Engineering Science* **6**, 583–589.

[5] Ayzenberg-Stepanenko MV, Slepyan LI (2008) Resonant-frequency primitive waveforms and star waves in lattices. *Journal of Sound and Vibration* **313**, 812–821.

[6] Barenblatt GI (1962) The mathematical theory of equilibrium cracks in brittle fracture. *Advances in applied mechanics* **7**, 55–129.

[7] Bender CM, Orszag SA (1999) *Advanced mathematical methods for scientists and engineers I: Asymptotic methods and perturbation theory*, vol. 1. Springer Verlag.

[8] Bigoni D, Movchan AB (2002) Statics and dynamics of structural interfaces in elasticity. *International Journal of Solids and Structures* **39**, 4843 – 4865.

[9] Born M, Huang K (1954) *Dynamical Theory of Crystal Lattices*. International series of monographs on physics. Oxford University Press on Demand.

[10] Born M, Wolf E (1959) *Principles of Optics*. London: Pergamon, first edn.

[11] Borwein J, Glasser L, McPhedran R, Wan J, Zucker J (2013) Lattice sums: Then and now. *Encyclopedia of Mathematics and its Applications* **150**.

[12] Brillouin L (1926) La mécanique ondulatoire de schrödinger; une méthode générale de résolution par approximations successives. *Comptes Rendus de l'Academie des Sciences* **183**, 24–26.

[13] Brillouin L (1926) Remarques sur la mécanique ondulatoire. *J. Phys. Radium* **7**, 353–368.

[14] Brillouin L (1953) *Wave propagation in periodic structures*. Dover.

[15] Broberg KB (1999) *Cracks and fracture*. Academic Press.

[16] Brun M, Guenneau S, Movchan A, Bigoni D (2010) Dynamics of structural interfaces: Filtering and focussing effects for elastic waves. *Journal of the Mechanics and Physics of Solids* **58**, 1212 – 1224.

[17] Brun M, Guenneau S, Movchan AB (2009) Achieving control of in-plane elastic waves. *Applied Physics Letters* **94**, 061903–061903.

[18] Bueckner HF (1970) Novel principle for the computation of stress intensity factors. *Zeitschrift fuer Angewandte Mathematik & Mechanik* **50**.

[19] Bühring W (1992) Generalized hypergeometric functions at unit argument. *Proceedings of the American Mathematical Society* **114**, pp. 145–153.

[20] Callaway J (1964) Theory of scattering in solids. *Journal of Mathematical Physics* **5**, 783.

[21] Cantoni A, Butler P (1976) Eigenvalues and eigenvectors of symmetric centrosymmetric matrices. *Linear Algebra and its Applications* **13**, 275–288.

[22] Carta G, Brun M (2012) A dispersive homogenization model based on lattice approximation for the prediction of wave motion in laminates. *Journal of applied mechanics* **79**.

[23] Carta G, Jones IS, Brun M, Movchan NV, Movchan AB (2013) Crack propagation induced by thermal shocks in structured media. *International Journal of Solids and Structures* .

[24] Chen H, Zheng B (2012) Broadband polygonal invisibility cloak for visible light. *Scientific Reports* **2**.

[25] Chen X, Luo Y, Zhang J, Jiang K, Pendry JB, Zhang S (2011) Macroscopic invisibility cloaking of visible light. *Nature Communications* **2**, 176.

[26] Cherepanov G (1967) The propagation of cracks in a continuous medium. *Journal of Applied Mathematics and Mechanics* **31**, 503–512.

[27] Christensen RM (2000) Mechanics of cellular and other low-density materials. *International Journal of Solids and Structures* **37**, 93–104.

[28] Colquitt DJ, Jones IS, Movchan NV, Brun AB, McPhedran RC (2013) Making waves round a structured cloak: Lattices, negative refraction and fringes. *Proceedings of the Royal Society A: Mathematical, Physical and Engineering Science* .

[29] Colquitt DJ, Jones IS, Movchan NV, Movchan AB (2011) Dispersion and localization of elastic waves in materials with microstructure. *Proceedings of the Royal Society A: Mathematical, Physical and Engineering Science* **467**, 2874–2895.

[30] Colquitt DJ, Jones IS, Movchan NV, Movchan AB, Brun M, McPhedran RC (2013). Supplementary material. (doi: 10.6084/m9.figshare.746922).

[31] Colquitt DJ, Jones IS, Movchan NV, Movchan AB, McPhedran RC (2012) Dynamic anisotropy and localization in elastic lattice systems. *Waves in Random and Complex Media* **22**, 143–159.

[32] Colquitt DJ, Nieves MJ, Jones IS, Movchan AB, Movchan NV (2013) Localization for a line defect in an infinite square lattice. *Proceedings of the Royal Society A: Mathematical, Physical and Engineering Science* **469**.

[33] Colquitt DJ, Nieves MJ, Jones IS, Movchan NV, Movchan AB (2012) Trapping of a crack advancing through an elastic lattice. *International Journal of Engineering Science* .

[34] Craster RV, Antonakakis T, Makwana M, Guenneau S (2012) Dangers of using the edges of the brillouin zone. *Physical Review B* **86**, 115130.

[35] Craster RV, Guenneau S, Kaplunov J, Nolde E (2011) On a class of three-phase checkerboards with unusual effective properties. *Comptes Rendus Mécanique* **339**, 411–417.

[36] Craster RV, Kaplunov J, Nolde E, Guenneau S (2011) High-frequency homogenization for checkerboard structures: defect modes, ultrarefraction, and all-angle negative refraction. *JOSA A* **28**, 1032–1040.

[37] Craster RV, Kaplunov J, Pichugin A (2010) High-frequency homogenization for periodic media. *Proceedings of the Royal Society A: Mathematical, Physical and Engineering Science* **466**, 2341–2362.

[38] Craster RV, Kaplunov J, Postnova J (2010) High-frequency asymptotics, homogenisation and localisation for lattices. *The Quarterly Journal of Mechanics and Applied Mathematics* **63**, 497–519.

[39] Cummer SA, Schurig D (2007) One path to acoustic cloaking. *New Journal of Physics* **9**, 45–45.

[40] Delves RT, Joyce GS (2007) Derivation of exact product forms for the simple cubic lattice green function using fourier generating functions and lie group identities. *Journal of Physics A: Mathematical and Theoretical* **40**, 8329–8343.

[41] Dossou KB, Botten LC, McPhedran RC, Poulton CG (2008) Shallow defect states in two-dimensional photonic crystals. *Physical Review A* **77**, 1–18.

[42] Dowling J. Photonic & sonic band-gap and metamaterial bibliography. `http://phys.lsu.edu/~jdowling/pbgbib.html`.

[43] Eringen A (1966) Linear theory of micropolar elasticity. *Indiana Univ. Math. J.* **15**, 909–923.

[44] Eringen AC (1999) *Theory of micropolar elasticity*. Berlin: Springer.

[45] Farhat M, Guenneau S, Enoch S (2009) Ultrabroadband elastic cloaking in thin plates. *Physical Review Letters* **103**, 24301.

[46] Farhat M, Guenneau S, Enoch S, Movchan AB, Zolla F, Nicolet A (2008) A homogenization route towards square cylindrical acoustic cloaks. *New Journal of Physics* **10**, 115030.

[47] Fett T, Munz D (1997) *Stress intensity factors and weight functions*. Computational Mechanics Publications Southampton.

[48] Gallina I, Castaldi G, Galdi V, Alù A, Engheta N (2010) General class of metamaterial transformation slabs. *Physical Review B* **81**, 125124.

[49] Gei M, Movchan AB, Bigoni D (2009) Band-gap shift and defect-induced annihilation in prestressed elastic structures. *Journal of Applied Physics* **105**, 063507–063507.

[50] Gibson LJ, Ashby MF (1997) *Cellular solids*. Cambridge Solid State Science Series. Cambridge: Cambridge University Press, second edn.

[51] Gonella S, Ruzzene M (2008) Homogenization and equivalent in-plane properties of two-dimensional periodic lattices. *International Journal of Solids and Structures* **45**, 2897–2915.

[52] Goodman J (2005) *Introduction to Fourier Optics*. Colorado: Roberts & Company, third edn.

[53] Graff KF (1975) *Wave motion in elastic solids*. London: Oxford University Press.

[54] Greenleaf A, Kurylev Y, Lassas M, Leonhardt U, Uhlmann G (2012) Cloaked electromagnetic, acoustic, and quantum amplifiers via transformation optics. *Proceedings of the National Academy of Sciences* **109**, 10169–10174.

[55] Greenleaf A, Kurylev Y, Lassas M, Uhlmann G (2007) Full-wave invisibility of active devices at all frequencies. *Communications in Mathematical Physics* **275**, 749–789.

[56] Greenleaf A, Kurylev Y, Lassas M, Uhlmann G (2008) Comment on "Scattering theory derivation of a 3D acoustic cloaking shell". *arXiv preprint arXiv:0801.3279* .

[57] Greenleaf A, Lassas M, Uhlmann G (2003) Anisotropic conductivities that cannot be detected by EIT. *Physiological Measurement* **24**, 413.

[58] Greenleaf A, Lassas M, Uhlmann G (2003) On nonuniqueness for Calderon's inverse problem. *Mathematical Research Letters* **10**, 685–694.

[59] Griffith AA (1921) The phenomena of rupture and flow in solids. *Philosophical transactions of the royal society of london. Series A, containing papers of a mathematical or physical character* **221**, 163–198.

[60] Guenneau S, Amra C, Veynante D (2012) Transformation thermodynamics: cloaking and concentrating heat flux. *Optics Express* **20**, 8207–8218.

[61] Guenneau S, McPhedran RC, Enoch S, Movchan AB, Farhat M, Nicorovici NP (2010) The colours of cloaks. *Journal of Optics* **13**, 024014.

[62] Guenneau S, Movchan A, Pétursson G, Ramakrishna S (2007) Acoustic metamaterials for sound focusing and confinement. *New Journal of Physics* **9**, 399.

[63] Guinea GV, Planas J, Elices M (2000) KI evaluation by the displacement extrapolation technique. *Engineering Fracture Mechanics* **66**, 243–255.

[64] Irwin GR (1957) Analysis of stresses and strains near the end of a crack traversing a plate. *J. Appl. Mech.* .

[65] Irwin GR (1960) Fracture mechanics. In JN Goodyear, NJ Hoff, eds., *Structural Mechanics: Proceedings of the 1st Symposium on Naval Structural Mechanics*, 557–591. New York: Pergamon Press.

[66] Jacques V, Wu E, Grosshans F, Treussart F, Grangier P, Aspect A, Roch JF (2007) Experimental realization of wheeler's delayed-choice gedanken experiment. *Science* **315**, 966–968.

[67] Jacques V, Wu E, Grosshans F, Treussart F, Grangier P, Aspect A, Roch JF (2008) Delayed-choice test of quantum complementarity with interfering single photons. *Physical review letters* **100**, 220402.

[68] Jeffreys H (1925) On certain approximate solutions of linear differential equations of the second order. *Proceedings of the London Mathematical Society* **2**, 428–436.

[69] Jiang WX, Chin JY, Cui TJ (2009) Anisotropic metamaterial devices. *Materials Today* **12**, 26–33.

[70] Joannopoulos JD, Johnson SG, Winn JN, Meade RD (2011) *Photonic crystals: molding the flow of light*. Princeton university press.

[71] Jones IS (1997) The frequency response model of thermal striping for cylindrical geometries. *Fatigue & Fracture of Engineering Materials & Structures* **20**, 871–882.

[72] Jones IS (1999) The application of a displacement controlled weight function for a single edge cracked plate to thermal fatigue damage assessment. *Engineering fracture mechanics* **62**, 249–266.

[73] Jones IS (2003) Small edge crack in a semi-infinite solid subjected to thermal stratification. *Theoretical and applied fracture mechanics* **39**, 7–21.

[74] Jones IS (2004) Methods of assessment of thermal striping fatigue damage. In *IUTAM Symposium on Asymptotics, Singularities and Homogenisation in Problems of Mechanics*, 229–239. Springer.

[75] Jones IS (2005) Impulse response model of thermal striping for hollow cylindrical geometries. *Theoretical and applied fracture mechanics* **43**, 77–88.

[76] Jones IS (2006) Thermal striping fatigue damage in multiple edge-cracked geometries. *Fatigue & fracture of engineering materials & structures* **29**, 123–134.

[77] Jones IS, Lewis MWJ (1994) A frequency response method for calculating stress intensity factors due to thermal striping loads. *Fatigue & Fracture of Engineering Materials & Structures* **17**, 709–720.

[78] Jones IS, Lewis MWJ (1995) The effect of various constraint conditions in the frequency response model of thermal striping. *Fatigue & Fracture of Engineering Materials & Structures* **18**, 489–502.

[79] Jones IS, Lewis MWJ (1996) An impulse response model for the prediction of thermal striping damage. *Engineering fracture mechanics* **55**, 795–812.

[80] Jones IS, Movchan AB (2007) Bloch–floquet waves and controlled stop bands in periodic thermo-elastic structures. *Waves in Random and Complex Media* **17**, 429–438.

[81] Jones IS, Movchan AB, Gei M (2011) Waves and damage in structured solids with multi-scale resonators. *Proceedings of the Royal Society A: Mathematical, Physical and Engineering Science* **467**, 964–984.

[82] Joyce G, Zucker IJ (2001) Evaluation of the watson integral and associated logarithmic integral for the d-dimensional hypercubic lattice. *Journal of Physics A: Mathematical and General* **34**, 7349–7354.

[83] Kafadar CB, Eringen AC (1971) Micropolar media□i the classical theory. *International Journal of Engineering Science* **9**, 271–305.

[84] Kevorkian J, Cole JD (1996) Multiple scale and singular perturbation methods(book). *New York: Springer-Verlag, Inc, 1996.* .

[85] Kittel C (1995) *Introduction to Solid State Physics*. London: John Wiley & Sons, 7th edn.

[86] Kohn RV, Shen H, Vogelius MS, Weinstein MI (2008) Cloaking via change of variables in electric impedance tomography. *Inverse Problems* **24**, 015016.

[87] Kramers HA (1926) Wellenmechanik und halbzahlige quantisierung. *Zeitschrift für Physik* **39**, 828–840.

[88] Kunin IA (1982) *Elastic media with microstructure*. Berlin: Springer-Verlag.

[89] Landy N, Smith DR (2012) A full-parameter unidirectional metamaterial cloak for microwaves. *Nature Materials* .

[90] Langley R (1996) The Response of Two-Dimensional Periodic Structures To Point Harmonic Forcing. *Journal of Sound and Vibration* **197**, 447–469.

[91] Langley R (1997) The Response of Two-Dimensional Periodic Structures To Impulsive Point Loading. *Journal of Sound and Vibration* **201**, 235–253.

[92] Leonhardt U (2006) Optical conformal mapping. *Science* **312**, 1777–1780.

[93] Li J, Huang Y (2012) Mathematical simulation of cloaking metamaterial structures. *Advances in Applied Mathematics and Mechanics* **4**, 93–101.

[94] Li J, Pendry JB (2008) Hiding under the carpet: a new strategy for cloaking. *Physical Review Letters* **101**, 203901.

[95] Mahmoodian S, McPhedran RC, de Sterke C, Dossou KB, Poulton CG, Botten LC (2009) Single and coupled degenerate defect modes in two-dimensional photonic crystal band gaps. *Physical Review A* **79**, 1–12.

[96] Makwana M, Craster RV (2013) Localised point defect states in asymptotic models of discrete lattices. *The Quarterly Journal of Mechanics and Applied Mathematics* .

[97] Maradudin AA (1965) Some effects of point defects on the vibrations of crystal lattices. *Reports on Progress in Physics* **28**, 331–380.

[98] Maradudin AA, Lifshitz I, Kosevich A, Cochran W, Musgrave M (1969) *Lattice dynamics*. Benjamin.

[99] Martin PA (2006) Discrete scattering theory: Green's function for a square lattice. *Wave Motion* **43**, 619–629.

[100] Martinsson PG, Babuška I (2007) Homogenization of materials with periodic truss or frame micro-structures. *Mathematical Models and Methods in Applied Sciences* **17**, 805–832.

[101] Martinsson PG, Movchan A (2003) Vibrations of Lattice Structures and Phononic Band Gaps. *The Quarterly Journal of Mechanics and Applied Mathematics* **56**, 45–64.

[102] Maz'ya VG, Nazarov SA, Plamenevskiĭ BA (2000) *Asymptotic theory of elliptic boundary value problems in singularly perturbed domains*, vol. 2, chap. 20. Birkhäuser.

[103] McPhedran RC, Botten LC, McOrist J, Asatryan AA, de Sterke CM, Nicorovici NA (2004) Density of states functions for photonic crystals. *Phys. Rev. E* **69**, 016609.

[104] Milton GW, Briane M, Willis JR (2006) On cloaking for elasticity and physical equations with a transformation invariant form. *New Journal of Physics* **8**, 248.

[105] Milton GW, Willis JR (2007) On modifications of Newton's second law and linear continuum elastodynamics. *Proceedings of the Royal Society A: Mathematical, Physical and Engineering Science* **463**, 855–880.

[106] Mishuris GS, Movchan AB, Slepyan LI (2009) Localised knife waves in a structured interface. *Journal of the Mechanics and Physics of Solids* **57**, 1958–1979.

[107] Morozov NF (1984) *Mathematical problems of crack theory*. Moscow: Nauka.

[108] Movchan AB, Jones IS (2006) Asymptotic and numerical study of a surface breaking crack subject to a transient thermal loading. *Acta Mechanica Sinica* **22**, 22–27.

[109] Movchan AB, Slepyan LI (2007) Band gap green's functions and localized oscillations. *Proceedings of the Royal Society A: Mathematical, Physical and Engineering Sciences* **463**, 2709–2727.

[110] Musgrave MJ (1970) *Crystal acoustics*, vol. 184. Holden-Day San Francisco.

[111] Nazarov SA, Paukshto MV (1984) *Discrete models and homogenization in problems of the elastic theory*. Leningrad: Leningrad University.

[112] Newton I (1687) *Principia*. London, UK: The Royal Society.

[113] Nieves M, Movchan A, Jones I (2012) Analytical model of thermal striping for a micro-cracked solid. *International Journal of Solids and Structures* **49**, 1189 – 1194.

[114] Nieves MJ, Movchan AB, Jones IS (2011) Asymptotic study of a thermoelastic problem in a semi-infinite body containing a surface-breaking crack and small perforations. *The Quarterly Journal of Mechanics and Applied Mathematics* **64**, 349–369.

[115] Nieves MJ, Movchan AB, Jones IS, Mishuris G (2013) Propagation of slepyan's crack in a non-uniform elastic lattice. *Journal of the Mechanics and Physics of Solids* .

[116] Norris AN (2008) Acoustic cloaking theory. *Proceedings of the Royal Society A: Mathematical, Physical and Engineering Science* **464**, 2411–2434.

[117] Norris AN, Shuvalov AL (2011) Elastic cloaking theory. *Wave Motion* **48**, 525–538.

[118] Nye J (1999) *Natural Focusing and Fine Structure of Light*. London: Institute of Physics Publishing, first edn.

[119] Olver F (1974) *Asymptotics and special functions*. New York: Academic Press.

[120] Olver FWJ, Lozier DW, Boisvert RF, Clark CW (2010) *NIST handbook of mathematical functions*. Cambridge University Press.

[121] Osharovich G, Ayzenberg-Stepanenko M, Tsareva O (2010) Wave propagation in elastic lattices subjected to a local harmonic loading. II. Two-dimensional problems. *Continuum Mechanics and Thermodynamics* **22**, 599–616.

[122] Osharovich GG, Ayzenberg-Stepanenko MV (2012) Wave localization in stratified square-cell lattices: The antiplane problem. *Journal of Sound and Vibration* **331**, 1378–1397.

[123] Ostojastarzewski M (2002) Lattice models in micromechanics. *Applied Mechanics Reviews* **55**, 35.

[124] Paris PC, Sih GC (1965) Stress analysis of cracks. In *Fracture Toughness Testing and Its Applications*, 30–83. American Society for Testing and its Applications.

[125] Paul O, Urzhumov Y, Elsen C, Smith D, Rahm M (2012) Construction of invisibility cloaks of arbitrary shape and size using planar layers of metamaterials. *Journal of Applied Physics* **111**, 123106–123106.

[126] Pendry JB, Schurig D, Smith DR (2006) Controlling electromagnetic fields. *Science* **312**, 1780–1782.

[127] Phani AS, Woodhouse J, Fleck NA (2006) Wave propagation in two-dimensional periodic lattices. *The Journal of the Acoustical Society of America* **119**, 1995.

[128] Popa B, Zigoneanu L, Cummer SA (2011) Experimental acoustic ground cloak in air. *Physical Review Letters* **106**, 253901.

[129] Post E (1962) *Formal Structure of Electromagnetics: General Covariance and Electromagnetics*. Amsterdam: North-Holland Pub. Co.

[130] Poulton CG, Movchan AB, McPhedran RC, Nicorovici NA, Antipov YA (2000) Eigenvalue problems for doubly periodic elastic structures and phononic band gaps. *Proceedings of the Royal Society A: Mathematical, Physical and Engineering Sciences* **456**, 2543–2559.

[131] Prudnikov AP, Brychkov YA, Marichev OI (1992) *Integrals and Series*, vol. 4. Amsterdam: Gordon and Breach Science Publishers.

[132] Rahm M, Schurig D, Roberts DA, Cummer SA, Smith DR, Pendry JB (2008) Design of electromagnetic cloaks and concentrators using form-invariant coordinate transformations of Maxwell's equations. *Photonics and Nanostructures-Fundamentals and Applications* **6**, 87–95.

[133] Lord Rayleigh (1892) On the influence of obstacles arranged in rectangular order upon the properties of a medium. *Philosophical Magazine* **34**, 481–502.

[134] Rice J (1968) A path independent integral and the approximate analysis of strain concentration by notches and cracks. *Journal of Applied Mechanics* **35**, 379.

[135] Saigo M, Srivastava HM (1990) The behavior of the zero-balanced hypergeometric series ${}_pF_{p-1}$ near the boundary of its convergence region. *Proceedings of the American Mathematical Society* **110**, pp. 71–76.

[136] Savić SV, Notaroš BM, Ilić MM (2013) Conformal cubical 3D transformation-based metamaterial invisibility cloak. *JOSA A* **30**, 7–12.

[137] Schurig D, Mock JJ, Justice BJ, Cummer SA, Pendry JB, Starr AF, Smith DR (2006) Metamaterial electromagnetic cloak at microwave frequencies. *Science* **314**, 977–980.

[138] Schurig D, Pendry JB, Smith DR (2006) Calculation of material properties and ray tracing in transformation media. *Optics Express* **14**, 9794–9804.

[139] Slepyan L (2002) *Models and phenomena in fracture mechanics*, vol. 11. Springer Berlin.

[140] Spadoni A, Ruzzene M, Gonella S, Scarpa F (2009) Phononic properties of hexagonal chiral lattices. *Wave Motion* **46**, 435–450.

[141] Stenger N, Wilhelm M, Wegener M (2012) Experiments on elastic cloaking in thin plates. *Physical Review Letters* **108**, 14301.

[142] Trefethen LN, et al. (2011) *Chebfun Version 4.2*. The Chebfun Development Team. `http://www.maths.ox.ac.uk/chebfun/`.

[143] van der Pol B, Bremmer H (1950) *Operational Calculus based on the two-sided Laplace Transform*. London: Cambridge University Press.

[144] Ward AJ, Pendry JB (1996) Refraction and geometry in Maxwell's equations. *Journal of Modern Optics* **43**, 773–793.

[145] Wentzel G (1926) Eine verallgemeinerung der quantenbedingungen für die zwecke der wellenmechanik. *Zeitschrift für Physik* **38**, 518–529.

[146] Willis JR (1967) A comparison of the fracture criteria of griffith and barenblatt. *Journal of the Mechanics and Physics of Solids* **15**, 151–162.

[147] Wilson W, Yu IW (1979) The use of the j-integral in thermal stress crack problems. *International Journal of Fracture* **15**, 377–387.

[148] Zhang B, Luo Y, Liu X, Barbastathis G (2011) Macroscopic invisibility cloak for visible light. *Physical Review Letters* **106**, 33901.

[149] Zhelezina E, Jones IS, Movchan AB (2006) Singular perturbation analysis of dynamic fields in a thermoelastic solid with a small surface-breaking crack. *Acta Mechanica Sinica* **22**, 449–454.

[150] Zucker IJ (2011) 70+ Years of the Watson Integrals. *Journal of Statistical Physics* **145**, 591–612.

# Appendices

# WKB expansions

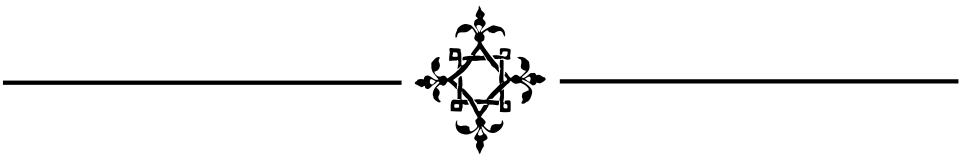

The WKB (also WKBJ and occasionally LG) expansion is a semiclassical method for approximating solutions to singularly perturbed problems. In particular, WKB expansions are employed to find approximate solutions to differential equations where the highest order derivative is multiplied by some small positive parameter, $\varepsilon$. The method was developed in the 1920's by Wentzel, Kramers, Brillouin, and Jeffreys [12, 13, 68, 87, 145], although the foundations of the method can be considered to have been developed almost a century earlier by Carlini, Liouville, and Green. The method is now standard and is included in many graduate level texts, see [7, 119] for example.

Consider the second order ordinary differential equation (Helmholtz equation in 1D)

$$\left(\varepsilon^2 \frac{\mathrm{d}^2}{\mathrm{d}x^2} + Q(x)\right) u(x) = 0, \qquad Q(x) > 0,\ 0 < \varepsilon \ll 1. \tag{1}$$

It would be natural to seek a solution of the form $u(x) \sim A(x)e^{iS(x)/\delta}$, $\delta \to 0^+$, where $A(x)$ and $S(x)$ are commonly referred to as the amplitude and phase functions respectively. However, it should be noted that in this form, the amplitude and phase functions depend on the small parameter $\delta$. The implicit dependencies may be made explicit by expanding $A(x)$ and $S(x)$ as power series in $\delta$, whence

$$u(x) \sim \exp\left\{\sum_{n=0}^{\infty} \delta^{n-1} i^n S_n(x)\right\}, \qquad \text{as } \delta \to 0. \tag{2}$$

The form (2) is the classical WKB expansion (see [7]). Alternatively, (2) may be recast as

$$u(x) \sim e^{i\varphi(x)/\delta} \sum_{n=0}^{\infty} i^n A_n(x) \delta^n, \qquad \text{as } \delta \to 0. \tag{3}$$

The above form will be most convenient for the purposes of this thesis. Direct substitution of (3) into (1) yields

$$\sum_{n=0}^{\infty} \Big\{ i^n \delta^n [\varepsilon^2 A_n''(x) + Q(x) A_n] + i^{n+1} \delta^{n-1} \varepsilon^2 [\varphi''(x) A_n(x) + 2\varphi'(x) A_n'(x)] - i^n \delta^{n-2} \varepsilon^2 [\varphi'(x)]^2 \Big\} = 0 \tag{4}$$

In order to balance the term involving $Q(x)$, the ratio $\varepsilon^2/\delta^2$ must be of order unity. Hence, $\delta \propto \varepsilon$

and for convenience one may chose $\varepsilon = \delta$. Comparing power of $\varepsilon$, a hierarchy of equations is obtained, the first of which is the *eikonal* equation for the phase

$$\varphi'(x) = \pm\sqrt{Q(x)}, \tag{5a}$$

followed by the *transport* equation

$$2\varphi'(x)A_0'(x) + A_0\varphi''(x) = 0, \tag{5b}$$

with the higher order terms satisfying

$$\varphi''(x)A_n + 2\varphi'(x)A_n' + A_{n-1}'' = 0, \qquad \text{for } n \geq 1. \tag{5c}$$

The solution to leading order is then

$$u(x) \sim Q^{-1/4}(x)\left\{c_1 \exp\left[i\varepsilon^{-1}\int_{x_0}^{x}\sqrt{Q(t)}\,\mathrm{d}t\right] + c_2 \exp\left[-i\varepsilon^{-1}\int_{x_0}^{x}\sqrt{Q(t)}\,\mathrm{d}t\right]\right\}, \tag{6}$$

where $c_1$, $c_2$, and $x_0$ are arbitrary constants. Here $Q^{-1/4}(x)$ is the solution of the *transport* equation (up to a multiplicative constant, and the exponential functions satisfy the *eikonal* equation. It is remarked that the leading order solution (6) for the Helmholtz equation is equivalent to that derived in [7] for the Schrödinger equation, if $Q(x)$ is taken to be strictly negative in [7]; it is emphasised that Bender and Orsza [7] took the WKB expansion in the form (2), as opposed to the form (3) as is done here.

Of course, one may obtain more accurate representations of $u(x)$ by continuing to construct the hierarchy of equations (5). However, this isn't always necessary and much information may be extracted from the *eikonal* and *transport* equations without recourse to the leading, or higher order, solutions. Indeed, for the purposes of this thesis, it will be sufficient to simply consider the *eikonal* equation.

In chapter 7, the WKB expansion is applied to equations of the form

$$\left[\varepsilon^2\nabla\cdot P(\boldsymbol{x})\nabla + Q(\boldsymbol{x})\right]u(\boldsymbol{x}) = 0, \qquad \text{for } \boldsymbol{x} \in \Omega \subset \mathbb{R}^2 \tag{7}$$

Nevertheless, the WKB approach outlined here remains applicable with the extension to two dimensions adding only to the tediousness of the algebra, rather than any additional technical difficulty.